

Dissertation zur Erlangung des Doktorgrades
der Fakultät für Chemie und Pharmazie
der Ludwig-Maximilians-Universität München

**Directed invasion and migratory modes of
cancer cells in structured 3D collagen
matrices**

Florian Michael Geiger

aus

Memmingen, Deutschland

2021

Erklärung

Diese Dissertation wurde im Sinne von § 7 der Promotionsordnung vom 28. November 2011 von Frau Ass. Prof. Dr. Hanna Engelke betreut.

Eidesstattliche Versicherung

Diese Dissertation wurde eigenständig und ohne unerlaubte Hilfe erarbeitet.

München, den 28.05.2021

Florian Geiger

Dissertation eingereicht am 14.04.2021

1. Gutachter: Ass. Prof. Dr. Hanna Engelke
2. Gutachter: Prof. Dr. Stefan Zahler

Mündliche Prüfung am 26.05.2021

Danksagung

Ich möchte mich zuallererst ganz herzlich bei meiner Doktormutter Ass. Prof. Dr. Hanna Engelke bedanken, die mich für diese Arbeit in der Welt der Zellbiologie begeistert hat und als meine Betreuerin immer einen hilfreichen Rat bei Problemen hatte. Danke auch für dein Verständnis und für die Freiheiten, mich kreativ und handwerklich auszuleben, die du mir gegeben hast. Außerdem danke ich dir, dass du mein Potential erkannt und weiter gefördert hast.

Mein besonderer Dank gilt Prof. Dr. Thomas Bein, der es mir ermöglicht hat, in seinem Arbeitskreis meine Dissertation an solch einem interessanten Thema anzufertigen. Auch will ich mich für die informativen Gespräche und die Eröffnung neuer Blickwinkel bedanken. Danke auch für die Bereitstellung vieler hilfreicher Geräte und Materialien, die für meine Forschung unerlässlich waren.

Vielen Dank an Prof. Dr. Stefan Zahler für die Übernahme der Zweitkorrektur meiner Dissertation. Außerdem möchte ich mich für die erfolgreiche Zusammenarbeit während meines ersten großen Projekts und für die vielen guten Tipps und Verbesserungsvorschläge in meiner ersten Veröffentlichung bedanken.

Ein herzliches Dankeschön an unsere Sektretärin Corinna Heidt, die sich um die alltägliche Bürokratie gekümmert hat und bei Problemen immer mit Rat und Tat zur Seite stand. Vielen Dank auch an Tina Reuther für den Überblick über all unsere Chemikalien und Verbrauchsmaterialien und dass diese immer zur Genüge vorhanden waren. Danke Markus Döblinger für die kompetente Beratung in Sicherheitsfragen und den ein oder anderen Rat im Bezug auf Karriere und Zukunft. Dankeschön Steffen Schmidt für organisatorische Hilfe und die Zeit die du mich in deinem Büro unterkommen hast lassen.

Ich möchte mich zudem bei allen Kooperationspartnern, die ich im Laufe der Zeit hatte, bedanken. Vielen Dank Daniel Rüdiger für die tollen rheologischen Messungen am AFM und die netten Unterhaltungen, um die Wartezeiten zu überbrücken. Ein großes Dankeschön an Manuel Brugger, der mich mit der SAW Thematik vertraut gemacht hat, mir viele hilfreiche Geräte dazu gebaut hat und in Augsburg auch neue Sichtweisen auf diese Technik eröffnet hat. Danke Lukas Schnitzler und Dr. Christoph Westerhausen, die meinen Ergebnissen mit

vielen Skype Gesprächen, Experimenten und theoretischen Berechnungen den letzten Schliff gegeben haben. Especially, i want to thank Alex Borodavka for the productive discussions and measurements, during your visits in munich and for the funny conversations and little snacks we had back then. Danke auch an Nada Raddaoui für die gute Zusammenarbeit und Unterstützung mit der Click-Chemistry. Dankeschön auch an Dr. Evelyn Plötz, die mir immer weiterhelfen konnte, wenn ich Fragen zur Mikroskopie oder Bedarf an verschiedenen Farbstoffen oder Filtern hatte. Ein großer Dank geht auch an Ulrich Lächelt, Christof Mast, Charlott Leu und Christian Fritz, die mich alle bei meinem Mikrofluidikprojekt tatkräftig mit neuen Ideen, Ratschlägen und vor allem mit neuen Prototypen für meine Flusskammer versorgt haben. Dank euren Bemühungen konnte dieses Thema viel schneller veröffentlicht werden. Ein großes Dankeschön geht auch an meine Praktikantinnen Sarah Young, Laura Schwabbauer und Britta Weidinger. Es hat mir großen Spaß gemacht, mit euch zu forschen und euch die Arbeit mit Zellen und Mikroskopen näher zu bringen.

Als nächstes möchte ich mich beim kompletten Arbeitskreis Bein bedanken. Ich wurde von euch sehr herzlich aufgenommen und schnell in die Gruppe integriert. Ihr habt mich sehr geprägt und ich werde die Zeit mit euch nie vergessen. Danke auch an meinen langjährigen Freund und Bürokollegen Bernhard, dass du mich bei den alltäglichen Herausforderungen in der Uni immer unterstützt hast und es so lange mit mir ausgehalten hast.

Vielen lieben Dank an meine Freundin Tina. Danke, dass du diese doch anstrengende Zeit mit mir durchgestanden und mich mit deiner fröhlichen und offenen Art immer wieder aus Motivationstiefs herausgeholt hast. Du bist toll, vielen Dank dass du mich immer unterstützt.

Des Weiteren will ich mich bei meinen Freunden bedanken, mit denen ich schöne Zeiten außerhalb der Arbeit erleben durfte und die mir den nötigen Ausgleich an manchen Feierabenden oder Wochenden verschafft haben.

Zuletzt gilt mein besonderer Dank meiner Familie. Ihr habt mich in allen Entscheidungen immer unterstützt und bekräftigt. Ihr habt mir den Halt gegeben, diese lange Zeit problemlos durchzustehen. Dank euch stehe ich dort, wo ich heute bin und dafür bin ich euch sehr dankbar.

Abstract

Cancer is a disease responsible for a large number of deaths in society. Specifically, cancer cell migration is associated with malignancy and difficult to treat. Migration is influenced by mechanical and chemical properties of the environment as well as the cellular phenotype and behavior. Cancer cells can adapt to the properties of their environment by adjusting their phenotype and they can alter the tissue around them. In the following, the influence of fiber stiffness, confinement, and adhesion properties on cancer cell migration in porous collagen gels is investigated. Soft collagen gels with short fibers hinder migration and promote a round, non-invasive phenotype. Longer and stiffer collagen fibers lead to an adhesive phenotype and confined migration due to their more adhesive properties. With TGF- β , adhesion is lowered and the cancer cells switch from the adhesive phenotype to highly motile amoeboid phenotypes. In stiff collagen gels with pores of about cell size the highest migration speeds and longest displacements are achieved by cells with an amoeboid phenotype. The mechanical properties of collagen gels directly influence the phenotype and subsequently migration, which is most efficient with an amoeboid phenotype and in gels with stiff fibers, cell sized pores, and low adhesion.

This was also investigated for cancer cell aggregates in highly oriented collagen gels. By using a microfluidic channel setup the collagen fibers were aligned tangentially and radially with respect to the spheroid surface. The alignment can be described by finite element simulations. This specific orientation of the collagen matrix influenced invasion from the cancer cell spheroid, creating a strong bias of invasion towards radial as compared to tangential fiber orientation. Brownian diffusion model simulations suggest a completely blocked migration perpendicular to fibers, allowing migration only along fibers. The actual invasion is slowed down in areas with tangentially oriented fibers, but it is still possible.

Furthermore a new method to detect proliferating tumor cells in situ by using multiple consecutive click reactions with dendrimeric molecules and clickable dyes is presented. Cells are grown in the presence of ethynyl-dU (EdU), where the EdU becomes part of the genome during proliferation. After the cells were fixed and permeabilised, the incorporated alkynes of the EdU are functionalized with azide-containing fluorophores through the Cu^I-

catalysed alkyne–azide click reaction. These azide- and alkyne-modified dendrimers allow the establishment of sandwich-type detection assays, which have improved sensitivities, signal intensities and signal-to-noise ratios in reference to comparable techniques.

The RNA-FISH-based detection of RNA was also improved in the following by increasing the number of fluorophores per oligonucleotide probe. Currently, the RNA-FISH detection method uses sets of single-fluorophore-containing oligonucleotide probes that hybridize to the mRNA of interest. This reliable detection of transcription events and the localization and quantification of particular mRNA allows disease states to be characterized more directly. For the early detection of virus infections, when spreading of the virus in- and outside of the organism can be controlled much better, this is particularly important (e. g. Sars-CoV-2). To receive a reliable signal, a large number of probe strands (>30) is required, but the more oligonucleotide probes are used, the higher the off-target binding effects, which create background noise. Through the use of click chemistry and alkyne-modified DNA oligonucleotides multiple-fluorophore-containing probes were prepared. These triply labeled probes allow reliable detection and direct visualization of mRNA with only a very small number (5–10) of probe strands. In an *in situ* experiment this lead to lower background noise and a better signal to noise ratio, whereby viral transcripts can be detected 4 hours after infection.

RNA viruses induce formation of subcellular organelles that provide microenvironments beneficial to their replication. These replication factories of rotaviruses are protein-RNA condensates, formed via liquid-liquid phase separation. Through phase separation rotavirus proteins NSP5 and NSP2 form RNA-rich condensates, which can be reversibly dissolved *in vitro* by aliphatic diols. These RNA-protein condensates became less dynamic and impervious to aliphatic diols during infection, indicating a transition from a liquid to solid state. The selective enrichment of viral transcripts seems to be a unique feature of these condensates, but other aspects of assembly are similar to the formation of cytoplasmic ribonucleoprotein granules. By targeting these complex RNA-protein condensates, that underlie replication of RNA viruses, promising novel therapeutic approaches could be developed.

Table of contents:

1. Introduction	1
1.1. Characteristics of cancer	1
1.2. Tissue invasion and metastasis formation	5
1.2.1. Dormant cancer cells.....	7
1.2.2. Biochemical feedback on cancer cell invasion	7
1.3. Influence of the extracellular matrix on cancer cell invasion	10
1.3.1. Cancer cell mobility on surfaces	14
1.3.2. Movement of cancer cells in 3D model systems	16
1.4. Designed model systems for tumor cell motility	24
1.5. RNA labeling as tool to investigate cancer and virus replication	29
1.6. References.....	32
2. Characterization and methods.....	53
2.1. Fluorescence microscopy.....	53
2.1.1. Widefield microscopy	55
2.1.2. Spinning disk confocal microscopy	58
2.2. Rheology	61
2.3. Atomic force microscopy.....	64
2.3.1. Rheological measurements.....	66
2.4. Surface acoustic waves.....	67
2.5. Microfluidics.....	70
2.6. Polymerization control of collagen	73
2.7. References.....	76
3. Fiber stiffness, pore size and adhesion control migratory phenotype of MDA-MB-231 cells in collagen gels.....	81

3.1. Introduction.....	81
3.2. Results.....	83
3.3. Discussion.....	91
3.4. Experimental part	93
3.4.1. Cell culture.....	93
3.4.2. 3D collagen matrices	93
3.4.3. Spinning disk microscopy.....	94
3.4.4. Rheology.....	94
3.4.5. Image analysis.....	95
3.5. References	96
3.6. Appendix.....	101
4. Directed invasion of cancer cell spheroids inside 3D collagen matrices oriented by microfluidic flow in experiment and simulation	107
4.1. Introduction.....	107
4.2. Results.....	109
4.3. Discussion.....	118
4.4. Experimental part	120
4.5. References	125
4.6. Appendix.....	129
5. Dendrimer-based signal amplification of click-labelled DNA in situ.....	137
5.1. Introduction.....	138
5.2. Results and discussion.....	139
5.3. References	146
5.4. Appendix.....	148
5.4.1. General Methods	148

5.4.2. Chemical Synthesis	149
5.4.3. Proof of principle of the click reactions on oligonucleotides	155
5.4.4. High throughput screening.....	179
5.4.5. Microscopy and image analysis:	179
6. Supersensitive multicolor RNA-FISH for early virus detection and flow-FISH by using click chemistry	181
6.1. Introduction	182
6.2. Results and discussion	183
6.3. Conclusions.....	191
6.4. References.....	191
6.5. Appendix.....	194
7. Rotavirus Replication Factories Are Complex Ribonucleoprotein Condensates	211
7.1. Introduction	211
7.2. Results	213
7.3. Discussion	228
7.4. Materials and Methods.....	234
7.5. References.....	242
7.6. Appendix.....	252
8. Conclusion and Outlook.....	259

1. Introduction

1.1. Characteristics of cancer

Cancer is one of the main causes of death worldwide. In Germany alone there were nearly half a million diagnosed cases of cancer in 2016 [1]. Despite several decades of intense research on this illness the mechanisms and functions regarding cancer are not fully understood and will require a lot more research in the future. However there were found ten enabling characteristics (figure 1.1) that are shared in common by most types of human tumors [2, 3].

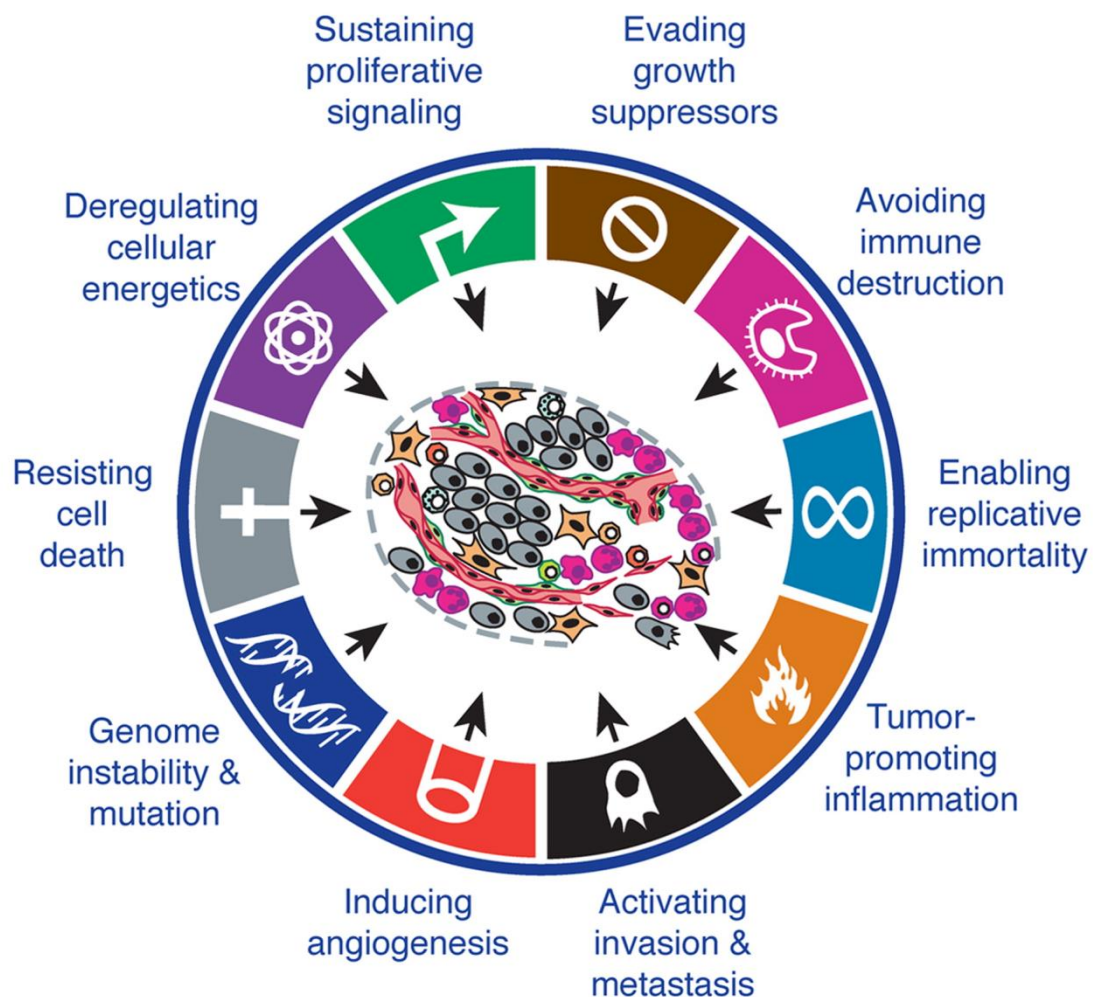


Figure 1.1: Ten criteria most types of human tumor share in common: evasion of growth suppressors (brown), avoidance of immune destruction (magenta), enabled replicative

immortality (light blue), inflammation promoting the tumor (orange), activated invasion and metastasis (black), induced angiogenesis (red), genome instability and mutation (dark blue), resistance to cell death (grey), deregulated cellular energetics (violet), sustain of proliferative signaling (green) [3].

Most prominent is a genomic instability in cancer cells, which leads to random mutations (figure 1.1: dark blue). These mutations can lead to the appearance of other enabling characteristics. The genomic instability can be derived directly from external influences (e.g. radiation, chemicals, viral infection) or from a breakdown in one or several components of the genomic maintenance machinery inside the cells [4]. Spontaneous mutation is usually very low during each cell generation. To acquire enough mutant genes to trigger tumorigenesis, cancer cells often increase their mutation rates through an increased sensitivity to mutagenic agents, altered genomic maintenance machinery or compromised surveillance systems for genomic integrity [4-9].

A second enabling characteristic involves the inflammatory state of premalignant and malignant lesions, driven by cells of the immune system (figure 1.1: orange) [10]. Inflammation can supply bioactive molecules to the tumor microenvironment, that support other tumor criteria, including growth factors that sustain proliferative signaling, survival factors that limit cell death, proangiogenic factors, extracellular matrix-modifying enzymes that facilitate angiogenesis, invasions and metastasis [11-14]. Additionally, inflammatory cells can release reactive oxygen species or other chemicals, which accelerate the genome instability and progress genetic mutations [12].

Cells and tissues are constantly monitored by the immune system and it can recognize and eliminate the vast majority of incipient cancer cells [15-17]. Solid tumors have avoided detection by the immune system and limited the immunological killing of cancer cells (figure 1.1: magenta). In fact highly immunogenic cancer cells are often eliminated by a sound immune system, but weakly immunogenic variants sometimes survive and can grow solid tumors [16-18]. Cancer cells also evade immune destruction by disabling components of the immune system, they for example paralyze infiltrating cytotoxic T lymphocytes (CTLs) and natural killer (NK) cells, by secreting TGF- β or other immunosuppressive

factors [19, 20]. Another mechanism is the recruitment of inflammatory cells that are actively immunosuppressive, e.g. regulatory T cells (Tregs) and myeloid-derived suppressor cells (MDSCs) [21, 22].

Another characteristic is the self supply with growth signals (figure 1.1: green). Normal tissues carefully control the production and release of growth-promoting signals that instruct entry into proliferation. Thereby, a homeostasis of cell number and thus a normal tissue architecture and function is ensured. Cancer cells can either produce growth factors by themselves, resulting in autocrine proliferation, or stimulate normal cells within the supporting tumor-associated stroma to supply them with various growth factors. Another way to deregulate the growth signals is to alter number or structure of the receptor proteins displayed at the cancer cell, or the activation of components of signaling pathways operating downstream of these receptors [23-28].

The uncontrolled cell proliferation requires adjustments of the energy metabolism in order to fuel cell growth and division (figure 1.1: violet). Cancer cells can reprogram their glucose metabolism by limiting their energy metabolism largely to glycolysis, even in the presence of oxygen, leading to a state that has been termed “aerobic glycolysis” [29-31]. To compensate for the ~18-fold lower efficiency of ATP production, glucose transporters, notably GLUT1, which increases glucose import into the cytoplasm are upregulated [32-24]. Increased glycolysis also allows the diversion of glycolytic intermediates into various biosynthetic pathways, which facilitate the biosynthesis of the macromolecules and organelles required for assembling new cells [35, 36]. Some tumors have been found to contain another population of cancer cells, which use the lactate produced by the glucose-dependent cells as their main energy source by employing part of the citric acid cycle [37-39].

The evasion of growth suppressors is also an important factor for cancer development (figure 1.1: brown). Antigrowth signals block proliferation and ensure cellular quiescence and tissue homeostasis. They are received via surface receptors on cell membranes, similar to their growth signal counterparts and are evaded by similar means [40]. Tumor cells disrupt for example the pRb pathway, governed by the transforming growth factor beta (TGF- β), by downregulating or altering their TGF- β receptors [41-44]. Cancer cells can also

1.1. Characteristics of cancer

turn off expression of integrins and other cell adhesion molecules that send antigrowth signals, favoring instead those that convey progrowth signals [2].

Another important criterion for tumor cells is the resistance against cell death (figure 1.1: gray). Programmed cell death by apoptosis is induced for example by DNA damage associated with hyperproliferation or signaling imbalances, resulting from elevated levels of oncogene signaling, and serves as a natural barrier to tumor development [45-47]. Most commonly, cancer cells lose a critical DNA-damage sensor that functions via the TP53 tumor suppressor and induces apoptosis. Alternatively, tumors increase expression of antiapoptotic regulators, or of survival signals, by downregulating proapoptotic factors [3].

Acquiring limitless replicative potential is another key factor for tumor formation (figure 1.1: light blue). In each cell cycle, during transcription of the chromosomes, normal cells lose 50–100 bp telomeric DNA and after too many doublings a massive cell death caused by karyotypic disarray associated with end-to-end fusion of chromosomes occurs [48, 49]. In cancer cells the expression of the telomerase enzyme, which adds hexanucleotide repeats onto the ends of telomeric DNA, is upregulated, or the telomeres are protected through recombination-based interchromosomal exchanges of sequence information [50-52]. These mechanisms keep the telomeres above the critical length and therefore enable a limitless replicative potential.

A tumor needs to be supplied with additional oxygen and nutrients due to the unregulated proliferation of the cancer cells. A stimulated angiogenesis is therefore a necessity for explosive growth of a tumor (figure 1.1: red). In a tumor several proangiogenic signals, such as different fibroblast growth factors (FGF), or vascular endothelial growth factor (VEGF), are upregulated and causing normally quiescent vasculature, to continually sprout new vessels that help sustain expanding neoplastic growths [53-57]. These blood vessels, produced within tumors, often show convoluted and excessive vessel branching, distorted and enlarged vessels, erratic blood flow, microhemorrhaging, leakiness, and abnormal levels of endothelial cell proliferation and apoptosis [58, 59].

The last criterion is the ability of a tumor to invade surrounding tissue and form metastasis (figure 1.1: black). During the development of most types of human cancer, primary tumor cells spawn pioneer cells that move out and invade adjacent tissue. Through the vascular

system these cells can travel to distant sites where they may succeed in founding new colonies. This formation of metastases is the cause of 90% of human cancer deaths [60].

These ten characteristics already give us some targets for possible therapeutics, but the more precise the mechanisms and processes behind tumor formation are understood the better the treatment of this mortal disease becomes [3]. The capability of cancer cells for tissue invasion and metastasis enables them to spread through the whole human body, which complicates treatment significantly. Therefore, the main focus of this thesis is on understanding the principles behind tumor cell movement through its surrounding tissue.

1.2. Tissue invasion and metastasis formation

Invasion and metastasis are extremely complex processes and the influence of genetic, biochemical or biophysical factors remain incompletely understood. The metastasis cascade (figure 1.2) is a multistep process, which begins with cells escaping from the confinement of the primary tumor site via breakdown of the basement membrane. This process is initiated by the activation of signaling pathways that regulate cytoskeletal dynamics, loss of adhesion amongst tumor cells and turnover of the surrounding extracellular matrix (ECM) [61]. Then tissues, as well as nearby blood and lymphatic vessels, are invaded (intravasation). Dispersion of tumor cells via the lymphatic system leads to lymph node metastasis in the first instance, while dissemination via the blood circulation (hematogenous) can lead to metastasis at distant sites [62, 63]. These circulating tumor cells (CTCs) exist as single cells or clusters coated with platelets and are transported via vascular systems to distant tissues, where they intercept into smaller capillaries, or adhere to the larger blood vessels. The cells, which survive shear stress and evade clearance by the immune system, exit the blood vessel through paracellular, or transcellular transendothelial migration (extravasation) and colonize the distant tissue [64]. This process can be promoted by alterations of the surrounding matrix, induced by secreted factors (cytokines) and extracellular vesicles (exosomes) derived from the primary tumor, before the establishment of metastases [65]. Pre-metastatic niches are formed through tissue alterations, which involve fibroblasts, endothelial cells and immune cells and provide a beneficial environment for the CTCs to

1.2. Tissue invasion and metastasis formation

settle down and grow [66, 67]. These CTCs are called disseminated tumor cells (DTCs) and form small nodules of cancer cells (micrometastases), which can grow into macroscopic tumors [68].

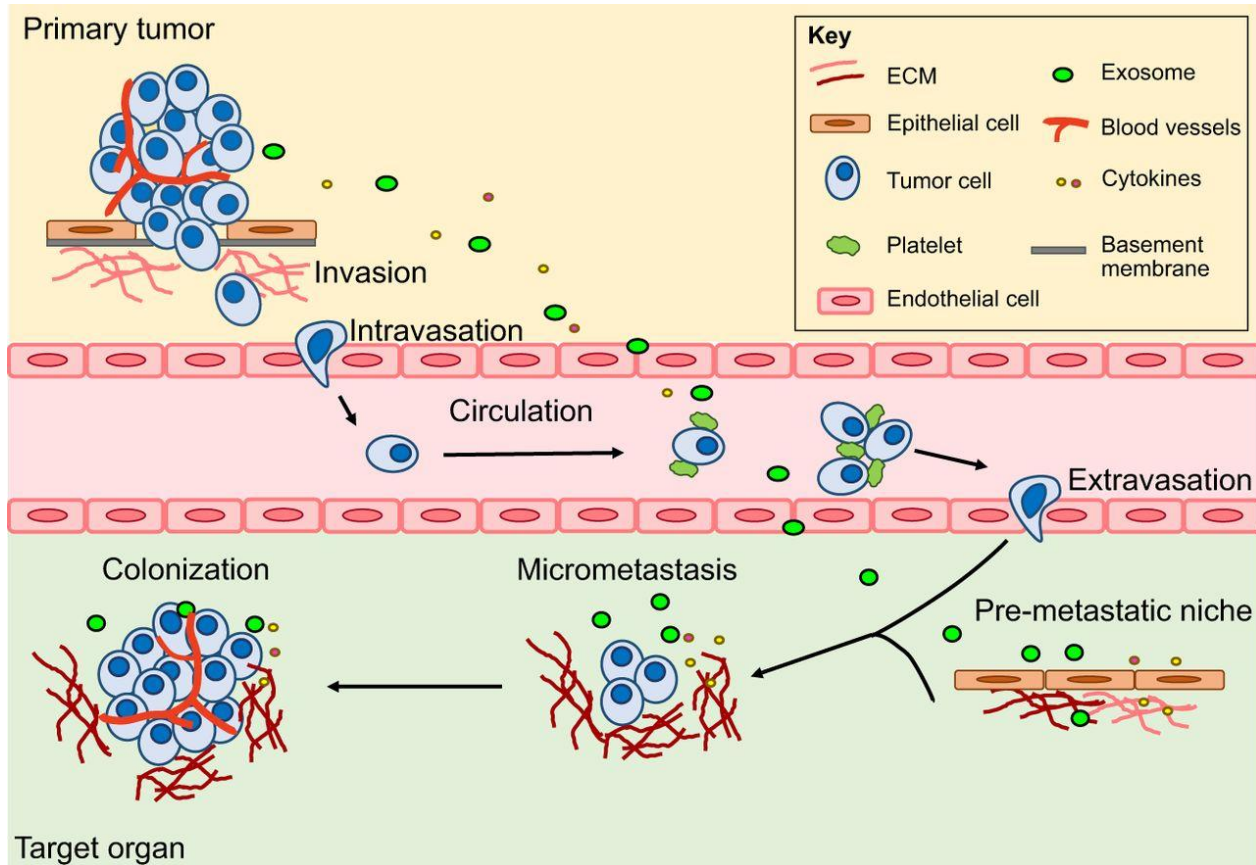


Figure 1.2: Schematic of the multistep metastatic cascade, involving tumor cells invading the surrounding tissue, intravasating into blood vessels, being transported to and extravasating into distant tissue. Sometimes tumor cells settle in pre-metastatic niches, form micrometastases and proliferate into large macrometastases during the colonization process [69].

Less than 1% of tumor cells undergo this process, but metastasis contributes to more than 90% of cancer-related deaths [70, 71]. Cells in metastatic colonies may proceed to spread, not only to new sites in the body, but they also can go back to the primary tumor site. This self-seeding can accelerate tumor growth, angiogenesis, and stromal recruitment [72].

Cancer cells not necessarily disseminate from the fully malignant primary tumor, but can disperse remarkably early from ostensibly noninvasive premalignant lesions [73, 74].

1.2.1. Dormant cancer cells

Successful dissemination, however, is not strictly coupled with an immediate colonization of the invaded tissue. DTCs can be present for years or decades and stay in a latent state as single cells or micrometastases [75-77]. This tumor dormancy can be induced for example by tissue microenvironments that are not suitable for the cancer cells, who try to colonize it. Most disseminated cancer cells are likely to be poorly adapted, at least initially, to the microenvironment of the tissue in which they have landed. They have to adapt to the new environment via tissue remodeling, or mutations until they thrive in the foreign tissue [76, 77]. A specific example is inadequate vascularization. When DTCs are not provided with sufficient nutrients they can shrink and adopt a state of reversible dormancy. They may exit this state and resume active growth when angiogenesis has progressed, and the explosive proliferation can be sustained with enough nutrients [78-80]. Another reason can be the release of systemic suppressor factors by the primary tumor. Once it has been surgically removed or pharmacologically destroyed, macroscopic metastases may erupt again from these dormant cells [76, 77]. The anti-growth signals can also be embedded in the normal extracellular matrix [81]. Other factors resulting in DTCs entering a quiescent state are clearance or suppression of the DTCs by the immune system. If the cancer cells were held in check, in a dormant state, by a fully functional immune system, they can be reactivated by an illness or the treatment of the primary tumor with chemotherapeutic agents, which weaken the immune system [76, 82].

1.2.2. Biochemical feedback on cancer cell invasion

Metastasis involves genetic and epigenetic alteration of tumor cells, but it also greatly depends on the biochemical and biophysical microenvironments of the cancer cells [83-85]. Transcriptional factors, for example, including Snail, Slug, Twist, and Zeb1/2, responsible

for the epithelial-mesenchymal transition (EMT) and related migratory processes during embryogenesis, have been found to cause metastasis, when overexpressed at the wrong place [86-88]. In addition, these transcription factors can cause loss of adherens junctions, expression of matrix-degrading enzymes, increased motility and heightened resistance to apoptosis, which are all important traits in the processes of invasion and metastasis. Several of these transcription factors can directly repress E-cadherin expression, a homotypic cell-to-cell interaction molecule on epithelial cells. E-cadherin induces bridges between adjacent cells, resulting in the suppression of growth, motility and invasiveness [89, 90]. Furthermore, an altered distribution of the intracellular transcriptional regulator β -catenin, e.g. caused by stromal cells, or cytokines, can change the tumor cells behavior and induce malignant cell phenotypes. The EMT-inducing transcription factors are able to orchestrate most steps of the invasion-metastasis cascade, except for the colonization process [14, 91].

Also several different protein classes, which are involved in the binding of cells to their surrounding tissue and convey regulatory signals, are altered in cells with invasive or metastatic properties. The affected proteins include cell-cell adhesion molecules (CAMs), members of the cell-to-cell interaction controlling, immunoglobulin and calcium-dependent cadherin families, and integrins, which link cells to extracellular matrix substrates. Changes in expression of these CAMs of the immunoglobulin superfamily also appear to play a critical role in the invasion and metastasis processes [92, 93]. N-cadherin, for example, which is normally expressed in migrating neurons and mesenchymal cells during organogenesis, is upregulated in many invasive carcinoma cells [94].

An adjusted integrin expression is also common in invasive and metastatic cells, due to the different tissue microenvironments they experience during their journeys. The cell biological effects of integrins can't be described by a small number of mechanistic rules, due to the large number of distinct integrin genes, the even larger number of heterodimeric receptors resulting from combinatorial expression of various α and β receptor subunits and the complex signals emitted by the cytoplasmic domains of these receptors [95, 96]. But evidently these integrin receptors can induce or inhibit invasive and metastatic behavior. A successful colonization of new sites demands adaptation through shifts in the spectrum of

integrin α or β subunits displayed by the migrating cells. These novel permutations result in different integrin subtypes with distinct substrate preferences. The carcinoma cells shift their expression to integrins that preferentially bind the degraded stromal components produced by extracellular proteases (e.g., $\alpha3\beta1$ and $\alphaV\beta3$) and thus facilitate invasion [97, 98].

Another parameter involved in the invasive and metastatic capability of cancer cells are extracellular proteases [99, 100]. In tumor cells protease genes get upregulated, inhibitor genes are downregulated and inactive zymogen forms of proteases are converted into active enzymes, causing matrix-degrading proteases to bind to specific protease receptors, or integrins on the cell surface [101, 102]. The increased release in the cells vicinity and docking of active proteases on the surface can facilitate invasion by cancer cells into nearby stroma, across blood vessel walls, and through normal epithelial cell layers. Additionally, other human tumor criteria are influenced by the proteases, including angiogenesis and growth signaling [101-103]. Furthermore, cancer cells recruit other cells to produce stimulants for invasion and metastasis formation. For example, mesenchymal stem cells (MSCs) present in the tumor stroma have been found to secrete CCL5/RANTES in response to signals released by cancer cells. The cytokine CCL5 in turn acts on the cancer cells to stimulate invasive behavior [104]. In many carcinoma types matrix-degrading proteases are produced by conscripted stromal and inflammatory cells [101, 105, 106]. These conscripted cells then release the proteases for the carcinoma cells. For example, certain cancer cells induce urokinase (uPA) expression in cocultured stromal cells, which then binds to the urokinase receptor (uPAR) expressed on the cancer cells [107]. This activation of extracellular proteases and the altered binding specificities of cadherins, CAMs, and integrins are a necessity to develop invasive and metastatic capabilities. But the molecular mechanisms and regulatory circuits that govern these processes remain poorly understood and seem to differ from one tissue environment to another.

1.3. Influence of the extracellular matrix on cancer cell invasion

The extracellular matrix is a mechanically stable network for epithelial cells. It is composed of a biopolymer fiber matrix of proteins, proteoglycans and glycosaminoglycans that differ in composition and structure throughout various parts of the body. The size of the biopolymer fibers, the density and interconnection of the fiber network determine the mechanical and morphological properties of the extracellular matrix (ECM) [108].

The ECM morphology has a direct impact on the cells travelling through it, for example if the elongated cell, or more precisely the nucleus cross-section, is the same size or slightly below the mesh size of the matrix, the cells can move freely through the network. But in an ECM with much larger mesh size, the cell migration is hindered due to a loss of cell-fiber attachment sites, which are needed for pushing or pulling the cells onward. On the other hand, if the mesh size is too small, the cells could get stuck in the matrix [109]. The cells sense these properties and can adapt to them by changing the mode of movement, e.g. if there is a high confinement and low adhesion, some cells switch to an amoeboid migration mode. Amoeboid migration is characterized through actin-rich pseudopods, hydrostatically-generated blebs and a highly-contractile uropod, resulting in a rapid motility. Furthermore; the cells show weak or absent adhesion to the network and little or no extracellular matrix proteolysis. If cells face a pore smaller than their cross section, they can force the fibers of the matrix out of the way and remodel their shape until they fit through, or degrade the network with proteolytic enzymes [110-112].

The ability of cells to perceive mechanical properties of their surroundings is known as mechano-sensing and can be facilitated by integrin-mediated adhesions and downstream mechanosensor protein signaling [113]. The force that cells need to apply on the fibers to move, while pushing them out of the way, is determined by the rheological properties of the ECM. Rheological properties that can influence the invasion are frequency-, strain- and strain-rate-dependent visco-elastic shear modulus, strain-dependent plasticity, compressibility, and Poisson-ratio. These mechanical parameters are strongly determined by structural protein content (e.g. collagen or elastin), fiber thickness and the extent of intrafibrillar cross-links [114]. A stiff matrix allows cell protrusions, high-traction forces

and elongated cell shapes, through a reinforcement of focal adhesions and increased RhoA-mediated actomyosin contraction [115]. In contrast, a soft surrounding ECM enables a round cell shape with little focal adhesion reinforcement and cytoskeletal contractility [116]. This effect on the cells leads to durotaxis, a stimulation of directed cell migration to a matrix region with greater stiffness [117].

Especially tumor cells remodel the ECM, making it stiffer and thus inducing invasion. The higher rigidity is accompanied by increased collagen crosslinking, enhanced PI3 kinase activity and increased focal adhesion formation [118]. Furthermore, cancer cells align the fibers of the matrix and orient themselves along these aligned fibers. This behaviour is mediated by mechanosensory integrins that, together with Rho/ROCK-mediated cytoskeletal orientation and directional contraction, further increases directional persistence in cell invasion [119, 120].

Tumor cells migrate either collectively through connective tissue, while retaining their intracellular junctions, or they convert into individually migrating cells. The loss of polarity and cell-cell adhesion in place of invasive properties is called epithelial-mesenchymal transition (EMT) and is caused by the downregulation of E-cadherin due, to the suppression of transcriptional regulators like Snail or Twist (figure 1.3) [121]. The EMT is a relatively slow process, due to the extensive alterations in gene transcription needed. The migration modes adapted by the invading single cells are referred to as either mesenchymal, or amoeboid [122]. During ECM invasion, single cancer cells can switch their migration mode depending on the suppression or enhancement of specific molecular pathways and depending on the surrounding ECM properties. This process is called mesenchymal-amoeboid transition (MAT), or amoeboid-mesenchymal transition (AMT), depicted in figure 1.3. Cancer cells have an abnormal plasticity and can quickly adapt to their surrounding tissue environment, for example through switching between those two modes. This process is very fast compared to the EMT and can happen in minutes [108].

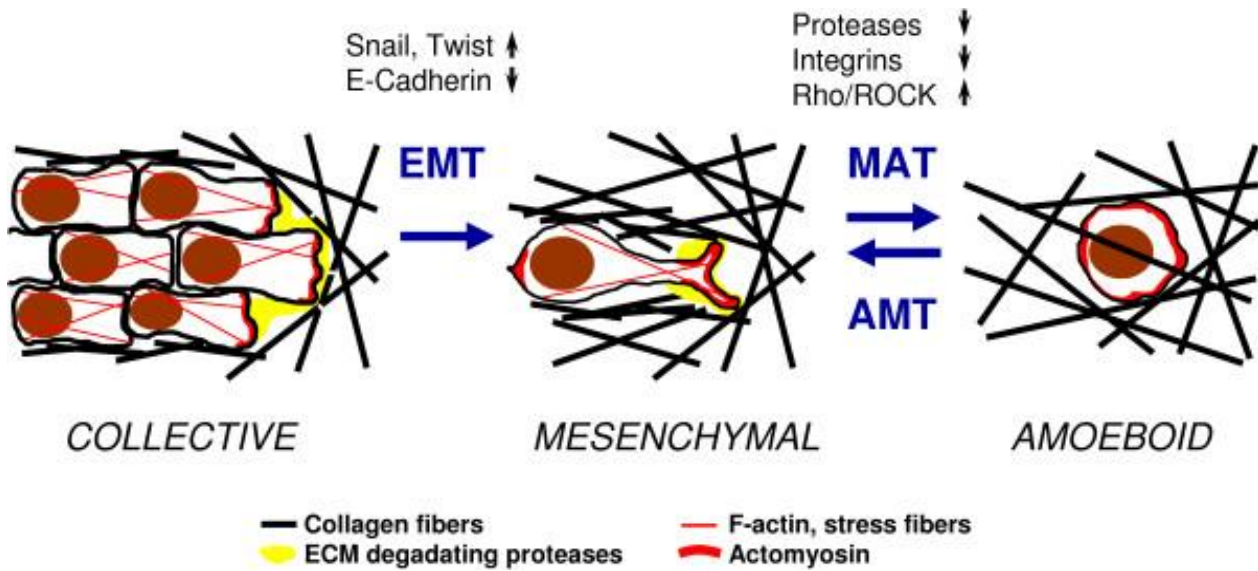


Figure 1.3: Collective and single cell invasion modes of cancer cells with the different transition capabilities, epithelial-mesenchymal transition (EMT), mesenchymal-amoeboid transition (MAT) and amoeboid-mesenchymal transition (AMT) [108].

The mesenchymal invasion mode can be observed with fibroblasts, keratinocytes, endothelial cells, macrophages and many tumor cells types. The cells are polarized and have an elongated shape with one or more leading pseudopods. They move through the formation of actin-rich filopodia and lamellipodia at the leading edge, which is regulated by the Rac-GTPase and Cdc42. The cells then adhere to the ECM, where they form stress fibers and after a contraction, the cells detach from the matrix at their rear end. By repeating the adherence, contraction and detachment process the cells move forward [123-125]. This process can be supported by ECM-degrading enzymes (e.g. MT1-MMP, cathepsins), if the surrounding matrix is too dense [126, 127]. The proteolytic remodeling of the ECM is critical for mesenchymal tumor cell invasion. Migrating cancer cells can undergo a MAT through the influence of physical properties of the surrounding matrix, or after the blocking of pericellular proteolysis or integrins, to continue their movement with an amoeboid-like invasion [128, 129].

The amoeboid migration mode is derived from the motility of amoeba and has been observed with leukocytes and many different tumor cells. The usually round cells have a

more uniform distribution of cortical actin and move through alternating expansion and contraction of the cell body. This process relies on Rho-GTPase activated myosin contractility. They form either F-actin networks, which are regulated by actin-myosin interactions, or membrane blebs in the direction of migration [129-133]. A strong characteristic of amoeboid migration is weak or absent adhesion to the matrix and independency on proteolytic degradation of the ECM. Amoeboid cells can squeeze through the network at relatively high velocities. Depending on the stiffness of the tissue and the used cell line, velocities up to 25 $\mu\text{m}/\text{min}$ can be observed in a 3D environment *in vitro* [134].

In a stiff ECM fibroblasts use a lobopodial movement mode, where they have an elongated shape and translocate using blunt, cylindrical protrusions. When surrounded by a soft collagen matrix the cells move in a lamellipodial fashion with branched, finger-like pseudopodia with Rac1 and Cdc42 activated at the tips. Both these movement modes can be canceled by integrin inhibition, because their motion depends on integrin-based adhesions. The nuclei of the fibroblasts migrating in the ECM are located at the center or rear of the cells [153]. However, epithelial cells migrating in 3D collagen matrices have their nuclei at the cell front, with the cell body trailing behind. The nuclei are driven forward with actomyosin contraction, leading the migration of these cells. Normally, cell migration in ECMs depends on myosin based contraction within the pseudopodia [154].

The network's rigidity not only changes cell migration behavior, but also affects the tumor. A stiff ECM leads to an overexpression of ErbB2, a transmembrane receptor tyrosine kinase, which indirectly regulates cell growth, differentiation, and apoptosis, among other critical processes in tumor cells [136]. ErbB2 protein is overexpressed in $\sim 25\%$ of all invasive and metastatic breast cancers and increases intracellular mechanical sensitivity, which in turn results in a bigger intracellular apparent stiffness [137, 138].

However, a deep understanding of underlying mechanisms of tumor formation and invasion related to the mechanical properties of the surrounding ECM is still hampered by the complexity of the involved signaling cascades, the heterogeneity of relevant cell populations and the shortcomings of model systems.

1.3.1. Cancer cell mobility on surfaces

Cell migration has been extensively studied on two-dimensional (2D) substrates. The involved mechanism usually is a combination of front protrusion, rear contraction and graded adhesion [139]. Actin polymerization forms protruding lamellipodia at the leading edge. At the rear myosin-induced contraction and disassembly of the actin network generates contraction and a forward movement of the cell [140]. In the lamellipodia region dynamic adhesions are formed, which mature and disassemble as they move closer to the centre of the cell [141]. The balance between actin polymerization, retrograde actin flow and adhesion drag, dictates the migration speed of the cells [142]. The big advantage experiments in 2D have is the lower complexity compared to studies in 3D environments. The complex motility of cells can be understood more clearly in controlled and confined microenvironments and these environments can be designed, tuned and reproduced most easily in 2D.

Artificial micropatterns are widely used to examine the shape, migration and internal chemistry of cells in a well-controlled and high-throughput fashion. Studies with cells on microlanes have shown for example a relation between persistence and cell velocity or novel migratory behavior [143, 144]. Microlanes with ratchet geometries induced directed migration, circular adhesion islands lead to rotational migration of small cohorts of cells and introducing gaps into the microlanes induced a stochastic cell reversal and transits [145-147]. Another insight was the change of persistent cell migration, on linear microlanes, to striking oscillations upon depolymerization of microtubules, or by depletion of zyxin, a protein that concentrates at focal adhesions and actin cytoskeleton components [148, 149]. In combination with computer simulations, migration of cells can be predicted and reproduced with these micropatterns.

Zhou et al. designed short microlanes and investigated the migration of single cells on them [150]. Both ends (poles) of the microlane were coated with polyethylene glycol (PEG). The cells showed a quasi oscillatory pole-to-pole migration mode, with repetitive depolarization-repolarization cycles. At the poles of the microlanes, actin polymerization in the leading protrusion is quenched due to the reduced capability to form focal adhesions in

the PEGylated area. The cell stops, protrusions form at the opposite edge of the cell and the cell moves in the opposite direction. The time needed for this reversal mechanism does not depend on the length of the microlanes and hence appears to be independent of the migration history. Furthermore, by changing the shape of the ends of the microlanes, it was found that a concave tip shape leads to split protrusions, showing local quenching of actin activity in the middle. However, in microlanes ending in sharp tips, the lamellipodium does not split and enters the sharp tip. Thus, protrusions into constrictions are enhanced, while protrusions at concave interfaces are split. The general mechanism behind the pole-to-pole cell migration and the behavior at the microlane poles is driven by the dynamics and reinforcement of exploring protrusions at both ends of the cell.

By designing a two-state micropattern system with two adhesive sites, connected by a thin constriction, Brückner et al. studied the dynamics of cell migration in a confined system [151]. They observed migrating cells perform repeated stochastic transitions and found a deterministic driving that controls the traversal of the thin constriction with MDA-MB-231 and MCF10A cells. The MCF10A cell line shows an amplification of velocity at the constriction, ensuring a rapid transition to the other side of the micropattern. The MDA-MB-231 cells don't accelerate, indicating that this may be a cell line specific response to the presence of the constriction. With many recorded single-cell trajectories, an equation of cell motion with deterministic and stochastic contributions, that reproduces the observed migration statistics, could be determined. The experiments also show a deterministic trend to invade the thin bridge of the micropattern, which suggests that constrictions can provide guidance cues to cells and excitable bistable dynamics for MCF10A cells, which are known to be less invasive. With this theoretical framework distinct dynamical features of cell locomotion and their response to physical obstacles can be captured. Additionally the importance of environmental factors is shown through the use of different adhesion site areas or geometries in the experiment. The effect of the environment on cell migration can be quantified through comparison of mean dwell times and steady-state occupancy probabilities. Statistical evaluation of individual trajectories and transition rates show an indirect connection between escape rates, protrusion dynamics and cell polarization in confining microenvironments [152]. The results of these experiments can be used to

describe cells moving along filaments, or through pores of a biopolymer meshwork and to further understand microscopic processes driving cell migration, as well as the dynamics of cells in more complex environments.

The big drawback of these experiments in 2D is the lack of comparability to the actual *in vivo* situation for tumor cells and therefore the lack of transferability of the insights to real tumors in humans.

1.3.2. Movement of cancer cells in 3D model systems

The study of tumor cells in three dimensions (3D) is closer to *in vivo* tumor studies, than experiments on surfaces. Cancer cells can be introduced to hydrogels, the properties (e.g. rigidity) of which are not as well defined as on surfaces, but they can be altered fairly easily, compared to *in vivo* experiments. The pore size, or stiffness of a hydrogel model system, for example, changes with the used concentration, and this in turn influences the cell motility or phenotype. In pathology studies metastatic tumor cells were found to have highly branched morphologies and a bias to move parallel to an aligned ECM during metastatic tumor progression [84, 85]. With a 3D hydrogel network a tunable orientation in the matrix and an environment close to *in vivo* can be achieved in one experiment.

The complex migratory behavior of tumor cells in a 3D environment was examined in the computational study of J. Zhu and A. Mogilner [155]. They demonstrate the importance of protrusion formation in different directions and the contraction of the cytoskeleton for cell migration in 3D. Furthermore, they show that a steady flow of actin is the main driving force for cell migration. However, adhesion to the ECM is dispensable if there are strong steric interactions between cell and ECM. Also, the migration strategy a cell uses based on the physical properties of the ECM and the interactions between cell and ECM was predicted. By altering the spatial distribution and dynamics of actin protrusion, actin-myosin contraction and adhesion, six migration modes were determined, which were similar to observed ones in normal and tumor cells (figure 1.4).

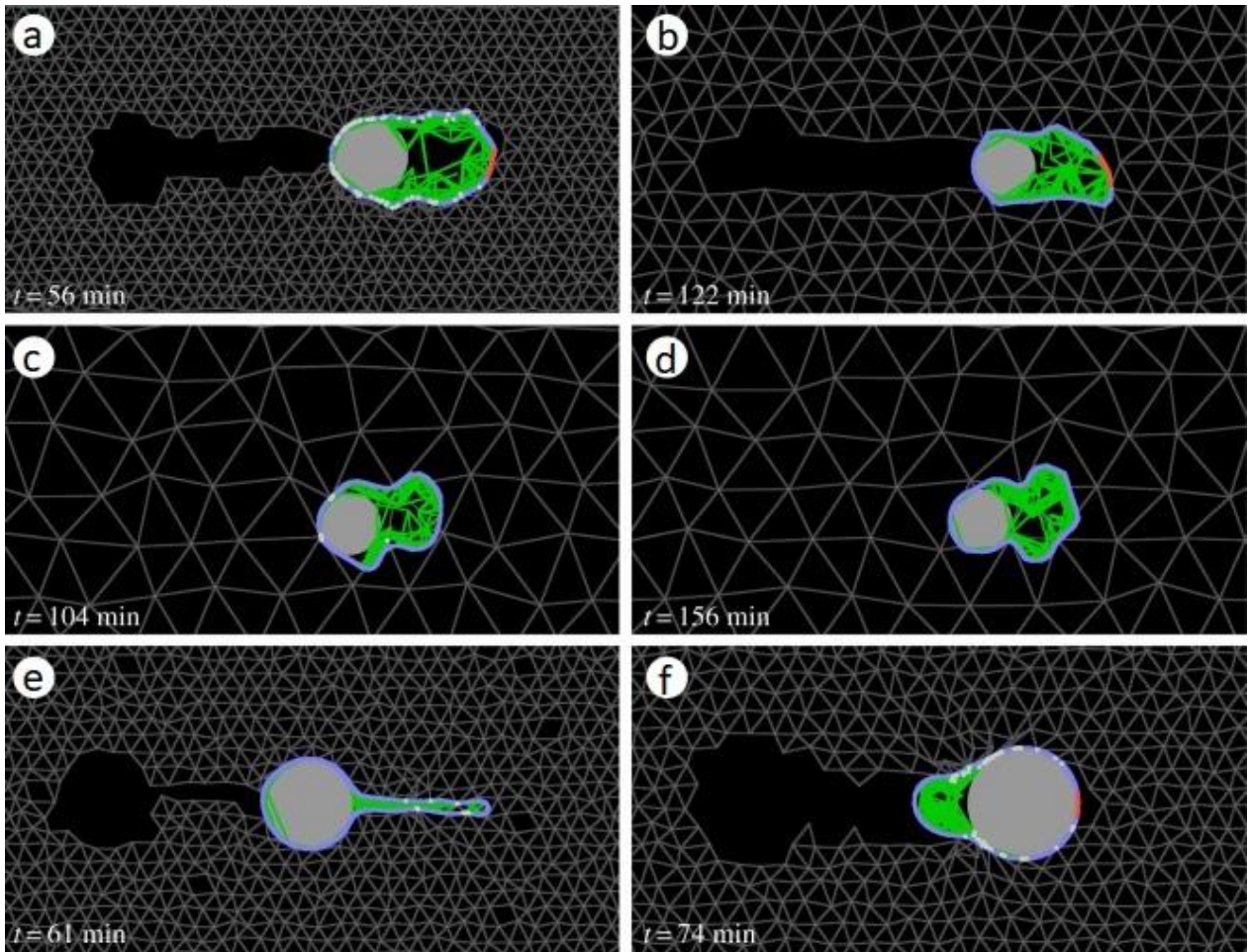


Figure 1.4: Snapshots of the simulated movement modes. a) Mesenchymal mode, b) chimneying mode, c) amoeboid mode, d) blebbing mode, e) finger-like mode and f) rear-squeezing mode. The actin network is shown in green, the nuclei are depicted as grey circles and the cell membrane is colored blue. The ECM is shown as grey triangular meshwork outside the cell, the proteolytic region is colored in red and cell–ECM adhesion sites are depicted as white dots on the membrane [155].

The mesenchymal mode is common in cancer cells with strong proteolytic activity and adhesions (also described in 1.3). The simulated cells have an elongated shape and the nucleus is located at the rear of the cell (figure 1.4a). The polymerization and expansion of the actin network pushes the front end through the matrix, and at the same time the rear end is retracted by the adhesion sites between the cell and the ECM. In addition, transient

adhesion bonds are formed at the cell front, connecting the actin network and the ECM. These bonds detach from the cell as they move towards its rear, during the continuous migration through the matrix. In this mode, efficient migration is only possible through proteolytic activity, which removes the hindering ECM nodes at the front [155].

If adhesion is inhibited, the simulated cells switch to the chimneying movement mode. Through the formation of protrusions, which invade ECM pores next to the cell, it can move through dense ECM structures (figure 1.4b). The actin inside the protrusions is connected with the whole actin network of the cell, and thus a retrograde actin flow in the cell generates traction forces via steric effect between the protrusions and the ECM. This mode is less efficient than the mesenchymal mode, because the generation of the traction forces is more complex [155, 156].

With an inhibited proteolysis and low adhesion levels, simulated cells resort to amoeboid modes of movement. In this mode, the cells form random pseudopodia-like protrusions and push them into adjacent pores of the ECM (figure 1.4c). Through actin polymerization at the front, the protrusions grow and the cell is pulled in the direction of the dominating protrusion, due to the conservation of cell volume [155].

The simulated blebbing movement mode looks similar to the amoeboid mode, but the cell doesn't form any adhesion sites and moves based on steric effects (figure 1.4d). This results in a lower movement speed, due to the ineffective generation of traction forces [155, 157, 158].

In the finger-like protrusion mode, the simulated cells form long protrusions from the cell body into the surrounding ECM (figure 1.4e). During cell movement, actin polymerization and adhesion formation occur in the protrusion, and generate many adhesion sites and traction forces at the tip. Then, the cell induces a strong myosin-mediated contraction between the protrusion and the rest of the cell body through the actin network, and the cell is pulled along the protrusion. For continuous migration, the protrusion tip is pushed deeper into the ECM pore through actin polymerization. Due to the necessity of severing ECM links in the neck region of the migrating cell, the migration mode is greatly enhanced by local proteolysis [155, 159].

In the last migration mode simulated, most of the actin network is concentrated behind the cell nucleus, which squeezes the nucleus, and hence the cell forward. Therefore, this mode is called rear-squeezing mode (figure 1.4f). The contact region, and thus the steric interactions between the cell and the ECM are very small during the migration, that's why cell-ECM adhesion is essential in this movement mode [154, 155]. These simulated movement modes suggest that cell migration is driven by continuous front polymerization and rear contraction of the actin-myosin network, generating a steady retrograde flow inside the cell. If the cell is additionally connected to the ECM through adhesion molecules or steric effects, this flow generates traction forces and moves the cell through the ECM. The traction forces of the cell are countered with resisting adhesion and friction forces of the ECM [160].

The migration speed of the cell is influenced by the flow of actin network as well as the contraction rate of the cell. Finger-like, mesenchymal and rear-squeezing modes rely on myosin-induced contraction of actin networks, while amoeboid, blebbing and chimneying modes depend on the expansion of the cortex into the pores of the ECM. The transient adhesion of cells to the ECM also has a great impact on cell movement speed. Strong adhesion and a low detachment rate enable cell movement by providing traction, but if it is too strong the cell can't detach from the ECM and gets stuck. A high detachment rate also can slow down the cell by lowering the traction. Especially the mesenchymal and rear-squeezing modes are affected by this balance. Another factor on migration speed is the mesh size of the matrix surrounding the cell. Due to the different movement mechanism used, each cell has an optimal simulated mesh size (ξ_{ECM}), where the highest movement speed (v_{cell}) can be achieved (figure 1.5a). For the amoeboid and blebbing mode, the best ξ_{ECM} is 13 μm . Cells in finger-like or chimneying mode move fastest in 3 to 4 μm pores, and a smaller poresize of 2 μm is best for the mesenchymal and rear-squeezing mode. Smaller pores hinder the formation of pseudopodia and the passing of cell nuclei into the ECM pores, however in large pores the cells can't build up enough traction with the pseudopodia to push themselves forward [155].

1.3. Influence of the extracellular matrix on cancer cell invasion

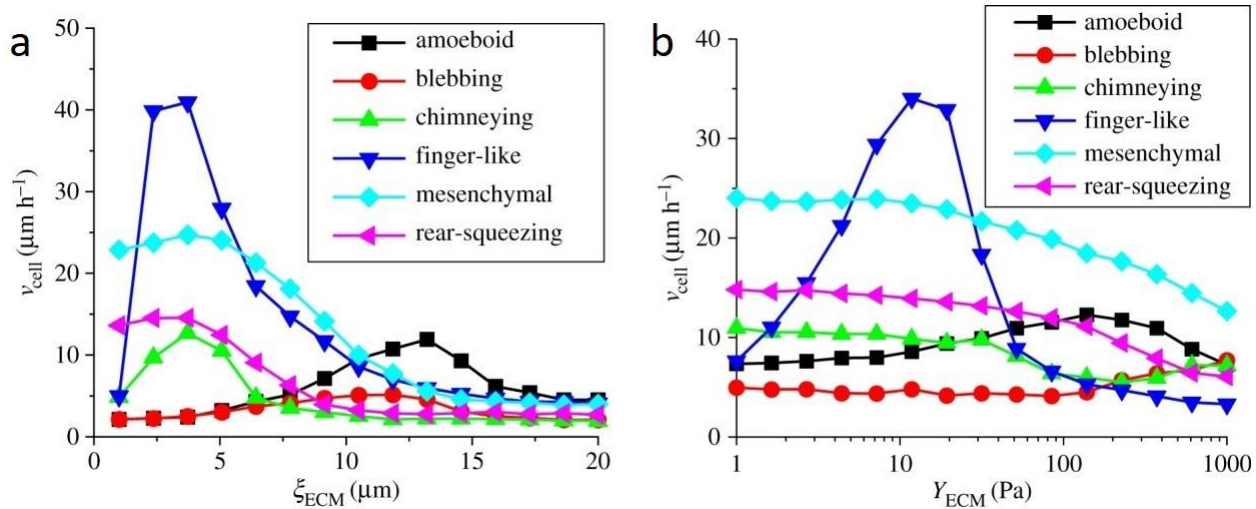


Figure 1.5: Cell speed in different movement modes depending on simulated matrix properties, a) Cell speed (v_{cell}) dependence on the ECM mesh size (ξ_{ECM}), b) Cell speed (v_{cell}) dependence on the ECM Young's modulus (Y_{ECM}) [155].

The simulation results of J. Zhu and A. Mogilner explain 3D cell migration by a single model with protrusion, contraction and adhesion as its three main components. The most important matrix property, regarding the cell's movement speed, is stiffness or Young's modulus. A cell can exert stronger traction forces through adhesion on a stiff matrix than a soft one, and therefore move faster through it. But the higher stiffness aggravates the deformation of the ECM by a cell and will increase the above mentioned resisting and friction forces. Also, a stiff ECM with a tight mesh size and tunnel like structures leads to persistent movement. According to simulations, a stiff matrix seems to be beneficial for the blebbing and amoeboid mode, with an optimal Y_{ECM} of 120 Pa for the amoeboid movement. Whereas, cells in mesenchymal, rear-squeezing, chimneying and finger-like mode are suggested to move faster in a soft environment by the simulations, with a maximum for finger-like mode at 12 Pa [155]. Experiments on this change of cancer cell migration modes, due to the physical properties of the ECM, are discussed further in chapter 3. There, the relation between the migratory phenotype of MDA-MB-231 cancer cells and collagen matrix stiffness, pore size and adhesion is further described [190].

Illina et al. reconstructed collagen with low to high interfibre space (0.46–12 μm), which is in the space range detected in human tumors. Additionally, the collagen gels contained tube-like tracks of variable width, which were created by laser ablation and used as a cell-derived tissue pattern. MCF-7 cell aggregates were introduced to these networks with different collagen densities. With sufficient space, the MCF-7 cells showed a collective invasion, decreasing with increasing collagen density. By repressing E-cadherin in the introduced cell aggregates, the cell-cell adhesion was decreased and single-cell migration was detected in networks with low to intermediate collagen density. In an ECM with high collagen density, the cells switched to collective dissemination. Thus, multicellular invasion persists, despite compromised adherens junction organization, when tissue confinement is high. Furthermore, the collective invasion of MCF-7 cells depends on either pre-existing, or by means of proteolysis, freshly generated 3D tissue space [191].

The interaction of cancer cells with the ECM, while they pass through its pores, can alter the structure of the matrix and prepare it for following cancer cells, as mentioned at the beginning of chapter 1.3.2. Han et al. conducted *in vitro* experiments to study the influence of aligned ECMs on migration behavior of cancer cells [161]. In a parallel aligned Collagen I matrix, the nuclei of MDA-MB-231 breast cancer cells show an elongation along the alignment axis, compared to cells in a randomly aligned environment. This indicates the guidance of the metastatic breast cancer cells by the locally organized collagen fibers. During 96 hours of observation, the cells moved along the direction of alignment [162]. This persistent and sometimes collective migration of the cancer cells might occur due to contact guidance and mechanical regulation, caused by the aligned ECM. The cells intravasation speed was about 3 $\mu\text{m}/\text{h}$, and some cells invaded up to 200 μm into the matrix. Also, the collagen fiber network was remodeled during this invasion by the cells, possibly through the expression of matrix metalloproteinases (MMPs), that degrade the ECM and generate local paths, which help following cells [161].

To further understand the mechanisms in a tumor, Carey et al. investigated multicellular spheroids, made of MCF10A cells and malignant MDA-MB-231 cells, embedded in three-dimensional collagen matrices, which mimicked the *in vivo* tumor stroma [163]. These cell aggregates consisted of a core of MDA-MB-231 cells, which was encased within a densely-

1.3. Influence of the extracellular matrix on cancer cell invasion

packed shell of MCF10A epithelial cells, which was in turn surrounded by an outer rim of highly motile malignant MDA-MB-231 cells. The surrounding uniform collagen matrices contained randomly organized collagen fibers, with a concentration of 1.5 mg/ml. MCF10A cells (red) in the spheroid were unable to invade the matrix on their own and exhibited non-invasive expansive growth, but malignant MDA-MB-231 cells (green) invaded the surrounding tissue in a disorganized manner. After 48 hours the malignant cells (green) reached maximal invasion distances around 300 μm and triggered a small portion of non-invasive epithelial MCF10A cells (red) to invade into the matrix in cohesive strands (white arrowheads, figure 1.6a). In figure 1.6b, one or more leading malignant cells can be seen positioned at the tip of invasive strands with red, non-invasive cells trailing behind. Apparently, this phenomenon is not limited to MDA-MB-231/MCF10A co-cultures, and for example can also be seen in MCF10CA1a/MCF10A or PC-3/PrEC co-cultures [163].

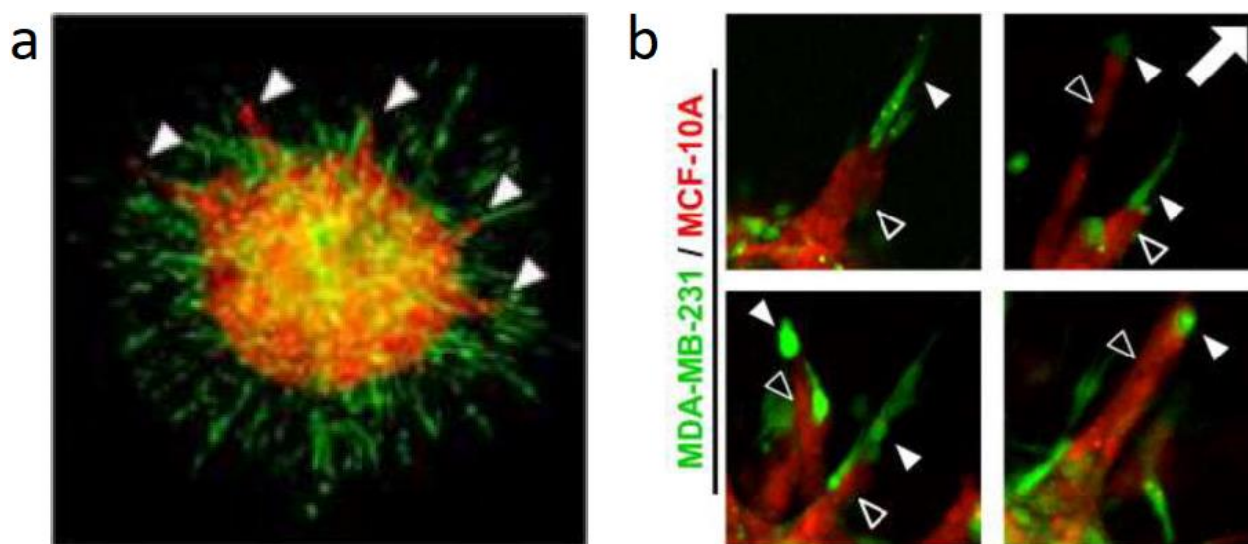


Figure 1.6: Fluorescence image of multicellular tumor spheroid invasion into a randomly organized collagen matrix after 48 hours. a) expansive growth of MCF10A cells (red), disorganized invasion of MDA-MB-231 cells (green) into the surrounding tissue, and cohesive strands of MCF10A cells invading tissue (white arrowheads). b) MDA-MB-231 cells (green) leading (white arrowheads) strands of MCF10A (red, black arrowhead) cells into the collagen matrix [163].

The leading MDA-MB-231 cells were elongated and radially-oriented, whereas the following MDA-MB-231 and MCF10A cells tended to show rounded morphologies. The invading malignant MDA-MB-231 leader cells left cell-scale microtracks in the matrix, that facilitated collective cell invasion, as shown by Wolf, et al. [111]. If extracellular matrix remodeling is prevented by treating the cells with inhibitors of MMPs (GM6001) and ROCK-mediated cell contractility (Y27632), no matrix microtracks are formed, malignant cell invasion and matrix alignment is reduced, and epithelial co-invasion is prevented [164]. Also, invasion from spheroids into high-density collagen matrices (~6.0 mg/ml) is less efficient in presence of these inhibitors, as they provided a barrier to MMP- and ROCK-independent invasion [163].

Spheroids, consisting only of epithelial MCF10A cells, remodel the collagen fibers tangentially around their surface, due to their non-invasive expansive growth and rotation. The persistent and coordinated rotation of the spheroid is part of an unjamming mechanism, which increases tissue fluidization and rearrangement dynamics at the periphery of the spheroid in contact with the ECM [189]. In MDA-MB-231/MCF10A co-cultured spheroids, the reorganization and alignment was driven by the invading tumor cells. The fibers were oriented in invasion direction and perpendicular to the spheroid surface through cell contractility-mediated matrix reorganization [120]. While the underlying mechanisms how cancer cells react to the changed properties of the ECM microstructure are not fully understood, the metastatic potential of tumor cells is suggested to be significantly increased by the orientation of the collagen matrix [161]. This claim is further substantiated by the experiments and simulations described in chapter 4. There, cancer spheroids were placed in aligned collagen networks via a microfluidic chamber. It was shown, that the spread of the spheroid directly correlated to the fiber orientation relating to its surface. This data was described by several simulations of cell spheroids and collagen fibers inside the microfluidic channel.

1.4. Designed model systems for tumor cell motility

While the study of *in vivo* systems on how tumor cells are influenced by the extracellular matrix are elaborate to investigate and difficult to reproduce, they still hold the most accurate information [165]. To come closer to these *in vivo* experiments, tunable model systems have to be developed, which can be adjusted exactly to the requirements of the experiment. *In vitro* experiments try to recreate the situation of single tumor cells or bulk tumor aggregates in different 3D tissues. This offers a better representation of physiologically and pathologically relevant conditions, than 2D experiments. The most commonly used compounds are matrigel or collagen [166, 167]. Type I collagen is often used for cell experiments, due to its high biocompatibility and the microenvironment it provides, which is close to *in vivo*. This is because of its natural derive and high abundance in mammalian tissues [168]. Collagen I matrices facilitate cell attachment, proliferation and differentiation, through receptor-mediated interactions predominantly via integrins [169]. Additionally, its physical properties, such as tensile strength, resistance to deformation and poresize, can be tuned fairly easily by changing the rate of cross-linked collagen fibers, collagen concentration, pH-value, or the temperature during polymerization. Collagen also exhibits strain stiffening behavior, whereby the material stiffness increases when strained. It can be manipulated even after the polymerization, to fit the experimental requirements [165-173].

As mentioned before, the intrinsic fibril alignment of collagen in the ECM has a strong influence on the cell behaviour. Currently, there are several available methods to align collagen fibers in artificial tissues, including electrospinning and directional solidification. These methods are expensive, elaborate and expose the sample to high voltage or lyophilization, which means cells have to be introduced to the matrix after alignment [174-176]. This could lead to inhomogeneity or the distortion of the data by boundaries, which influence cells behavior greatly. But these methods give the possibility to design the matrix with a precision down to single fibers.

The same holds true for 3D bioprinting. In this case the whole tissue is build layer-by-layer and cells can be introduced throught the bioink during the printing, because of the milder

conditions. 3D bioprinting technologies are already used in hospitals to manufacture hard tissue engineering scaffolds. The technique is relatively fast, cheap, readily available and has a high resolution, but the heat, ultrasound, and mechanical stresses affect cell viability. Furthermore, expensive hardware and software are needed, and only low cell numbers can be printed [177, 178].

Another related method is two-photon polymerization. In this case, the network can be directly built using a photosensitive compound, which generates free radicals upon light absorption. The free radicals then promote polymerization of monomers, or crosslinking of polymers [179]. With this technique biomaterials can be fabricated and manipulated *in situ* and fiber stiffness or poresize can be adjusted, by selectively crosslinking collagen fibers [180]. On top, it is a nozzle free method with a high precision, but therefore it is a very time-consuming process to print large matrices and the laser or the free radicals can damage cells [177].

A non-destructive method for structuring collagen gel is the use of mechanical strain during or after the polymerization. A polymerized collagen sample can be perforated and connected to two linear transducers and then the gel can be stretched at defined strain rates, or to specific distances. Above 5% strain, the fibers inside the gel get aligned and network density increases. This alignment is maximal along the pulling axis of the two transducers and decays further away from it. This effect is elastic and can be reversed, if the strain on the gel was not too big. Nonetheless, this method produces an inhomogeneous matrix and the physical properties are not extensively tunable, despite being cheap, fast and gentle to cells [181].

Other methods, like magnetic bead alignment, Surface Acoustic Waves (SAWs) or microfluidic approaches, use shear flow during the polymerization of collagen, to create permanently structured artificial tissues (figure 1.7). The alignment via magnetic beads allows for controlled fiber orientation with streptavidin coated iron oxide beads, which get dragged through the polymerizing collagen-cell mixture by a strong magnet or a magnetic stir bar [120]. The beads move according to the magnetic field lines and align fibers parallel to these lines [182, 183]. The resulting alignment is rather weak for thicker gels, but can be amplified slightly by using a u-shaped magnet and dragging the beads through the sample

1.4. Designed model systems for tumor cell motility

multiple times. Despite the rather weak rate of alignment this method is cheap, easy to use and doesn't damage cells or spheroids (figure 1.7).

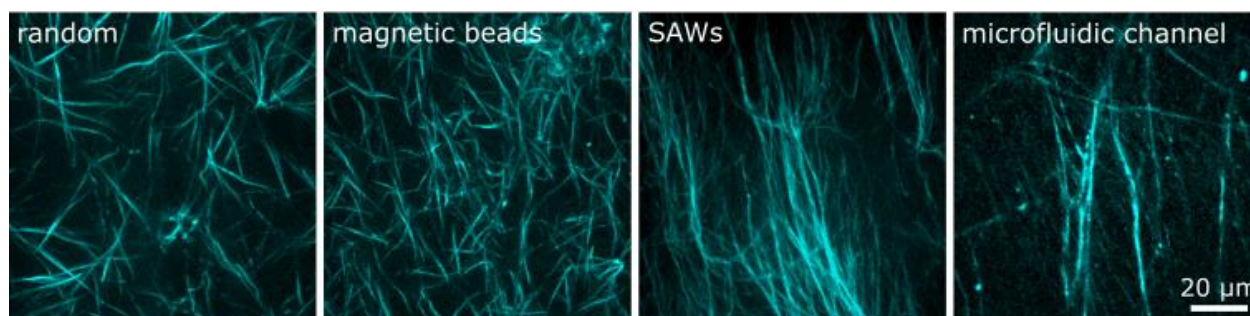


Figure 1.7: Collagen fiber without orientation (random) and aligned via different shear flow methods, these being magnetic beads, surface acoustic waves (SAWs) and in a microfluidic channel.

SAWs also use shear flow to align collagen beads, but the force transferred into the collagen gel can be tuned much better, and therefore the rate of alignment can be controlled easier compared to magnetic bead alignment. The function of SAWs is described in more detail in chapter 2.4. Depending on the architecture and the combination of interdigital transducers (IDTs) used, many different flow patterns can be designed to align collagen fibers. Since the SAW essentially only stirs the collagen in an elaborate manner, inhomogeneities of collagen concentration and fiber alignment can occur depending on the SAW architecture and force of the flow created in the gel. However, it is possible to arrange cells in collagen during polymerization in a precise manner by using acoustic waves, and the fiber orientation is rather strong in bigger volumes of collagen gel compared to magnetic alignment (figure 1.7) [184-186].

Another shear force driven method is the use of a combination of two different matrix components, layered over one another. A matrigel collagen sandwich ECM can be assembled in a microfluidic chip, and it mimics the interface between interstitial matrix (collagen) and basement membrane (matrigel). Collagen is injected while fluid onto the matrigel, and during the composite ECM solidification, the matrigel volume expands while the collagen section shrinks, resulting in a collagen fiber orientation induced by internally developing strain fields. This alignment is different in degree and orientation, depending on

the force and direction of the strain field, making it rather inhomogeneous. Additionally, the interface between the two components might also influence cell behavior [161].

A promising method to orient collagen fibers is the alignment through microfluidic chips (figure 1.7). The technique, different designs, and combination of microfluidics with SAWs are described in chapter 2.5. Usually, flow chips with different dimensions are built from polydimethyl siloxane (PDMS) and glass substrates, in combination with one or more syringe pumps. Then collagen is pumped through the chip with different rates, during or before polymerization, which results in a structured collagen gel. Lee et al. show, that in a simple microchannel the degree of alignment depends mostly on the applied flow and the channel width (figure 1.8). The control, made without microchannels, had an average orientation of 41° (solid line) with a standard deviation of 8° (dashed line). The fiber orientation was analysed without initial flow (white circle), meaning the collagen mixture was filled directly into the channel and then sealed with a glass slide. The other experiment used initial flow (black square), where the channels were subjected to initial pressure, filling them with collagen. The fiber alignment was parallel to the channel axis and varied with channel size. The orientation was only statistically significant in channels up to $200\ \mu\text{m}$ in width and with initial flow [187].

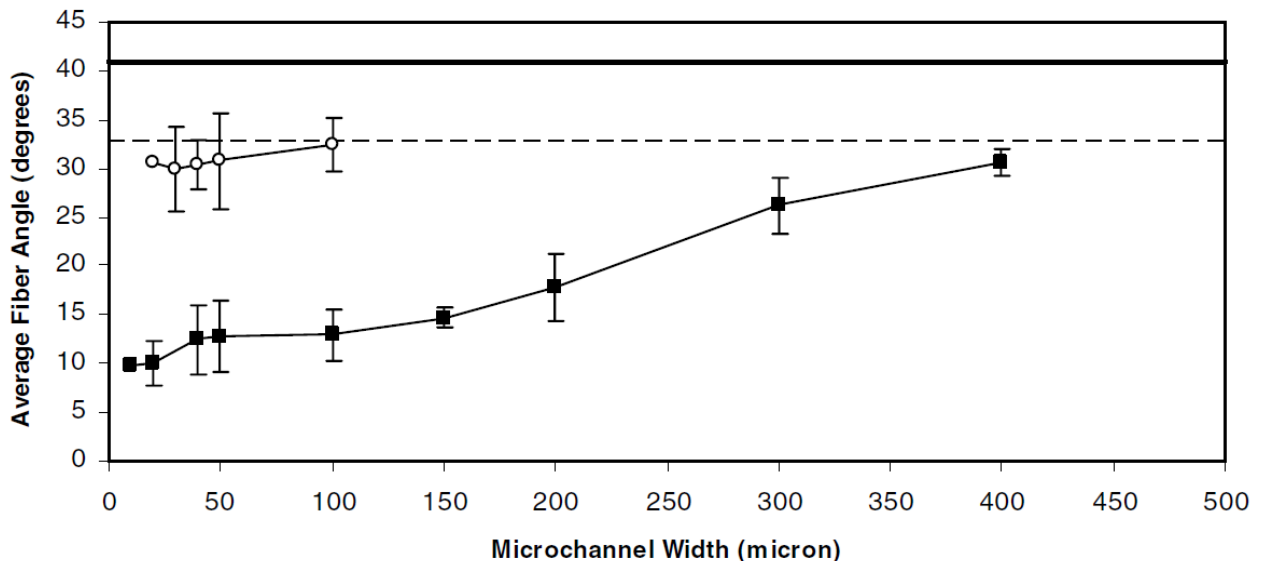


Figure 1.8: Average collagen fiber alignment angle as a function of channel width, without initial flow (\circ) and with initial pressure driven flow (\blacksquare). The solid line describes the

fiber angle in the absence of microchannels, with the dashed line as its standard deviation [187].

The rate of alignment in the whole channel was uniform, suggesting that the flow within the channel induced the collagen “seeding” units to align in the microfluidic channel. If the shape of fiber precursors is assumed cylindrical or elongated, a flow field could orient them in a parallel fashion, and if these nucleation sites remained immobile, subsequent fiber polymerization would occur in an aligned manner. The larger the channels get, the weaker the shear forces generated by the applied flow field become, resulting in less uniform aligned collagen fibers. Additionally, the vicinity of the channel walls might be vital for creating collagen nucleation sites. The microfluidic method is also suitable for cells and cell aggregates, which can be incorporated into the used collagen mixture [187, 188]. These different methods enable a wide variety and many possibilities, on how an artificial model system for cell mobility experiments can be designed, and have to be chosen depending on the application. For the experiments in this thesis, only methods using shear flow were applied, due to their simplicity and high biocompatibility.

In this thesis, the influence of the mechanical properties of hydrogels on cancer cell migration properties was investigated. Due to minimal matrix remodeling by the cells in the presented study, the influences of environment on cell phenotype could be analyzed without further complexity, due to changes in the environment. The migratory phenotype and migration parameters are significantly influenced by confinement and adhesion on continuous substrates, such as glass or plastic channels [192]. Usually, tissue is highly heterogeneous and resembles porous collagen meshworks [193–196], which has a different influence on migration properties of cells, compared to a continuous substrate. Fiber stiffness, confinement and the number of adhesion sites strongly influence the migratory phenotype of cancer cells and consequently their migration parameters in porous hydrogels.

This strong effect of the surrounding matrix on cell migration was further studied in highly oriented collagen gels and with cell aggregates, mimicking the conditions in a tumor.

1.5. RNA labeling as tool to investigate cancer and virus replication

To further understand cellular mechanisms, it is important to detect and quantify molecules related to the respective mechanism. Proliferation, for example, is an important process in cells and its rate often has to be determined precisely [197–199]. In cancer diagnostics, it is required to measure the proliferation of cells with high precision, and to identify single cancer cells in a sample, to be able to begin treatment as soon as possible, if necessary [200, 201]. A precise way to measure cell proliferation is to introduce C5-ethynyl-dU (EdU) during proliferation, where it is incorporated into the genome [202, 203]. EdU is an antimetabolite, which interferes with cell growth and cell division. The incorporated EdU quantity can be measured by treating the alkynes of the EdU within the DNA with azido-modified fluorescent dyes, through the Cu^I-catalysed alkyne–azide click reaction [204, 205]. The Cu^I-atoms are loosely precoordinated to the electron-rich centres at the nucleobases, making this DNA labeling method very efficient [205]. This technique is used in several commercially available kits, where each alkyne is functionalized with one dye molecule. The sensitivity is limited by the number of EdU incorporated during the culturing phase, often leaving slowly proliferating, but still carcinogenic cells unmarked and undetected [206].

In the following, sandwich-type detection assays were established using a dendrimer-type tetraazide and a dendrimer-type tetraalkyne. First, cells are grown in the presence of ethynyl-dU (EdU). Then the alkynes of the incorporated EdU are functionalized through multiple consecutive Cu^I-catalysed alkyne–azide click reaction with dendrimeric molecules. Finally, clickable dyes are attached to the dendrimer-type molecules. These assays yield enhanced signal intensities with better signal-to-noise ratios, which improve their suitability for imaging and high-throughput-content assays.

Another technique to detect specific DNA or RNA sequences is the fluorescence in situ hybridization (FISH) [207]. It can be used to get an early diagnosis and characterization of a viral infection, due to the specific detection of early transcriptions of virus-specific genes. Since, in general, most pathologies induce transcriptional changes, which alter the levels of specific messenger RNAs (mRNAs) inside the cell, detection and quantification of a specific mRNA is highly desirable from a diagnostic point of view [208, 209]. The method also

1.5. RNA labeling as tool to investigate cancer and virus replication

reveals localization patterns of individual RNA transcripts in cells or tissues, which is very interesting for example for understanding the mechanisms and progression of a virus infection in a cell [210–212]. RNA-FISH is based on multiple (up to 50) individual anti-sense single-stranded (ss) DNA probes, which are about 22 nucleotides long (figure 1.9; Probe DNA). A fluorophore is attached to each probe oligonucleotide, which is typically introduced in the form of an activated NHS ester to an amino group at the 3'-end of the probe [210, 211]. When these fluorescent ssDNA probes are added to fixed and permeabilized cells, they hybridize with the target RNA, and can be detected via fluorescence microscopy (figure 1.9; Denature and Hybridize).

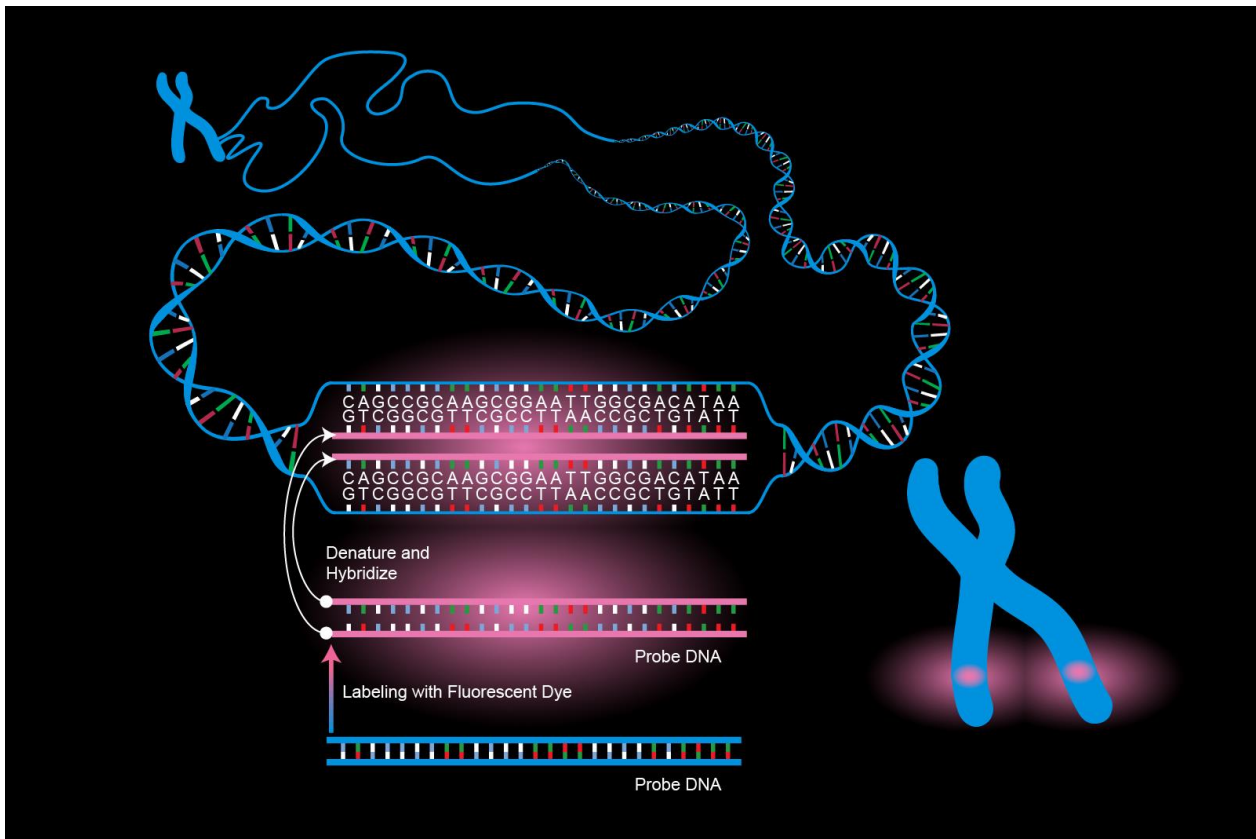


Figure 1.9: Scheme of an in situ hybridization for DNA detection. First the DNA probe is labeled with a fluorescent dye, then the Probe DNA denaturizes into single strands, which hybridizes with its matching segment in the denatured target DNA [213].

However, intracellular localization and quantification of mRNA faces a number of challenges that hinder routine use. One challenge is high off-target staining, due to the large number of probe strands needed to create a sufficiently strong fluorescent signal. This can be countered by reducing the number of probe strands needed for a successful detection. This has led to efforts to modify the probe oligonucleotides with, for example locked nucleic acids (LNAs), which increase the thermal duplex stability and the discrimination between perfectly matched and mismatched target nucleic acids [214]. By using LNAs, more dye molecules bind to the desired complementary DNA or RNA, increasing the signal to noise ratio, and thereby less probe is needed to detect the signal. Another strategy to reduce the number of probe strands, while staying above detection limit, is to increase the signal per strand.

In the following a DNA probe for mRNA with three fluorophores, instead of one, was developed. The additional fluorophores were attached using the Cu^I-catalyzed azide-alkyne click reaction [215–218]. They were functionalized with two additional sulfonate groups, to prevent stacking of the fluorophores on top of each other, which might induce self-quenching. The negatively charged sulfonate groups minimize the interaction of the fluorophores with each other and with the negatively charged DNA. This design allows visualization, quantification and localization of RNA transcripts with a small number of probe strands (5–10) and enables transcript analysis using flow-cytometry.

The RNA labeling techniques described above can be used to quantify and localize for example viral RNA. Viruses gather their replicative enzymes within specialized organelles, called viral factories to replicate. These factories bind and concentrate cognate nucleic acids and proteins, which form virus assembly lines that support viral replication. Most viral RNA replication requires membrane-delimited replication compartments, but recent studies suggests that this is also possible through liquid-liquid phase separation (LLPS) [219–222]. With LLPS RNA-rich replication factories could be assembled, while solely depending upon physical forces [223–226].

In chapter 7. we show the formation of rotavirus replication factories via phase separation of the non-structural multivalent protein NSP5 and viral RNA chaperone NSP2. NSP5 and NSP2 form liquid condensates when mixed *in vitro* at low micromolar concentrations, or

when co-expressed in cells. Cytoplasmically dissolved proteins (NSP5) and viral RNA (NSP2) is re-distributed and exchanged between these spherical condensates during the early infection stage. Small aliphatic alcohols, like 1,6-hexanediol, or lower molecular weight 1,3- and 1,2-propylene diols, rapidly and reversibly dissolve these NSP5/NSP2 condensates as well as the spherical rotavirus replication factories. Upon dissolution, rotavirus transcripts are released, which can reassociate upon removal of the aliphatic alcohols. At a later stage of infection (>12 h) the exchange of NSP5-EGFP between the cytoplasm and viroplasm decreases and the replication factories are no longer spherical shaped. Furthermore, the rotavirus replication factories are no longer dissolved by small aliphatic diols, suggesting a liquid-to-solid transition of the condensates during infection. These properties of the rotavirus replication factories are similar to those of cytoplasmic ribonucleoprotein granules, with the exception of the selective enrichment of viral transcripts in the condensates. The rapid and reversible response of the RNA-protein condensates to external stimuli shifts the understanding of the replication mechanism of multi-segmented viral RNA genomes and could be used as a target for novel antiviral therapeutics.

1.6. References

1. https://www.rki.de/DE/Content/Service/Presse/Pressemitteilungen/2019/16_2019.html. 23.04.2020.
2. Hanahan D, Weinberg RA. The hallmarks of cancer. *Cell*. 2000; 100(1):57–70.
3. Hanahan D, Weinberg RA. Hallmarks of cancer: The next generation. *Cell*. 2011; 144(5):646–74.
4. Negrini S, Gorgoulis VG, Halazonetis TD. Genomic instability — an evolving hallmark of cancer. *Nat Rev Mol Cell Biol*. 2010; 11(3):220–8.
5. Salk JJ, Fox EJ, Loeb LA. Mutational heterogeneity in human cancers: origin and consequences. *Ann Rev Pathol*. 2010; 5:51–75.

6. Jackson SP, Bartek J. The DNA-damage response in human biology and disease. *Nature*. 2009; 461(7267):1071–8.
7. Kastan MB. DNA damage responses: mechanisms and roles in human disease: 2007 G.H.A. Clowes Memorial Award Lecture. *Mol Cancer Res*. 2008; 6(4):517–24.
8. Sigal A, Rotter V. Oncogenic mutations of the p53 tumor suppressor: the demons of the guardian of the genome. *Cancer Res*. 2000; 60(24):6788–93.
9. Renan MJ. How many mutations are required for tumorigenesis? Implications from human cancer data. *Mol Carcinog*. 1993; 7(3): 139–46.
10. Colotta F, Allavena P, Sica A, Garlanda C, Mantovani A. Cancer-related inflammation, the seventh hallmark of cancer: links to genetic instability. *Carcinogenesis*. 2009; 30(7):1073–81.
11. DeNardo DG, Andreu P, Coussens LM. Interactions between lymphocytes and myeloid cells regulate pro- versus anti-tumor immunity. *Cancer Metastasis Rev*. 2010; 29(2):309–16.
12. Grivennikov SI, Greten FR, Karin M. Immunity, inflammation, and cancer. *Cell*. 2010; 140(6):883–99.
13. Qian BZ, Pollard JW. Macrophage diversity enhances tumor progression and metastasis. *Cell*. 2010; 141(1):39–51.
14. Karnoub AE, Weinberg RA. Chemokine networks and breast cancer metastasis. *Breast Dis*. 2006–2007; 26:75–85.
15. Vajdic CM, van Leeuwen MT. Cancer incidence and risk factors after solid organ transplantation. *Int J Cancer*. 2009; 125(8):1747–54.
16. Teng MWL, Swann JB, Koebel CM, Schreiber RD, Smyth MJ. Immune-mediated dormancy: an equilibrium with cancer. *J Leukoc Biol*. 2008; 84(4):988–93.
17. Kim R, Emi M, Tanabe K. Cancer immunoediting from immune surveillance to immune escape. *Immunology*. 2007; 121(1):1–14.

1.6. References

18. Smyth MJ, Dunn GP, Schreiber RD. Cancer immunosurveillance and immunoediting: the roles of immunity in suppressing tumor development and shaping tumor immunogenicity. *Adv Immunol.* 2006; 90:1–50.
19. Yang L, Pang Y, Moses HL. TGF-beta and immune cells: an important regulatory axis in the tumor microenvironment and progression. *Trends Immunol.* 2010; 31(6):220–7.
20. Shields JD, Kourtis IC, Tomei AA, Roberts JM, Swartz MA. Induction of lymphoidlike stroma and immune escape by tumors that express the chemokine CCL21. *Science.* 2010; 328(5979):749–52.
21. Mougiakakos D, Choudhury A, Lladser A, Kiessling R, Johansson CC. Regulatory T cells in cancer. *Adv Cancer Res.* 2010; 107:57–117.
22. Ostrand-Rosenberg S, Sinha P. Myeloid-derived suppressor cells: linking inflammation and cancer. *J Immunol.* 2009; 1828(8):4499–506.
23. Lemmon MA, Schlessinger J. Cell signaling by receptor tyrosine kinases. *Cell.* 2010; 141(7):1117–34.
24. Witsch E, Sela M, Yarden Y. Roles for growth factors in cancer progression. *Physiology (Bethesda).* 2010; 25(2):85–101.
25. Hynes NE, MacDonald G. ErbB receptors and signaling pathways in cancer. *Curr Opin Cell Biol.* 2009; 21(2):177–84.
26. Perona R. Cell signalling: growth factors and tyrosine kinase receptors. *Clin Transl Oncol.* 2006; 8(2):77–82.
27. Cheng N, Chytil A, Shyr Y, Joly A, Moses HL. Transforming growth factor-beta signaling-deficient fibroblasts enhance hepatocyte growth factor signaling in mammary carcinoma cells to promote scattering and invasion. *Mol Cancer Res.* 2008; 6(10):1521–33.
28. Bhowmick NA, Neilson EG, Moses HL. Stromal fibroblasts in cancer initiation and progression. *Nature.* 2004; 432(7015):332–7.

29. Warburg OH. The Metabolism of Tumours: Investigations from the Kaiser Wilhelm Institute for Biology, Berlin-Dahlem. Arnold Constable. London. 1930.
30. Warburg O. On the origin of cancer cells. *Science*. 1956; 123(3191):309–14.
31. Warburg O. On respiratory impairment in cancer cells. *Science*. 1956; 124(3215):269–70.
32. Jones RG, Thompson CB. Tumor suppressors and cell metabolism: a recipe for cancer growth. *Genes Dev*. 2009; 23(5):537–48.
33. DeBerardinis RJ, Lum JJ, Hatzivassiliou G, Thompson CB. The biology of cancer: Metabolic reprogramming fuels cell growth and proliferation. *Cell Metab*. 2008; 7(1):11–20.
34. Hsu PP, Sabatini DM. Cancer cell metabolism: Warburg and beyond. *Cell*. 2008; 134(5):703–7.
35. Potter VR. The biochemical approach to the cancer problem. *Fed Proc*. 1958; 17(2):691–7.
36. Vander Heiden MG, Cantley LC, Thompson CB. Understanding the Warburg effect: the metabolic requirements of cell proliferation. *Science*. 2009; 324(5930):1029–33.
37. Kennedy KM, Dewhirst MW. Tumor metabolism of lactate: the influence and therapeutic potential for MCT and CD147 regulation. *Future Oncol*. 2010; 6(1):127–148.
38. Feron O. Pyruvate into lactate and back: from the Warburg effect to symbiotic energy fuel exchange in cancer cells. *Radiother Oncol*. 2009; 92(3):329–333.
39. Semenza GL. Tumor metabolism: cancer cells give and take lactate. *J Clin Invest*. 2008; 118(12):3835–3837.
40. Weinberg RA. The retinoblastoma protein and cell cycle control. *Cell*. 1995; 81(3):323–30.
41. Moses HL, Yang EY, Pietsenpol JA. TGF- β stimulation and inhibition of cell proliferation new mechanistic insights. *Cell*. 1990; 63(2):245–7.

1.6. References

42. Hannon GJ, Beach D. P15^{INK4B} is a potential effector of TGF-beta-induced cell cycle arrest. *Nature*. 1994; 371(6494):257–61.
43. Datto MB, Hu PP, Kowalik TF, Yingling J, Wang XF. The viral oncoprotein E1A blocks transforming growth factor β -mediated induction of p21/WAF1/Cip1 and p15/INK4B. *Mol Cell Biol*. 1997; 17(4):2030–7.
44. Fynan TM, Reiss M. Resistance to inhibition of cell growth by transforming growth factor- β and its role in oncogenesis. *Crit Rev Oncog*. 1993; 4(5):493–540.
45. Adams JM, Cory S. The Bcl-2 apoptotic switch in cancer development and therapy. *Oncogene*. 2007; 26(9):1324–37.
46. Lowe SW, Cepero E, Evan G. Intrinsic tumour suppression. *Nature*. 2004; 432(7015):307–15.
47. Evan G, Littlewood T. A matter of life and cell death. *Science*. 1998; 281(5381):1317–22.
48. Counter CM, Avilion AA, LeFeuvre CE, Stewart NG, Greider CW, Harley C.B, et al. Telomere shortening associated with chromosome instability is arrested in immortal cells which express telomerase activity. *EMBO J*. 1992; 11(5):1921–9.
49. Wright WE, Pereira-Smith OM, Shay JW. Reversible cellular senescence implications for immortalization of normal human diploid fibroblasts. *Mol. Cell. Biol*. 1989; 9(7):3088–92.
50. Shay JW, Bacchetti S. A survey of telomerase activity in human cancer. *Eur J Cancer*. 1997; 33(5):787–91.
51. Bryan TM, Cech TR. Telomerase and the maintenance of chromosome ends. *Curr Opin Cell Biol*. 1999; 11(3):318–24.
52. Bryan TM, Englezou A, Gupta J, Bacchetti S, Reddel RR. Telomere elongation in immortal human cells without detectable telomerase activity. *EMBO J*. 1995; 14(17):4240–4248.
53. Ferrara N. Vascular endothelial growth factor. *Arterioscler Thromb Vasc Biol*. 2009; 29(6):789–91.

54. Mac Gabhann F, Popel AS. Systems biology of vascular endothelial growth factors. *Microcirculation*. 2008; 15(8):715–38.
55. Carmeliet P. VEGF as a key mediator of angiogenesis in cancer. *Oncology*. 2005; 69 Suppl 3:4–10.
56. Baeriswyl V, Christofori G. The angiogenic switch in carcinogenesis. *Semin Cancer Biol*. 2009; 19(5):329–337.
57. Hanahan D, Folkman J. Patterns and emerging mechanisms of the angiogenic switch during tumorigenesis. *Cell*. 1996; 86(3):353–364.
58. Nagy JA, Chang SH, Shih SC, Dvorak AM, Dvorak HF. Heterogeneity of the tumor vasculature. *Semin Thromb Hemost*. 2010; 36(3):321–31.
59. Baluk P, Hashizume H, McDonald DM. Cellular abnormalities of blood vessels as targets in cancer. *Curr Opin Genet Dev*. 2005; 15(1):102–11.
60. Sporn MB. The war on cancer. *Lancet*. 1996; 347:1377–81.
61. Friedl P, Alexander S. Cancer invasion and the microenvironment: plasticity and reciprocity. *Cell*. 2011; 147(5):992–1009.
62. Chiang SP, Cabrera RM, Segall JE. Tumor cell intravasation. *Am J Physiol Cell Physiol*. 2016; 311(1):C1–4.
63. Wong SY, Hynes RO. Lymphatic or hematogenous dissemination: how does a metastatic tumor cell decide? *Cell Cycle*. 2006; 5(8):812–7.
64. Reymond N, d'Água BB, Ridley AJ. Crossing the endothelial barrier during metastasis. *Nat Rev Cancer*. 2013; 13(12):858–70.
65. McAllister SS, Weinberg RA. The tumour-induced systemic environment as a critical regulator of cancer progression and metastasis. *Nat Cell Biol*. 2014; 16(8):717–27.
66. Liu Y, Cao X. Characteristics and significance of the pre-metastatic niche. *Cancer Cell*. 2016; 30(5):668–81.

1.6. References

67. Peinado H, Zhang H, Matei IR, Costa-Silva B, Hoshino A, Rodrigues G, et al. Pre-metastatic niches: organ-specific homes for metastases. *Nat Rev Cancer*. 2017; 17:302–17.
68. Talmadge JE, Fidler IJ. AACR centennial series: the biology of cancer metastasis: historical perspective. *Cancer Res*. 2010; 70(14):5649–69.
69. Gómez-Cuadrado L, Tracey N, Ma R, Qian B, Brunton VG. Mouse models of metastasis: progress and prospects. *Dis Model Mech*. 2017; 10(9):1061–74.
70. Sleeman J, Steeg PS. Cancer metastasis as a therapeutic target. *Eur J Cancer*. 2010; 46(7):1177–80.
71. Steeg PS, Theodorescu D. Metastasis: A therapeutic target for cancer. *Nat Clin Pract Oncol*. 2008; 5(4):206–19.
72. Kim MY, Oskarsson T, Acharyya S, Nguyen DX, Zhang XH, Norton L, et al. Tumor self-seeding by circulating cancer cells. *Cell*. 2009; 139(7): 1315–26.
73. Coghlin C, Murray GI. Current and emerging concepts in tumour metastasis. *J Pathol*. 2010; 222(1):1–15.
74. Klein CA. Parallel progression of primary tumours and metastases. *Nat Rev Cancer*. 2009; 9(4):302–12.
75. Massagué J, Obenauf AC. Metastatic colonization by circulating tumour cells. *Nature*. 2016; 529(7586), 298–306.
76. Aguirre-Ghiso JA. Models, mechanisms and clinical evidence for cancer dormancy. *Nat Rev Cancer*. 2007; 7(11):834–46.
77. Townson JL, Chambers AF. Dormancy of solitary metastatic cells. *Cell Cycle*. 2006; 5(16):1744–50.
78. Gupta GP, Minn AJ, Kang Y, Siegel PM, Serganova I, Cordon-Cardo C, et al. Identifying sitespecific metastasis genes and functions. *Cold Spring Harb Symp Quant Biol*. 2005; 70:149–58.

79. Gay LJ, Malanchi I. The sleeping ugly: tumour microenvironment's act to make or break the spell of dormancy. *Biochim Biophys Acta Rev Cancer*. 2017; 1868(1):231–38.
80. Folkman J. Role of angiogenesis in tumor growth and metastasis. *Semin Oncol*. 2002; 29(6, Suppl 16):15–8.
81. Barkan D, Green JE, Chambers AF. Extracellular matrix: a gatekeeper in the transition from dormancy to metastatic growth. *Eur J Cancer*. 2010; 46(7):1181–8.
82. Teng MW, Swann JB, Koebel CM, Schreiber RD, Smyth MJ. Immune-mediated dormancy: an equilibrium with cancer. *J Leukoc Biol*. 2008; 84(4):988–93.
83. Fang M, Yuan J, Peng C, Li Y. Collagen as a double-edged sword in tumor progression. *Tumour Biol*. 2014; 35(4):2871–82.
84. Gelain F, Bottai D, Vescovi A, Zhang S. Designer self-assembling peptide nanofiber scaffolds for adult mouse neural stem cell 3-dimensional cultures. *PLoS One*. 2006; 1(1):e119.
85. Xu J, Rodriguez D, Petitclerc E, Kim JJ, Hangai M, Moon YS, et al. Proteolytic exposure of a cryptic site within collagen type IV is required for angiogenesis and tumor growth in vivo. *J Cell Biol*. 2001; 154(5):1069–79.
86. Micalizzi DS, Farabaugh SM, Ford HL. Epithelial-mesenchymal transition in cancer: parallels between normal development and tumor progression. *J Mammary Gland Biol Neoplasia*. 2010; 15(2):117–34.
87. Schmalhofer O, Brabletz S, Brabletz T. E-cadherin, beta-catenin, and ZEB1 in malignant progression of cancer. *Cancer Metastasis Rev*. 2009; 28(1-2):151–66.
88. Yang J, Weinberg RA. Epithelial-mesenchymal transition: At the crossroads of development and tumor metastasis. *Dev Cell*. 2008; 14(6):818–29.
89. Peinado H, Marin F, Cubillo E, Stark HJ, Fusenig N, Nieto MA, et al. Snail and E47 repressors of E-cadherin induce distinct invasive and angiogenic properties in vivo. *J Cell Sci*. 2004; 117(Pt 13):2827–39.

1.6. References

90. Christofori G, Semb H. The role of the cell-adhesion molecule E-cadherin as a tumour-suppressor gene. *Trends Biochem Sci.* 1999; 24(2):73–76.
91. Brabletz T, Jung A, Reu S, Porzner M, Hlubek F, Kunz-Schughart LA, et al. Variable beta-catenin expression in colorectal cancers indicates tumor progression driven by the tumor environment. *Proc Natl Acad Sci U S A.* 2001; 98(18):10356–61.
92. Aplin AE, Howe A, Alahari SK, Juliano RL. Signal transduction and signal modulation by cell adhesion receptors the role of integrins, cadherins, immunoglobulin-cell adhesion molecules, and selectins. *Pharmacol Rev.* 1998; 50(2):197–263.
93. Johnson JP. Cell adhesion molecules of the immunoglobulin supergene family and their role in malignant transformation and progression to metastatic disease. *Cancer Metastasis Rev.* 1991; 10(1):11–22.
94. Cavallaro U, Christofori G. Cell adhesion and signalling by cadherins and Ig-CAMs in cancer. *Nat Rev Cancer.* 2004; 4(2):118–32.
95. Aplin AE, Howe A, Alahari SK, Juliano RL. Signal transduction and signal modulation by cell adhesion receptors the role of integrins, cadherins, immunoglobulin-cell adhesion molecules, and selectins. *Pharmacol Rev.* 1998; 50(2):197–263.
96. Giancotti FG, Ruoslahti E. Integrin signaling. *Science.* 1999; 285(5430):1028–32.
97. Varner JA, Cheresch DA. Integrins and cancer. *Curr Opin Cell Biol.* 1996; 8(5):724–30.
98. Lukashev ME, Werb Z. ECM signaling orchestrating cell behaviour and misbehaviour. *Trends Cell Biol.* 1998; 8(11):437–41.
99. Coussens LM, Werb Z. Matrix metalloproteinases and the development of cancer. *Chem Biol.* 1996; 3(11):895–904.
100. Chambers AF, Matrisian LM. Changing views of the role of matrix metalloproteinases in metastasis. *J Natl Cancer Inst.* 1997; 89(17):1260–70.
101. Werb Z. ECM and cell surface proteolysis regulating cellular ecology. *Cell.* 1997; 91(4):439–42.

102. Stetler-Stevenson WG. Matrix metalloproteinases in angiogenesis a moving target for therapeutic intervention. *J Clin Invest.* 1999; 103(9):1237–41.
103. Bergers G, Coussens LM. Extrinsic regulators of epithelial tumor progression metalloproteinases. *Curr Opin Genet Dev.* 2000; 10(1):120–7.
104. Karnoub AE, Dash AB, Vo AP, Sullivan A, Brooks MW, Bell GW, et al. Mesenchymal stem cells within tumour stroma promote breast cancer metastasis. *Nature.* 2007; 449(7162):557–63.
105. Kessenbrock K, Plaks V, Werb Z. Matrix metalloproteinases: Regulators of the tumor microenvironment. *Cell.* 2010; 141(1):52–67.
106. Joyce JA, Pollard JW. Microenvironmental regulation of metastasis. *Nat Rev Cancer.* 2009; 9(4):239–52.
107. Johnsen M, Lund LR, Romer J, Almholt K, Dano K. Cancer invasion and tissue remodeling common themes in proteolytic matrix degradation. *Curr Opin Cell Biol.* 1998; 10:667–71.
108. Brábek J, Mierke CT, Rösel D, Veselý P, Fabry B. The role of the tissue microenvironment in the regulation of cancer cell motility and invasion. *Cell Commun Signal.* 2010; 8:22.
109. Harley BA, Kim HD, Zaman MH, Yannas IV, Lauffenburger DA, Gibson LJ. Microarchitecture of three-dimensional scaffolds influences cell migration behavior via junction interactions. *Biophys J.* 2008; 95(8):4013–24.
110. Dahl KN, Ribeiro AJ, Lammerding J. Nuclear shape, mechanics, and mechanotransduction. *Circ Res.* 2008; 102(11):1307–18.
111. Wolf K, Wu YI, Liu Y, Geiger J, Tam E, Overall C, et al. Multi-step pericellular proteolysis controls the transition from individual to collective cancer cell invasion. *Nat Cell Biol.* 2007; 9(8):893–904.
112. Friedl P, Wolf K. Plasticity of cell migration: a multiscale tuning model. *J Cell Biol.* 2010; 188(1):11–9.

1.6. References

113. Gehler S, Baldassarre M, Lad Y, Leight JL, Wozniak MA, Riching KM, et al. Filamin A-beta1 integrin complex tunes epithelial cell response to matrix tension. *Mol Biol Cell*. 2009; 20(14):3224–38.
114. Shoulders MD, Raines RT. Collagen structure and stability. *Annu Rev Biochem*. 2009; 78:929–58.
115. Peyton SR, Kim PD, Ghajar CM, Seliktar D, Putnam AJ. The effects of matrix stiffness and RhoA on the phenotypic plasticity of smooth muscle cells in a 3-D biosynthetic hydrogel system. *Biomaterials*. 2008; 29(17):2597–607.
116. Ulrich TA, de Juan Pardo EM, Kumar S. The mechanical rigidity of the extracellular matrix regulates the structure, motility, and proliferation of glioma cells. *Cancer Res*. 2009; 69(10):4167–74.
117. Lo CM, Wang HB, Dembo M, Wang YL. Cell movement is guided by the rigidity of the substrate. *Biophys J*. 2000; 79(1):144–52.
118. Levental KR, Yu H, Kass L, Lakins JN, Egeblad M, Erler JT, et al. Matrix crosslinking forces tumor progression by enhancing integrin signaling. *Cell*. 2009; 139(5):891–906.
119. Abercrombie M, Turner AA. Contact reactions influencing cell locomotion of a mouse sarcoma in culture. *Med Biol*. 1978; 56(6):299–303.
120. Provenzano PP, Inman DR, Eliceiri KW, Trier SM, Keely PJ. Contact guidance mediated three-dimensional cell migration is regulated by Rho/ROCK-dependent matrix reorganization. *Biophys J*. 2008; 95(11):5374–84.
121. Kopfstein L, Christofori G. Metastasis: cell-autonomous mechanisms versus contributions by the tumor microenvironment. *Cell Mol Life Sci*. 2006; 63(4):449–68.
122. Panková K, Rösel D, Novotný M, Brábek J. The molecular mechanisms of transition between mesenchymal and amoeboid invasiveness in tumor cells. *Cell Mol Life Sci*. 2010; 67(1):63–71.

123. Nobes CD, Hall A. Rho, rac, and cdc42 GTPases regulate the assembly of multimolecular focal complexes associated with actin stress fibers, lamellipodia, and filopodia. *Cell*. 1995; 81(1):53–62.
124. Ridley AJ, Paterson HF, Johnston CL, Diekmann D, Hall A. The small GTP-binding protein rac regulates growth factor-induced membrane ruffling. *Cell*. 1992; 70(3):401–10.
125. Sheetz MP, Felsenfeld DP, Galbraith CG. Cell migration: regulation of force on extracellular-matrix-integrin complexes. *Trends Cell Biol*. 1998; 8(2):51–4.
126. Brooks PC, Strömblad S, Sanders LC, von Schalscha TL, Aimes RT, Stetler-Stevenson WG, et al. Localization of matrix metalloproteinase MMP-2 to the surface of invasive cells by interaction with integrin alpha v beta 3. *Cell*. 1996; 85(5):683–93.
127. Goel A, Chauhan SS. Role of proteases in tumor invasion and metastasis. *Indian J Exp Biol*. 1997; 35(6):553–64.
128. Maaser K, Wolf K, Klein CE, Niggemann B, Zänker KS, Bröcker EB, et al. Functional hierarchy of simultaneously expressed adhesion receptors: integrin alpha2beta1 but not CD44 mediates MV3 melanoma cell migration and matrix reorganization within three-dimensional hyaluronan-containing collagen matrices. *Mol Biol Cell*. 1999; 10(10):3067–79.
129. Wolf K, Mazo I, Leung H, Engelke K, von Andrian UH, Deryugina EI, et al. Compensation mechanism in tumor cell migration: mesenchymal-amoeboid transition after blocking of pericellular proteolysis. *J Cell Biol*. 2003; 160(2):267–77.
130. Rosel D, Brabek J, Tolde O, Mierke CT, Zitterbart DP, Raupach C, et al. Up-regulation of Rho/ROCK signaling in sarcoma cells drives invasion and increased generation of protrusive forces. *Mol Cancer Res*. 2008; 6(9):1410–1420
131. Friedl P, Borgmann S, Bröcker EB. Amoeboid leukocyte crawling through extracellular matrix: lessons from the Dictyostelium paradigm of cell movement. *J Leukoc Biol*. 2001; 70(4):491–509.

1.6. References

132. Yumura S, Mori H, Fukui Y. Localization of actin and myosin for the study of ameboid movement in Dictyostelium using improved immunofluorescence. *J Cell Biol.* 1984; 99(3):894–9.
133. Sanz-Moreno V, Gadea G, Ahn J, Paterson H, Marra P, Pinner S, et al. Rac activation and inactivation control plasticity of tumor cell movement. *Cell.* 2008; 135(3):510–523.
134. Sahai E, Marshall CJ. Differing modes of tumour cell invasion have distinct requirements for Rho/ROCK signalling and extracellular proteolysis. *Nat Cell Biol.* 2003; 5(8):711–9.
135. Baker EL, Lu J, Yu D, Bonnecaze RT, Zaman MH. Cancer Cell Stiffness: Integrated Roles of Three-Dimensional Matrix Stiffness and Transforming Potential. *Biophys J.* 2010; 99(7):2048–57.
136. Yu DH, Hung MC. Overexpression of ErbB2 in cancer and ErbB2-targeting strategies. *Oncogene.* 2000; 19(53):6115–21.
137. Slamon DJ, Godolphin W, Ullrich A. Studies of the HER-2/neu proto-oncogene in human breast and ovarian cancer. *Science.* 1989; 244(4905):707–12.
138. Paszek MJ, Zahir N, Johnson KR, Lakins JN, Rozenberg GI, Gefen A, et al. Tensional homeostasis and the malignant phenotype. *Cancer Cell.* 2005; 8(3):241–54.
139. Bray D. *Cell movements: from molecules to motility.* 2nd Edition. Garland Science. New York. 2001.
140. Svitkina TM, Verkhovskiy AB, McQuade KM, Borisy GG. Analysis of the Actin-Myosin II System in Fish Epidermal Keratocytes: Mechanism of Cell Body Translocation. *J Cell Biol.* 1997; 139(2):397–415.
141. Gardel ML, Schneider IC, Aratyn-Schaus Y, Waterman CM. Mechanical Integration of Actin and Adhesion Dynamics in Cell Migration. *Annu Rev Cell Dev Biol.* 2010; 26:315–33.

142. Lammermann T, Bader BL, Monkley SJ, Worbs T, Wedlich-Söldner R, Hirsch K, et al. Rapid Leukocyte Migration by Integrin-Independent Flowing and Squeezing. *Nature*. 2008; 453(7191):51–5.
143. Lautenschläger F, Piel M. Microfabricated devices for cell biology: all for one and one for all. *Curr Opin Cell Biol*. 2013; 25(1):116–24.
144. Maiuri P, Rupprecht J-F, Wieser S, Ruprecht V, Bénichou O, Carpi N, et al. Actin Flows Mediate a Universal Coupling between Cell Speed and Cell Persistence. *Cell*. 2015; 161(2):374–86.
145. Segerer FJ, Thüroff F, Alberola AP, Frey E, Rädler JO. Emergence and persistence of collective cell migration on small circular micropatterns. *Phys Rev Lett*. 2015; 114(22):228102.
146. Caballero D, Voituriez R, Riveline D. The cell ratchet: Interplay between efficient protrusions and adhesion determines cell motion. *Cell Adhesion & Migration*. 2015; 9(5):327–34.
147. Schreiber C, Segerer FJ, Wagner E, Roidl A, Rädler JO. Ring-Shaped Microlanes and Chemical Barriers as a Platform for Probing Single-Cell Migration. *Scientific Reports*. 2016; 6:26858.
148. Zhang J, Guo WH, Wang YL. Microtubules stabilize cell polarity by localizing rear signals. *Proc Natl Acad Sci U S A*. 2014; 111(46):16383–8.
149. Fraley SI, Feng Y, Giri A, Longmore GD, Wirtz D. Dimensional and temporal controls of three-dimensional cell migration by zyxin and binding partners. *Nat Commun*. 2012; 3:719.
150. Zhou F, Schaffer SA, Schreiber C, Segerer FJ, Goychuk A, Frey E, et al. Quasi-periodic migration of single cells on short microlanes. 2020; 15(4):e0230679.
151. Brückner DB, Fink A, Schreiber C, Röttgermann PJF, Rädler JO, Broedersz CP. Stochastic nonlinear dynamics of confined cell migration in two-state systems. *Nat Phys*. 2019; 15:595–601.

1.6. References

152. Fink A, Brückner DB, Schreiber C, Röttgermann PJF, Broedersz CP, Rädler JO. Area and Geometry Dependence of Cell Migration in Asymmetric Two-State Micropatterns. *Biophys J*. 2020; 118(3):552–64.
153. Petrie RJ, Gavara N, Chadwick RS, Yamada KM. Nonpolarized signaling reveals two distinct modes of 3D cell migration. *J Cell Biol*. 2012; 197(3):439–55.
154. Shih W, Yamada S. Myosin IIA dependent retrograde flow drives 3D cell migration. *Biophys J*. 2010; 98(8):L29–31.
155. Zhu J, Mogilner A. Comparison of cell migration mechanical strategies in three-dimensional matrices: a computational study. *Interface Focus*. 2016; 6(5):20160040.
156. Hawkins RJ, Piel M, Faure-Andre G, Lennon-Dumenil AM, Joanny JF, Prost J, et al. Pushing off the walls: a mechanism of cell motility in confinement. *Phys Rev Lett*. 2009; 102(5):058103.
157. Bergert M, Chandradoss SD, Desai RA, Paluch E. Cell mechanics control rapid transitions between blebs and lamellipodia during migration. *Proc Natl Acad Sci USA*. 2012; 109(36):14434–9.
158. Strychalski W, Guy RD. A computational model of bleb formation. *Math Med Biol*. 2013; 30(2):115–30.
159. Legant WR, Miller JS, Blakely BL, Cohen DM, Genin GM, Chen CS. Measurement of mechanical tractions exerted by cells in three-dimensional matrices. *Nat Methods*. 2010; 7(12):969–71.
160. Hawkins RJ, Poincloux R, Bénichou O, Piel M, Chavrier P, Voituriez R. Spontaneous contractility-mediated cortical flow generates cell migration in three-dimensional environments. *Biophys J*. 2011; 101(5):1041–5.
161. Han W, Chen S, Yuan W, Fan Q, Tian J, Wang X, et al. Oriented collagen fibers direct tumor cell intravasation. *Proc Natl Acad Sci U S A*. 2016; 113(40): 11208–13.
162. Zhao X, Chen H, Liu X, Cang J. Orientation-selective responses in the mouse lateral geniculate nucleus. *J Neurosci*. 2013; 33(31):12751–63.

163. Carey SP, Starchenko A, McGregor AL, Reinhart-King CA. Leading malignant cells initiate collective epithelial cell invasion in a three-dimensional heterotypic tumor spheroid model. *Clin Exp Metastasis*. 2013; 30(5):615–30.
164. Sabeh F, Ota I, Holmbeck K, Birkedal-Hansen H, Soloway P, Balbin M, et al. Tumor cell traffic through the extracellular matrix is controlled by the membrane-anchored collagenase MT1-MMP. *J Cell Biol*. 2004; 167(4):769–81.
165. Griffith LG, Swartz MA. Capturing complex 3D tissue physiology in vitro. *Nat Rev Mol Cell Biol*. 2006; 7(3):211–24.
166. Infanger DW, Lynch ME, Fischbach C. Engineered culture models for studies of tumor-microenvironment interactions. *Annu Rev Biomed Eng*. 2013; 15:29–53.
167. Nyga A, Cheema U, Loizidou M. 3D tumour models: novel in vitro approaches to cancer studies. *J Cell Commun Signal*. 2011; 5(3):239–48.
168. Stamov DR, Pompe T. Structure and function of ECM-inspired composite collagen type I scaffolds. *Soft Matter*. 2012; 8(40):10200–12.
169. Jokinen J, Dadu E, Nykvist P, Kapyla J, White DJ, Ivaska J, et al. Integrin-mediated cell adhesion to type I collagen fibrils. *J Biol Chem*. 2004; 279(30):31956–63.
170. Franke K, Sapudom J, Kalbitzer L, Anderegg U, Pompe T. Topologically defined composites of collagen types I and V as in vitro cell culture scaffolds. *Acta Biomater*. 2014; 10(6):2693–702.
171. Sung ES, Su G, Pehlke C, Trier SM, Eliceiri KW, Keely PJ, et al. Control of 3-dimensional collagen matrix polymerization for reproducible human mammary fibroblast cell culture in microfluidic devices. *Biomaterials*. 2009; 30(27):4833–41.
172. Shannon GS, Novak T, Mousoulis C, Voytik-Harbin SL, Neu CP. Temperature and concentration dependent fibrillogenesis for improved magnetic alignment of collagen gels. *Rsc Adv*. 2015; 5(3):2113–21.
173. Levental KR, Yu H, Kass L, Lakins JN, Egeblad M, Ertler JT, et al. Matrix cross-linking forces tumor progression by enhancing integrin signaling. *Cell*. 2009; 139(5):891–906.

1.6. References

174. Zeugolis DI, Khew ST, Yew ES, Ekaputra AK, Tong YW, Yung LY, et al. Electrospinning of pure collagen nano-fibres—just an expensive way to make gelatin? *Biomaterials*. 2008; 29(15):2293–305.
175. Law JX, Liau LL, Saim A, Yang Y, Idrus R. Electrospun Collagen Nanofibers and Their Applications in Skin Tissue Engineering. *Tissue Eng Regen Med*. 2017; 14(6):699–718.
176. Caliari SR, Ramirez MA, Harley BA. The development of collagen-GAG scaffold-membrane composites for tendon tissue engineering. *Biomaterials*, 2011; 3234:8990–8.
177. Wang X, Ao Q, Tian X, Fan J, Wei Y, Hou W, et al. 3D bioprinting technologies for hard tissue and organ engineering. *Materials*. 2016; 9(10):802.
178. Wang C, Huang W, Zhou Y, He L, He Z, Chen Z, et al. 3D printing of bone tissue engineering scaffolds. *Bioact. Mater*. 2020; 5(1):82–91.
179. Fisher JP, Dean D, Engel PS, Mikos AG. Photoinitiated Polymerization of Biomaterials. *Annu Rev Mater Res*. 2001; 31:171–81.
180. Kwok SJJ, Kuznetsov IA, Kim M, Choi M, Scarcelli G, Yun SH. Selective two-photon collagen crosslinking *in situ* measured by Brillouin microscopy. *Optica*. 2016; 3(5):469–72.
181. Vader D, Kabla A, Weitz D, Mahadevan L. Strain-induced alignment in collagen gels. *PLoS ONE*. 2009; 4(6):e5902.
182. Guo C, Kaufman LJ. Flow and magnetic field induced collagen alignment. *Biomaterials*. 2007; 28(6):1105–14.
183. Novak T, Voytik-Harbin SL, Neu CP. Cell encapsulation in a magnetically aligned collagen-GAG copolymer microenvironment. *Acta Biomater*. 2015; 11:274–82.
184. Delsing P, Cleland AN, Schuetz MJA, Knörzer J, Giedke G, Cirac JI, et al. The 2019 surface acoustic waves roadmap. *J Phys D: Appl Phys*. 2019; 52(35):353001.

185. Cohen S, Sazan H, Kenigsberg A, Schori H, Piperno S, Shpaisman H, et al. Large-scale acoustic-driven neuronal patterning and directed outgrowth. *Sci. Rep.* 2020; 10(1):4932.
186. Guo F, Li P, French JB, Mao Z, Zhao H, Li S, et al. Controlling cell-cell interactions using surface acoustic waves. *PNAS.* 2015; 112(1):43–8.
187. Lee P, Lin R, Moon J, Lee PL. Microfluidic alignment of collagen fibers for in vitro cell culture. *Biomed Microdevices.* 2006;8(1):35–41.
188. Haynl C, Hofmann E, Pawar K, Förster S, Scheibel T. Microfluidics-Produced Collagen Fibers Show Extraordinary Mechanical Properties. *Nano Lett.* 2016; 16(9):5917–22.
189. Palamidessi A, Malinverno C, Frittoli E, Corallino S, Barbieri E, Sigismund S, et al. Unjamming overcomes kinetic and proliferation arrest in terminally differentiated cells and promotes collective motility of carcinoma. *Nat Mater.* 2019; 18(11):1252–63.
190. Geiger F, Rüdiger D, Zahler S, Engelke H. Fiber stiffness, pore size and adhesion control migratory phenotype of MDA-MB-231 cells in collagen gels. *PLoS ONE.* 2019; 14(11):e0225215.
191. Ilina O, Gritsenko PG, Syga S, Lippoldt J, La Porta CAM, Chepizhko O, et al. Cell-cell adhesion and 3D matrix confinement determine jamming transitions in breast cancer invasion. *Nat Cell Biol.* 2020; 22(9):1103-15.
192. Liu YJ, Le Berre M, Lautenschlaeger F, Maiuri P, Callan-Jones A, Heuze M, et al. Confinement and low adhesion induce fast amoeboid migration of slow mesenchymal cells. *Cell.* 2015; 160(4):659–72.
193. Wolf K, Alexander S, Schacht V, Coussens LM, von Andrian UH, van Rheenen J, et al. Collagen-based cell migration models in vitro and in vivo. *Semin Cell Dev Biol.* 2009; 20(8):931–41.
194. Provenzano PP, Eliceiri KW, Campbell JM, Inman DR, White JG, Keely PJ. Collagen reorganization at the tumor-stromal interface facilitates local invasion. *BMC Med.* 2006; 4(1):38.

1.6. References

195. Sauer F, Oswald L, Ariza de Schellenberger A, Tzschatzsch H, Schrank F, Fischer T, et al. Collagen networks determine viscoelastic properties of connective tissues yet do not hinder diffusion of the aqueous solvent. *Soft Matter*. 2019; 15(14):3055–64.
196. Tozluoglu M, Tournier AL, Jenkins RP, Hooper S, Bates PA, Sahai E. Matrix geometry determines optimal cancer cell migration strategy and modulates response to interventions. *Nat Cell Biol*. 2013; 15 (7):751–62.
197. Daidone MG, Silvestrini R. Prognostic and predictive role of proliferation indices in adjuvant therapy of breast cancer. *J Natl Cancer Inst Monogr*. 2001; (30):27-35.
198. Aleskandarany MA, Green AR, Benhasouna AA, Barros FF, Neal K, Reis-Filho JS, et al. Prognostic value of proliferation assay in the luminal, HER2-positive, and triple-negative biologic classes of breast cancer. *Breast Cancer Res*. 2012; 14(1):R3.
199. Chen H, Gu X, Liu Y, Wang J, Wirt SE, Bottino R, et al. PDGF signalling controls age-dependent proliferation in pancreatic beta-cells. *Nature*. 2011; 478(7369):349-55.
200. Evan GI, Vousden KH. Proliferation, cell cycle and apoptosis in cancer. *Nature*. 2001; 411(6835):342-8.
201. Evan G, Littlewood T. A matter of life and cell death. *Science*. 1998; 281(5381):1317-22.
202. Salic A, Mitchison TJ. A chemical method for fast and sensitive detection of DNA synthesis in vivo. *Proc Natl Acad Sci U S A*. 2008; 105(7):2415-20.
203. Cavanagh BL, Walker T, Norazit A, Meedeniya AC. Thymidine analogues for tracking DNA synthesis. *Molecules*. 2011; 16(9):7980-93.
204. Gramlich PM, Wirges CT, Manetto A, Carell T. Postsynthetic DNA modification through the copper-catalyzed azide-alkyne cycloaddition reaction. *Angew Chem Int Ed Engl*. 2008; 47(44):8350-8.
205. Gierlich J, Burley GA, Gramlich PM, Hammond DM, Carell T. Click chemistry as a reliable method for the high-density postsynthetic functionalization of alkyne-modified DNA. *Organic Letters*. 2006; 8(17):3639-42.

206. Nik-Zainal S, Van Loo P, Wedge DC, Alexandrov LB, Greenman CD, Lau KW, et al. The life history of 21 breast cancers. *Cell*. 2012; 149(5):994-1007.
207. Itzkovitz S, van Oudenaarden A. Validating Transcripts with Probes and Imaging Technology. *Nat Methods*. 2011. 8(4 Suppl):S12-9.
208. Raj A, van Oudenaarden A. Nature, Nurture, or Chance: Stochastic Gene Expression and Its Consequences. *Cell*. 2008; 135(2):216-26.
209. Eldar A, Elowitz MB. Functional Roles for Noise in Genetic Circuits. *Nature*. 2010; 467(7312):167-73.
210. Raj A, van den Bogaard P, Rifkin SA, van Oudenaarden A, Tyagi S. Imaging Individual mRNA Molecules Using Multiple Singly Labeled Probes. *Nat Methods*. 2008; 5(10):877-9.
211. Raj A, Tyagi S. Detection of individual endogenous RNA transcripts in situ using multiple singly labeled probes. In: *Single molecule Tools: Chapter 17, Fluorescence based approaches, Part A*; Walter, N G B T-M in E, Ed; Academic Press, 2010; 472:365-8.
212. Semrau S, Crosetto N, Bienko M, Boni M, Bernasconi P, Chiarle R, et al. FuseFISH: Robust Detection of Transcribed Gene Fusions in Single Cells. *Cell Rep*. 2014, 6(1):18-23.
213. <https://www.genome.gov/genetics-glossary/Fluorescence-In-Situ-Hybridization>. 13.02.2021
214. Silahatoglu A, Pfundheller H, Koshkin A, Tommerup N, Kauppinen S. LNA-modified oligonucleotides are highly efficient as FISH probes. *Cytogenet Genome Res*. 2004; 107(1-2):32-7.
215. Rostovtsev VV, Green LG, Fokin VV, Sharpless KB. A Stepwise Huisgen Cycloaddition Process: copper(I)-catalyzed Regioselective "Ligation" of Azides and Terminal Alkynes. *Angew Chem Int Ed Engl*. 2002; 41(14):2596-9.

1.6. References

216. Gierlich J, Burley GA, Gramlich PME, Hammond DM, Carell T. Click Chemistry as a Reliable Method for the High-Density Postsynthetic Functionalization of Alkyne-Modified DNA. *Org Lett*. 2006; 8(17):3639–42.
217. Gramlich PME, Warncke S, Gierlich J, Carell T. Click-click-click: Single to Triple Modification of DNA. *Angew Chem Int Ed Engl*. 2008; 47(18): 3442–4.
218. Gramlich PME, Wirges CT, Manetto A, Carell T. Postsynthetic DNA Modification through the Copper-Catalyzed Azide–Alkyne Cycloaddition Reaction. *Angew Chem Int Ed Engl*. 2008; 47(44): 8350–8.
219. Nikolic J, Le Bars R, Lama Z, Scrima N, Lagaudrière-Gesbert C, Gaudin Y, et al. Negri bodies are viral factories with properties of liquid organelles. *Nat Commun*. 2017; 8(1):58.
220. Heinrich BS, Maliga Z, Stein DA, Hyman AA, Whelan SPJ. Phase transitions drive the formation of vesicular stomatitis virus replication compartments. *MBio*. 2018; 9(5):1–10.
221. Alenquer M, Vale-Costa S, Etibor TA, Ferreira F, Sousa AL, Amorim MJ. Influenza A virus ribonucleoproteins form liquid organelles at endoplasmic reticulum exit sites. *Nat Commun*. 2019; 10(1):1–19.
222. Guseva S, Milles S, Jensen MR, Salvi N, Kleman JP, Maurin D, et al. Measles virus nucleo- and phosphoproteins form liquid-like phase-separated compartments that promote nucleocapsid assembly. *Sci Adv*. 2020; 6(14):eaaz7095.
223. Bergeron-Sandoval LP, Safaee N, Michnick SW. Mechanisms and Consequences of Macromolecular Phase Separation. *Cell*. 2016; 165(5):1067–79.
224. Alberti S. Phase separation in biology. *Curr Biol*. 2017; 27(20):R1097–R1102.
225. Wang J, Choi JM, Holehouse AS, Lee HO, Zhang X, Jahnke M, et al. A molecular grammar governing the driving forces for phase separation of prion-like RNA binding proteins. *Cell*. 2018; 174(3):688–699.e16.
226. Alberti S, Gladfelter A, Mittag T. Considerations and Challenges in Studying Liquid-Liquid Phase Separation and Biomolecular Condensates. *Cell*. 2019; 176(3):419–434.

2. Characterization and methods

2.1. Fluorescence microscopy

The advantage of fluorescence microscopy, compared to regular microscopy, is that the features of interest can be highlighted with fluorescence. If the probe has no auto fluorescence, it is stained with a dye and is excited with a light source, for example a laser or a light-emitting diode. The dyes have to be excited with light of a specific range around an optimal excitation wavelength and energy ($h\nu$), which is specific for each dye. The light excites electrons to a higher energetic state (S_0 to S_1). This excited species is not stable and can decay in two ways. The first is the non-radiative decay. The excited species dissipates thermal energy as motion into the surrounding medium, by transferring it into its vibrational modes and in the transfer itself. This is described in a cut-out of a Jablonski diagram (figure 2.1) with the relaxation from 5 to 0 in the S_1 state. The second way is the radiative decay, where the excess energy is released as a photon ($h\nu_f$), and these photons can be observed with a microscope as fluorescence [1, 2].

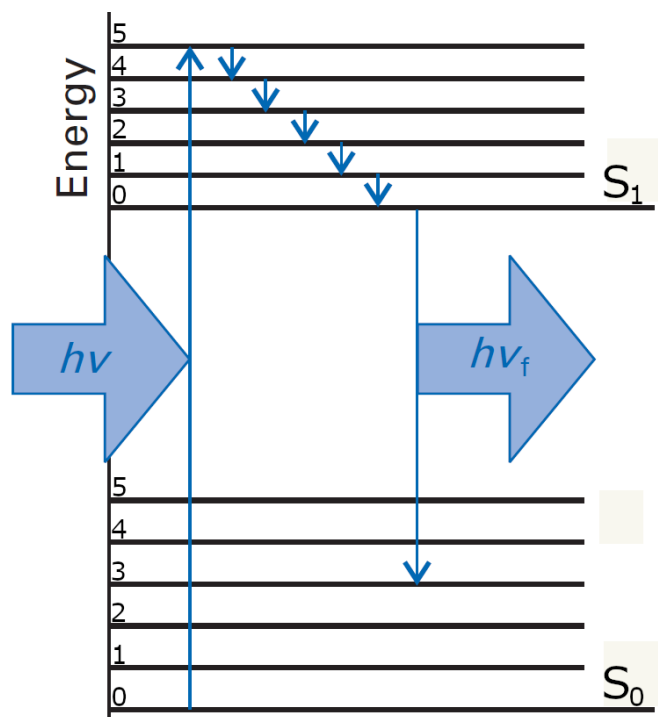


Figure 2.1: Jablonski diagram showing the formation and decay of an excited species including vibrational energy levels [2].

2.1. Fluorescence microscopy

Due to the non-radiative decay the light that is emitted by the dye molecules has a bigger wavelength and a lower intensity compared to the absorbed light (figure 2.2). This red shift is also called stokes shift, and occurs due to the loss of energy during the non-radiative decay, that takes place prior to the radiative one [3, 4].

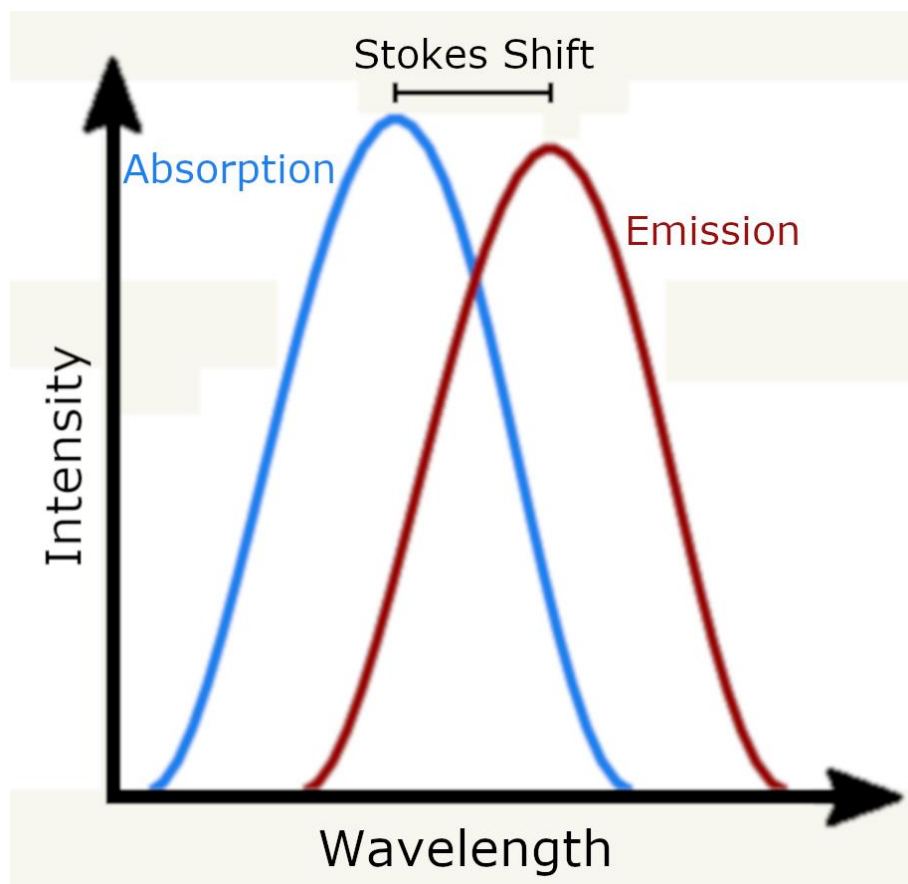


Figure 2.2: Schematic absorption and emission spectra of a fluorescent dye [4].

Additional, relaxation processes that can occur amongst others are quenching, photo bleaching, fluorescence energy transfer, or intersystem crossing, which leads to phosphorescence. These are other ways for the excited species to get rid of the excess energy, but they have other effects, and can for example damage the dye molecule (photo bleaching).

2.1.1. Widefield microscopy

With a widefield microscope, the interaction of cells with their environment, like different hydrogels or particles, can be observed down to the molecular level. With multiple fluorescent dyes, even several different aspects can be observed simultaneously in real time. A widefield fluorescence microscopy setup is build according to figure 2.3 and can be used to monitor intracellular components, as well as their associated diffusion coefficients, or the membrane potential. It can also be used to investigate the pH value, viscosity, refractive index, ionic concentrations, solvent polarity and other environmental parameters.

The schematic in figure 2.3 shows a setup with incident reflected light illumination. The microscope is built with a trinocular observation head, which is coupled to a cooled charge-coupled device (CCD) camera system. One light source is used for transmitted light images and another is used for the excitation of the fluorophores (tungsten-halogen lamp for UV wavelengths and mercury arc-discharge lamp for the visible range). Optical excitation filters cut off all wavelengths, except the specific one needed to excite the used fluorophore in the sample through the objective. The emitted light from the sample is collected with an objective and then separated from the excitation wavelength with a dichroic mirror. This is possible, because of the previously described Stokes shift happening in the fluorophore. The separation of the lightbeams maximizes the amount of light the sample is excited with and the amount redirected to the cameras. An emission filter cuts off unwanted background and finally the signal can be observed with the eyepieces or the CCD camera.

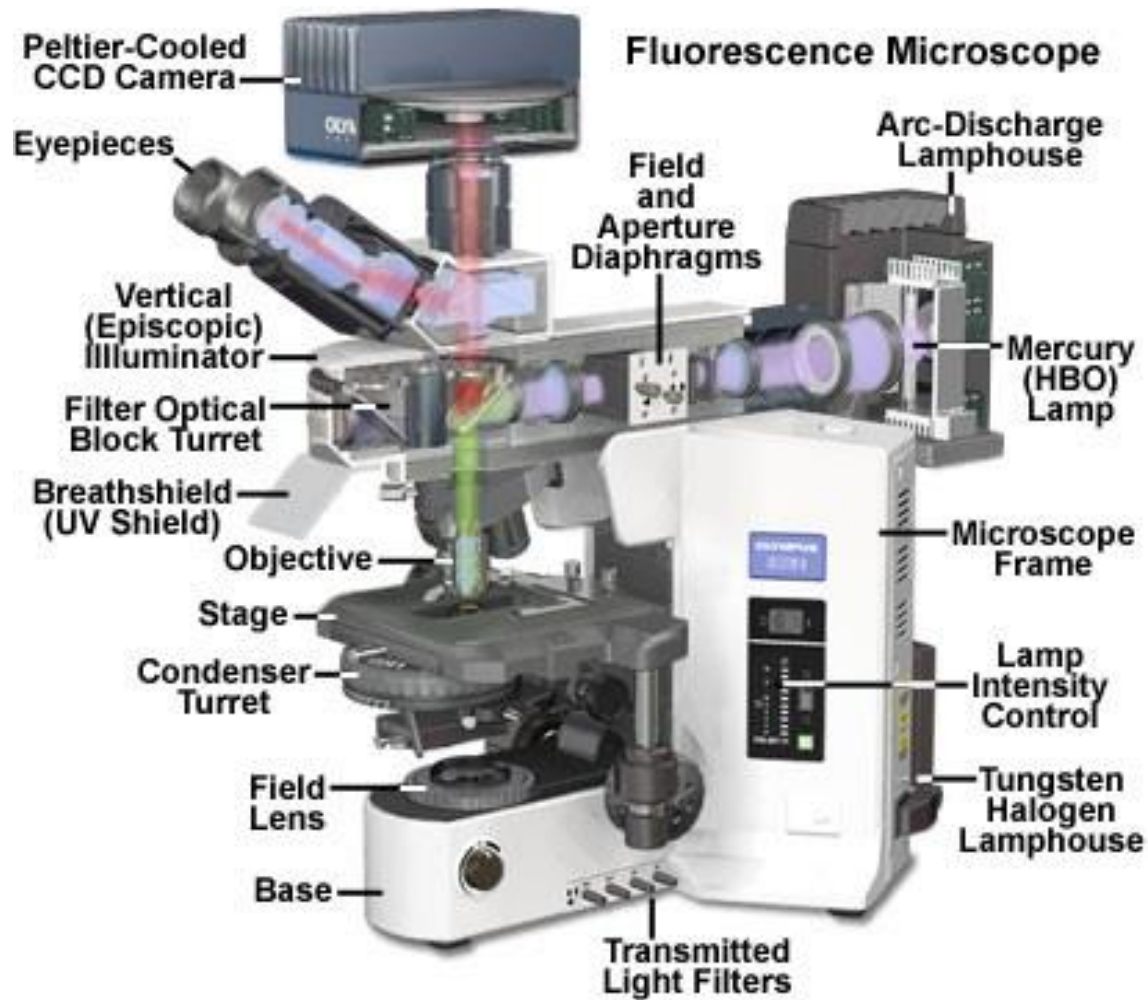


Figure 2.3: Schematic of a upright fluorescence microscope setup [5].

In a widefield microscope, a much bigger volume of the specimen is exposed to the excitation light, compared to a confocal microscope (figure 2.4). In confocal microscopes, the light is focused through a pinhole, before it is focused on the regions of interest of the sample. The light emitted from the sample is collected by the same objective and passes a second pinhole, before reaching the detector behind the focussing lens. The second pinhole blocks most of the light emitted by planes above or below the focal spot in the sample, resulting in a lower background.

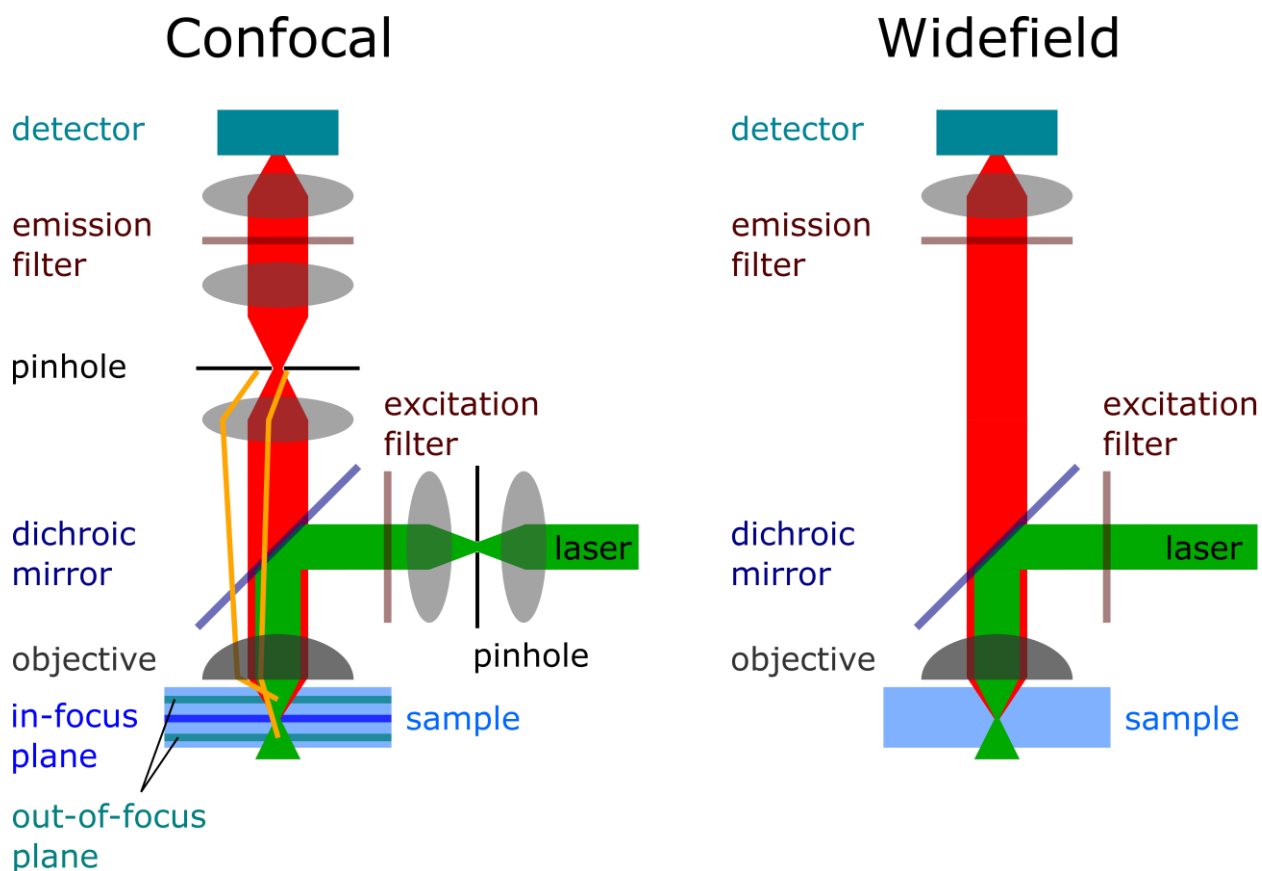


Figure 2.4: Schematic of the optical path in a confocal microscope, compared to a widefield microscope. Excitation light (green) is redirected by a dichroic mirror (dark blue), hits the sample (lightblue) and the emitted light (red) reaches the detector. In the confocal microscope the light emitted by out-of-focus planes is blocked (orange lines).

Widefield microscopes are therefore less complex build, but there is less exclusion of out-of-focus or background fluorescence. In turn, a lot more signal is collected by the camera and weaker light sources can be used for illumination. Also, the damage done to the probe through the light is not focused as it is with confocal microscopy, but distributed over the specimen, when high excitation intensities are used [8, 9].

The used widefield microscope in chapter 7 was the Eclipse Ti-E from Nikon. The images were acquired with a 0.7 NA 60x S Plan Fluor ELWD oil immersion objective from Nikon. Measurements were performed at room temperature. A pE-4000 illumination system (CoolLED) was used as light source. DAPI was imaged using a 385 nm LED at 30.1 μ W

intensity and 55 ms exposure time. EGFP and ATTO 488 were imaged using a 470 nm LED at 69.5 μW intensity with 300 ms exposure time and 7.8 μW intensity with 55 ms exposure time respectively. mCherry was imaged with a 550 nm LED at 40.8 μW intensity and 300 ms exposure time. The light path was regulated with a Dapi/FITC/Cy3/Cy5 Quad HC Filter Set (Semrock). The images were acquired using a scientific complementary metal–oxide–semiconductor (sCMOS) camera (Andor Technology).

Image acquisition was controlled using the NIS-Elements AR V.4.50 Software (Nikon).

2.1.2. Spinning disk confocal microscopy

A further specialization of the classic widefield microscope is the spinning disk confocal microscope, which uses a different setup, that can focus distinct sections of the observed specimen. The spinning disk microscope was used to study the intracellular mechanisms of virus infected, fixed cells in 2D. It was also used to study the migration of hydrogel embedded cancer cells in 3D over a long time period. Figure 2.5 shows the schematic build of a spinning disk confocal microscope. The main difference compared to a widefield fluorescence microscope is the introduction of two spinning disks with holes in the excitation and detection pathway to block the out-of-focus fluorescence. The excitation light (blue line) first passes through the microlenses on the surface of the first spinning disk, then it traverses the 50-micrometer pinholes in the second disk (Nipkow spinning disk). This light hits the probe through the microscope optical camera port and an objective (pink line). The emission light goes the same way back from the sample through the confocal pinholes of the Nipkow spinning disk and is redirected via a dichromatic beamsplitter (pink, then yellow line). A second dichromatic beamsplitter divides the shorter emission wavelengths (green line) and the longer wavelengths (red line). Then they respectively pass through a filter wheel, to the camera [6].

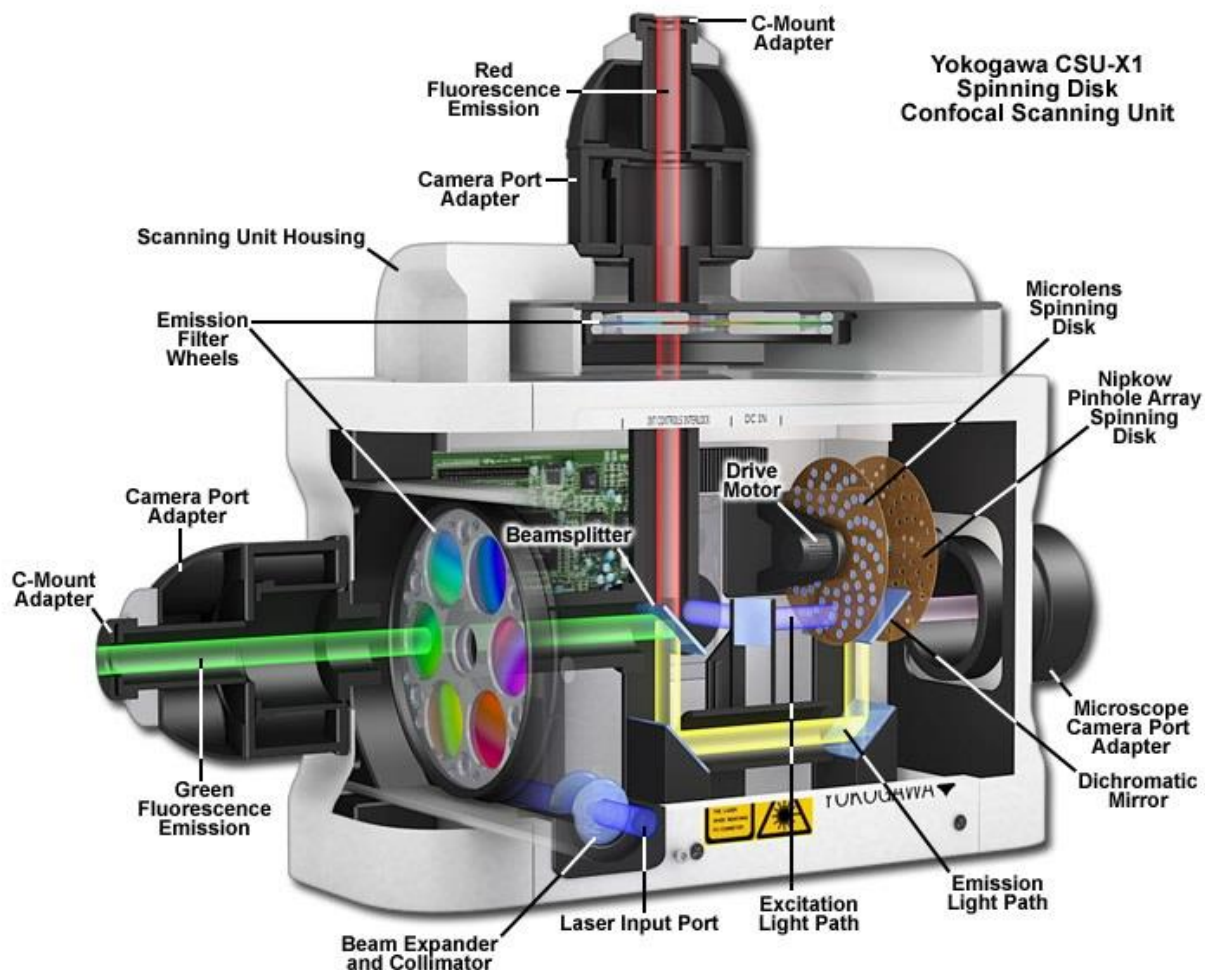


Figure 2.5: Setup and light pathways of the used Spinning disk microscope (Zeiss Cell Observer SD with a Yokogawa CSU-X1 spinning disk unit) [6].

Due to this setup, the spinning disk microscope is capable of recording thin optical sections even in thick samples very fast, with high spatial resolution. Especially the axial resolution is increased. This is acquired with the spinning disks that create many confocal spots which are screened over the sample. A drawback is the necessity of strong lasers when using this method, because a huge part of the light gets blocked by the spinning disk, while passing through the pinholes [6, 7].

The cell migration experiments (chapter 3. and 4.) were conducted with a 1.40 NA 63x Plan apochromat oil immersion objective from Zeiss. Measurements were performed at 37 °C

2.1. Fluorescence microscopy

and a 5% CO₂ humidified atmosphere. Hoechst 33342 was excited with a 405 nm laser at 11.2 μW intensity for 200 ms. FITC-collagen and LifeAct-TagGFP2 were imaged using a 488 nm laser at 13.0 μW intensity with 100 ms exposure time and at 50.6 μW intensity with 200 ms exposure time respectively. LifeAct-TagRFP and Alexa Fluor 546 were imaged with a 561 nm laser at 70.7 μW intensity and 200 ms and 1000 ms exposure time respectively. Images with ATTO-633 dye were taken with a 639 nm laser at 3.7 μW intensity and 100 ms exposure time or at 5.5 μW intensity and 200 ms exposure time. Cell spheroids were imaged with a tungsten-halogen lamp with 682.0 μW and 200 ms exposure time. Each image was a z-stack consisting of 50 frames with a 0.7 μm distance between them. A cell spheroid's image consisted of 120 to 160 pictures, depending on the spread of the spheroid over time, and each picture had an 11 frame z-stack with a 1.5 μm distance between them. In the excitation path a quad-edge dichroic beamsplitter (FF410/504/582/669-Di01-25x36, Semrock) was used. For two color detection of FITC-collagen and LifeAct-TagRFP fusion protein or LifeAct-TagGFP2 fusion protein and ATTO-633, a dichroic mirror (660 nm, Semrock) and band-pass filters 525/50 and 690/60 (both Semrock) were used in the detection path. Separate images for each fluorescence channel were acquired using two separate electron multiplier charge coupled devices (EMCCD) cameras (PhotometricsEvolve™). Time-lapse images were acquired either with a frame time of 20 min and 50 frames, or for cell spheroids with a frame time of 2 hours over several days.

Experiments concerning RNA and DNA detection via click chemistry (chapter 5. and 6.) were conducted with a 1.40 NA 100x Plan apochromat oil immersion objective from Zeiss. Measurements were performed at room temperature. DAPI was imaged using a 405 nm laser at 11.2 μW intensity and 800 ms exposure time, eGFP was imaged using a 488 nm laser at 16.9 μW intensity and 200 ms exposure time and 5-TAMRA was imaged with a 561 nm laser at 29.2 μW intensity and 200 ms exposure time. In the excitation path a quad-edge dichroic beamsplitter (FF410/504/582/669-Di01-25x36, Semrock) was used. For two color detection of eGFP and 5-TAMRA a dichroic mirror (660 nm, Semrock) and band-pass filters 525/50 and 690/60 (both Semrock) were used in the detection path. Separate images for each fluorescence channel were acquired using two separate electron multiplier charge coupled devices (EMCCD) cameras (PhotometricsEvolve™).

The experiments in chapter 7. were conducted with a 1.40 NA 63x Plan apochromat oil immersion objective from Zeiss. Measurements were performed at room temperature. Photo bleaching for FRAP (Fluorescence recovery after photo bleaching) experiments was done with a 488 nm laser at 148.3 μW intensity and 3000 ms exposure time. eGFP was imaged using a 488 nm laser at 36.9 μW intensity and 200 ms exposure time and mCherry was imaged with a 561 nm laser at 29.2 μW intensity and 200 ms exposure time. Images recorded as z-stacks consisted of either 10 or 50 frames, with a 0.5 μm distance between them, depending on the sample. In the excitation path a quad-edge dichroic beamsplitter (FF410/504/582/669-Di01-25x36, Semrock) was used. For two color detection of eGFP and mCherry a dichroic mirror (660 nm, Semrock) and band-pass filters 525/50 and 690/60 (both Semrock) were used in the detection path. Separate images for each fluorescence channel were acquired using two separate electron multiplier charge coupled devices (EMCCD) cameras (Photometrics EvolveTM).

Image acquisition was controlled using the Zeiss Zen (blue edition) 2011 Software (Zeiss).

2.2. Rheology

A rheometer can measure the flow and deformation behavior of a substance. For such a measurement three factors have to be taken into account, first the internal structure of the sample, second the external force applied to the sample, and third the environmental conditions (e.g. room temperature). The plate rheometer depicted in figure 2.6 applies a defined torque to the sample and measures the resulting deflection. To get the viscosity of a sample, it is first fixed between the measuring system (e.g. cone-plate, parallel plate or cylinder) and the lower pressure plate. Then a defined current is set at the electrical motor that corresponds to a certain torque. Upon the force application the sample provides resistance or a reset torque, resulting in a deflection angle, which is measured at the optical encoder [10, 11].

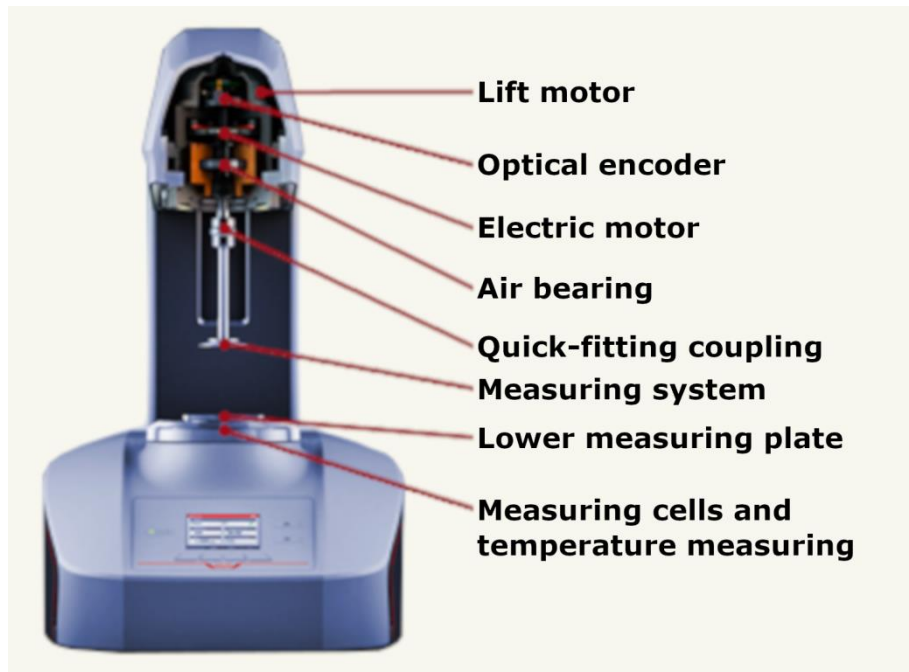


Figure 2.6: Setup of an air-bearing rotational and oscillatory rheometer [11].

The rotational speed of the measuring system is calculated from the deflection angle and the duration of the deformation. From these parameters the rheological properties of the material can be calculated [11].

Shear stress τ is the ratio of the force F (torque) and the area A it is applied to.

$$\tau = \frac{F}{A} [Pa]$$

Deformation γ is calculated with the deflection angle φ .

$$\gamma = \frac{\varphi}{2\pi \text{ rad}} \cdot 100 [\%]$$

The shear rate $\dot{\gamma}$ is calculated with the difference in speed of the two measuring systems (rotational speed) dv and the distance between them dy .

$$\dot{\gamma} = \frac{dv}{dy} [s^{-1}]$$

The viscosity η in turn is defined by the shear stress τ and the shear rate $\dot{\gamma}$.

$$\eta = \frac{\tau}{\dot{\gamma}} [Pa \cdot s]$$

A rheometer can measure in two different modes, the rotational or the oscillatory test. For the rotational measurement the measuring system only moves in one direction. This mode is usually used for more liquid samples, because they are deformed instantly by the applied torque. Therefore the determination of the deflection of the measuring system is more accurate and the calculation of the rheological parameters is not as difficult. An oscillatory measurement is usually used with samples, where the viscoelastic properties are important. The rheometer again determines the deflection of the measuring system and the required torque. The viscoelastic properties of the sample cause a phase lag δ meaning the response wave is time-delayed compared to the set oscillation.

The storage modulus G' and loss modulus G'' are calculated with the values measured by the rheometer (deflection angle, torque, and phase shift) and the conversion factors for the measuring system [10-13].

For the bulk rheology measurements in chapter 3. a MCR 100 rheometer (Anton Paar) with a PP25 measuring plate was used (figure 2.7). The sample was prepared directly on the rheometer and measured at 37 °C and a gap size of 0.5 mm. The deformation was measured stepwise up to 10% at a frequency of 1 Hz. (oscillatory measurement).



Figure 2.7: MCR 100 rheometer (left) with a PP25 measuring plate (right) used for bulk rheology measurements.

2.3. Atomic force microscopy

An atomic force microscope (AFM) is a scanning probe microscope with a resolution in the nanometer regime. It can be used for force measurement, topographic imaging and manipulation of the sample [14]. The microscope is build with a specimen table, where the sample is fixed upon, as depicted in figure 2.8. Then a cantilever with a sharp tip is lowered onto the sample in a stressed position and scans over the surface of the sample. At the same time a laser beam is deflected of the surface at the tip of the cantilever and detected by a photodiode. During the scan the cantilever gets bent up or down, due to the topography of the sample or other forces between the tip and the surface (e.g. van-der-Waals, coulombic or capillary forces). The photodiode can detect these changes and map an elevation profile of the sample. The cantilever or the specimen table is moved precisely by piezo elements until the whole area of interest is mapped.

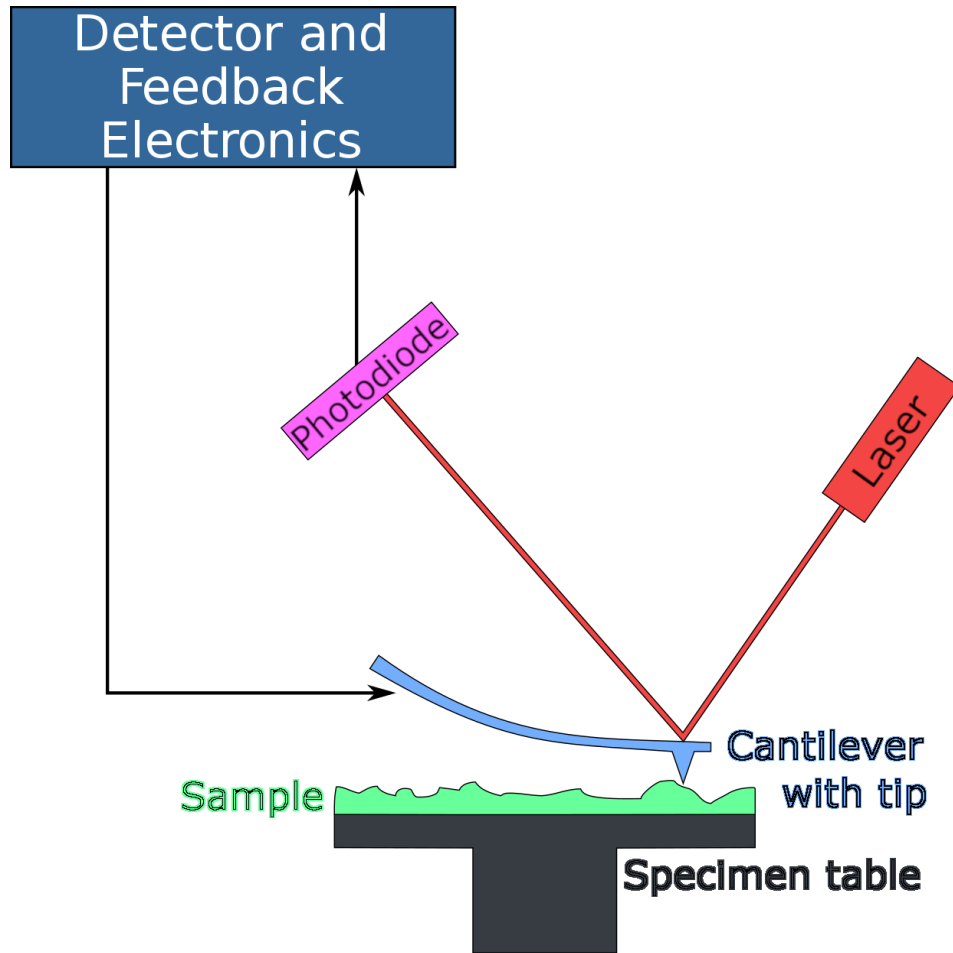


Figure 2.8: Schematic drawing of the setup and working principle of an AFM [15].

The described method is called contact mode, because the cantilever tip touches the sample. This is the most basic method, but it has several drawbacks. The sharp tip for example gets worn down quickly and can even break during the scanning. This can be prevented with the second mode, the non-contact mode, where the cantilever oscillates close to the resonance frequency over the sample with a distance between 10 to 100 nm. That way the tip is safe, but the measurement is not as precise as with the first method. The third mode is the tapping mode, where the tip is tapped at defined distances on the sample. It is an intermediate between contact and non-contact mode, but takes more time to measure the sample [14-16]. These methods are used to create topographic maps of the sample surface, with a high resolution. The modified method, used to measure the Young's modulus of fibers and gels in rheological measurements, is described in the following chapter.

2.3.1. Rheological measurements

In chapter 3. the stiffness of collagen fibers was measured with the AFM NanoWizard® 4 (JPK Instruments) and SPM software (JPK Instruments) with an integrated Axiovert 200 inverted microscope (Zeiss). Collagen gels were prepared on a 35 mm round glass dish (MatTek). The gel had to be very thin (around 100 μm) to get a good contrast of the spaces with and without fibers on the glass bottom of the dish, otherwise the elasticity of the gel blurs the outlines of the collagen fibers. V-shaped cantilevers (Bruker; MLCT-D silicon nitride, resonance frequency 15 kHz, spring constant 0.03 N/m) were calibrated with the contact free method and used in the QITM Mode (Advanced Imaging). The QITM Mode is a modified tapping mode, where a complete force-distance curve is recorded at each pixel. The following values have been set: setpoint 0.2–0.4 nN, z-length 5 μm ; speed 80 $\mu\text{m}/\text{s}$ and pixel size 128x128 on a 20x20 μm grid. During the measurement the height and the slope of the force-distance curves were determined. Data processing was performed using the corresponding software version 6.0.50 (JPK Instruments). After median filtering, background subtraction and a low pass filter, stiffness was calculated on representative data points using the Hertzian contact model (Young's modulus). The tip shape was modeled as quadratic pyramid, the half-front angle of the cantilever as 15° and its Poisson ratio was set to 0.5.

With the use of this AFM method we were able to obtain an approximate value of the stiffness of a single collagen fiber in its 3D network. This is crucial to know, because it is the same stiffness a cell senses while moving through the pores of said 3D network. The AFM with its high resolution was able to resolve the physical properties of the direct environment of a cancer cell. However, we could only measure a small section of the collagen gel. The rheometer with its measuring plate lacks the high resolution of the AFM, but could measure the average stiffness of the collagen fibers and pores over the whole gel.

2.4. Surface acoustic waves

Surface acoustic waves or SAWs are acoustic waves, that travel along the surface of an elastic material. They have a longitudinal and a vertical shear component, that can couple with any media in contact with the surface. The amplitude of the acoustic wave decays exponentially with penetration depth into the material (figure 2.9). They were first described by Lord Rayleigh [17].

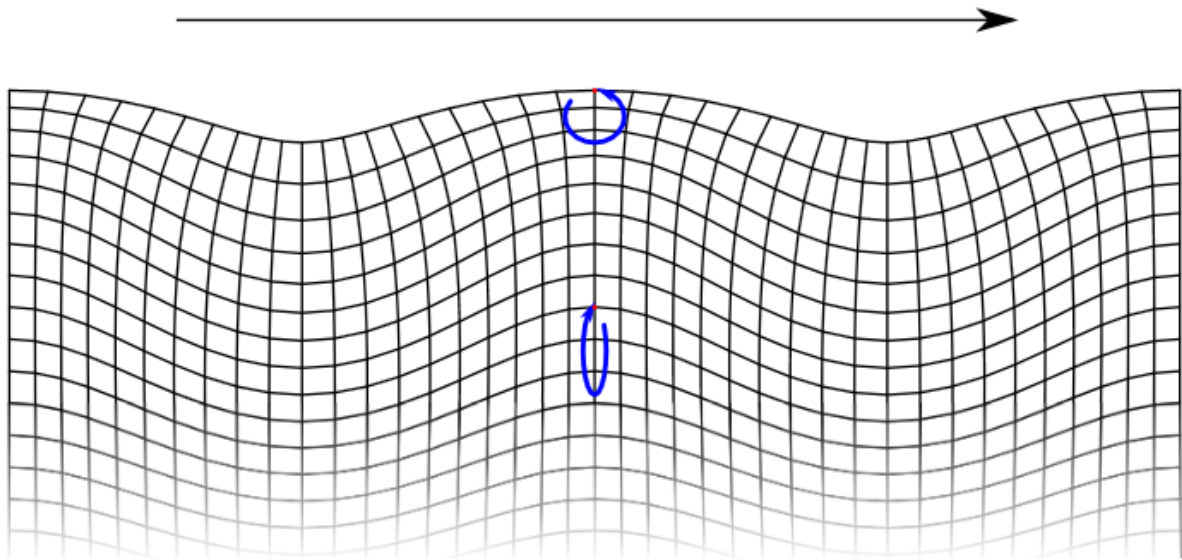


Figure 2.9: SAW on an elastic material with longitudinal and vertical shear component (blue) [18].

The easiest way to produce a SAW chip is to build the desired interdigital transducer (IDT) structure on a piezoelectric substrate (LiNbO_3). Then the SAW can be easily induced by applying a current and a voltage at the resonance frequency to the piezoelectric substrate. This moves the IDT structure in a way that a periodically distributed mechanical force (or a wave) is created. The IDT is build of two electrodes that are intertwined like fingers (figure 2.10) [19].

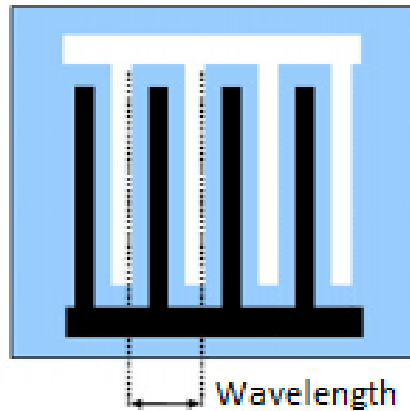


Figure 2.10: IDT structure on a piezoelectric substrate [20].

SAW devices can be used in electronic components, but also in life sciences, microfluidics, or even for cell manipulation. The SAWs are incorporated on so called “lab-on-a-chip” devices, where they are stirring, mixing or pumping very small amounts of fluids. For this purpose the SAW is transferred into a liquid phase. At the liquid-substrate interface the wave transforms from a transverse wave into a longitudinal wave, which creates flow (figure 2.11) [21].

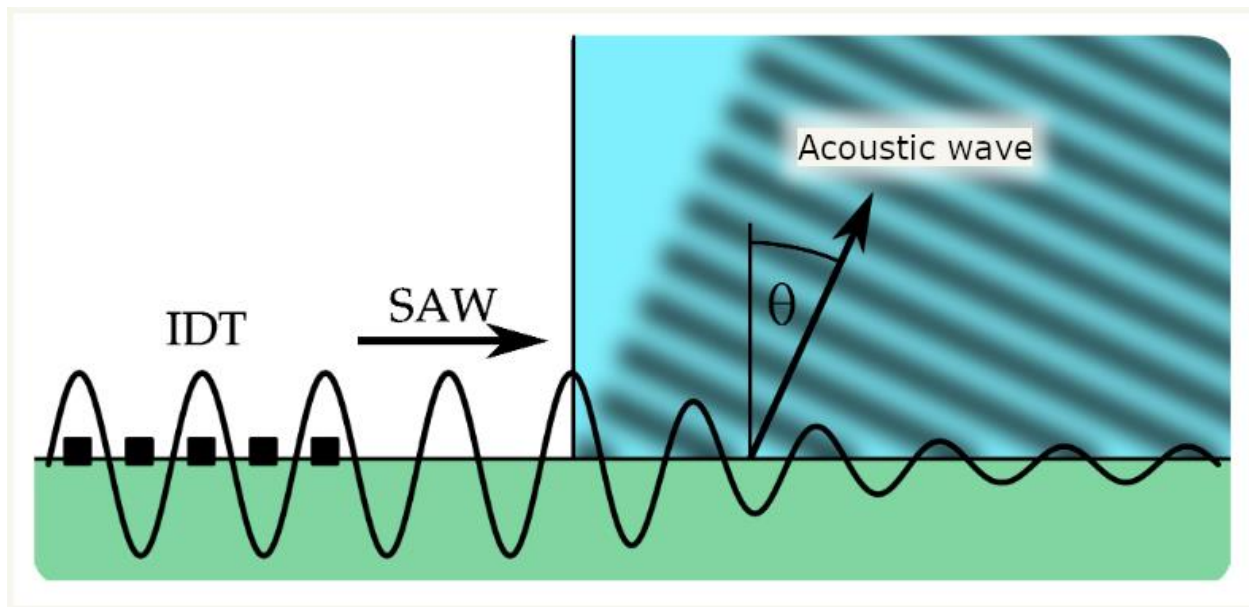


Figure 2.11: Interconnection of a SAW into a liquid (blue) as acoustic wave [18].

The wave is dampened and the direction of propagation changes according to the Snell's law with the propagation velocity of the SAW (c_{SAW}) and the speed of sound inside the liquid (c_f) [18].

$$\sin \theta = \frac{c_f}{c_{SAW}}$$

Standing wave fields created by SAWs were used to align collagen fibers in a 3D gel during the polymerization via the shear flow, depicted in figure 2.12. The SAW operated at a resonance frequency of 126.3 MHz and an intensity of 19 dBm.

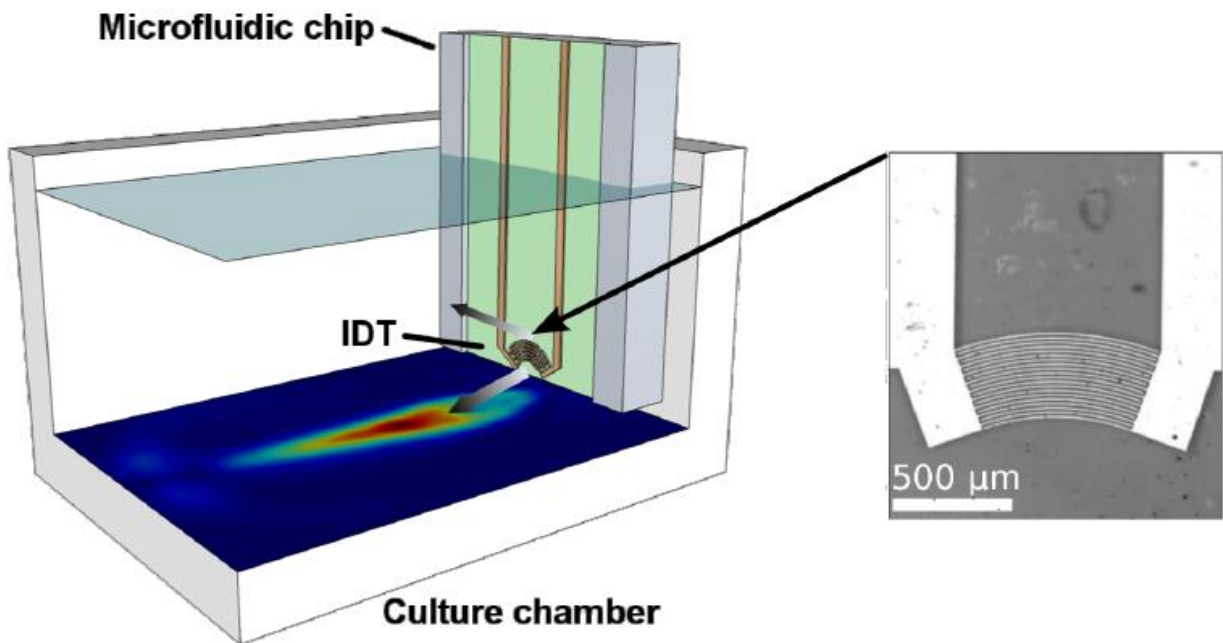


Figure 2.12: Microfluidic chip in collagen gel for fiber alignment via shear flow [22].

Another application was the trapping of cells in a microfluidic chamber with phase detuned SAWs (figure 2.13). These SAWs overlap with one another and create high pressure regions where particles (cells) with a sufficient acoustic contrast to the medium are pushed out of (red) and other regions without pressure, where they become trapped (blue).

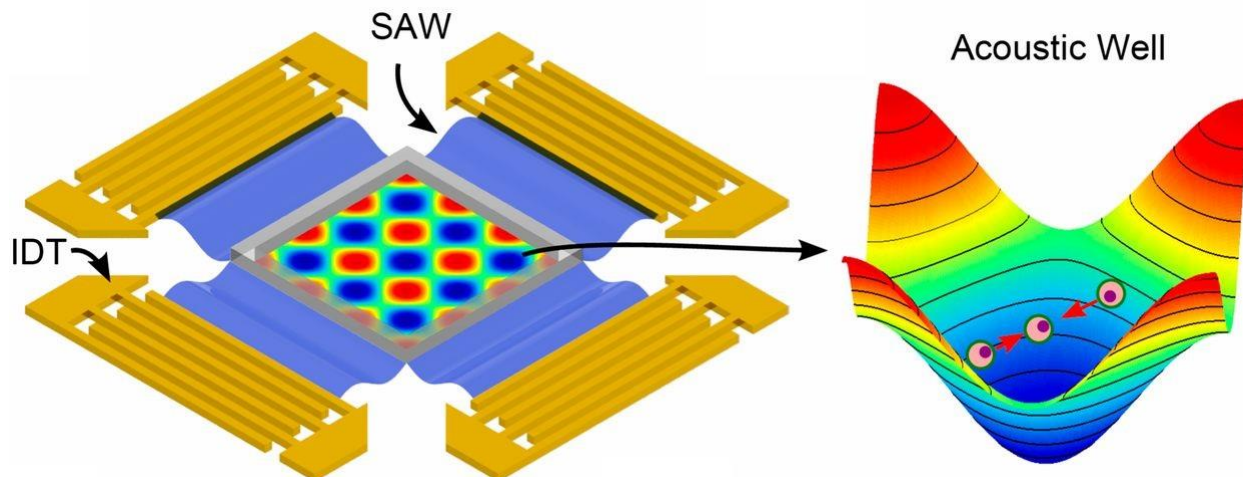


Figure 2.13: Phase detuned SAWs creating acoustic wells for cell trapping. Color of the acoustic well indicates a pressure gradient (red equals high, blue low or no pressure) [23].

These static cells serve as anchor points for long collagen fibers, which form in a constant flow of collagen gel. Additionally, these fibers are all aligned parallel to the flow direction in the microfluidic chamber, which is an ideal scenario to study the effect of long aligned collagen fibers on the motility of cells. The SAW operated at a resonance frequency of 71 MHz and an intensity of 25 dBm.

2.5. Microfluidics

Microfluidics deals with liquid flows in channel networks, with dimensions in the micrometer range. The used systems can be roughly divided into two categories. On the one hand, microfluidic systems that occur in nature are examined and simulated. An important example here is the blood flow in thin capillaries. On the other hand, analysis and synthesis methods are miniaturized and automated in microfluidics. (e.g. chromatography. PCR or nanoparticles). This miniaturization means fewer reagents are used, the sample quantities are massively reduced and many processes can be done simultaneously [24].

Polydimethylsiloxan (PDMS) is widely used in experiments with living cells, because of its biocompatibility and the simple creation of microfluidic channels via a mold. The silicone

based elastomeric kit SYLGARD® 184 was used to polymerize PDMS with a ratio of ten parts polymeric base and one part curing agent. The molds were either printed in 3D out of epoxy or, in the case of more delicate structures, the photoresist SU8-2150 was applied via photolithography onto a silica wafer (figure 2.14).

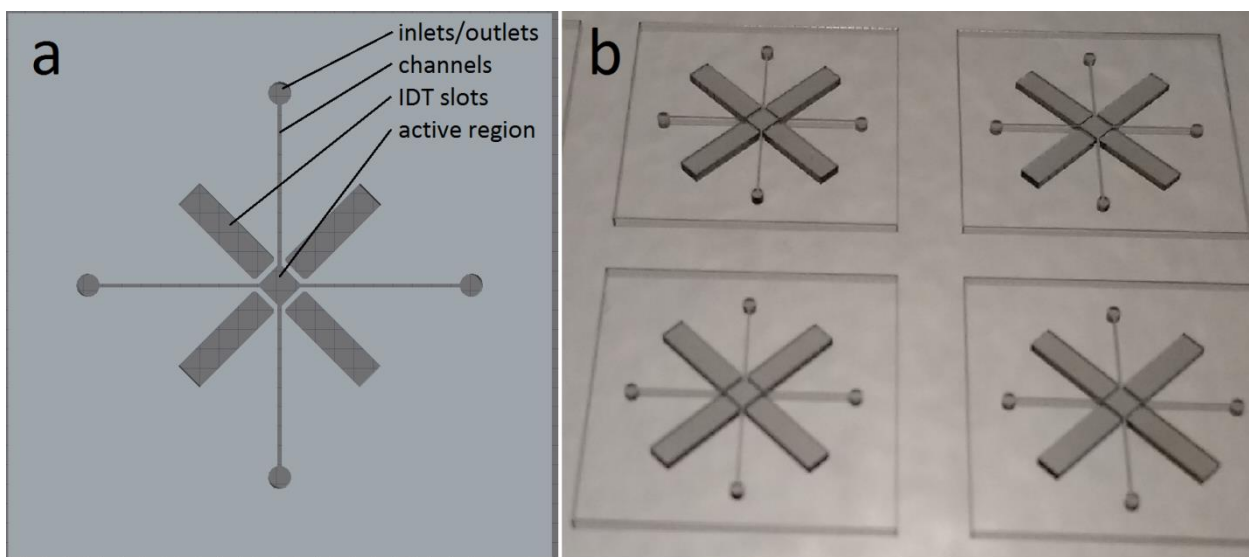


Figure 2.14: a) simulated PDMS chamber with 100 μm channel thickness, active region with 800 μm edge length and recesses for the IDTs. b) Photography of the negative mold printed onto a silica wafer.

The 3D printed molds were not designed to be used with phase detuned SAWs for cell trapping. They were missing the slots for the IDT, had a channel thickness of 650 μm , and an active region with 5.2 mm edge length. At the four cylindrical ends of the microchannels holes are punched out and the chamber is fixed on a SAW chip or on a microscope slide. Then a syringe on a pump is connected via a tube with an inlet of the chamber. To pump the collagen mixture through the microfluidic chip the syringe pump LA-120 from Landgraf was used. First, the chip was flooded with PBS to remove air bubbles and then the collagen mixture was drawn into it until the mixture polymerized. For the SAW compatible chambers the initial withdraw speed was 3 $\mu\text{l}/\text{min}$, but as soon as the collagen mixture reached the active region of the chip the withdraw speed was lowered to 1 $\mu\text{l}/\text{min}$ and the acoustic trapping wells were turned on for the entire polymerization time of 10 minutes.

2.5. Microfluidics

The 650 μm channel chambers were run with a withdraw speed of 10 $\mu\text{l}/\text{min}$ and the polymerization took 20 minutes.

Another microfluidic system used with the syringe pump LA-120 from Landgraf was the μ -Slide VI 0.4, with ibiTreat from Ibidi. First, the slide was flooded with PBS to remove air bubbles and one reservoir of the slide was plugged with a PDMS plug and connected to the syringe on the LA-120 pump via a tube (figure 2.15a). Then the collagen mixture was drawn from the second reservoir into the channel with 400 μm height at 90.2 $\mu\text{l}/\text{min}$ withdraw speed, until a HeLa cell aggregate reached the middle of the channel. The mixture was polymerized on ice for 30 minutes with a withdraw speed of 0.2 $\mu\text{l}/\text{min}$ and after that, at room temperature for 15 minutes at a withdraw speed of 0.1 $\mu\text{l}/\text{min}$. Finally, the tube was removed from the slide and the collagen mixture was completely polymerized in the incubator at 37 $^{\circ}\text{C}$ and 5% CO_2 . The reservoirs of the slide were extended and sealed with shortened and medium filled syringes, to avoid a drying out of the sample (figure 2.15b). The syringes used in all cases were 1 ml Norm-Ject[®]-F Luer Solo (B.Braun) Syringes with a diameter of 5 mm.

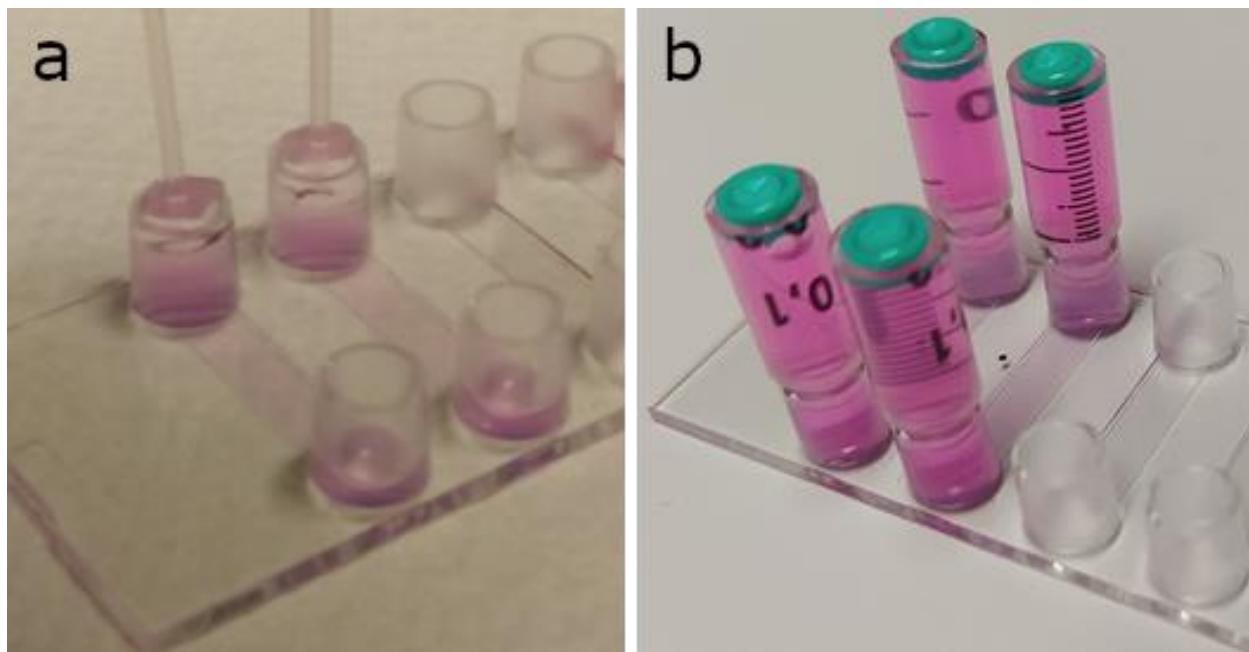
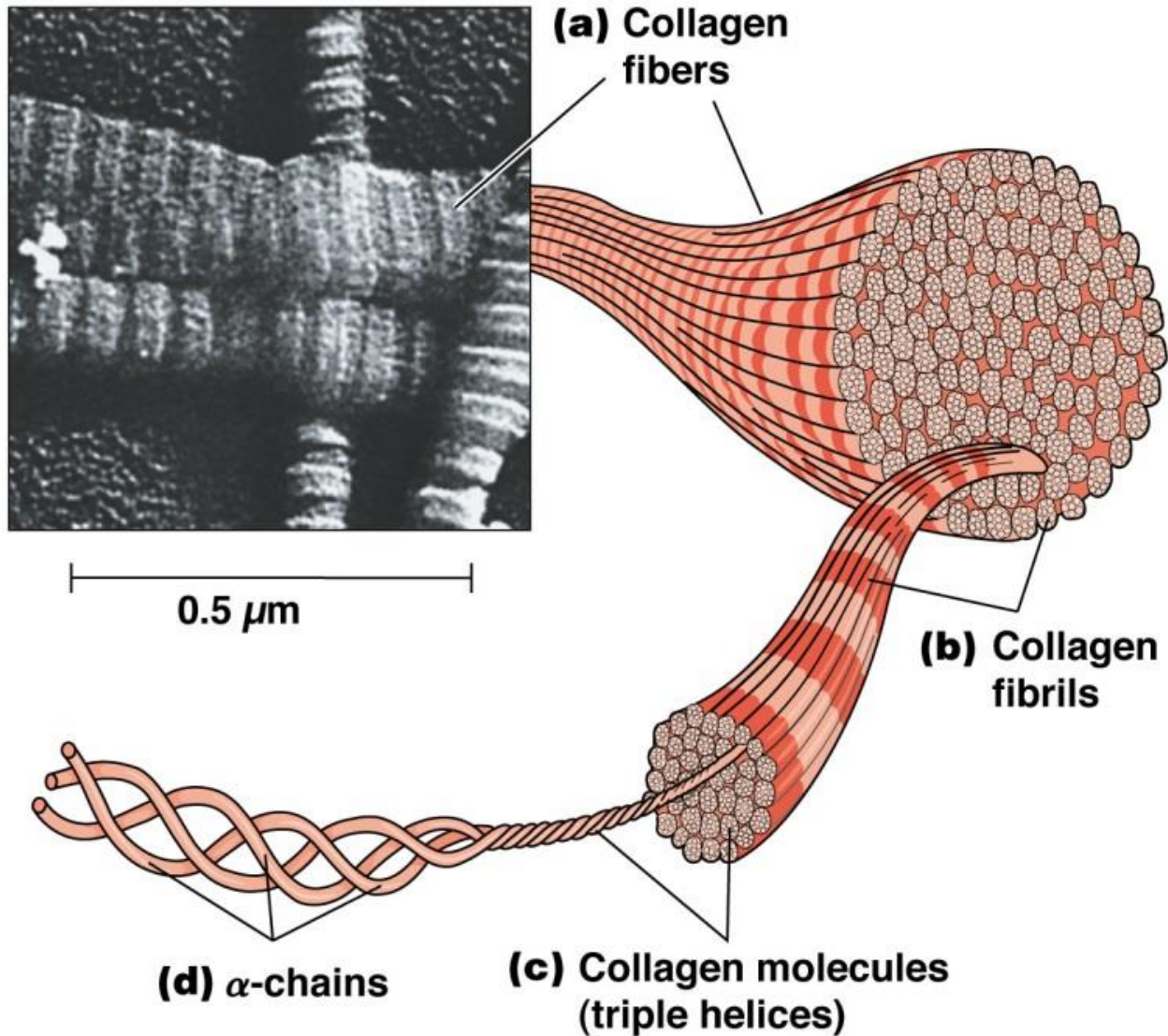


Figure 2.15: μ -Slide VI 0.4 from Ibidi, a) during the polymerization process of the collagen mixture, b) after incubation at 37 $^{\circ}\text{C}$ and with sealed reservoirs.

2.6. Polymerization control of collagen

Collagen is a structural protein that is widely used as extracellular matrix (ECM) component, due to its very high abundance in mammalian tissues. It is perfectly suited for constructing 3D scaffolds for cell experiments, because of its high biocompatibility and the microenvironment it provides for cells that is close to native tissue. Cell migration and invasion in 3D matrices are dynamical processes, which are highly influenced by biophysical features of their surrounding tissue. Therefore, physical attributes, such as pore size, stiffness or degree of fiber alignment, of these artificial ECMs must be tuned to create suitable model systems for cell studies [26-31].

In the following, the formation of collagen I is described, which is a natural polymer and the most abundant collagen of the human body. It forms large collagen fibers and defines the mechanical properties of the connective tissue. The formation of a such a fiber starts with three helical α polypeptide chains, two $\alpha 1(I)$ and a single $\alpha 2(I)$ chain (figure 2.16d). These α -chains are built in the ribosome from different sequences of amino acids, then coil together and form a heterotrimeric procollagen molecule. Hydroxylation of specific proline and lysine residues of the α -chains contribute to the stabilization of the triple helix (figure 2.16c) [32-34]. Upon extrusion into the extracellular space, both amino- and carboxy-terminal propeptides are cleaved by procollagen peptidase, resulting in tropocollagen, which is capable of fibril formation [35, 36]. Lysyl oxidase links hydroxylysine and lysine residues and forms covalent cross-links (aldol reaction) of multiple self assembled procollagen molecules to create oligomers, which in turn combine to form collagen fibrils (figure 2.16b) [37]. Finally, multiple collagen fibrils form into collagen fibers (figure 2.16a) [38, 39].



© 2012 Pearson Education, Inc.

Figure 2.16: Different stages of the assembly of collagen fibers. Three helical α polypeptide chains (d) together form procollagen collagen molecules (c) via hydroxylation, which in turn cross-link to oligomers and form collagen fibrils (b). Multiple collagen fibrils together form collagen fibers (a) [40].

This polymerization of collagen I depends on multiple factors, such as collagen concentration, pH value, or reaction temperature and can result in networks with very different properties, given any of the reaction conditions is changed [31, 42]. Figure 2.17 shows this for a change in temperature and concentration.

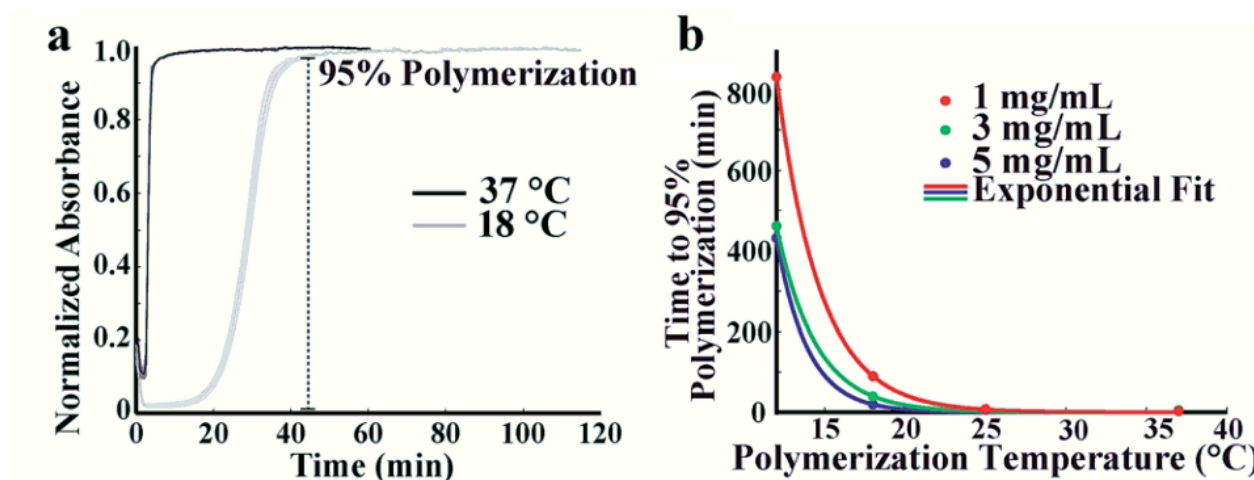


Figure 2.17: a) Temperature dependence of collagen oligomer polymerization; b) Polymerization time dependence on both temperature and concentration [43].

The delayed polymerization of the collagen oligomers, with decreasing temperature, is due to the slowdown of the cross-linking steps described above. This delay can be described with the Arrhenius equation using the rate constant (frequency of collisions resulting in a reaction) k , the temperature T , the pre-exponential factor (frequency of collisions in the correct orientation) A , the activation energy E_a and the universal gas constant R .

$$k = Ae^{\frac{-E_a}{RT}}$$

Hence, the lower the polymerization temperature the longer the collagen oligomers can move around in the liquid collagen gel via Brownian motion. This leads to the formation of thicker and longer collagen fibers and a bigger poresize of the resulting network. Also, the network resulting from a low polymerization temperature is more rigid compared to a gel made at a high polymerization temperature [30]. Another modification that can be made in the gel during polymerization is applying shear forces to the liquid gel, which results in an oriented collagen network [44].

2.7. References

1. Atkins P, de Paula J. *Physikalische Chemie*. 4th Edition. Wiley-VCH. Weinheim. 2006
2. Atkins P, Friedman R. *Molecular Quantum Mechanics*. 4th Edition. Oxford University Press. Oxford. 2005.
3. Lackowicz JR. *Principles of Fluorescence Spectroscopy*. Plenum Press. 1983
4. Pranav K, Usha M. *Fundamental Techniques of Biophysics and Molecular Biology*. Pathfinder Publication. New Delhi. 2016.
5. <https://micro.magnet.fsu.edu/primer/techniques/fluorescence/anatomy/fluoromicroanatomy.html>. 26.03.2020.
6. <http://zeiss-campus.magnet.fsu.edu/articles/spinningdisk/introduction.html>. 26.03.2020.
7. <http://zeiss-campus.magnet.fsu.edu/articles/livecellimaging/techniques.html>. 27.03.2020.
8. <https://www.leica-microsystems.com/science-lab/introduction-to-widefield-microscopy/>. 27.03.2020.
9. <https://www.zeiss.com/microscopy/int/solutions/reference/all-tutorials/optical-sectioning/confocal-versus-widefield-microscopy.html>. 27.03.2020.
10. Malkin A, Isayev A. *Rheology: Concepts, Methods and Applications*. 3rd Edition. ChemTec Publishing. Toronto. 2017.
11. <https://wiki.anton-paar.com/de-de/grundlagen-der-rheologie/rheometer-messungen/>. 28.03.2020.
12. Gallegos C. *Rheology - Volume I*. Eolss Publisher. London. 2010.
13. <https://wiki.anton-paar.com/de-de/grundlagen-der-rheologie/rheometrie-messsysteme/>. 28.03.2020.
14. Binnig G, Quate CF, Gerber C. Atomic force microscope. *Phys Rev Lett*. 1986; 56(9):930-3.

15. https://en.wikipedia.org/wiki/Atomic_force_microscopy. 29.03.2020
16. Eaton P, West P. Atomic Force Microscopy. Oxford University Press. Oxford. 2010.
17. Rayleigh L. On Waves Propagated along the Plane Surface of an Elastic Solid. Proc London Math Soc. 1885; 17(1):1–17.
18. Schmid L. SAW-Aktuation in mikrofluidischen Kanälen zum Pumpen, Sortieren und Herstellen von Mikroemulsionen. Dissertation. 2017.
19. White RM, Voltmer FM. Direct piezoelectric coupling to surface elastic waves. Appl Phys Lett. 1965; 7(12):314–6.
20. Dissanayake DW, Al-Sarawi S, Lu T, Abbott D. Finite element modelling of surface acoustic wave device based corrugated microdiaphragms. Smart Mater Struct. 2009; 18(9):095030.
21. Delsing P, Cleland AN, Schuetz MJA, Knörzer J, Giedke G, Cirac JI, et al. The 2019 surface acoustic waves roadmap. J Phys D: Appl Phys. 2019; 52(35):353001.
22. Strobl FG, Breyer D, Link P, Torrano AA, Bräuchle C, Schneider MF, et al. A surface acoustic wave-driven micropump for particle uptake investigation under physiological flow conditions in very small volumes. Beilstein J Nanotechnol. 2015; 6:414–9.
23. Guo F, Li P, French JB, Mao Z, Zhao H, Li S, et al. Controlling cell–cell interactions using surface acoustic waves. PNAS. 2015; 112(1):43–8.
24. Squires TM, Quake ST. Microfluidics: Fluid physics at the nanoliter scale. Rev Mod Phys. 2005; 77(3):977–1026.
25. Stamov DR, Pompe T. Structure and function of ECM-inspired composite collagen type I scaffolds. Soft Matter. 2012; 8:10200.
26. Franke K, Sapudom J, Kalbitzer L, Anderegg U, Pompe T. Topologically defined composites of collagen types I and V as in vitro cell culture scaffolds. Acta Biomater. 2014; 10:2693e702.

2.7. References

27. Wolf K, Te Lindert M, Krause M, Alexander S, Te Riet J, Willis AL, et al. Physical limits of cell migration: control by ECM space and nuclear deformation and tuning by proteolysis and traction force. *J Cell Biol.* 2013; 201:1069e84.
28. Harjanto D, Maffei JS, Zaman MH. Quantitative analysis of the effect of cancer invasiveness and collagen concentration on 3D matrix remodeling. *PLoS One.* 2011; 6:e24891.
29. Friedl P, Sahai E, Weiss S, Yamada KM. New dimensions in cell migration. *Nat Rev Mol Cell Biol.* 2012; 13:743e7.
30. Geiger F, Rüdiger D, Zahler S, Engelke H. Fiber stiffness, pore size and adhesion control migratory phenotype of MDA-MB-231 cells in collagen gels. *PLoS ONE.* 2019; 14(11):e0225215.
31. Bailey JL, Critser PJ, Whittington C, Kuske JL, Yoder MC, Voytik-Harbin SL. Collagen oligomers modulate physical and biological properties of three-dimensional self-assembled matrices. *Biopolymers.* 2011; 95(2):77–93.
32. Brodsky B, Persikov AV. Molecular structure of the collagen triple helix. *Adv Protein Chem.* 2005; 70:301–39.
33. Persikov AV, Ramshaw JA, Brodsky B. Prediction of collagen stability from amino acid sequence. *J Biol Chem.* 2005; 280(19):19343–9.
34. Burjanadze TV. Hydroxyproline content and location in relation to collagen thermal stability. *Biopolymers.* 1979; 18(4):931–8.
35. Hojima Y, McKenzie JA, van der Rest M, Prockop DJ. Type I procollagen N-proteinase from chick embryo tendons. Purification of a new 500-kDa form of the enzyme and identification of the catalytically active polypeptides. *J Biol Chem.* 1989; 264(19):11336–45.
36. Prockop DJ, Kivirikko KI. Heritable diseases of collagen. *N Engl J Med.* 1984; 311(6):376–86.
37. Cronlund AL, Smith BD, Kagan HM. Binding of lysyl oxidase to fibrils of type I collagen. *Connect Tissue Res.* 1985; 14(2):109–19.

38. Grant M, Prockop D. The biosynthesis of collagen. 1. *N Engl J Med.* 1972; 286(4):194–9.
39. Barbul A., Proline precursors to sustain Mammalian collagen synthesis. *J. Nutr.* 2008; 138(10):2021S–2024S.
40. http://www.mun.ca/biology/desmid/brian/BIOL2060/BIOL2060-17/17_14.jpg. 01.04.2020.
41. Raub, C.B.; Suresh, V.; Krasieva, T.; Lyubovitsky, J.; Mih, J.D.; Putnam, A.J.; Tromberg, B.J.; George, S.C. Noninvasive assessment of collagen gel microstructure and mechanics using multiphoton microscopy. *Biophys. J.* 2007; 92:2212–22.
42. Roeder BA, Kokini K, Sturgis JE, Robinson JP, Voytik-Harbin SL. Tensile mechanical properties of three-dimensional type I collagen extracellular matrices with varied microstructure. *J Biomech Eng.* 2002; 124(2):214–22.
43. Shannon GS, Novak T, Mousoulis C, Voytik-Harbin SL, Neu CP. Temperature and concentration dependent fibrillogenesis for improved magnetic alignment of collagen gels. *Rsc Adv.* 2015; 5(3):2113–21.
44. Han W, Chen S, Yuan W, Fan Q, Tian J, Wang X, et al. Oriented collagen fibers direct tumor cell intravasation. *Proc Natl Acad Sci U S A.* 2016; 113(40):11208–13.

3. Fiber stiffness, pore size and adhesion control migratory phenotype of MDA-MB-231 cells in collagen gels

This chapter is based on the following publication:

Geiger F, Rüdiger D, Zahler S, Engelke H. Fiber stiffness, pore size and adhesion control migratory phenotype of MDA-MB-231 cells in collagen gels. PLoS ONE. 2019; 14(11): e0225215.

Abstract

Cancer cell migration is influenced by cellular phenotype and behavior as well as by the mechanical and chemical properties of the environment. Furthermore, many cancer cells show plasticity of their phenotype and adapt it to the properties of the environment. Here, we study the influence of fiber stiffness, confinement, and adhesion properties on cancer cell migration in porous collagen gels. Collagen gels with soft fibers abrogate migration and promote a round, non-invasive phenotype. Stiffer collagen fibers are inherently more adhesive and lead to the existence of an adhesive phenotype and in general confined migration due to adhesion. Addition of TGF- β lowers adhesion, eliminates the adhesive phenotype and increases the amount of highly motile amoeboid phenotypes. Highest migration speeds and longest displacements are achieved in stiff collagen fibers in pores of about cell size by amoeboid phenotypes. This elucidates the influence of the mechanical properties of collagen gels on phenotype and subsequently migration and shows that stiff fibers, cell sized pores, and low adhesion, are optimal conditions for an amoeboid phenotype and efficient migration.

3.1. Introduction

Migration of cancer cells is a complex process. It is influenced by properties of the migrating cells as well as their environment [1]. While the environmental properties, such as stiffness,

size, and density as well as spatial distribution of adhesion sites, are well controllable for migration on two-dimensional, continuous substrates, these properties are significantly more complex in three-dimensional porous hydrogels [2]. Consequently, migration in two dimensions is fairly well understood, but the influence of environmental parameters on three-dimensional migration still remains to be understood [1, 3]. Key parameters of the environment that influence migration in three dimensions are confinement, adhesion sites and stiffness [4, 5]. Strong confinement below a certain threshold can stall migration entirely, since it blocks movement of the nucleus [6]. The influence of adhesion sites depends on cell phenotype. Some migration phenotypes are dependent on force transmission via adhesion, while other phenotypes are independent of adhesion [7–9]. Adding to the complexity is the fact, that cells can switch migratory phenotype not only due to biochemical stimuli, but also depending on the environmental properties [10–14]. Since the phenotype strongly impacts migratory properties, this switching behavior influences migration significantly and impacts speed, persistence and other parameters. In complex heterogeneous environments such plasticity may promote invasion [15]. On the other hand, cells can remodel their environment and thus influence its properties that impact migration [16, 17]. A prominent example is matrix degradation via enzymes, which allows for directed movement in strongly confined matrices [18, 19]. The dependence of three-dimensional migration on cell phenotype and the environment with the mutual feedback interactions opens a huge phase space of influences on three-dimensional migration [1]. Here, we investigated the influence of the mechanical properties of hydrogels on migratory phenotype and with that on migration properties. Hydrogel remodeling of cells in our study was minimal. This allowed us to analyze the influences of environment on cell phenotype without further complexity due to changes in the environment induced by cell remodeling. Confinement and adhesion have been shown to significantly influence migratory phenotype and migration parameters in continuous substrates [10]. Yet, tissue is highly heterogeneous and parts of it resemble porous collagen meshworks rather than continuous glass or plastic channels [20–22] and the difference between continuous and porous substrates may significantly alter migration properties [23]. Here, we show that fiber stiffness, confinement and adhesion behavior of the cell strongly influenced migratory phenotype and with that

migration parameters in porous hydrogels. While some influences resembled those in continuous substrates, we also found strong differences.

3.2. Results

To investigate the influence of different local hydrogel structures on cell migration, we prepared two different types of collagen gels. Both gel types consisted of 1.85 mg/ml rat tail collagen. The first type of gel (HT) was polymerized instantly at 37 °C. The other was first cooled on ice and then polymerized at room temperature (LT). The polymerization at different temperatures created gels differing in pore size as well as fiber thickness. Figure 3.1a shows the fine structure of the HT gels with thin fibers and small pore sizes of 12.5 μm on average. The LT gels in figure 3.1b consist of thicker fibers and larger pore sizes of about 18 μm on average (figure 3.1c). The cell size is on average $15.5 \pm 5.5 \mu\text{m}$ in HT gels and $13.4 \pm 4.8 \mu\text{m}$ in LT gels. Both gel types however contain pores that are comparable to the size of cells. Thus, we can exclude that cells are stuck due to pore sizes that do not allow for penetration of the cell nucleus as described in [6].

While the overall concentration of collagen and with that the amount of adhesion sites is the same for both types of gels, the local amount of adhesion sites on collagen fibers will be higher on the thicker fibers of the LT gels [24]. The difference in fiber thickness will also affect fiber stiffness and with that local compliance of the gel. We measured fiber stiffness of the gels using atomic force microscopy and the resulting maps of the slope of the force-distance curves that are proportional to the local stiffness are displayed in figure 3.1d and e. While LT gels show clearly visible, stiff fibers, the stiffness of HT fibers is barely above background. Quantitatively, we obtained an average Young's modulus of $19 \pm 16 \text{ Pa}$ for HT fibers with a background of $12.7 \pm 7.6 \text{ Pa}$ and a Young's modulus of more than an order of magnitude higher of $584 \pm 296 \text{ Pa}$ with a background of $35 \pm 26 \text{ Pa}$ for LT gels (figure 3.1f). Thus, the fiber to background ratio of HT gels is only about 1.5, while it is 16.6 for LT gels. Bulk measurements on a rheometer revealed a Young's modulus of $12.8 \pm 2.5 \text{ Pa}$ for HT gels and $82 \pm 14 \text{ Pa}$ for LT gels in accordance with literature [25].

3.2. Results

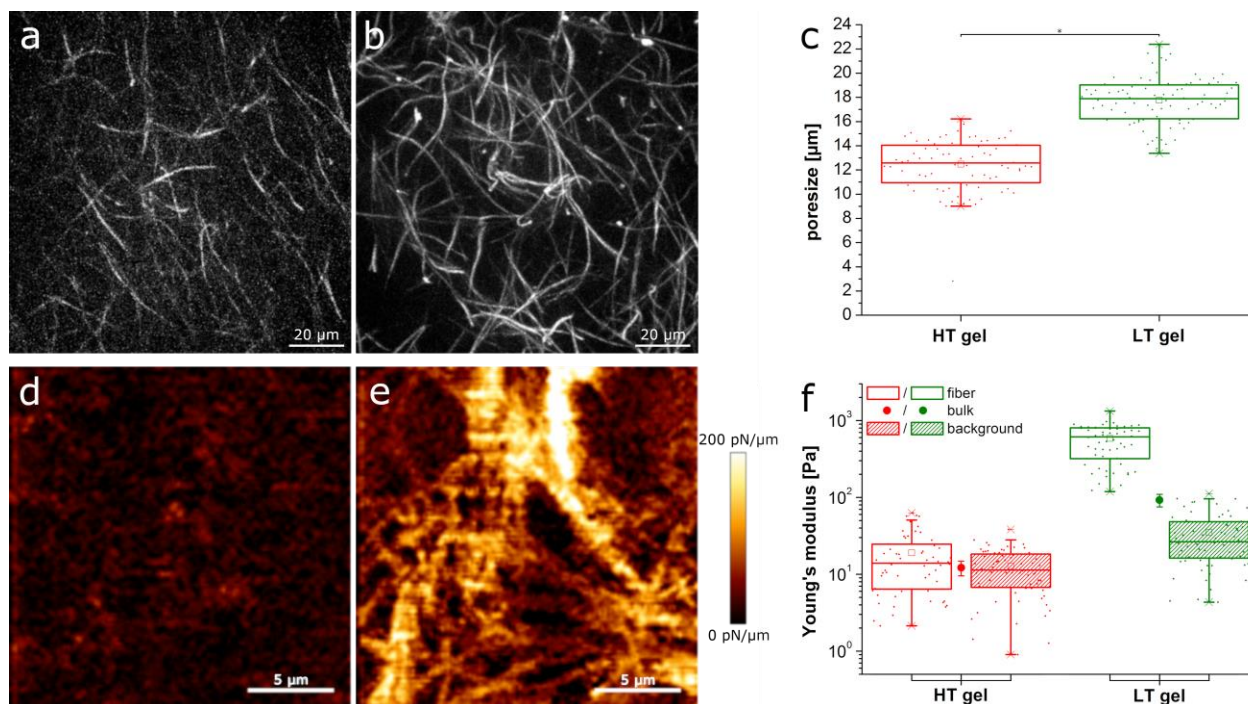


Figure 3.1: Collagen gel characterization. a) Fluorescence image of an HT gel polymerized at 37 °C and b) of a LT gel polymerized at lower temperatures; c) pore sizes of HT and LT gels respectively ($p < 0.001$, two-sample t-test); AFM image proportional to the local stiffness of d) an HT and e) an LT gel; f) Young's modulus of fibers and background as measured by AFM and Young's modulus of the bulk gel as measured with a rheometer for HT and LT gels respectively.

Next, we analyzed migration of MDA-MB-231 cells in fluorescently labeled LT and HT gels. MDA-MB-231 is an invasive breast cancer cell line. They migrate in various phenotypes and adapt their phenotype and migration behavior flexibly depending on the prevalent conditions [26–28]. Cells were labeled with lifeAct-GFP marking filamentous actin within the cell. Representative images of cells and their migration tracks imaged every 20 min over 15 h are displayed in figure 3.2a-c. Cells in HT gels (figure 3.2a) show very small displacements and seem stuck at their initial position. In LT gels, cells explore a larger space over time, yet the observed movement is still very limited (figure 3.2b). Thus, we added TGF- β to cells in LT gels. TGF- β is a drug that is known to promote cell migration. Indeed, upon addition of TGF- β we find cells to be more motile with a significant amount of cells

3. Fiber stiffness, pore size and adhesion control migratory phenotype of MDA-MB-231 cells

moving through pores of the collagen matrix yielding fairly straight trajectories (figure 3.2c). Addition of TGF- β to cells in HT gels on the other hand, did not lead to any visible changes in migration. We did not observe any significant matrix degradation or remodeling in any of the experiments except for occasional small deformations of the matrix resulting from cells pushing themselves through pores of the matrix or pushing fiber ends out of their way while passing.

Quantitative analysis revealed a distribution of cell speed as displayed in figure 3.2d (see also figure S3.1 for statistical analysis and figure S3.2 for HT gels with TGF- β). While cells move with a similarly low average speed in HT gels and LT gels, their speed distribution is clearly shifted to higher speeds upon addition of TGF- β in LT gels, but not in HT gels. The distribution of angles (figure 3.2e, S3.2) between steps in LT and HT gels shows a tendency toward backtracking, i.e. 180° turns, which may result from confined movement for example due to pore size or strong adhesion [29]. Migration tracks in the presence of TGF- β show a fairly uniform angle distribution resembling that of a random walk. Also the average mean squared displacement (MSD) showed an increase in slope upon addition of TGF- β to LT gels confirming the decrease in confinement (figure 3.2f). Fitting the MSD of each single trajectory to a random walk equation and accounting for anomalous diffusion with the exponent α , we obtained a distribution of the exponent α as shown in figure 3.2g (see also figure S3.1 for statistical analysis and figure S3.2 for HT gels with TGF- β). Values of α around 1.0 reveal diffusive behavior and values below 1.0 subdiffusive behavior, e.g. due to confinement. Values above 1.0 indicate superdiffusive behavior, which is typical for cells migrating with persistence for example through channels or on surfaces. In HT gels the exponent α is below 1 with very few exceptions, indicating subdiffusive behavior for most of the cells independent of TGF- β . In LT gels without drug, α is slightly higher with more cells (33%) reaching values above 1. However, on average, most of the cells still show subdiffusive behavior. In the presence of TGF- β in LT gels more than 43% of the cells reach α values above 1.0.

Taken together, these results show confined migration for both gel types. This confinement is removed upon addition of TGF- β to LT gels. This drug is known to activate RhoA signaling

3.2. Results

[30], which favors myosin driven contractility over actin polymerization and thus less adhesive amoeboid migration modes over adhesive mesenchymal migration [31, 32].

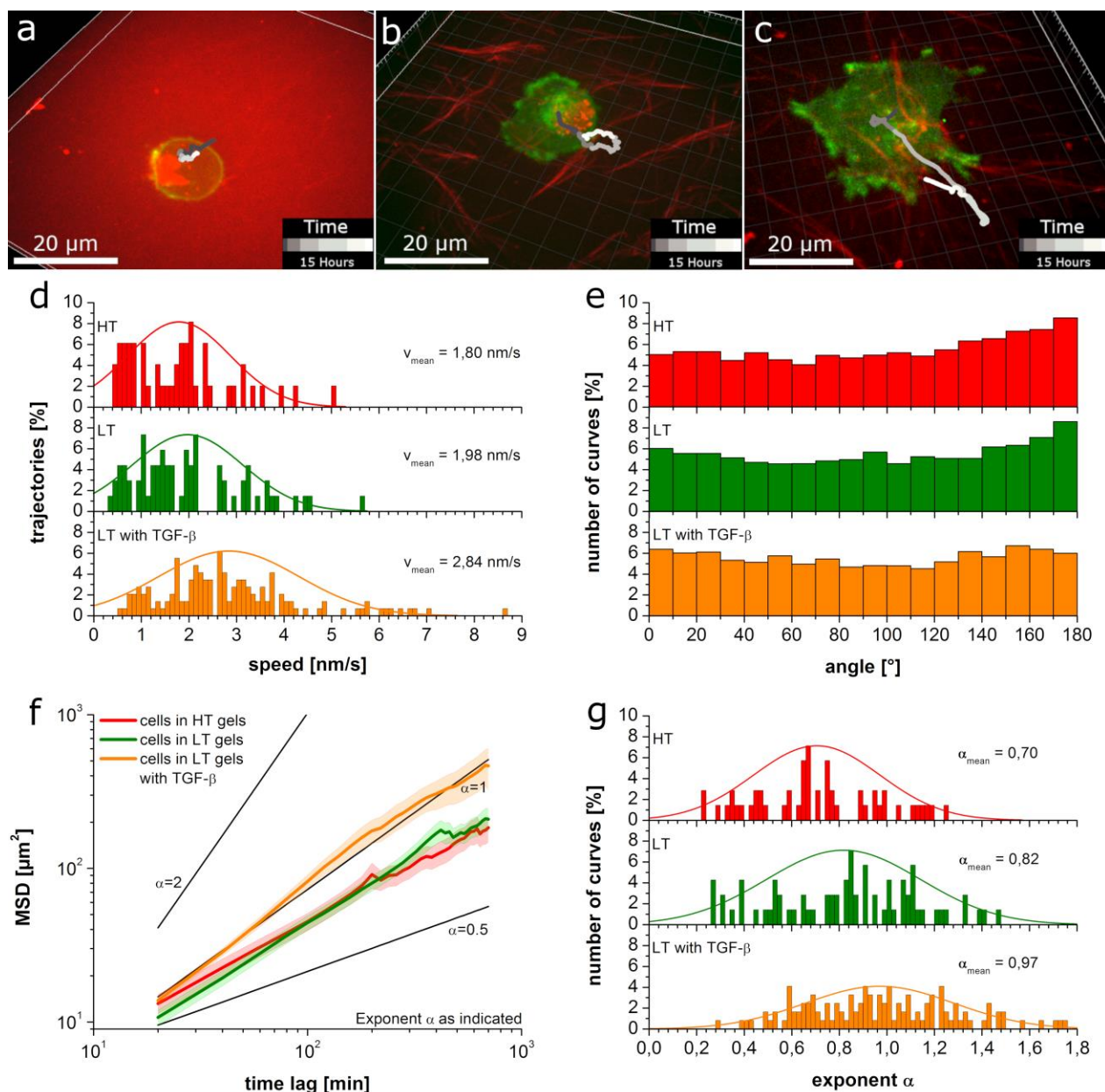


Figure 3.2: MDA-MB-231 migration in collagen gels. a)-c) representative images of cells (green) and their migratory tracks (gray shades) in HT gels (a), LT gels (b) and LT gels in presence of TGF-β (c) respectively (collagen fibers in red); images represent 3D xyz-stacks at the first measured time point and trajectories (in gray shades) represent the 3D path over time with a time scale as indicated in the color bar in the lower right corners; d) histogram of speed distributions show the increase in speed upon addition of TGF-β; e)

3. Fiber stiffness, pore size and adhesion control migratory phenotype of MDA-MB-231 cells

angle distribution between different steps shows significant backtracking due to confinement for HT and LT gels (HT compared to LT: $p < 0.005$, HT compared to LT with TGF- β : $p < 0.001$, LT compared to LT with TGF- β : $p < 0.001$); f) average mean square displacements for the different conditions show subdiffusive behavior in the absence of TGF- β ; g) histogram of exponent α values show the increase of α upon addition of TGF- β .

To analyze the influence of local environment and TGF- β on cell migration, we thus determined the cell phenotypes (figure 3.3a-d, S3.3). In HT gels we find exclusively round cells and cells with pseudopods. Round cells represent the majority in HT gels without TGF- β . In LT gels cells with pseudopods are the majority and only about 10% show a round phenotype. Additionally, we find a spread, adherent phenotype and few cells show amoeboid character. Addition of TGF- β to LT gels enhances the amount of amoeboid cells and it removes the adherent, spread phenotype entirely. The amoeboid cells show several subforms, namely a movement with a fairly round or ellipsoid cell body and a leading edge, a movement consisting of squeezing through pores with a dented cell body, and occasionally the rear driven movement described for MDA-MB-231 cells in matrigel by Poincloux et al. [33]. Very few cells showed a blebbing phenotype.

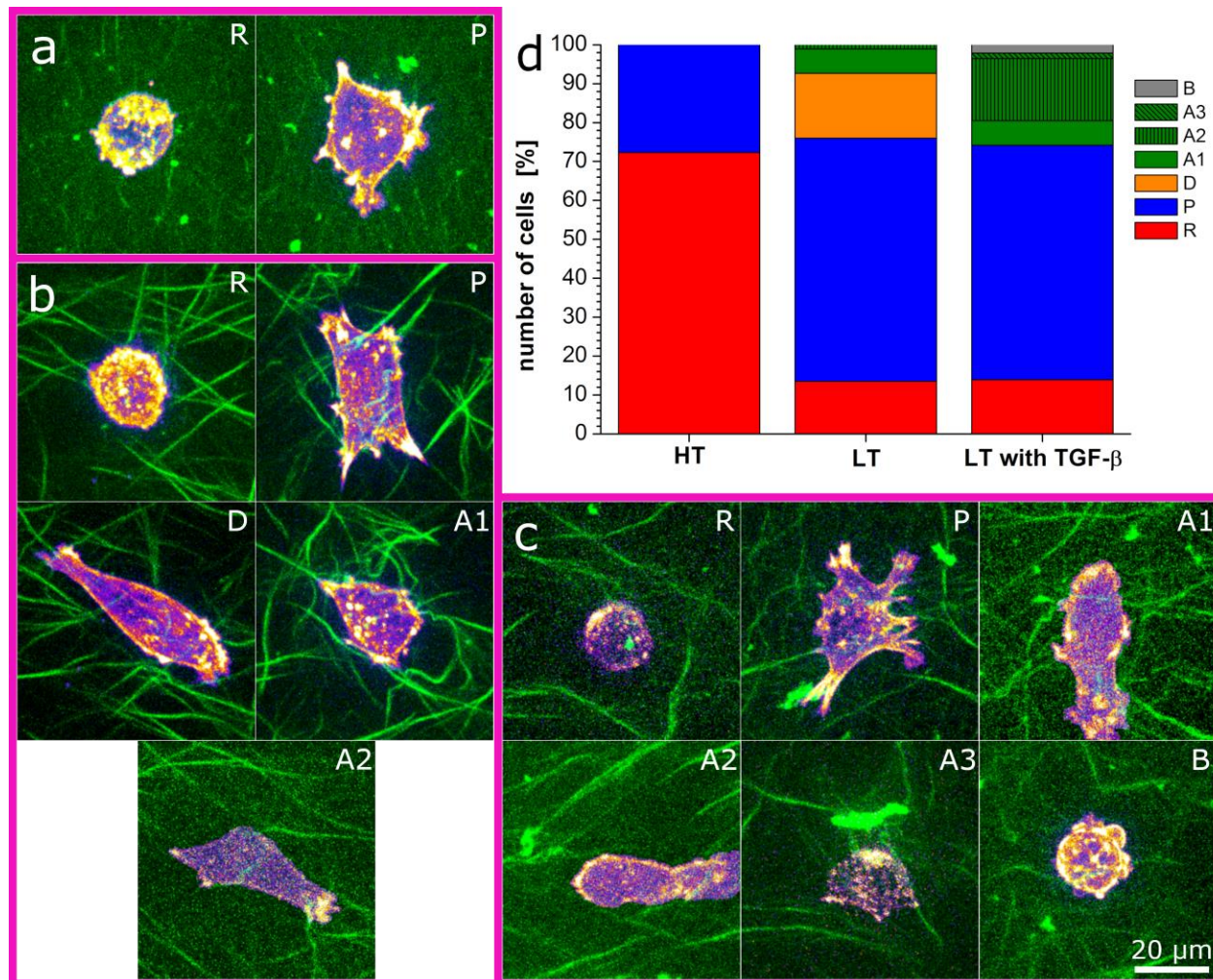


Figure 3.3: Migratory phenotypes of MDA-MB-231 cells in collagen gels. a) round (R) and pseudopodial (P) phenotype in HT gels; b) round (R), pseudopodial (P), adherent (D), amoeboid, including ellipsoid with leading edge (A1) and squeeze (A2) phenotype in LT gels, c) round (R), pseudopodial (P), amoeboid including ellipsoid with leading edge (A1), squeezing (A2), and rear driven (A3), and blebbing (B) phenotype in LT gels upon addition of TGF- β ; collagen fibers are displayed in green and cellular actin is shown in purple (low concentration) and yellow (high concentration) d) phenotype distribution within the different gel types showing the high amount of round cells in HT gels, the adherent cells specifically occurring in LT gels and the increase in amoeboid cells in LT gels upon addition of TGF- β .

3. Fiber stiffness, pore size and adhesion control migratory phenotype of MDA-MB-231 cells

Analysis of the motility parameters for the observed migration phenotypes shows that the amoeboid phenotype is fastest and least confined leading to high α -values and the longest track displacements, i.e. end-to-end-distances (figure 3.4a-d, S3.4). The round phenotype on the other hand is the slowest (figure 3.4a) and most confined with low α -values (figure S3.4) and very short track displacements (figure 3.4c). Thus, the altered phenotype distribution combined with an observed increase in motility of pseudopodial cells might explain the enhanced average cell motility upon addition of TGF- β to LT gels.

Further analysis of the influence of the local pore size at the cell location on phenotype and migration parameters reveals pore sizes much larger than cell size to impede migration leading to a lower fraction of fast cells and a lower fraction of high track displacements (figure 3.4b, 3.4d-g, fast speed and high displacement cells being defined as cells with the respective value higher than 75% of all cells). Also the amount of cells with amoeboid phenotype is reduced at large pore sizes. At the same time this phenotype reaches highest speeds, α -values and track displacements (figure 3.4a, 3.4c, S3.4). Looking at the maximum values in figure 3.4b, 3.4d, also confirms that amoeboid cells at pores of around cell size reach highest speeds and longest track displacements. A round phenotype on the other hand can be found at all pore sizes with its relative amount increasing with pore size (figure S3.5). Its speed, α -value, and track displacement is low. The pseudopod phenotype occurs in all pore sizes with almost uniform distribution except for a small tendency toward pores smaller than cell size (figure S3.5).

3.2. Results

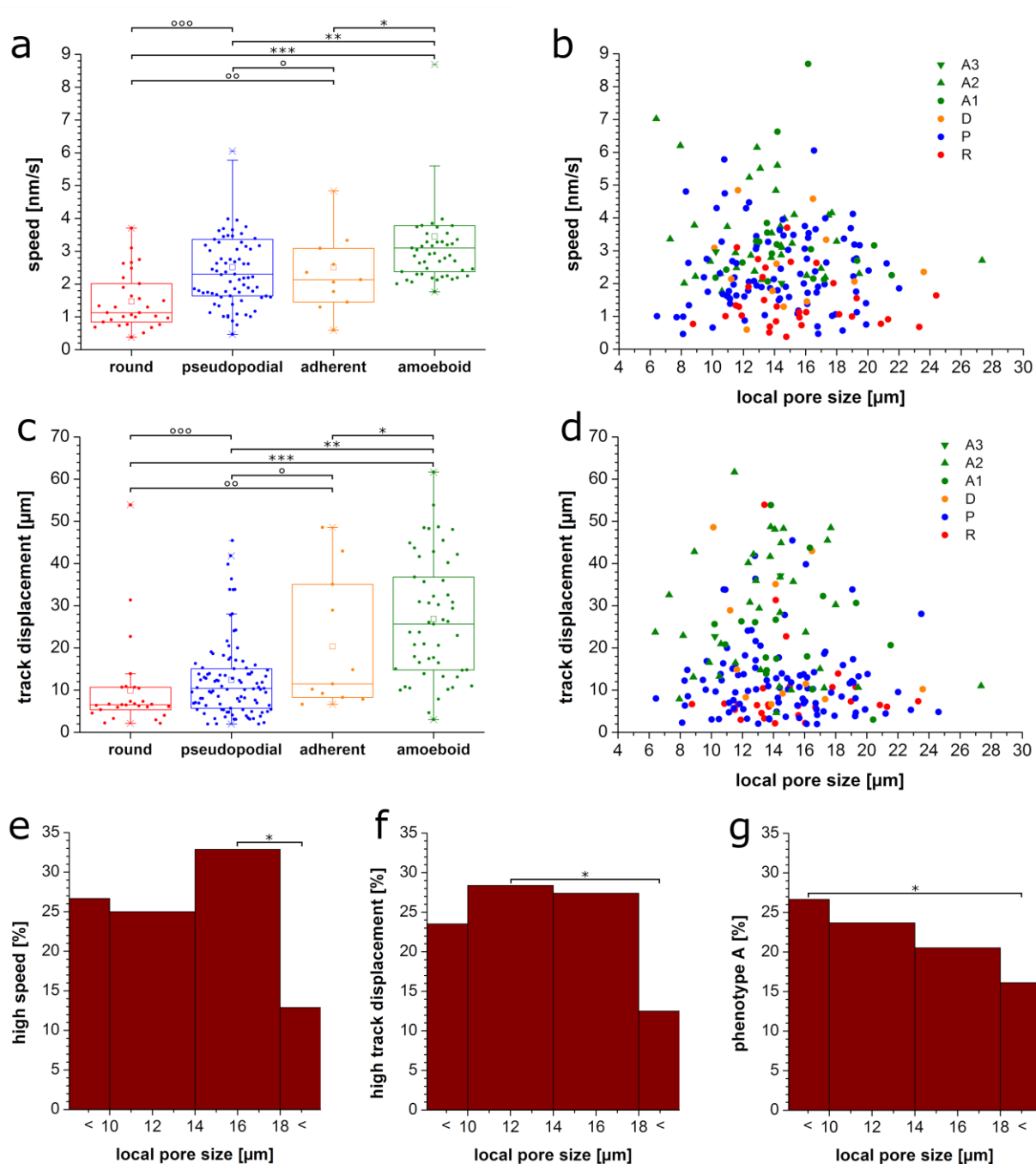


Figure 3.4: Migration parameters depending on phenotype and pore size. a) speeds for different phenotypes, $p < 0.001$ (* $p < 0.02$, ** $p < 0.001$, *** $p < 0.001$, ° $p < 0.95$, °° $p < 0.02$, °°° $p < 0.001$); b) speed versus local pore size for different phenotypes; c) track displacement for different phenotypes, $p < 0.001$,(* $p < 0.1$, ** $p < 0.001$, *** $p < 0.001$, ° $p < 0.2$, °° $p < 0.005$, °°° $p < 0.02$); d) track displacement versus local pore size for different

3. Fiber stiffness, pore size and adhesion control migratory phenotype of MDA-MB-231 cells

phenotypes including round (R), pseudopodial (P), adherent (D), and amoeboid with the subforms ellipsoid with leading edge (A1), squeezing (A2), and rear driven (A3) cells; e) fraction of cells in respective pore size with speed values greater than 3.2 nm/s (0.75 percentile of all cells), 4 μm binning, (* $p < 0.01$, ** $p < 0.1$, *** $p < 0.06$); f) fraction of cells in respective pore size with track displacement values greater than 22.8 nm/s (0.75 percentile of all cells), 4 μm binning, (* $p < 0.05$, ** $p < 0.05$, *** $p < 0.1$); g) fraction of cells in respective pore size with amoeboid phenotype, 4 μm binning, (* $p < 0.1$, ** $p < 0.1$).

3.3. Discussion

Taken together, HT gels impede migration. Although their pore size is in a range that does not obstruct migration and the low amount of adhesion sites on the thin HT gel fibers should promote amoeboid migration, these gels entirely abrogate migration even in the presence of TGF- β . Thus, the missing compliance due to the low fiber stiffness of HT gels supposedly inhibits migration. The missing fiber stiffness blocks force transmission along the fibers independent of the cell behavior. Hence, sufficient fiber stiffness is a prerequisite of migration and reducing it, a save measure to inhibit migration independent of cell type. This encourages therapeutic efforts that target the extracellular matrix stiffness, which otherwise increases with age and cancer progression [34]. Interestingly, the low fiber stiffness does not only impair movement itself, but also prevents establishment of motile amoeboid phenotypes suggesting that cells react to the stiffness [35] and that motile phenotypes result from a mechanically coupled feedback as discussed in [1]. While pore size and fiber stiffness of LT gels allow for migration, the high amount of adhesion sites favors adhesive phenotypes of low motility, which is removed by lowering adhesion with TGF- β . Highest speeds and longest track displacements are achieved at pores that are no larger than a cell. Hence, low adhesion, pores, which are no larger than cell size, and comparably high fiber stiffness offers best conditions for migration. Here, the fiber stiffness allows for good force transmission and low adhesion prevents confinement due to long lasting focal adhesions [24]. At the same time low adhesion does not allow for force transmission via integrins. This necessitates the pore sizes, which are not much larger than

cell size. They allow for chimneying movements as described by Malawista et al [36] where the cell pushes itself along fibers [37]. Accordingly, we observe amoeboid migration mainly between two parallel fibers at a distance of about cell size and slightly smaller. This allows for fairly straight movement along the parallel fibers without the necessity of reorientation. At the same time this distance allows for easy movement without barriers for the nucleus to pass. The requirement of low adhesion and confinement for a switch to an amoeboid phenotype is in accordance to movement in continuous substrates [10, 13].

Other than in continuous substrates, where round cells were found under no confinement and low adhesion [10], in the porous meshwork of collagen gels studied here, round cells occurred under all confinements. Yet, their proportion increased with increasing pore size in LT gels. They were also the prevalent phenotype in migration inhibiting HT gels without TGF- β . This suggests that they arise from the absence of a mechanical compliance, such as adhesion, confinement or stiffness. Mechanically non-compliant environments lack cues for a symmetry break, thus the cell stays in the symmetric round phenotype. In other words, the absence of compliance in HT gels favors a round phenotype, the porous, non-continuous meshwork in LT gels that provide less mechanical compliance than continuous substrates support round phenotypes less than HT gels, yet still in almost all situations, and the highly compliant continuous substrates allow for the round phenotype only in the least compliant situation of low adhesion and low confinement. Finally, while the blebbing state was reported to be the transition state in homogenous, continuous substrates [10], in porous collagen networks, the pseudopodial state is the state, in which cells reside most often in LT gels and from which they switch to other phenotypes. This might be due to the inhomogeneous meshwork, within which cells have to probe the different directions with pseudopods before transitioning into the most favored phenotype. Probing of the different spatial directions of course is not necessary in homogenous substrates.

In conclusion we show the plasticity of MDA-MB-231 cells in porous hydrogels. Even small differences of biochemical or mechanical stimuli can have huge impact on migratory phenotype and resulting migration properties.

3.4. Experimental part

3.4.1. Cell culture

MDA-MB-231 were obtained from ATCC (ATCC1HTB-26™) and cultured in Dulbecco's modified Eagle's medium (DMEM, Gibco), supplemented with 10% fetal bovine serum (FBS, Gibco) and 1% Penicillin Streptomycin (Gibco), at 37 °C in a 5% CO₂ atmosphere. Cells were regularly checked to be mycoplasma free with PCR Myoplasma Test Kit I/C (PromoKine). To image cells, their actin was labeled with LifeAct-TagRFP (Ibidi) or LifeAct-TagGFP2 (Ibidi). To stably express LifeAct-proteins, selection was performed using 50 ng/ml of G418 (Geneticin).

3.4.2. 3D collagen matrices

Collagen gels were prepared with ice-cooled compounds. Rat tail collagen I stock solution (Corning, high concentration) was mixed with DMEM-Medium (45% of final volume), containing 100000 cells/ml and neutralized with Sodium hydroxide (1 N, Fluka). The mixture was diluted with Dulbecco's phosphate-buffered saline (DPBS(1x), Gibco) to a final collagen concentration of 1.85 mg/ml. To label the fibers of the gel either 0.5% w of the collagen was replaced by fluorescein isothiocyanate (FITC) conjugated type I collagen (AnaSpec) or the collagen was mixed with 1 µg ATTO-633 (NHS-Ester, ATTO-TEC) per 2.74 mg collagen. If indicated TGF-β was added to the mixture to a final concentration of 26.7 ng/ml. After preparation the gel mixture was immediately filled into a sample carrier (Nunc™ Lab-Tek™ II, 8 wells) on ice for the gelation process.

For HT gels, the gelation process was at 37 °C. For LT gels, the sample is kept on ice for 30 minutes, followed by 15 minutes at room temperature and finally at 37 °C for at least about 30 minutes. After the gelation all gels were overlaid with DMEM.

3.4.3. Spinning disk microscopy

Microscopy for live-cell imaging was performed on a Zeiss Cell Observer SD with a Yokogawa spinning disk unit CSU-X1. The objective was a 1.40 NA 63x Plan apochromat oil immersion objective from Zeiss. Measurements were performed at 37 °C and a 5% CO₂ humidified atmosphere. FITC-collagen and LifeAct-TagGFP2 were imaged using a 488 nm laser, ATTO-633 with a 639 nm laser and LifeAct-TagRFP with a 561 nm laser. For two color detection of FITC-collagen and LifeAct-TagRFP fusion protein or LifeAct-TagGFP2 fusion protein and ATTO-633, a dichroic mirror (660 nm, Semrock) and band-pass filters 525/50 and 690/60 (both Semrock) were used in the detection path. Separate images for each fluorescence channel were acquired using two separate electron multiplier charge coupled devices (EMCCD) cameras (Photometrics Evolve™). Time-lapse images were acquired with a frame time of 20 min and 50 frames.

3.4.4. Rheology

Bulk rheology was performed on a MCR 100 rheometer (Anton Paar) and gels were prepared directly on the rheometer. The chemicals and preparation was the same as described above. 400 µl were filled between a PP25 measuring plate and a thermostatic plate. After 48 min 400 µl of water were spread around the polymerizing gel to prevent drying out. The gap size during gelation was 0.6 mm and was reduced to 0.5 mm during the measurement. The deformation was measured stepwise up to a final deformation of 10% at 37 °C and a frequency of 1 Hz.

Stiffness of the fibers was measured with the AFM NanoWizard® 4 (JPK Instruments) and SPM software (JPK Instruments) with an integrated Axiovert 200 inverted microscope (Zeiss). Collagen gels were prepared as described above and 100 µl gel were distributed in a 35 mm round glass dish (MatTek). Briefly, V-shaped cantilevers (Bruker; MLCT-D silicon nitride, resonance frequency 15 kHz, spring constant 0.03 N/m) were calibrated with the contact free method and used in the QI™ Mode (Advanced Imaging). The following values have been set: setpoint 0.2–0.4 nN, z-length 5 µm; speed 80 µm/s and pixel size 128x128 on a 20x20 µm grid. During the measurement the height and the slope of the force-distance

curves were recorded. Data processing was performed using the corresponding software version 6.0.50 (JPK Instruments). After median filtering, background subtraction and a low pass filter, stiffness was calculated on representative data points using the Hertzian contact model (Young's modulus). The tip shape was modeled as quadratic pyramid, the half-front angle of the cantilever as 15° and its Poisson ratio was set to 0,5.

3.4.5. Image analysis

Analysis of pore and cell size was performed with ImageJ employing BoneJ [38–40]. Migration trajectories and related properties were analyzed with Imaris (v 8.2.0, Bitplane, AG Zurich, Switzerland) and further processed with custom-written code in Octave (version 4.2.0). Statistics and data presentation was done with OriginPro (Version 8.0891, OriginLab Corporation, Northampton, MA, USA). Phenotypes were analyzed by visual inspection. Normality was tested with a Shapiro-Wilk test and depending on the outcome, a two-sample t-test (pore size of gels, indicated in the respective figure caption) or a non-parametric test (all other cases) was used. In this case, Kruskal-Wallis Anova tests were used for tests with more than two groups and Mann-Whitney Tests for comparison of two groups. For statistical tests of differences between different fractions as a function of pore size, binomial tests were performed. Boxplots show mean (square), the box consisting of median, lower and upper quartile (25 th and 75 th percentile), whiskers (5th and 95th percentile), and outliers (marked x).

Speed was calculated as the square root of the MSD at $\tau = 0$ time lag divided by the frame time; angles from the distribution are calculated from the cosine between two successive steps of the trajectory; track displacement is calculated as the distance between first and last position of the center of mass of the cell; the exponent α is determined via a fit to the first 5 lag times of the MSD according to the equation $MSD(\tau) = D \cdot \tau^\alpha$ with D and α as free fit parameters. Cells with fast speed and high track displacement respectively, were defined as cells showing the respective value higher than 75% of all cells independent of pore size.

3.5. References

1. Charras G, Sahai E. Physical influences of the extracellular environment on cell migration. *Nat Rev Mol Cell Biol.* 2014; 15(12):813–24.
2. Ruprecht V, Monzo P, Ravasio A, Yue Z, Makhija E, Strale PO, et al. How cells respond to environmental cues—insights from bio-functionalized substrates. *J Cell Sci.* 2017; 130(1):51–61.
3. Caswell PT, Zech T. Actin-Based Cell Protrusion in a 3D Matrix. *Trends Cell Biol.* 2018; 28(10):823–34.
4. Harley BA, Kim HD, Zaman MH, Yannas IV, Lauffenburger DA, Gibson LJ. Microarchitecture of threedimensional scaffolds influences cell migration behavior via junction interactions. *Biophys J.* 2008; 95 (8):4013–24.
5. Wu P-H, Gilkes DM, Wirtz D. The Biophysics of 3D Cell Migration. *Annu Rev Biophys.* 2018; 47(1):549–67.
6. Wolf K, Te Lindert M, Vortmeyer, Alexander S, te Riet J, L Willis A, et al. Physical limits of cell migration: Control by ECM space and nuclear deformation and tuning by proteolysis and traction force2013. 1069–84 p.
7. Lammermann T, Bader BL, Monkley SJ, Worbs T, Wedlich-Soldner R, Hirsch K, et al. Rapid leukocyte migration by integrin-independent flowing and squeezing. *Nature.* 2008; 453(7191):51–5.
8. Bergert M, Chandradoss SD, Desai RA, Paluch E. Cell mechanics control rapid transitions between blebs and lamellipodia during migration. *Proc Natl Acad Sci USA.* 2012; 109(36):14434–9.
9. Renkawitz J, Schumann K, Weber M, Lammermann T, Pflücke H, Piel M, et al. Adaptive force transmission in amoeboid cell migration. *Nat Cell Biol.* 2009; 11(12):1438–43.
10. Liu YJ, Le Berre M, Lautenschlaeger F, Maiuri P, Callan-Jones A, Heuze M, et al. Confinement and low adhesion induce fast amoeboid migration of slow mesenchymal cells. *Cell.* 2015; 160(4):659–72.

3. Fiber stiffness, pore size and adhesion control migratory phenotype of MDA-MB-231 cells

11. Kick K, Nekolla K, Rehberg M, Vollmar AM, Zahler S. New View on Endothelial Cell Migration: Switching Modes of Migration Based on Matrix Composition. *Arterioscler Thromb Vasc Biol.* 2016; 36(12):2346–57.
12. Paszek MJ, Zahir N, Johnson KR, Lakins JN, Rozenberg GI, Gefen A, et al. Tensional homeostasis and the malignant phenotype. *Cancer Cell.* 2005; 8(3):241–54.
13. Holle AW, Govindan Kutty Devi N, Clar K, Fan A, Saif T, Kemkemer R, et al. Cancer Cells Invade Confined Microchannels via a Self-Directed Mesenchymal-to-Amoeboid Transition. *Nano Lett.* 2019; 19 (4):2280–90.
14. Anguiano M, Castilla C, Maska M, Ederra C, Pelaez R, Morales X, et al. Characterization of threedimensional cancer cell migration in mixed collagen-Matrigel scaffolds using microfluidics and image analysis. *PLoS One.* 2017; 12(2):e0171417.
15. Talkenberger K, Cavalcanti-Adam EA, Voss-Bohme A, Deutsch A. Amoeboid-mesenchymal migration plasticity promotes invasion only in complex heterogeneous microenvironments. *Scientific reports.* 2017; 7(1):9237.
16. Vader D, Kabla A, Weitz D, Mahadevan L. Strain-induced alignment in collagen gels. *PLoS One.* 2009; 4(6):e5902.
17. Wisdom KM, Adebowale K, Chang J, Lee JY, Nam S, Desai R, et al. Matrix mechanical plasticity regulates cancer cell migration through confining microenvironments. *Nat Commun.* 2018; 9(1):4144.
18. Dietrich M, Le Roy H, Bruckner DB, Engelke H, Zantl R, Radler JO, et al. Guiding 3D cell migration in deformed synthetic hydrogel microstructures. *Soft Matter.* 2018; 14(15):2816–26.
19. Wu PH, Giri A, Sun SX, Wirtz D. Three-dimensional cell migration does not follow a random walk. *Proc Natl Acad Sci USA.* 2014; 111(11):3949–54.
20. Wolf K, Alexander S, Schacht V, Coussens LM, von Andrian UH, van Rheenen J, et al. Collagen-based cell migration models in vitro and in vivo. *Semin Cell Dev Biol.* 2009; 20(8):931–41.

3.5. References

21. Provenzano PP, Eliceiri KW, Campbell JM, Inman DR, White JG, Keely PJ. Collagen reorganization at the tumor-stromal interface facilitates local invasion. *BMC Med.* 2006; 4(1):38.
22. Sauer F, Oswald L, Ariza de Schellenberger A, Tzschatzsch H, Schrank F, Fischer T, et al. Collagen networks determine viscoelastic properties of connective tissues yet do not hinder diffusion of the aqueous solvent. *Soft Matter.* 2019; 15(14):3055–64.
23. Tozluoglu M, Tournier AL, Jenkins RP, Hooper S, Bates PA, Sahai E. Matrix geometry determines optimal cancer cell migration strategy and modulates response to interventions. *Nat Cell Biol.* 2013; 15 (7):751–62.
24. Doyle AD, Carvajal N, Jin A, Matsumoto K, Yamada KM. Local 3D matrix microenvironment regulates cell migration through spatiotemporal dynamics of contractility-dependent adhesions. *Nat Commun.* 2015; 6:8720.
25. Licup AJ, Muˆnster S, Sharma A, Sheinman M, Jawerth LM, Fabry B, et al. Stress controls the mechanics of collagen networks. *Proc Natl Acad Sci USA.* 2015; 112(31):9573–8.
26. Broda E, Torrano AA, Loˆbbert L, Moˆckl L, Braˆuchle C, Engelke H. Invasiveness of Cells Leads to Changes in Their Interaction Behavior with the Glycocalyx. *Adv Biosyst.* 2018; 2(8):1800083.
27. Lammermann T, Sixt M. Mechanical modes of 'amoeboid' cell migration. *Curr Opin Cell Biol.* 2009; 21 (5):636–44.
28. Condor M, Mark C, Gerum RC, Grummel NC, Bauer A, Garcia-Aznar JM, et al. Breast Cancer Cells Adapt Contractile Forces to Overcome Steric Hindrance. *Biophys J.* 2019; 116(7):1305–12.
29. Burov S, Tabei SM, Huynh T, Murrell MP, Philipson LH, Rice SA, et al. Distribution of directional change as a signature of complex dynamics. *Proc Natl Acad Sci USA.* 2013; 110(49):19689–94.
30. Bhowmick NA, Ghiassi M, Bakin A, Aakre M, Lundquist CA, Engel ME, et al. Transforming growth factor-beta1 mediates epithelial to mesenchymal

3. Fiber stiffness, pore size and adhesion control migratory phenotype of MDA-MB-231 cells

- transdifferentiation through a RhoA-dependent mechanism. *Molecular biology of the cell*. 2001; 12(1):27–36.
31. Sanz-Moreno V, Gadea G, Ahn J, Paterson H, Marra P, Pinner S, et al. Rac activation and inactivation control plasticity of tumor cell movement. *Cell*. 2008; 135(3):510–23.
 32. Sahai E, Marshall CJ. Differing modes of tumour cell invasion have distinct requirements for Rho/ROCK signalling and extracellular proteolysis. *Nat Cell Biol*. 2003; 5(8):711–9.
 33. Poincloux R, Collin O, Liza'rraga F, Romao M, Debray M, Piel M, et al. Contractility of the cell rear drives invasion of breast tumor cells in 3D Matrigel. *Proc Natl Acad Sci USA*. 2011; 108(5):1943–8.
 34. Lampi MC, Reinhart-King CA. Targeting extracellular matrix stiffness to attenuate disease: From molecular mechanisms to clinical trials. *Science translational medicine*. 2018; 10(422).
 35. Discher DE, Janmey P, Wang YL. Tissue cells feel and respond to the stiffness of their substrate. *Science*. 2005; 310(5751):1139–43.
 36. Malawista SE, de Boisfleury Chevance A, Boxer LA. Random locomotion and chemotaxis of human blood polymorphonuclear leukocytes from a patient with leukocyte adhesion deficiency-1: normal displacement in close quarters via chimneying. *Cell Motil Cytoskeleton*. 2000; 46(3):183–9.
 37. Hawkins RJ, Piel M, Faure-Andre G, Lennon-Dumenil AM, Joanny JF, Prost J, et al. Pushing off the walls: a mechanism of cell motility in confinement. *Phys Rev Lett*. 2009; 102(5):058103.
 38. Schindelin J, Arganda-Carreras I, Frise E, Kaynig V, Longair M, Pietzsch T, et al. Fiji: an open-source platform for biological-image analysis. *Nat Methods*. 2012; 9(7):676–82.
 39. Schneider CA, Rasband WS, Eliceiri KW. NIH Image to ImageJ: 25 years of image analysis. *Nat Methods*. 2012; 9(7):671–5.

3.5. References

40. Doube M, Klosowski MM, Arganda-Carreras I, Cordelieres FP, Dougherty RP, Jackson JS, et al. BoneJ: Free and extensible bone image analysis in ImageJ. *Bone*. 2010; 47(6):1076–9.

3.6. Appendix

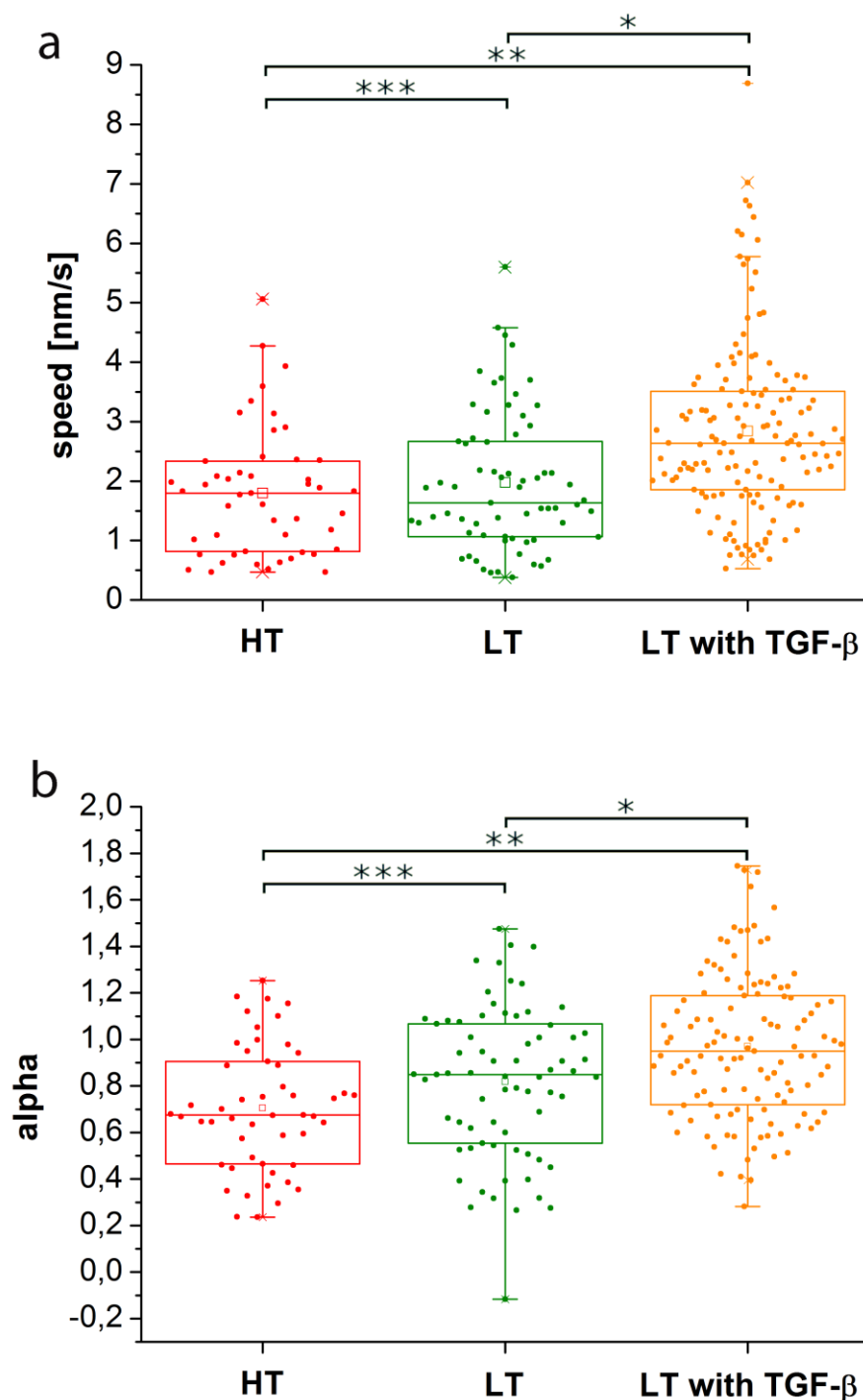


Figure S3.1: Statistical analysis of MDA-MB-231 migration in collagen gels. a) box plots of speed distributions show statistical differences between LT with TGF- β and the gels

3.6. Appendix

without, but no difference between the two gels without TGF- β (* $p < 0.001$, ** $p < 0.001$, *** $p < 0.49$); b) box plots of exponent α values show a significant increase of α upon addition of TGF- β to LT gels, as well as a significant difference between LT and HT gels (* $p < 0.002$, ** $p < 0.001$, *** $p < 0.05$).

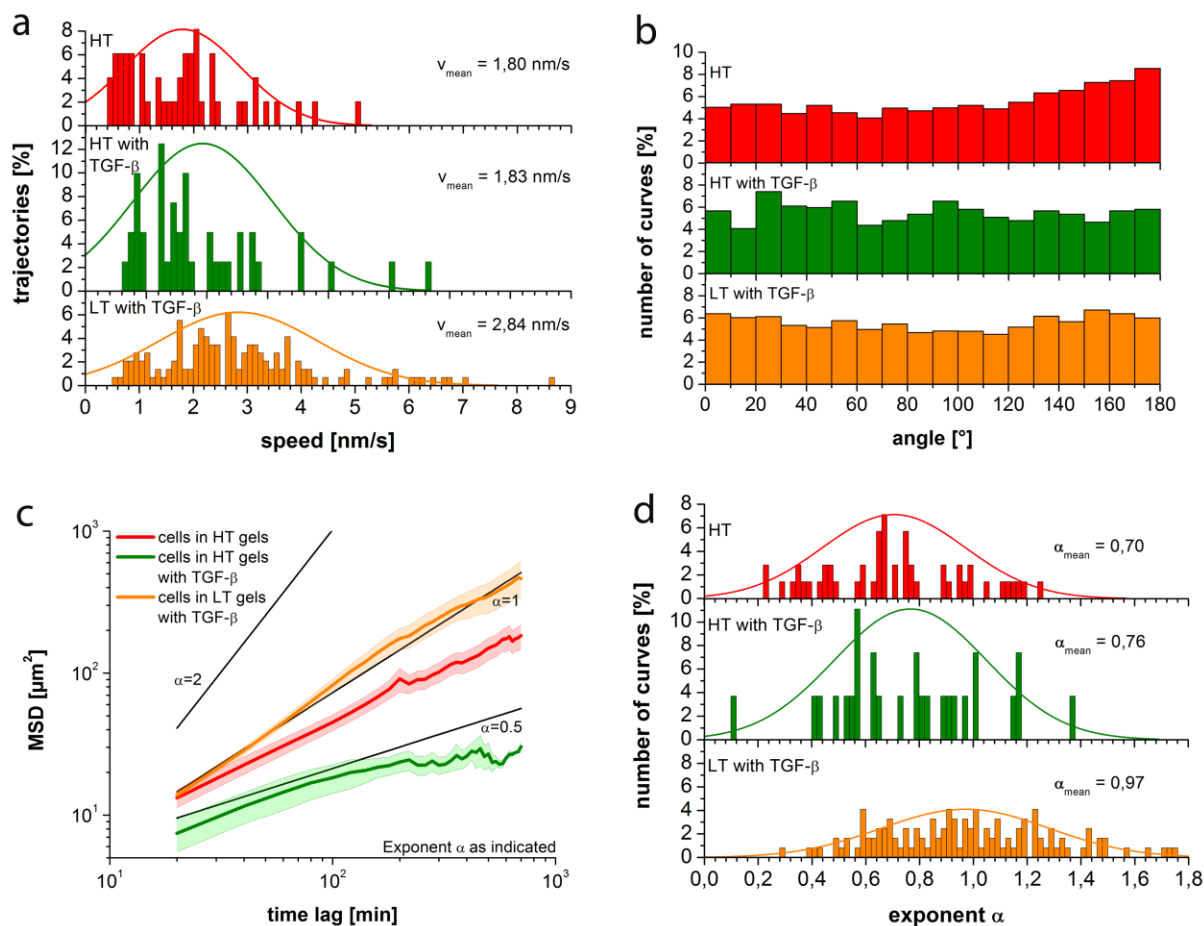


Figure S3.2: MDA-MB-231 migration in collagen gels—addition of TGF- β to HT gels. a) histograms of speed distributions show no increase in speed upon addition of TGF- β to HT gels (HT compared to HT with TGF- β , $p < 0.6$); b) angle distribution between different steps shows significant backtracking due to confinement for HT gels, which is removed upon addition of TGF- β (HT compared to HT with TGF- β , $p < 0.001$, HT with TGF- β compared to LT with TGF- β , $p < 0.4$) c) average mean square displacements for the different conditions

3. Fiber stiffness, pore size and adhesion control migratory phenotype of MDA-MB-231 cells

show subdiffusive behavior in HT gels independent of TGF- β ; d) histograms of exponent α values show no increase of α upon addition of TGF- β to HT gels (HT compared to HT with TGF- β , $p < 0.4$).

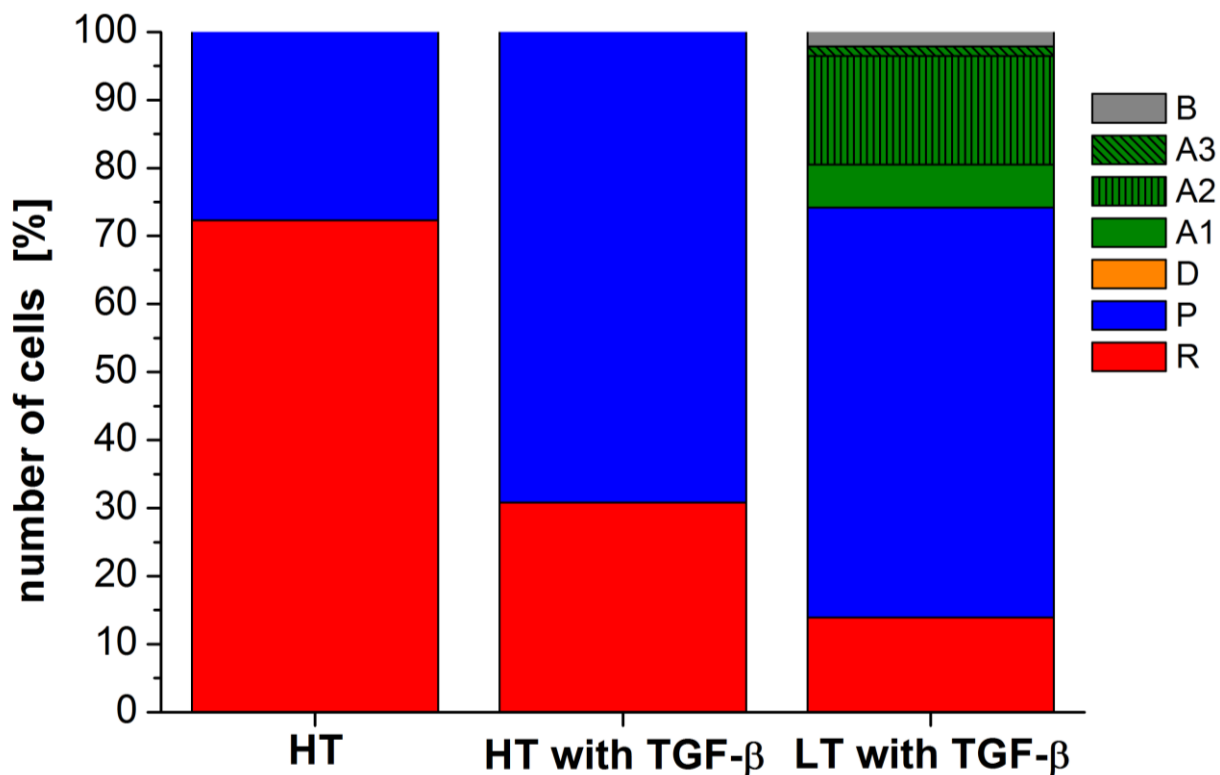


Figure S3.3: Phenotype distribution in HT gels and both gels with TGF- β . In HT gels only round and pseudopodial phenotypes were observed (with and without TGF- β), while LT gels with TGF- β show a wider variety of phenotypes including amoeboid cells.

3.6. Appendix

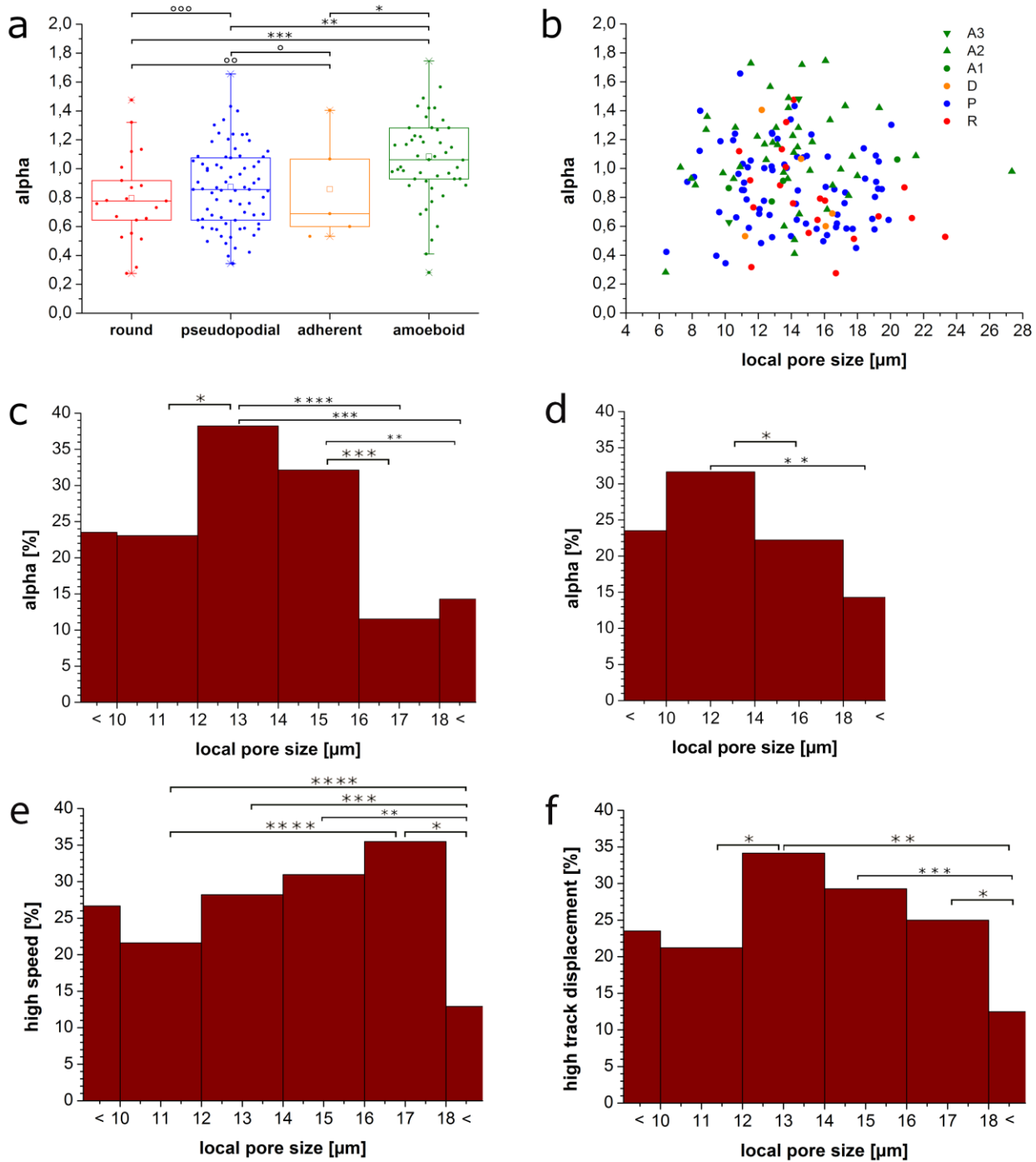


Figure S3.4: Distribution of α -values depending on phenotype. a) α -values for different phenotypes show an enhanced α -value for amoeboid cells, $p < 0.01$ ($^*p < 0.17$, $^{**}p < 0.01$, $^{***}p < 0.001$, $^{\circ}p < 0.83$, $^{\circ\circ}p < 0.95$, $^{\circ\circ\circ}p < 0.28$); b) α -values versus local pore size for different phenotypes including round (R), pseudopodial (P), adherent (D), and amoeboid with the subforms ellipsoid with leading edge (A1), squeezing (A2)), and rear driven (A3) cells; c)

3. Fiber stiffness, pore size and adhesion control migratory phenotype of MDA-MB-231 cells

fraction of cells in respective pore size with alpha values greater than 1.14 (0.75 percentile of all cells), 2 μm binning, (*p < 0.08, **p < 0.07, ***p < 0.02, ****p < 0.005); d) fraction of cells in respective pore size with alpha values greater than 1.14 (0.75 percentile of all cells), 4 μm binning, (*p < 0.08, **p < 0.07); e) fraction of cells in respective pore size with speed values greater than 3.2 nm/s (0.75 percentile of all cells), 2 μm binning, (*p < 0.008, **p < 0.03, ***p < 0.05, ****p < 0.06); f) fraction of cells in respective pore size with track displacement values greater than 22.8 nm/s (0.75 percentile of all cells), 2 μm binning, (*p < 0.08, **p < 0.008, ***p < 0.03).

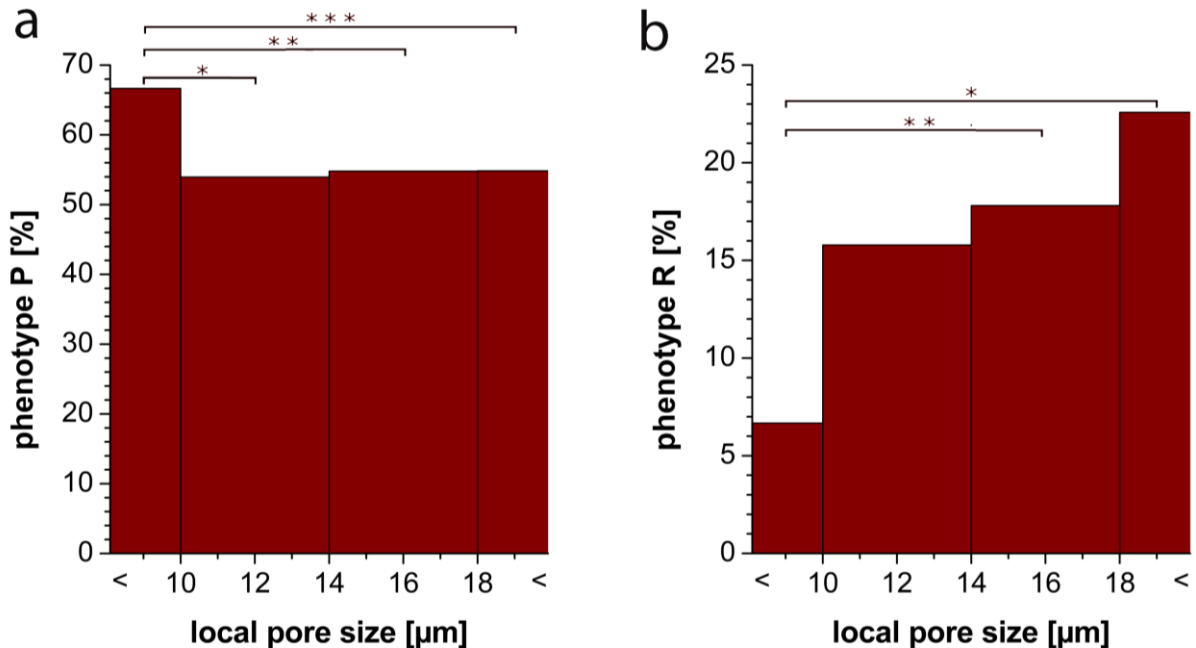


Figure S3.5: Fraction of phenotypes depending on pore size. a) fraction of cells in respective pore size with pseudopodial phenotype, 4 μm binning, (*p < 0.01, **p < 0.02, ***p < 0.1); b) fraction of cells in respective pore size with round phenotype, 4 μm binning, (*p < 0.1, **p < 0.09).

4. Directed invasion of cancer cell spheroids inside 3D collagen matrices oriented by microfluidic flow in experiment and simulation

This chapter is based on the following manuscript:

Geiger F, Schnitzler LG, Brugger MS, Westerhausen C, Engelke H. Directed invasion of cancer cell spheroids inside 3D collagen matrices oriented by microfluidic flow in experiment and simulation. 2021; manuscript submitted.

Abstract

Invasion is strongly influenced by the mechanical properties of the extracellular matrix. Here, we use microfluidics to align fibers of a collagen matrix and study the influence of fiber orientation on invasion from a cancer cell spheroid. The microfluidic setup allows for highly oriented collagen fibers of tangential and radial orientation with respect to the spheroid, which can be described by finite element simulations. In invasion experiments, we observe a strong bias of invasion towards radial as compared to tangential fiber orientation. Simulations of the invasive behavior with a Brownian diffusion model suggest complete blockage of migration perpendicularly to fibers allowing for migration exclusively along fibers. This slows invasion toward areas with tangentially oriented fibers down, but does not prevent it.

4.1. Introduction

Invasion from tumor spheroids is influenced by cellular signaling as well as by the properties of the extracellular matrix. The onset of invasion has been described as fluidization of the spheroid, which is triggered by a phase transition from a jammed state to an unjammed, fluid-like state [1]. After this transition and the accompanying onset of invasion, single cells often start to stream out of the collective. This has been described as a

transition from fluid to gas-like state. Recent work has identified molecular mechanisms of the unjamming transition. One such mechanism is based on Rab5a activating the ERK1/2 pathway [2]. Other molecular influences are e.g. e-cadherins and in general an epithelial to mesenchymal transition [3]. Next to these cellular properties, characteristics of the extracellular matrix that drive such unjamming transitions have been identified. For example matrix density and extracellular confinement play a critical role in this transition [3].

Single cell migration is also strongly influenced by matrix properties, such as matrix density, mesh size, as well as fiber length and thickness [4-9]. Additionally, fiber alignment and orientation has been shown to impact single cell migration based on contact guidance and the non-linear rheological properties of the extracellular matrix [10, 11]. For invasion from a cell collective, such an influence of fiber alignment has been predicted from theoretical modeling [12]. Experimentally, short-range alignment has been shown to direct protrusions [13]. Furthermore, radially oriented fibers resulting from matrix remodeling of spheroids, lead to increased invasion [14, 15] and cells streaming along the oriented fibers [16]. Thus, fiber alignment may also be an important factor that influences invasion from a cell collective. Cell contractions however, only result in radial alignment and do not allow for a comparison of tangential and radial alignment.

Here, we investigate this influence of fiber alignment and orientation of tangentially versus radially oriented fibers on spheroid invasion. We use shear flow in a microfluidic channel during collagen polymerization to align collagen fibers of a matrix containing cancer cell spheroids. After polymerization of the gel, application of the external flow is stopped. Over time, the spheroids spread into the collagen gel. The observed invasion shows clear directionality along the radially aligned fibers. Combining live cell imaging with particle image velocimetry measurements and finite element simulations, the fiber alignment resulting from shear flow and the subsequent shape evolution of cell spheroids in the aligned fibers can be described by a strongly enhanced invasion speed of cells moving along fibers compared to perpendicular to fibers.

4.2. Results

Alignment of collagen gels. Shear flow in microfluidic channels can align collagen depending on flow rate and channel size [17]. Here, we used 400 μm high channels to accommodate spheroids embedded in collagen gels. We applied a pulse of high flow rate to fill the channel with collagen including HeLa cell spheroids followed by a phase of low flow rate during polymerization on ice. After polymerization, we stopped application of the external flow. This process resulted in gels with rather long collagen fibers oriented along the direction of the applied flow as displayed in Fig. 4.1a. Quantitative analysis of the distribution of fiber orientations (Fig. 4.1b, blue data) revealed a clear maximum at 90 degrees, which corresponds to alignment along the main flow direction. A control experiment without flow and outside the channel to minimize shear flow shows a fairly uniform distribution of fiber orientations (Fig. S4.1, and Fig. 4.1b, red data).

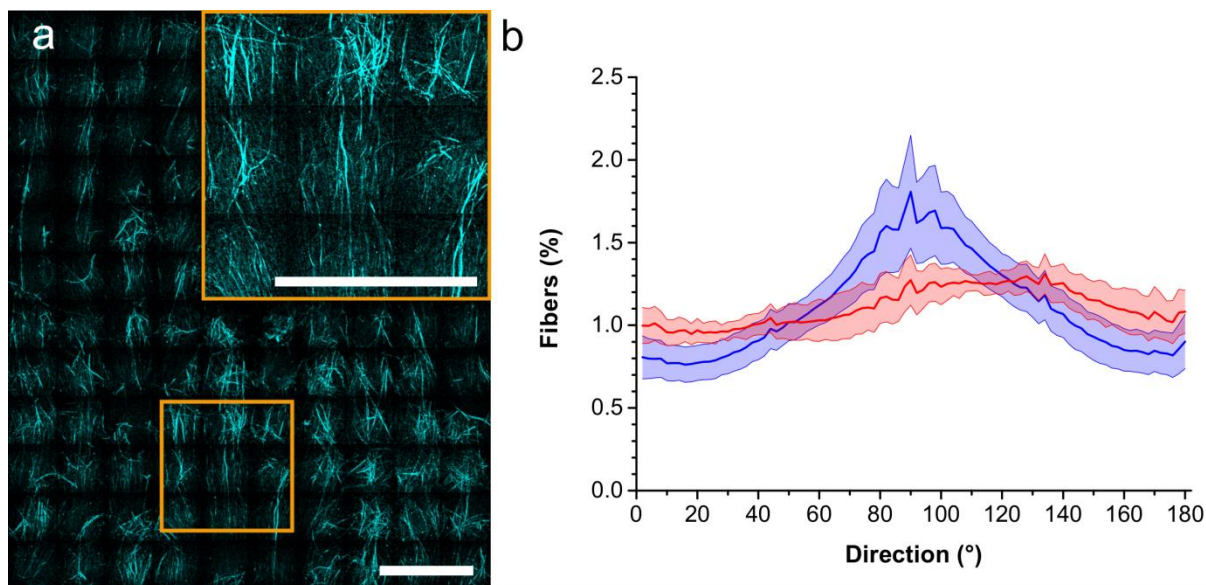


Figure 4.1: Alignment of Collagen Fibers. a) Collagen fibers aligned via microfluidic flow in a channel with 400 μm height. Insert: magnification of image marked with orange box. b) Orientation distribution of fibers in 33 gels aligned with microfluidics (mean values blue; standard error light blue) and in non-aligned gels prepared in a well (mean values red; standard error light red). Scale bars = 200 μm .

Collagen fibers around spheroid represent flow field. Focusing on collagen alignment in proximity to spheroids, we find fiber orientations around the spheroid mostly along the stream lines that one would expect to result from the applied flow field around the spheroid. However, the collagen fibers at the spheroid side facing upstream with respect to the applied flow were oriented perpendicularly to the flow direction (Fig. 4.2a). With respect to the spheroid, this lead to mostly tangential fibers around the spheroid with the exception of radial orientation at the side facing downstream of the main flow. To further characterize the flow field around the spheroid applied during polymerization and to understand the resulting fiber orientation after polymerization, we measured the flow in the region of the spheroid during collagen polymerization. Tracking of beads moving in the collagen gel during polymerization revealed traces as displayed in Fig. 4.2b. Analysis of the velocity field with particle image velocimetry (PIV) provides a qualitative description of the force field applied by the shear flow. Fig. 4.2c shows the direction and magnitude of the resulting velocity fields. It reveals a decrease in forces at the periphery of the spheroid – specifically at its sides facing up- and downstream of the main flow direction. The obtained velocity fields correspond very well to simulations of shear flow in a microfluidic channel around an immobilized sphere (Fig. 4.2d and Fig. S4.2). Based on this confirmation that the flow simulation describes the conditions of the experiment, we next ran a simulation of a single fiber in the respective flow field around a spheroid. Fig. 4.2d show the orientation of the fiber in the simulation. While it is oriented along flow direction far away from the spheroid, the force distribution close to the upstream side of the spheroid orients the fiber perpendicularly to main flow and tangentially to the spheroid. It then continues to exhibit a tangential orientation with respect to the spheroid until it reaches the downstream side of the spheroid, where it is oriented radially with respect to the spheroid and along main flow direction. This corresponds very well to the fiber orientation of the gel measured around the spheroid (Fig. 4.2a), suggesting that the forces of the flow are responsible for the obtained orientation of collagen fibers. In turn, the results also confirm that the collagen orientation displays and preserves the force field applied during polymerization.

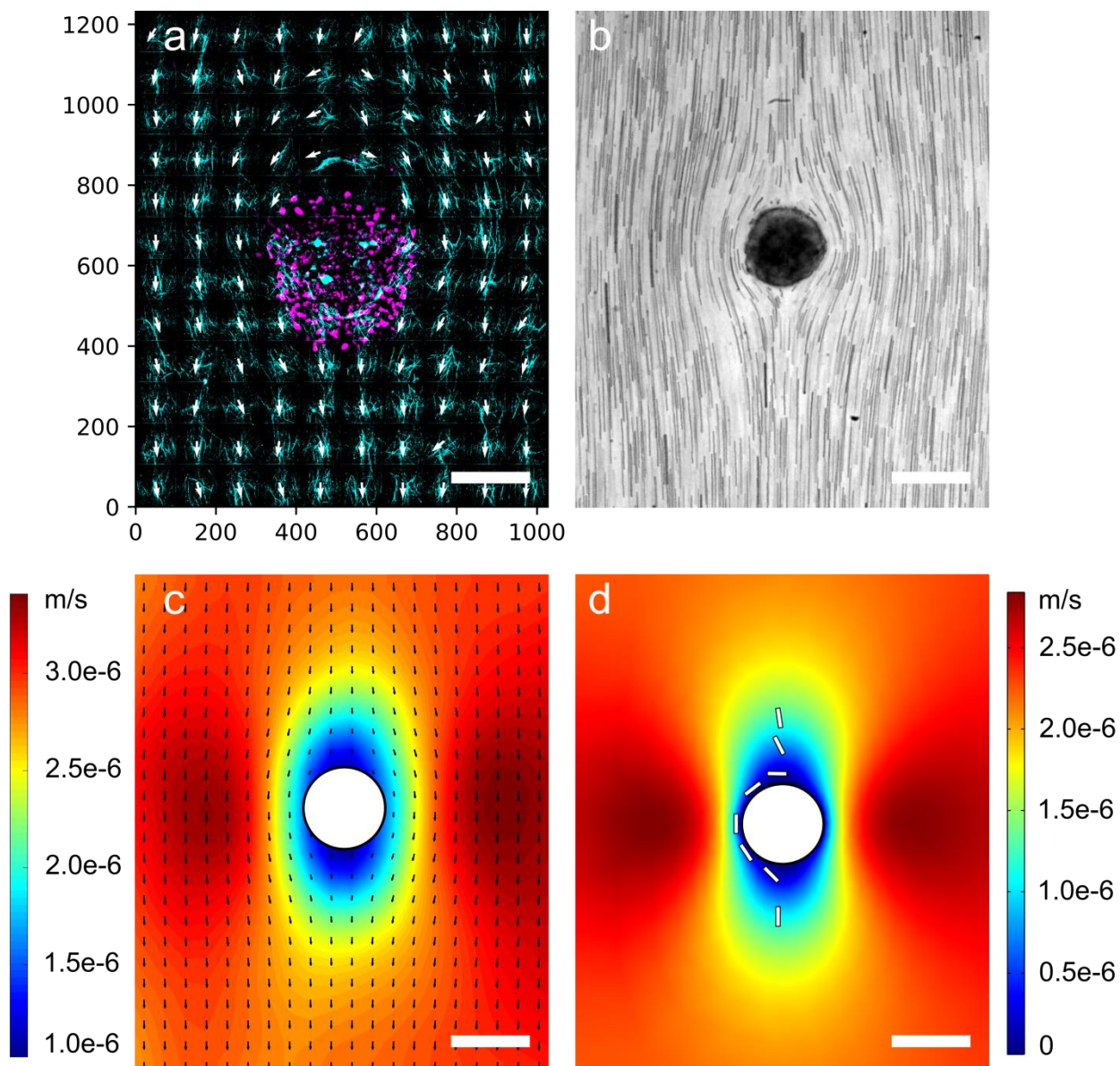


Figure 4.2: Characterization of shear flow and fiber alignment around the spheroid, while the main flow direction is from top to bottom. a) Spheroid (magenta) and aligned collagen fibers (cyan) with vectors in alignment direction (white) around the spheroid after polymerization. b) Flow trajectory of beads around a spheroid embedded in collagen during polymerization. c) Calculated velocity magnitude (color code) with flow vectors of the beads. d) Simulated velocity field (color code represents velocity magnitude) of the collagen mixture and the trajectory of a single collagen fiber (white bar) around the cell aggregate in the microfluidic channel. Scale bars = 200 μm .

Invasion of the spheroid. Next, we investigated the behavior of spheroids in the oriented hydrogels over time. The overall collagen concentration used is 1.85 mg/ml and allows for spontaneous invasion. Figure 4.3a shows that spheroids start to invade into the surrounding already one day after embedding them into the gels (see also Fig. S4.3). The invasion is much more pronounced along the radial fibers on the downstream side of the spheroid compared to the sides facing tangential collagen fibers. Over the course of 3 days, the observed invasion increases in all directions. Furthermore, we start to observe single cells streaming into the gel detached from the spheroid after two days. Quantitative analysis of the ratio of axes of the spheroid along and perpendicular to main flow direction shows that growth along the main flow direction during the first day is on average about a factor of 1.3 larger than that perpendicular to flow (Fig. 4.3b). The average axis ratio is not increased much stronger during the following days suggesting a fairly constant average asymmetry after the first day, despite some deviations in individual spheroids. Fig. 4.3c depicts the influence of degree of overall matrix alignment in main flow direction on growth asymmetry during the first day measured as axis ratio of day 1 relative to day 0. The degree of alignment is calculated as the amount of fibers aligned in main flow direction in the analyzed gel relative to that of a gel with uniform fiber distribution (further described in the materials and methods section). Highest relative axis ratios and thus pronounced asymmetry and strongest directionalities of invasion are reached in gels with high degrees of alignment. Analysis of the influence of overall matrix alignment in main flow direction on the two spheroid axes separately shows that a high degree of alignment yields reduced invasion perpendicular to the main flow- and thus alignment direction (a-axis), while it allows for strong invasion along main alignment direction (b-axis) (Fig. S4.4, S4.5). With respect to the spheroid, invasion perpendicular to the main alignment direction (i.e. along the a-axis) means invasion toward tangentially oriented fibers. The spheroid fronts invading along main alignment direction face tangentially oriented fibers on the upstream side and radially oriented fibers on the downstream side. Thus, the reduction in invasion perpendicular to main alignment direction with increasing degree of alignment and the reduced invasion perpendicular to main alignment compared to invasion along main alignment direction, suggests that tangential fiber orientation may hamper invasion compared to radial fiber orientation. So far, analysis of the axis along main alignment

4. Directed invasion of cancer cell spheroids in microfluidic flow oriented 3D collagen gels

direction includes one front facing tangential fibers and one front facing radially oriented fibers. This obscures the results on the influence of fiber orientation to a certain extent and may explain the less pronounced influence of overall degree of alignment on the invasion along alignment direction (Fig. S4.4b) compared to that perpendicular to alignment direction. Therefore, we next analyzed upstream and downstream front separately.

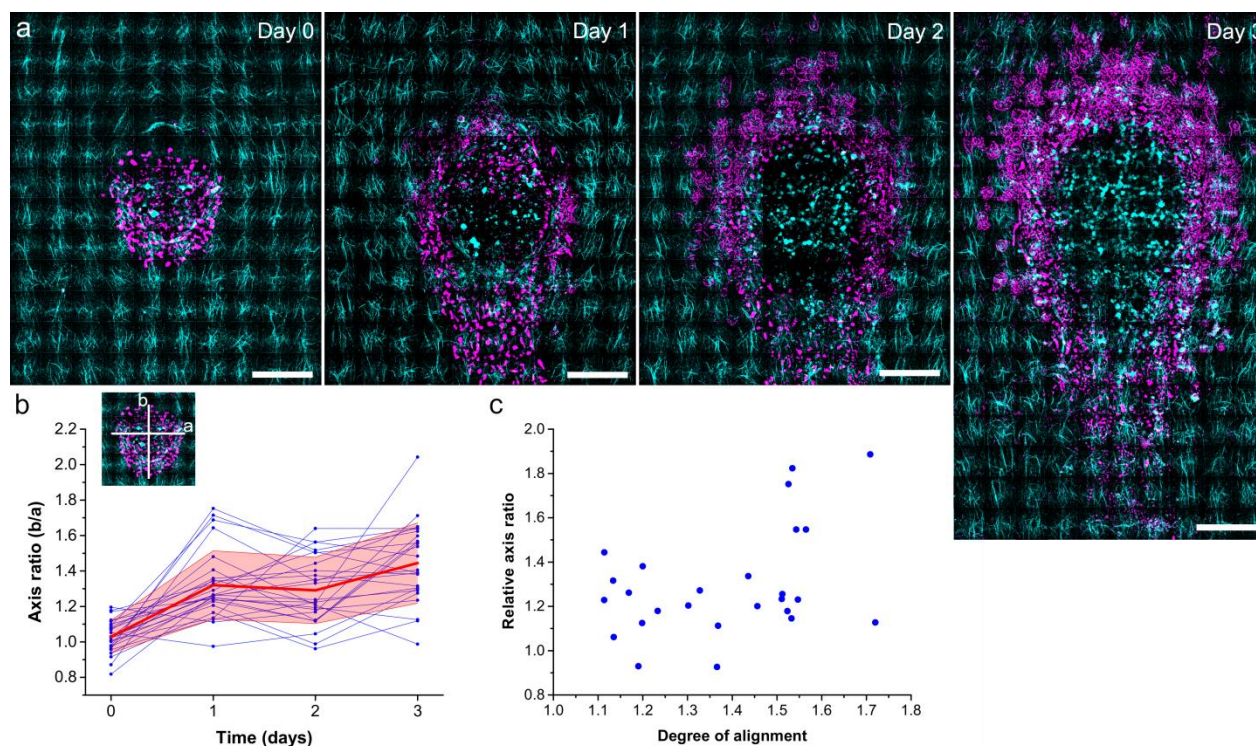


Figure 4.3: Invasion of Spheroids. a) Microscopy images of spheroids invading into the surrounding aligned matrix over the course of 3 days. Note: the spheroid remains filled with cells, the void in the center of the spheroid is a result of image editing for better contrast in the composite with the matrix. For original images see Fig. S3. b) Ratio of axis along main flow (b) vs. perpendicular to it (a) of 26 aggregates over the course of 3 days (single values: blue; mean +/- standard error: red and light red). c) Relative axis ratio (axis ratio of day 1 normalized by the ratio of day 0) as a function of the degree of fiber alignment. Correlation coefficient: 0.40 (Pearson's correlation). Scale bars = 200 μm .

Influence of tangentially and radially oriented fibers on migration. Figure 4.3a clearly shows increased invasion on the downstream side of the spheroid compared to the

upstream facing side. Focusing on these two sides of the spheroid (Fig. 4.4a and b) we find that the distance the invasion front travels on average during the first day is much longer ($228 \pm 33 \mu\text{m}$) for the downstream front compared to upstream ($97 \pm 23 \mu\text{m}$) (Fig. 4.4c). Also after three days, the downstream front shows similarly increased invasion compared to the upstream front (2.3 times increased distance of downstream compared to upstream after one day and 2.1 times after three days). Interestingly, the distance that the invasion front travelled after three days is in both directions only about a factor of 1.9 longer than after one day suggesting a non-linear time-evolution. Since the conditions of the two spheroid sides are the same with the only exception of the collagen fiber orientation with respect to the spheroid, we also analyzed the degree of alignment at the invasion fronts (see marked areas in Fig. 4.4a and b; Fig. S4.6). As expected from the microscopy images, the degree of alignment in main flow direction is much higher on the downstream side with the radially oriented fibers as compared to the upstream side with the tangential fibers (Fig. 4.4d). The degree of alignment does not change significantly between day 0 and day 1. Comparing the results on invasion of upstream and downstream front of the spheroid confirms that a high degree of alignment of collagen fibers in radial direction promotes invasion compared to tangentially oriented fibers.

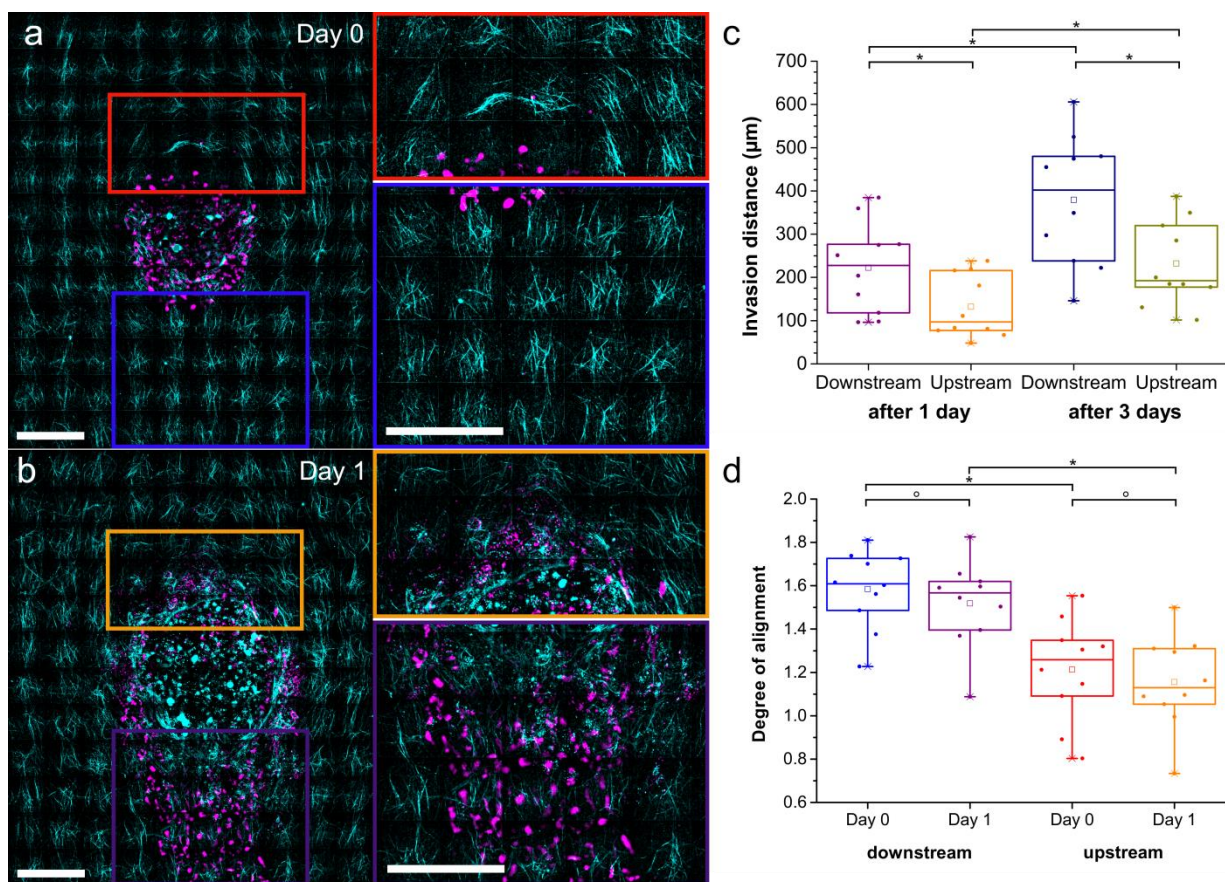


Figure 4.4: Invasion and fiber alignment on upstream and downstream front. a) Collagen fibers (cyan) and spheroid (magenta) at the upstream (red) and downstream (blue) side of the spheroid at day 0. b) Collagen fibers (cyan) and cells (magenta) at the upstream (orange) and downstream (purple) side of the spheroid at day 1. c) Position of invasion front with respect to initial spheroid surface (day 0) after 1 day and after 3 days on downstream and upstream side of 10 aggregates ($*p < 0.05$). d) Degree of alignment of the collagen fibers on downstream and upstream side of 10 aggregates at day 0 and day 1 ($^{\circ}p > 0.05$, $*p < 0.005$). Scale bars = 200 μm .

Simulation of invasion behavior. Having established that the aligned collagen fibers and specifically their orientation strongly influence invasion of the spheroids, we next asked whether the observed invasion process can be described by a model, in which we assume that cells can invade along fibers faster than compared to invasion perpendicular to fibers (Fig. 4.5). We assume a very simple model of cells distributed on a sphere the size of a

spheroid (Fig. 4.5a, Day 0). They are performing a random walk with some step size parallel and a smaller step size perpendicular to the fibers as derived from the traveled distance of the downstream and upstream front, respectively, on the first day. Fiber direction is determined and interpolated from the experimental data displayed in Fig. 4.2a. We reduce the model to include the influence of fiber orientation on cell migration and neglect cell overlap, cell-cell contacts and resulting jamming effects. Furthermore, we do not take proliferation into account, since it is expected to be very slow in spheroids in 3D-environments leading to an estimated increase in radius of about 1.2 over the entire 3 days. Nevertheless, potential effects of proliferation on the invasion behavior cannot be excluded, specifically, such that result from an increased proliferation due to influences by the matrix. The shape resulting from the simulation with the initial step size parameters did not match the shape evolution measured in the experiment very well (Fig. S4.7). The simulation data show very little asymmetry in shape and the difference between up- and downstream invasion is much smaller than in the experiment. The only parameter that fits with the experimental data to a certain extent is the axis ratio and its development over time (Fig. S4.7). To increase asymmetry and thus the difference between up- and downstream invasion, we next reduced the step size perpendicular to fiber orientation, while maintaining the step size derived from the experiment for movement parallel to fibers. Expectedly, the decrease in perpendicular step size increased the asymmetry in shape and the difference in travel distance of the invasion fronts up- and downstream (Fig. S4.7). With increased asymmetry of course, the overall b/a ratio was increased. Strikingly, the best match in spheroid shape between experiment and simulation was obtained with a perpendicular step size of 0, i.e. complete blockage of migration perpendicularly towards fibers (Fig. 4.5, S4.7). This simulation assuming complete blockage of perpendicular migration describes the experimentally obtained shapes remarkably well – including invasion towards areas with fibers tangentially oriented toward the spheroid. Also the differences in travel distance of upstream and downstream front are recapitulated with this parameter set by the model (Fig. 4.5c). Since the step size was calculated from the distance travelled during the first day at least for the movement along fibers, the numbers fit very well at that time. The distances after three days are slightly larger in the model compared to the experiment. This might be due to an overestimation of the step size based on effects of

the collective, such as jamming, which decrease with increasing amount of single cells at the front moving detached from the collective, leading to a decreased front speed. However, the differences are not large given the error bars. Overall, the model suggests an increase in travelled distance with the square root of time, which results from the diffusive character. The values measured in the experiments are in accordance with this increase, since the values on day 3 are less than a factor of 2 larger than on day 1. Analyzing the ratio of axes along and perpendicular to main flow direction (b/a) shows an interesting behavior in the simulation, which is not seen in the experiment: In the simulation, the ratio increases strongly, then it remains constant for a short time until it increases steadily again (Fig. 4.5b). This second increase is observed, when cells on the upstream front have passed the perpendicular fibers and start streaming along the fibers in main flow direction. This is as opposed to the sides along the a-axis perpendicular to flow, which face tangential fibers only and hence cells do not reach areas with fibers along this axis. Thus, the upstream front now also contributes to an increase in b/a ratio leading to the observed second increase in b/a ratio. The reason this is not found in the experimental data may be the large variance of data resulting from variability in matrix orientation and cells. Furthermore, it may originate in the assumptions of the model neglecting cell overlap, collective effects, proliferation, and remodeling of the matrix. This time interval showing a plateau of constant b/a ratio decreases, when the step size perpendicular to fibers is increased, since cells on the upstream front reached the area of fibers oriented in main flow direction more quickly.

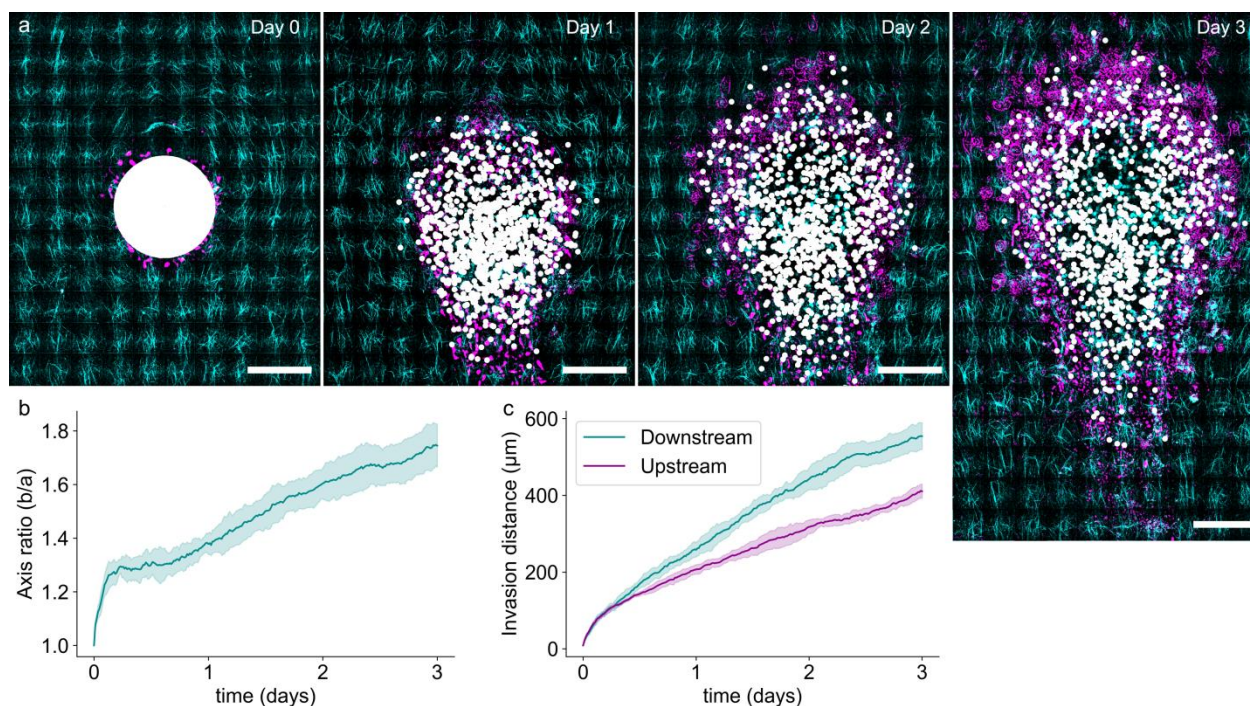


Figure 4.5: Simulation of invasion. a) Overlaid images of cell invasion in the collagen gel (cyan) during the experiment (magenta) and the simulated migration of cells (white) in a similar environment over the course of 3 days. b) Ratio of axis along main flow (b) vs. perpendicular to it (a) of the simulation over the course of 3 days (cyan; mean +/- standard deviation (n=10): light cyan). c) Position of simulated invasion front with respect to initial spheroid surface (day 0) during 3 days on downstream and upstream side of the spheroid. Scale bars = 200 μm .

4.3. Discussion

The fiber alignment with microfluidic flow during collagen polymerization that we describe here, allows for significant alignment in main flow direction. Analysis of the flow profile shows that the polymerized collagen gel preserves the flow field such that the fiber orientation mirrors the streamlines of the flow with the exception of the area around the upstream facing side of spheroids embedded in the collagen gel. The entire fiber orientation – including the upstream side of spheroids – can be described by the orientation of rods in the flow field of the applied flow. Thus, in principle, simulations of flow and of the effect of

the resulting flow field on rod orientation should allow for prediction of fiber orientations depending on the applied flow field providing a predictable platform of fiber alignment.

The fiber orientation around spheroids resulting from the microfluidic alignment allowed us to study the influence of fiber orientation – particularly of tangential versus radial orientation with respect to the spheroid. This orientation remains fairly constant over time - we do not observe strong changes in the degree of fiber orientation, which have been observed previously mainly in 2D settings or between neighboring spheroids [16], although the invasion of the entire spheroid does lead to slight, local remodeling not affecting the average degree of orientation in our experiments.

Spheroids in the aligned collagen gels invaded readily into the gels. Such invasion processes have been described as transition from a jammed state to an unjammed, fluid-like state followed by isolation of single cells in a gas-like state. In immuno-fluorescence images we see characteristics of jammed cells inside the spheroid (Fig. S4.8, red box), while they show more elongated and less adherent structures at the periphery of the spheroid resembling an unjammed state. Starting on day 1, we also observe single, isolated cells around the spheroid.

The influence of fiber alignment on invasion is very pronounced and leads to a bias in invasion along fibers oriented radially with respect to the spheroid. In a first approximation, the resulting shape of the invading spheroid and its evolution over time was described by a model assuming Brownian diffusion with larger step size along fibers compared to that perpendicular to fibers. The resulting simulations describe the shape evolution of the spheroid obtained in the experiments remarkably well. Strikingly, parameter sets with no invasion perpendicular to the fiber orientation fit best with the experimental data. Thus, the origin of the invasion bias toward radially oriented fibers may indeed be a strong bias towards faster invasion along radially oriented fibers compared to tangentially oriented fibers. Further analysis and refinement of the model may show the influence of jamming, slippage, proliferation and other effects, which may provide more insight into the influence of fiber orientation on invasion. This could also include modeling of the fiber orientation as a distribution with some finite width. Moreover, it may e.g.

decipher whether the effect of fiber orientation is mainly due to contact guidance or influenced by collective effects as has been described for unidirectional invasion [18].

We observe some single cells, which are elongated along the fibers, however many invading single cells as well as the fronts of the collective do not show a clear cell orientation. Thus, the reason for the bias in invasion along radially oriented fibers may partially be based in polarization, but other factors most likely contribute to the effect, too. One such factor might for example be the enhanced force propagation resulting from contractions along radially oriented fibers compared to tangential fibers due to the non-linear stress-strain relation of collagen [19, 20]. As for the molecular mechanisms underlying the invasion, nuclear YAP (Yes-associated protein) has been shown to be able to trigger invasion [21, 22] and YAP's translocation into the nucleus acts as mechanosensor [23]. In our case, however, it is mostly cytosolic and thus not active at the measured time of 3 days after embedding the spheroid in the gel (Fig. S4.8). Hence the underlying mechanisms of the biased invasion towards fibers oriented radially with respect to the spheroid remain to be investigated. The microfluidic platform we presented here, offers a well-defined system for such investigations. Understanding directional bias of invasion and its origins will not only be useful in cancer research, but also in many other fields such as tissue engineering, developmental biology and wound healing.

4.4. Experimental part

Cell culture and spheroid formation

HeLa cells were cultivated in liquid Dulbecco's modified Eagle's medium (DMEM, Gibco), supplemented with 10% fetal bovine serum (FBS, Gibco) and 1% Penicillin Streptomycin (Gibco), at 37 °C in a 5% CO₂ atmosphere.

For HeLa cell spheroid formation, 500 cells were seeded in a 96-well plate with ultra-low adhesion (Corning) and incubated at 37°C and 5% CO₂ for 48 h until the spheroid reached the desired size. At a diameter of 250-350 μm, the spheroids were transferred to a collagen gel mixture.

3D Antibody Staining

The primary and secondary antibodies used were YAP1 polyclonal rabbit antibody (PA1-46189; Thermo Fisher Scientific) and Donkey anti-Rabbit IgG (H+L) Highly Cross-Adsorbed Secondary Antibody, Alexa Fluor 546 (A10040; Thermo Fisher Scientific).

HeLa spheroids embedded into collagen were fixed with 4% PFA for 40 minutes and washed with PBS twice for 20 minutes. The cells were permeabilized for 20 minutes with 0.5% Triton X-100 in PBS and subsequently washed with PBS for 30 minutes. The cells were blocked with 1% BSA in PBS overnight. Primary antibodies were diluted 1:100 with 1% BSA in PBS and cells were incubated for 72 hours. Prior to incubation with secondary antibodies (1:200 in 1% BSA), the cells were washed twice with PBS for 30 minutes. The cells were incubated with secondary antibodies for 48 hours. Afterwards, the cells were washed with PBS for 30 minutes and Hoechst 33342 (0.5 µg/ml) for 40 minutes. Prior to imaging, the cells were washed again with PBS for 30 minutes. Finally, the PBS was renewed and kept in the reservoirs during confocal microscopy.

3D collagen matrices

Collagen gels were all prepared with the same compounds, which were kept on ice (except for the HeLa cells). Rat tail collagen I stock solution (Corning) was mixed with 1 µg ATTO-633 (NHS-Ester, ATTO-TEC) per 1.37 mg collagen to stain and later visualize the 3D network of the gels. Then, they were neutralized with Sodium hydroxide (1 N, Fluka) and diluted with Dulbecco's phosphate-buffered saline (DPBS(1x), Gibco) until the desired collagen concentration (3.32 mg/ml; final: 1.85 mg/ml) was reached. Finally, three HeLa cell aggregates, diluted in DMEM-Medium (45% of the final volume), were added.

The gel mixture was immediately filled in a µ-Slide VI 0.4 ibiTreat (Ibidi), which was connected to a LA-120 syringe pump (Landgraf). The mixture was sucked with 90.2 µl/min into the channel of the slide, until an aggregate reached the channel. Then the draw speed of the syringe pump was reduced to 0.2 µl/min during polymerization on ice. After 30 minutes the slide was handled at room temperature and 0.1 µl/min pump draw speed. After 15

minutes the gel was transferred to 37°C, without the syringe pump, to finish the gelation process. After a successful gelation all gels were overlaid with DMEM, to prevent them from drying out.

Analysis of the microfluidic chamber

The flow field in the channel was analyzed experimentally with digital particle velocimetry (DPIV) as well as numerically with finite element method (FEM) simulation. For the experimental characterization the same protocol as described in the part “3D collagen matrices” was used. In addition a latex microsphere suspension (Polybead Carboxylate Microspheres 3.00µm, Polysciences Inc., Warrington, PA, USA) was added (1 % of the final volume) to the HeLa cell aggregates. For the analysis, we used light microscopy in combination with a CCD camera (FASTCAM 1024PCI, Photron, Ottobrunn, Germany). The movement of the particles was recorded with a frame rate of 1 fps at a constant flow rate of 0.2 µl/min. A MATLAB (R2017b, The MathWorks Inc., Natick, MA, USA) script based on the open source PIVlab (version 2.37) toolkit was employed to extract the two-dimensional velocity profile [24, 25]. FEM simulation was done with the commercially available software COMSOL Multiphysics (5.6, Comsol Inc., Burlington, MA, USA). The Navier-Stokes equation together with the continuity equation is solved for a stationary 2D model of the channel in the laminar flow interface of the Computational Fluid Dynamics (CFD) module. The width and the length of the channel is 3.8 mm and 17 mm respectively. The height of the channel (0.4 mm) was taken into account by applying a shallow channel approximation. At the inlet of the channel a laminar inflow boundary condition with a flow rate of 0.2 µl/min and at the outlet a static pressure condition was applied. The size and location of the HeLa cell aggregate (diameter $d = 208 \mu\text{m}$) in the channel is taken from the experiment. A physics controlled mesh was used with element size ‘normal’. By coupling the CFD module together with the Solid Mechanics module via a Fluid Structure Interaction (FSI) we also simulated the time dependent trajectory of a fiber in the flow field. For the CFD module the same parameters were used as in the stationary study. The fiber is assumed to be rigid and has a length of 47.5 µm and a width of 5 µm. A physics controlled moving mesh was used with element size ‘normal’.

Spinning disk confocal microscopy

Confocal microscopy for live-cell imaging was performed on a setup based on the Zeiss Cell Observer SD utilizing a Yokogawa spinning disk unit CSU-X1. The system was equipped with a 1.40 NA 63x Plan apochromat oil immersion objective from Zeiss. The setup was heated to 37 °C and a CO₂ source was provided to keep the atmosphere at 5% CO₂ during the measurements. The resulting images were processed with the Zen software by Zeiss. Cell spheroids were imaged in brightfield mode with a tungsten-halogen lamp with 682.0 μW and 200 ms exposure time. For fluorescence images, Hoechst 33342 was excited with a 405 nm laser at 11.2 μW intensity for 200 ms and Alexa Fluor 546 of the secondary YAP antibody with a 561 nm laser at 70.7 μW intensity for 1000 ms. Images with ATTO-633 dye were taken with a 639 nm laser at 5.5 μW intensity and 200 ms exposure time. Each image consisted of 120 to 160 pictures, depending on the spread of the spheroid over time, and has an 11 frame z-stack with a 1.5 μm distance between z-planes. In the excitation path a quad-edge dichroic beamsplitter (FF410 /504/582/669-Di01-25x36, Semrock) was used. Band-pass filters 525/50 and 690/60 (both Semrock) were used in the detection path. Separate images for each fluorescence channel were acquired using two separate electron multiplier charge coupled devices (EMCCD) cameras (Photometrics Evolve™).

Image analysis

Analysis of fiber orientation was performed with ImageJ [26, 27]. Migration distances and aggregate axes were analyzed with Imaris (v 8.2.0, Bitplane, AG Zurich, Switzerland) and further processed with Microsoft Excel (version 2010). Statistics and data presentation was done with OriginPro (Version 8.0891/9.0.0, OriginLab Corporation, Northampton, MA, USA). Normality was tested with a Shapiro-Wilk test and statistical significance with the non-parametric Kruskal-Wallis test. Boxplots show mean (square), the box consisting of median, lower and upper quartile (25th and 75th percentile), whiskers (5th and 95th percentile), and outliers (marked x). The aggregate axes were defined by the distance between the average value of the 20 cells furthest away from the aggregate's center of mass

in the respective direction. The a axis is the difference between biggest and smallest x-value and the b axis the biggest and smallest y-value found for cell positions found by Imaris. The axis ratio b/a of these axes shows the asymmetry of the cell aggregate. At a ratio of 1 the aggregate is a sphere, below 1 it spreads mainly along the a axis and above 1 along the b axis. The relative axis ratio in figure 3c is the axis ratio of the aggregate at day 1 divided by the ratio of day 0, describing the change in asymmetry with respect to day 0. The degree of alignment was introduced to quantify the orientation of the collagen gel along the main flow direction (i.e. along b axis with respect to the spheroid). Orientation angles of all fibers were determined. Fibers between 68° and 112° ($90^\circ \pm 22^\circ$) are considered aligned with the main flow, which has an orientation of 90° . The degree of alignment was calculated as the percentage of aligned fibers of the analyzed gel divided by the percentage of aligned fibers calculated for a gel with uniform fiber distribution (25.56%). Thus, it measures the ratio of fibers oriented in main flow direction in the analyzed gel relative to a non-oriented gel. The invasion distance was determined by the difference of the average position of the 10 cells, which travelled furthest into the collagen gel at day 0 and day 1 or day 3 respectively. The brightfield images of cell aggregates presented together with collagen fibers were processed with ImageJ [26, 27], for better visibility of both channels in one picture. A set of gaussian blur ($\sigma=1$), subtract background and despeckle was applied three times, with a decreasing value for the rolling ball radius used in each cycle (rolling = 200, 100 and 50). Unprocessed pictures of all used aggregates can be found in the SI.

Simulation of invasion

In order to get a better understanding of the invasion of HeLa cell aggregates after collagen gel polymerization we introduced a numerical model, which is based on a simple 2D random walk algorithm. For the simulations we used the Python programming language (Python 3.8.3, Python Software Foundation). In our model we make two assumptions. First, we assume that the invasion is a diffusion-like process, which we model by a random walk. Second we assume that the step size is location- and direction-dependent. This dependency is given by the fiber orientation, which can be extracted from the experiment. Therefore we divided the field of view into boxes ($d = 103 \mu\text{m}$) and calculate the mean fiber orientation

for each box. At each time step there are four ways with the same probability how a single cell can move: Parallel or perpendicular to the fiber and for both options the two possible directions. A step parallel to the fiber orientation results in a shift of the location of:

$$\Delta x = \pm k_p \cos(\alpha) \text{ and } \Delta y = \pm k_p \sin(\alpha),$$

where k_p is the step size parallel to the fiber orientation and α is the fiber orientation at the location. The positive and negative sign indicates in which direction with respect to the fiber orientation the step is made. A step perpendicular to the fiber orientation results in a shift of the location of:

$$\Delta x = \pm k_v \cos(\alpha + 90^\circ) \text{ and } \Delta y = \pm k_v \sin(\alpha + 90^\circ),$$

where k_v is the step size perpendicular to the fiber orientation. We estimate the step size k_p and k_v from the data of the experiment:

$$k_p = r_p / \sqrt{N} \text{ and } k_v = r_v / \sqrt{N},$$

where r_p is the distance the cells travelled within one day downstream where most of the fibers are oriented parallel to the invasion, r_v is the distance the cells travelled within one day upstream where most of the fibers are oriented perpendicular to the invasion and N is the number of time steps.

4.5. References

1. Oswald L, Grosser S, Smith DM, Käs JA. Jamming transitions in cancer. *J Phys D Appl Phys.* 2017; 50(48):483001.
2. Palamidessi A, Malinverno C, Frittoli E, Corallino S, Barbieri E, Sigismund S, et al. Unjamming overcomes kinetic and proliferation arrest in terminally differentiated cells and promotes collective motility of carcinoma. *Nat Mater.* 2019; 18(11):1252–63.

4.5. References

3. Iлина O, Gritsenko PG, Syga S, Lippoldt J, La Porta CAM, Chepizhko O, et al. Cell-cell adhesion and 3D matrix confinement determine jamming transitions in breast cancer invasion. *Nature Cell Biology*. 2020; 22(9):1103–15.
4. Geiger F, Rüdiger D, Zahler S, Engelke H. Fiber stiffness, pore size and adhesion control migratory phenotype of MDA-MB-231 cells in collagen gels. *Plos One*. 2019; 14(11):e0225215.
5. Charras G, Sahai E. Physical influences of the extracellular environment on cell migration. *Nature Reviews: Molecular Cell Biology*. 2014; 15(12):813–24.
6. Dietrich M, Le Roy H, Bruckner DB, Engelke H, Zantl R, Radler JO, et al. Guiding 3D cell migration in deformed synthetic hydrogel microstructures. *Soft Matter*. 2018; 14(15):2816–26.
7. Harley BA, Kim HD, Zaman MH, Yannas IV, Lauffenburger DA, Gibson LJ. Microarchitecture of three-dimensional scaffolds influences cell migration behavior via junction interactions. *Biophysical Journal*. 2008; 95(8):4013–24.
8. Wu P-H, Gilkes DM, Wirtz D. The Biophysics of 3D Cell Migration. *Annual Review of Biophysics*. 2018; 47(1):549–67.
9. Caswell PT, Zech T. Actin-Based Cell Protrusion in a 3D Matrix. *Trends in Cell Biology*. 2018; 28(10):823–34.
10. Riching KM, Cox BL, Salick MR, Pehlke C, Riching AS, Ponik SM, et al. 3D collagen alignment limits protrusions to enhance breast cancer cell persistence. *Biophysical Journal*. 2014; 107(11):2546–58.
11. Han W, Chen S, Yuan W, Fan Q, Tian J, Wang X, et al. Oriented collagen fibers direct tumor cell intravasation. *Proc Natl Acad Sci U S A*. 2016; 113(40):11208–13.
12. Rubenstein BM, Kaufman LJ. The role of extracellular matrix in glioma invasion: a cellular Potts model approach. *Biophysical Journal*. 2008; 95(12):5661–80.
13. Carey SP, Goldblatt ZE, Martin KE, Romero B, Williams RM, Reinhart-King CA. Local extracellular matrix alignment directs cellular protrusion dynamics and migration through Rac1 and FAK. *Integr Biol (Camb)*. 2016; 8(8):821–35.

14. Ahmadzadeh H, Webster MR, Behera R, Jimenez Valencia AM, Wirtz D, Weeraratna AT, et al. Modeling the two-way feedback between contractility and matrix realignment reveals a nonlinear mode of cancer cell invasion. *Proc Natl Acad Sci U S A*. 2017; 114(9):E1617-e26.
15. Provenzano PP, Eliceiri KW, Campbell JM, Inman DR, White JG, Keely PJ. Collagen reorganization at the tumor-stromal interface facilitates local invasion. *BMC Med*. 2006; 4(1):38.
16. Shi Q, Ghosh RP, Engelke H, Rycroft CH, Cassereau L, Sethian JA, et al. Rapid disorganization of mechanically interacting systems of mammary acini. *Proc Natl Acad Sci U S A*. 2014; 111(2):658–63.
17. Lee P, Lin R, Moon J, Lee LP. Microfluidic alignment of collagen fibers for in vitro cell culture. *Biomedical Microdevices*. 2006; 8(1):35–41.
18. Ray A, Morford RK, Ghaderi N, Odde DJ, Provenzano PP. Dynamics of 3D carcinoma cell invasion into aligned collagen. *Integr Biol (Camb)*. 2018; 10(2):100–12.
19. Licup AJ, Münster S, Sharma A, Sheinman M, Jawerth LM, Fabry B, et al. Stress controls the mechanics of collagen networks. *Proceedings of the National Academy of Sciences*. 2015; 112(31):9573–8.
20. Kopanska KS, Alcheikh Y, Staneva R, Vignjevic D, Betz T. Tensile Forces Originating from Cancer Spheroids Facilitate Tumor Invasion. *Plos One*. 2016; 11(6):e0156442.
21. Park J, Kim DH, Shah SR, Kim HN, Kshitiz, Kim P, et al. Switch-like enhancement of epithelial-mesenchymal transition by YAP through feedback regulation of WT1 and Rho-family GTPases. *Nat Commun*. 2019; 10(1):2797.
22. Illes B, Fuchs A, Gegenfurtner F, Ploetz E, Zahler S, Vollmar AM, et al. Spatio-selective activation of nuclear translocation of YAP with light directs invasion of cancer cell spheroids. *ISCIENCE*. 2021.
23. Dupont S, Morsut L, Aragona M, Enzo E, Giulitti S, Cordenonsi M, et al. Role of YAP/TAZ in mechanotransduction. *Nature*. 2011; 474(7350):179–83.

4.5. References

24. Thielicke W. The Flapping Flight of Birds: Analysis and Application. Phd thesis, University of Groningen. 2014.
25. Thielicke W, Stamhuis EJ. PIVlab – Towards User-friendly, Affordable and Accurate Digital Particle Image Velocimetry in MATLAB. *Journal of Open Research Software*. 2014; 2.
26. Schindelin J, Arganda-Carreras I, Frise E, Kaynig V, Longair M, Pietzsch T, et al. Fiji: an open-source platform for biological-image analysis. *Nature Methods*. 2012; 9(7):676–82.
27. Schneider CA, Rasband WS, Eliceiri KW. NIH Image to ImageJ: 25 years of image analysis. *Nature Methods*. 2012; 9(7):671–5.

4.6. Appendix

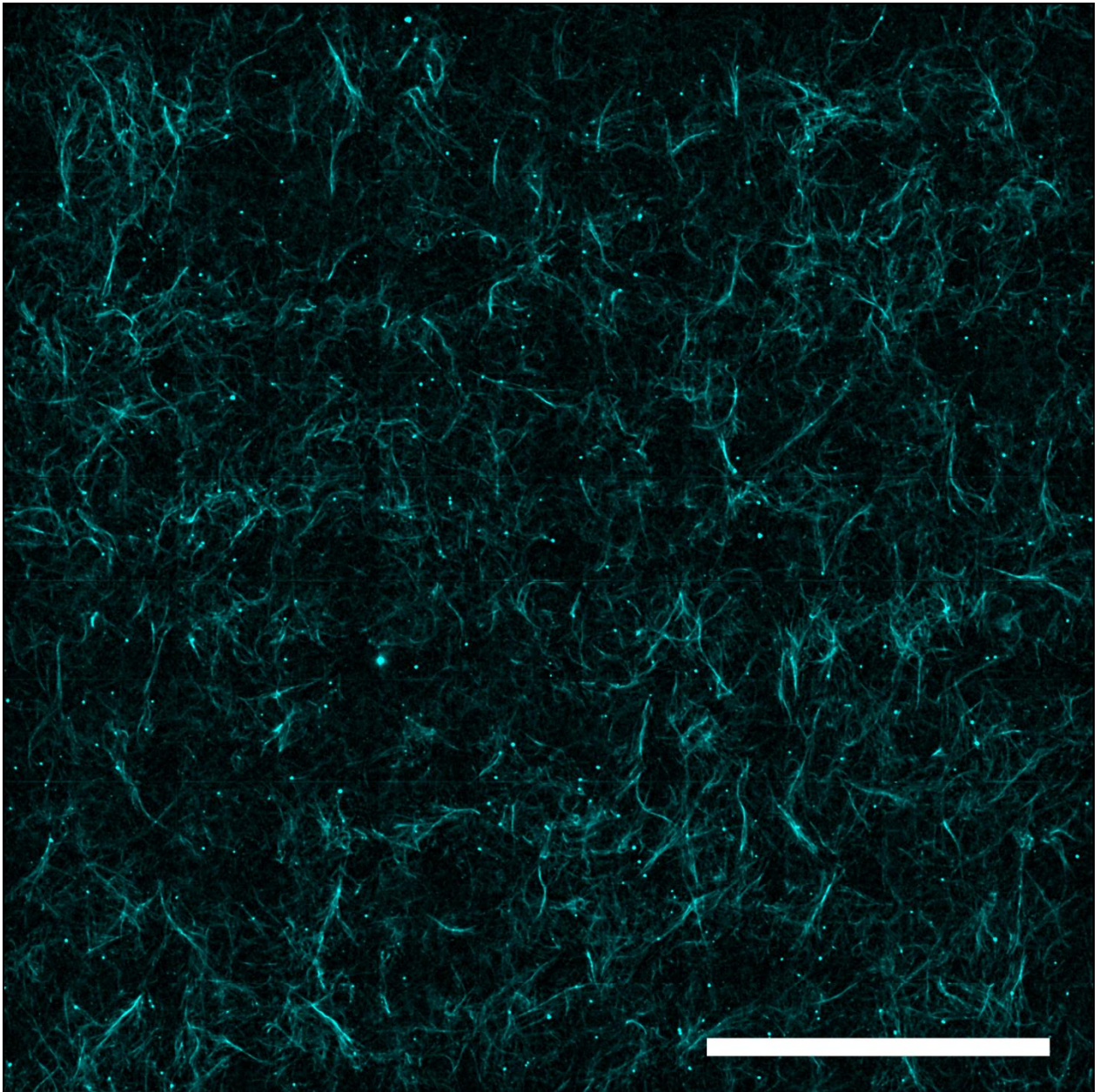


Figure S4.1: Non-aligned collagen fibers synthesized in a well without microfluidic flow. Scale bar = 200 μm .

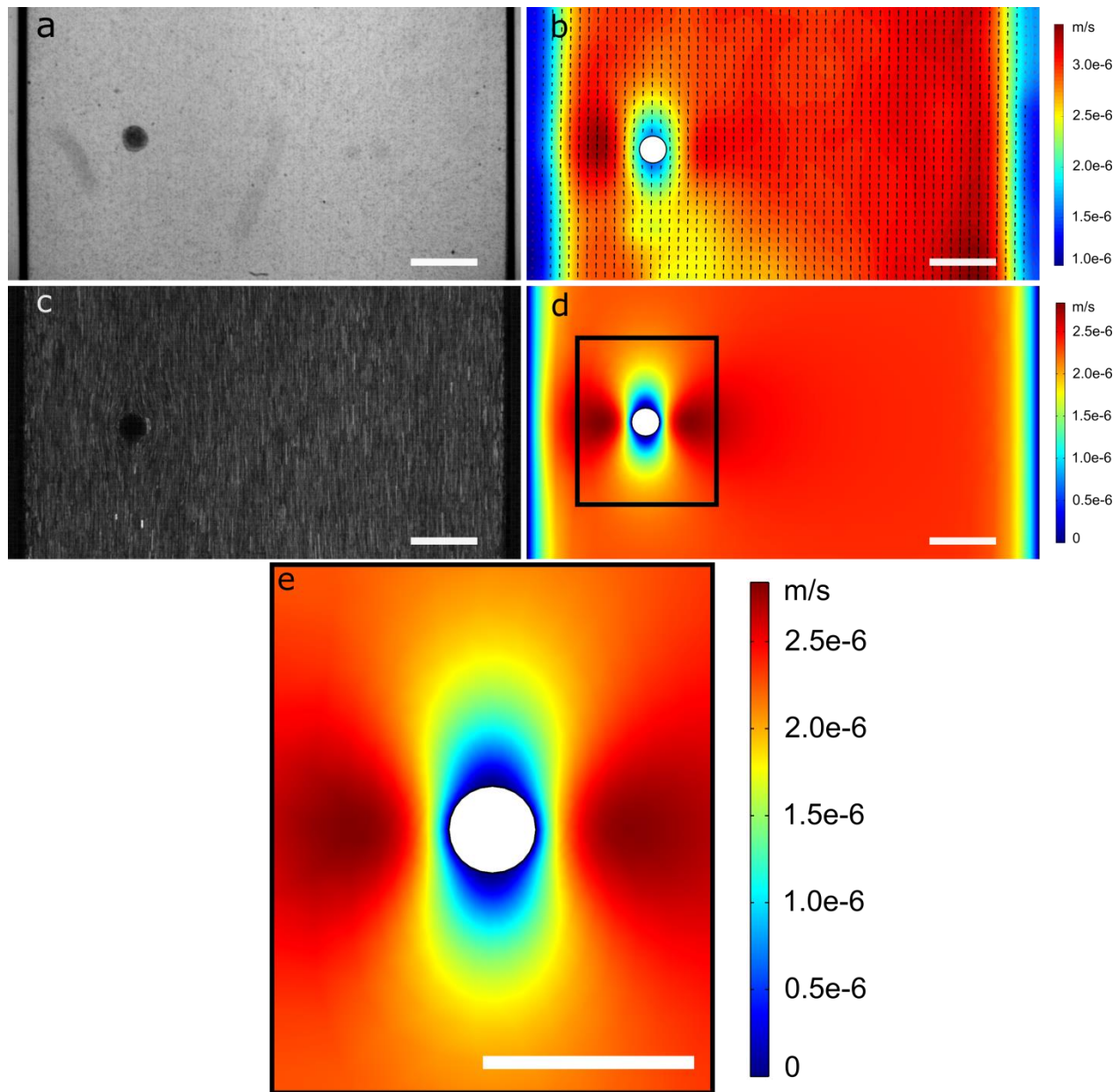


Figure S4.2: Characterization of the whole microfluidic channel with 4x magnification. a) Brightfield image of a cell aggregate embedded in a collagen bead mixture without applied flow. b) Calculated velocity magnitude with flow vectors of the beads. c) Flow trajectory of beads around a cell aggregate embedded in collagen during polymerization. d) Simulated velocity field of the collagen mixture around the cell aggregate in the microfluidic channel. e) Zoom in on the immediate surrounding of the cell aggregate in the simulation. Scale bars = 500 μm .

4. Directed invasion of cancer cell spheroids in microfluidic flow oriented 3D collagen gels

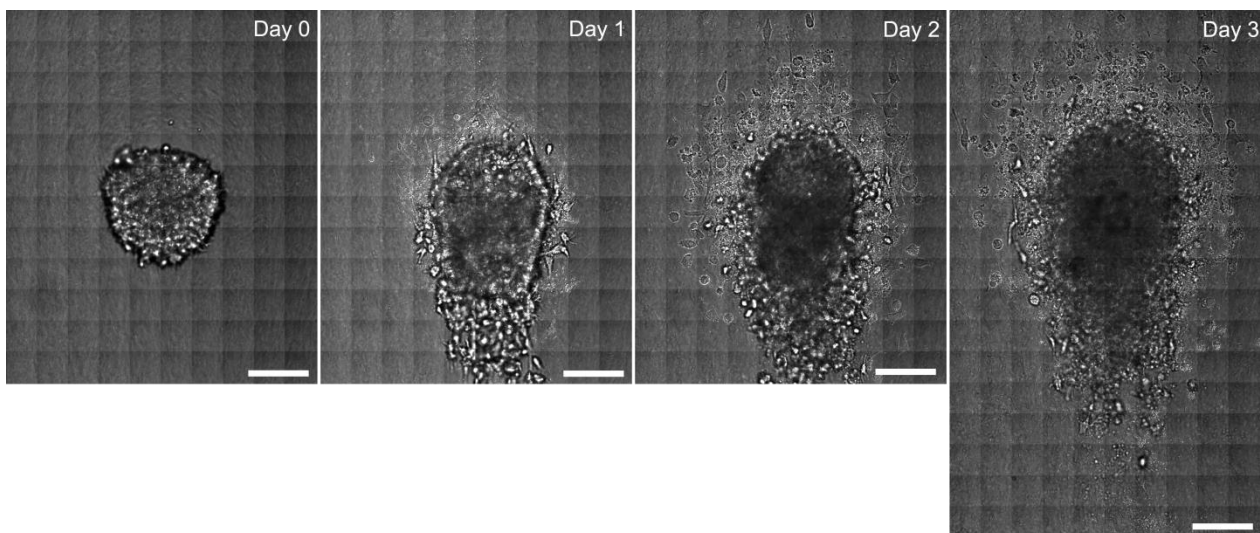


Figure S4.3: Original brightfield (BF) images of the spheroid displayed in Fig. 2 - 4.

Scale bars = 200 μm .

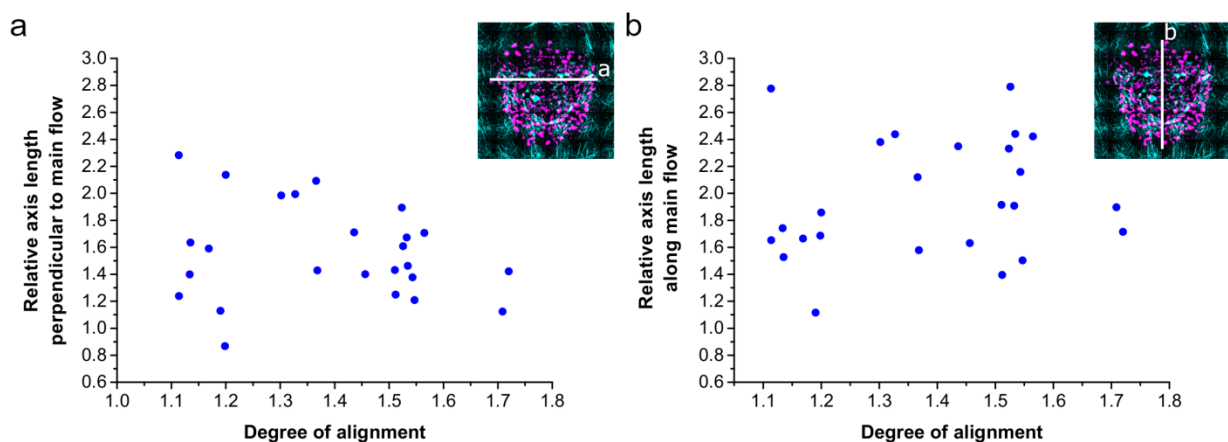


Figure S4.4: Spheroid axis increase versus degree of matrix alignment. a) Axis length of the spheroids on first day relative to day 0 perpendicular to the applied main flow direction. b) Axis length of the spheroids on first day relative to day 0 along the applied main flow direction.

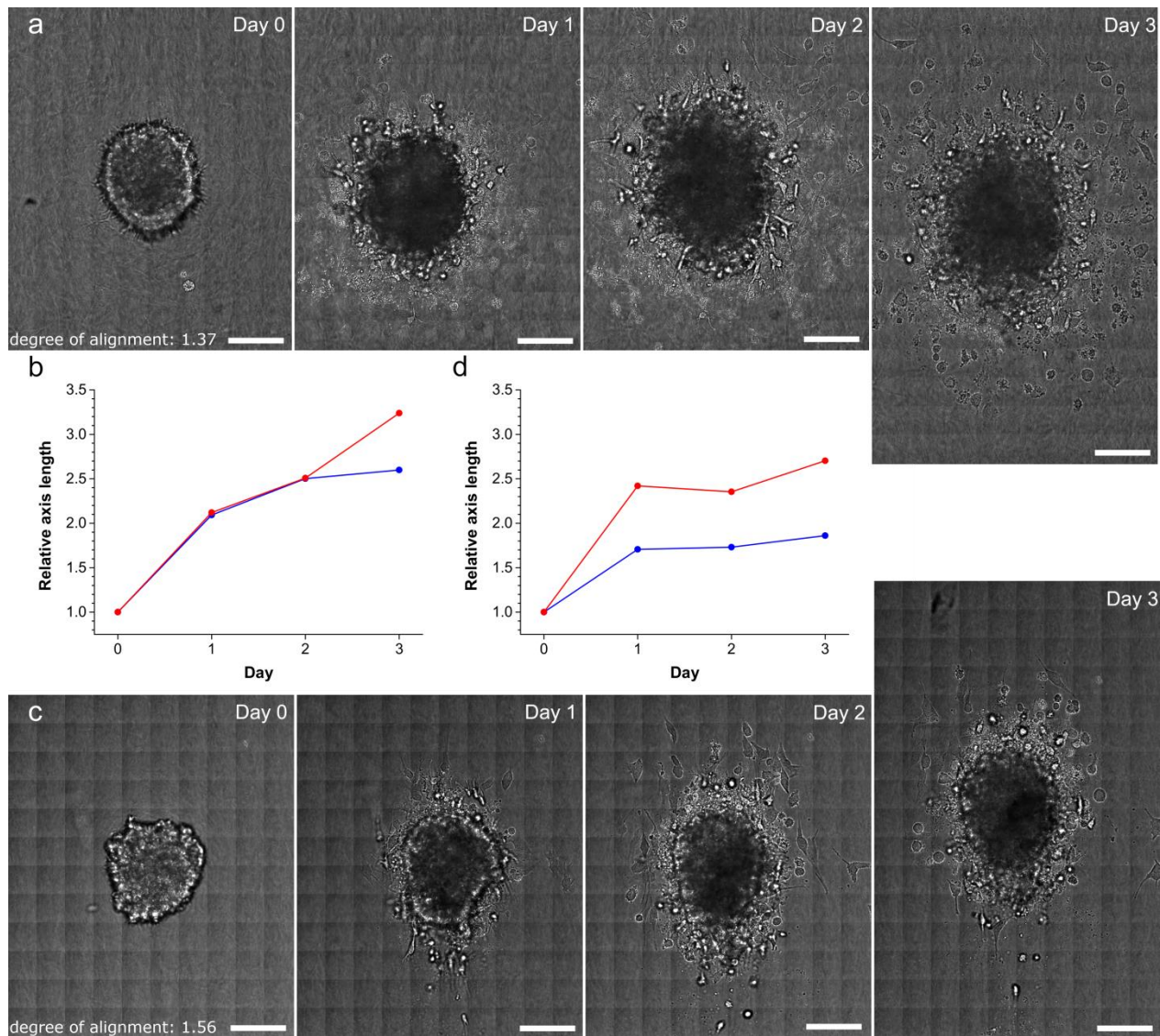


Figure S4.5: Invasion of spheroids in matrices of different degrees of alignment. a) Spheroid in matrix of low degree of alignment (1.37) spreading almost evenly in all directions. b) Relative axis length of the spheroid shown in a perpendicular (blue) and parallel (red) to the direction of the main flow (and consequently the main fiber orientation) over the course of 3 days. c) Spheroid in matrix of high degree of alignment (1.56) is spreading stronger in direction of main fiber alignment. d) Relative axis length of the spheroid shown in c perpendicular (blue) and parallel (red) to the direction of the main flow (and consequently the main fiber orientation) over the course of 3 days. Scale bars = 200 μm .

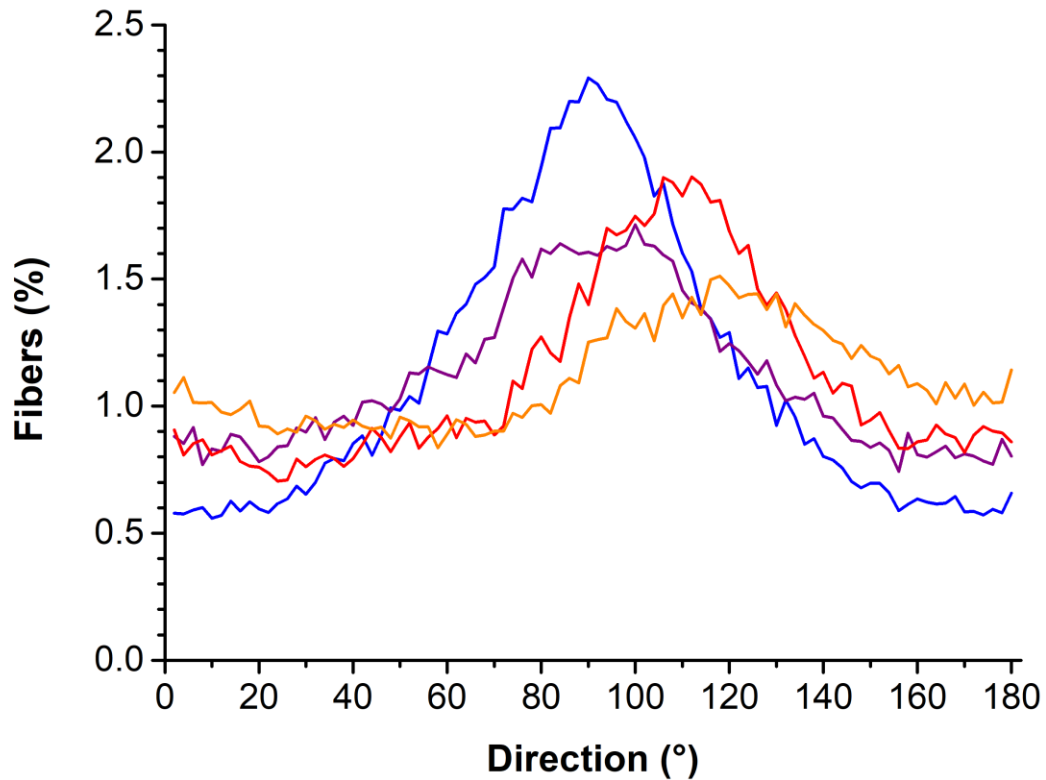


Figure S4.6: Orientation distribution of the collagen fibers on up- and downstream front of the spheroid. Orientation distribution of collagen fibers in the areas (as marked in Fig. 4.4) around the upstream front of the spheroid at day 0 (red) and day 1 (orange) and around the downstream front at day 0 (blue) and day 1 (purple).

4.6. Appendix

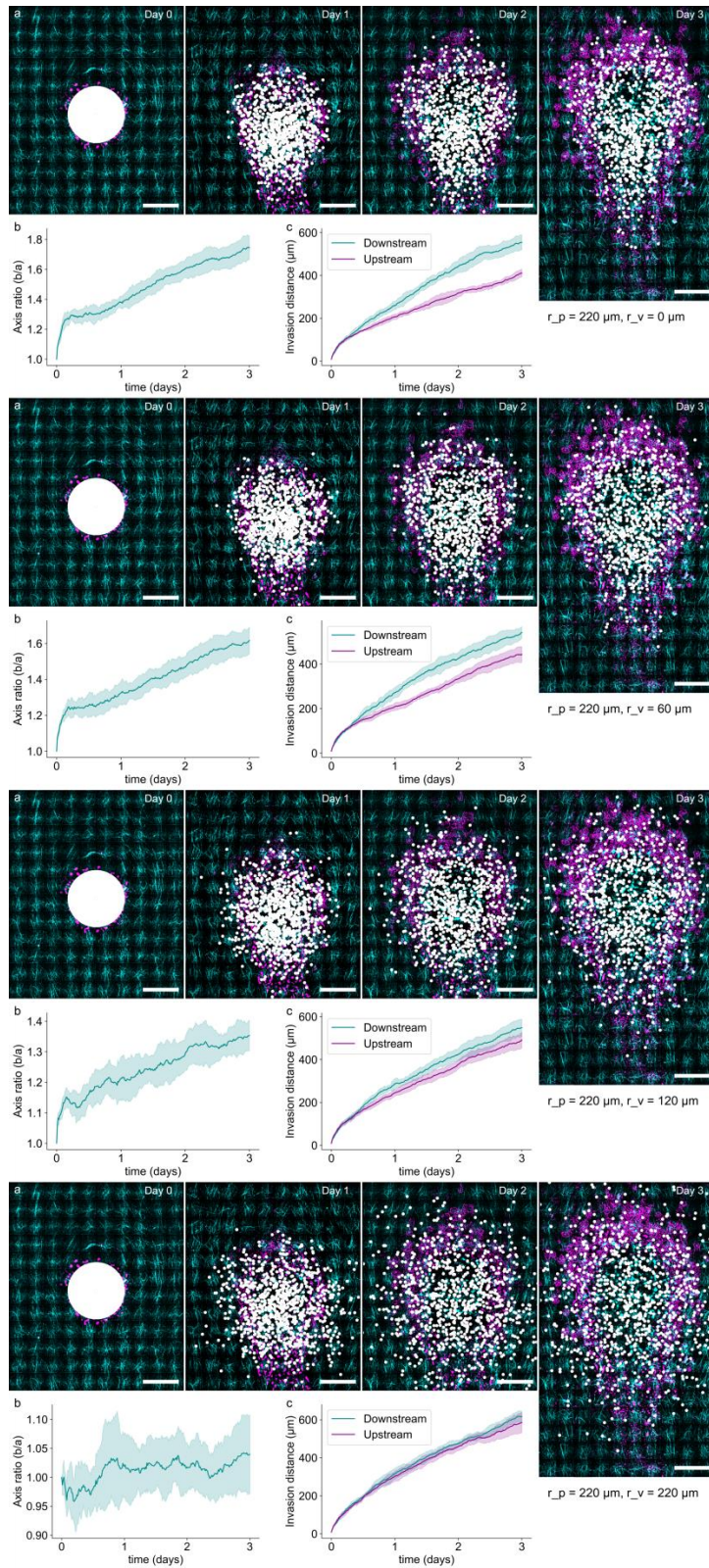


Figure S4.7: Simulation sweep with step sizes perpendicular to fiber orientation (r_v) per day of 0, 60, 120 and 220 μm respectively. a) Overlaid images of cell invasion in the

4. Directed invasion of cancer cell spheroids in microfluidic flow oriented 3D collagen gels

collagen gel (cyan) during the experiment (magenta) and the simulated migration of cells (white) in a similar environment over the course of 3 days. Parallel step size (r_p) = 220 b) Ratio of axis along main flow (b) vs. perpendicular to it (a) of the simulation over the course of 3 days (cyan; mean \pm standard deviation ($n=10$); light cyan). c) Position of simulated invasion front with respect to initial spheroid surface (day 0) during 3 days on downstream and upstream side of the spheroid. Scale bars = 200 μm .

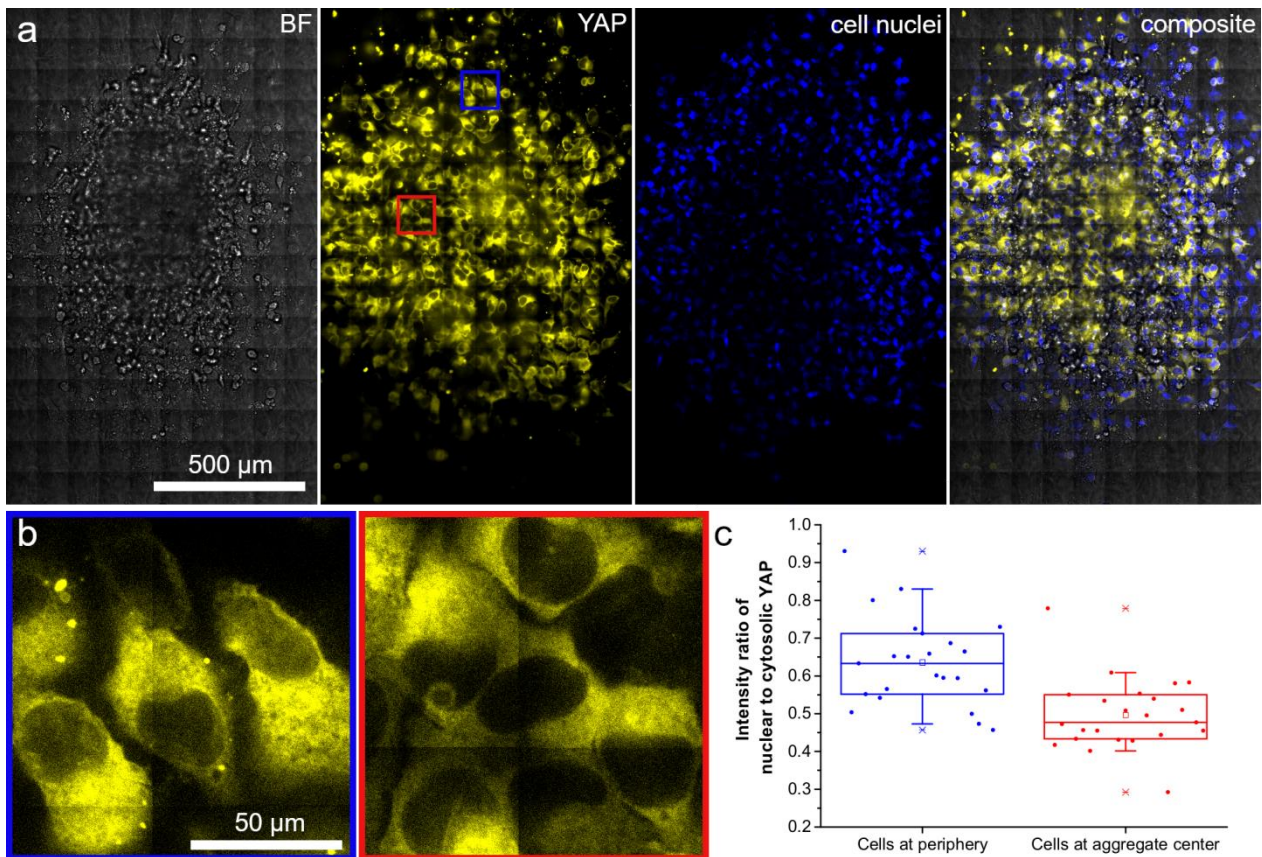


Figure S4.8: Immunostaining of invading spheroid. a) Spheroid fixed after 3 days in an aligned collagen gel in a microfluidic channel. The images show brightfield (BF), YAP immuno-staining (YAP, yellow), the nuclei stained with Hoechst 33342 (cell nuclei, blue), and a composite of YAP and Hoechst. b) zoom-in of YAP stained in cells at the spheroid periphery (blue box) and in the center of the spheroid (red box). c) Ratio of YAP intensity in the cell nuclei and cytosol for cells at the periphery (blue) and cells at the aggregate center (red); $p < 10^{-4}$.

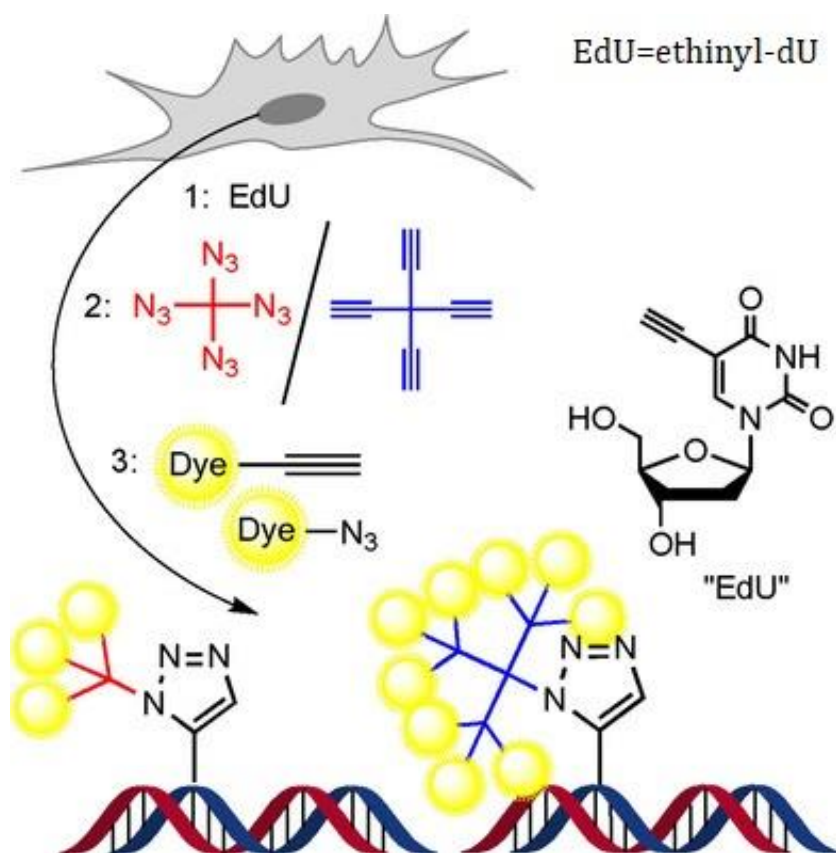
5. Dendrimer-based signal amplification of click-labelled DNA in situ

This chapter is based on the following publication:

Raddaoui N, Stazzoni S, Möckl L, Viverge B, Geiger F, Engelke H, Bräuchle C, Carell T. Dendrimer-Based Signal Amplification of Click-Labelled DNA in Situ. *ChemBioChem*. 2017; 18(17): 1716–1720.

Abstract

Finding a needle in a haystack: A new method to detect proliferating cells in situ by using multiple consecutive click reactions with dendrimeric molecules and clickable dyes is presented. These assays have outstanding sensitivities; signal intensities and signal-to-noise ratios are far better than those obtained by techniques that are currently available.



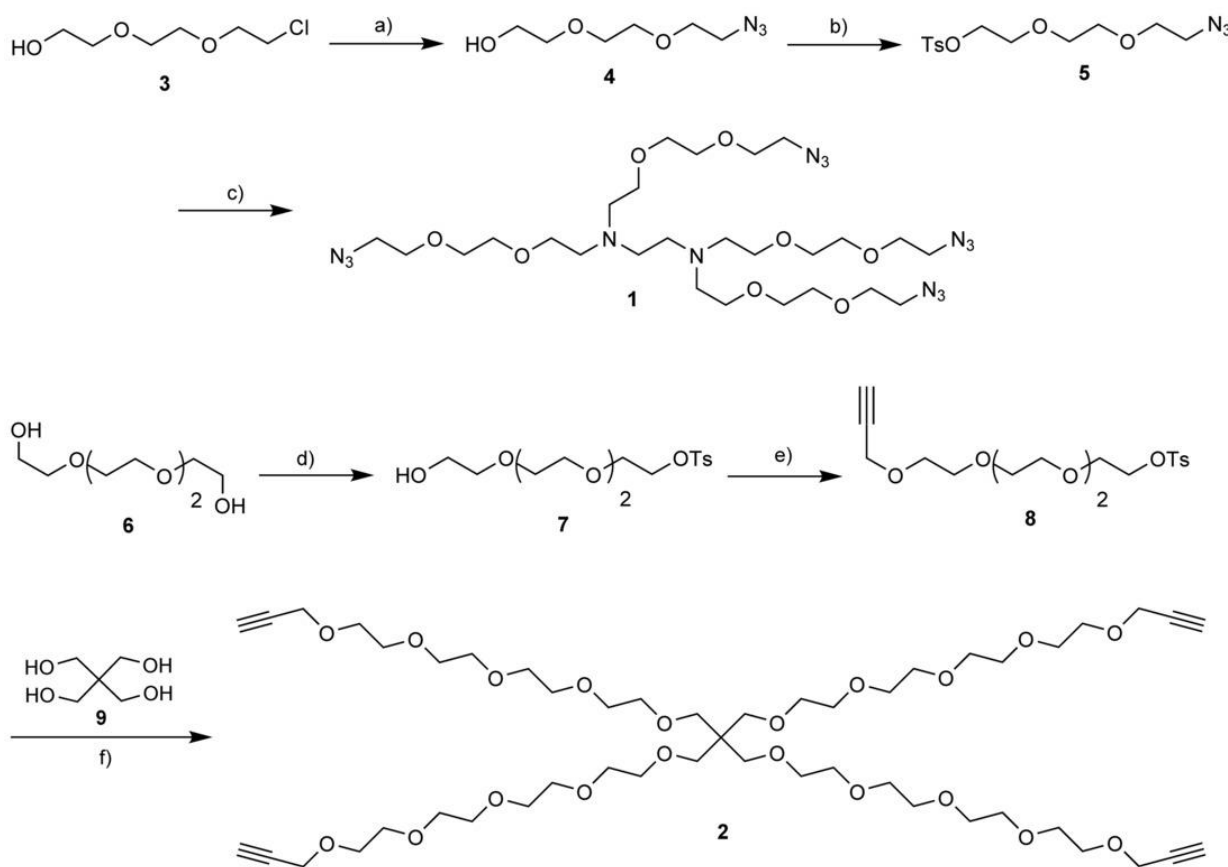
The *in vivo* incorporation of alkyne-modified bases into the genome of cells is today the basis for the efficient detection of cell proliferation. Cells are grown in the presence of ethynyl-dU (EdU), fixed and permeabilised. The incorporated alkynes are then efficiently detected by using azide-containing fluorophores and the CuI-catalysed alkyne–azide click reaction. For a world in which constant improvement in the sensitivity of a given method is driving diagnostic advancement, we developed azide- and alkyne-modified dendrimers that allow the establishment of sandwich-type detection assays that show significantly improved signal intensities and signal-to-noise ratios far beyond that which is currently possible.

5.1. Introduction

The proliferation rate of cells is a key parameter that in many contexts requires precise determination [1-8]. Cell-proliferation assays routinely help, for example, to evaluate the toxicity of compounds in the framework of the development of new pharmaceuticals [9-11]. Also, in cancer diagnostics, it is required to measure the proliferation of cells with high precision [12, 13]. In this field in particular, the highest sensitivity possible is desired to detect, at best, even single cancer cells in a patient sample. Today, the most precise way to measure cell proliferation is to culture the cells in the presence of C5-ethynyl-dU (EdU), which is incorporated into the genome of proliferating cells as a typical antimetabolite [14-16]. The amount of incorporated EdU is subsequently measured by treating the alkynes within the DNA with azido-modified fluorescent dyes by using the Cu^I-catalysed alkyne–azide click reaction and by detecting with fluorescent microscopy [17-19]. These reactions proceed on DNA with extreme efficiency, likely because Cu^I is loosely pre-coordinated to the electron-rich centres at the nucleobases [19]. This technology is used in established commercially available kits (e.g., EdU-Click kit from baseclick and Click-iT from Thermo Fisher). However, in all of the available methods, the sensitivity is limited by the number of alkynes that is incorporated during the culturing phase of the experiment in the presence of EdU (one alkyne). This creates the problem that slowly proliferating, but still carcinogenic, cells often escape detection [20].

5.2. Results and discussion

We report herein a sandwich-type approach with alkyne- and azide-containing dendrimers **1** and **2** (scheme 1) that allows significant chemical-signal amplification. The method was shown to provide unprecedented detection sensitivities for proliferating cells. The synthesis of needed amplifying tetraazide/alkyne molecules **1** and **2** is depicted in scheme 1 (see also figure S5.1 and S5.2 in the Supporting Information). In both cases, the principle design idea was to stay as close as possible to poly(ethylene glycol)-based structures, because of the needed high solubility in water. The starting point towards **1** was ethylene glycol derivative **3**, which we first converted into azide **4**. The hydroxy group was subsequently tosylated by using 4-toluenesulfonyl chloride (TsCl) to give **5** to enable the fourfold substitution reaction with ethylenediamine ultimately to give desired tetraazide compound **1**.



Scheme 5.1: Synthesis of ethylene glycol based tetraazide **1** and tetraalkyne **2** needed for the study. Reagents and conditions: a) NaN₃, DMF, 90 °C, overnight, 96%; b) TsCl, Et₃N,

CH₂Cl₂, overnight, 90%; c) ethylenediamine, **5**, KOH, LiBr, DMF, 60 °C, overnight, 63%; d) TsCl, Et₃N, THF, RT, overnight, 92%; e) propargyl bromide, NaH, THF, 0 °C to RT, 82%; f) **8**, K₂CO₃, acetone, 80 °C, overnight, 31%.

The synthesis of tetraalkyne **2** started with ethylene glycol derivative **6**, which was monotosylated in excellent yield to provide **7**. Reaction with propargyl bromide furnished compound **8**, which was used for a fourfold substitution reaction with pentaerythritol (**9**) to give dendrimer **2**. Both compounds **1** and **2** were subsequently purified by flash column chromatography.

In a first approach to amplify the cell-proliferation signal, we used poly(ethylene glycol)-based tetraazide molecule **1** (figures 5.1A and S5.3). For the experiments, we grew HeLa cells in μ -slides in the presence of 10 μ m EdU for 2 h. The medium was removed and 3.7% formaldehyde in phosphate-buffered saline supplemented with 0.02% Tween (1 \times PBS-T) buffer was added to fix the cells. After being washed twice with 1 \times PBS-T, the cells were permeabilised with 0.5% Triton X-100 in 1 \times PBS-T for 20 min at room temperature (RT). We then added the click cocktails successively. In one experiment, we just added TAMRA-azide **10** (20 μ m) as a positive control. In the other experiment, we performed a first reaction with dendrimer **1** (20 μ m) for 1 h followed by a second click reaction with TAMRA-alkyne **11** (5 μ m) for 30 min. (For more detailed characterisation of the reaction products, determined with a simplified model by using synthetic oligonucleotides, see the Supporting Information.) In both experiments, we washed the fixed cells twice with 3% bovine serum albumin (BSA) in PBS buffer. In the dendrimer-amplified experiment with TAMRA-alkyne **11**, we noted an unusually high background, even after the intensive washing steps. Screening for appropriate washing conditions showed that best results were obtained if we washed with a solution of guanidinium isocyanate (figure S5.4). We then determined the TAMRA fluorescence by using a fluorescence microscope. The data are depicted in figure 1B. Clearly visible is that the first click reaction with dendrimer-azide **1** furnished a sixfold increase in the fluorescence signal. This is particularly visible in the fluorescence microscopic evaluation of the click-modified cells (figure 1C).

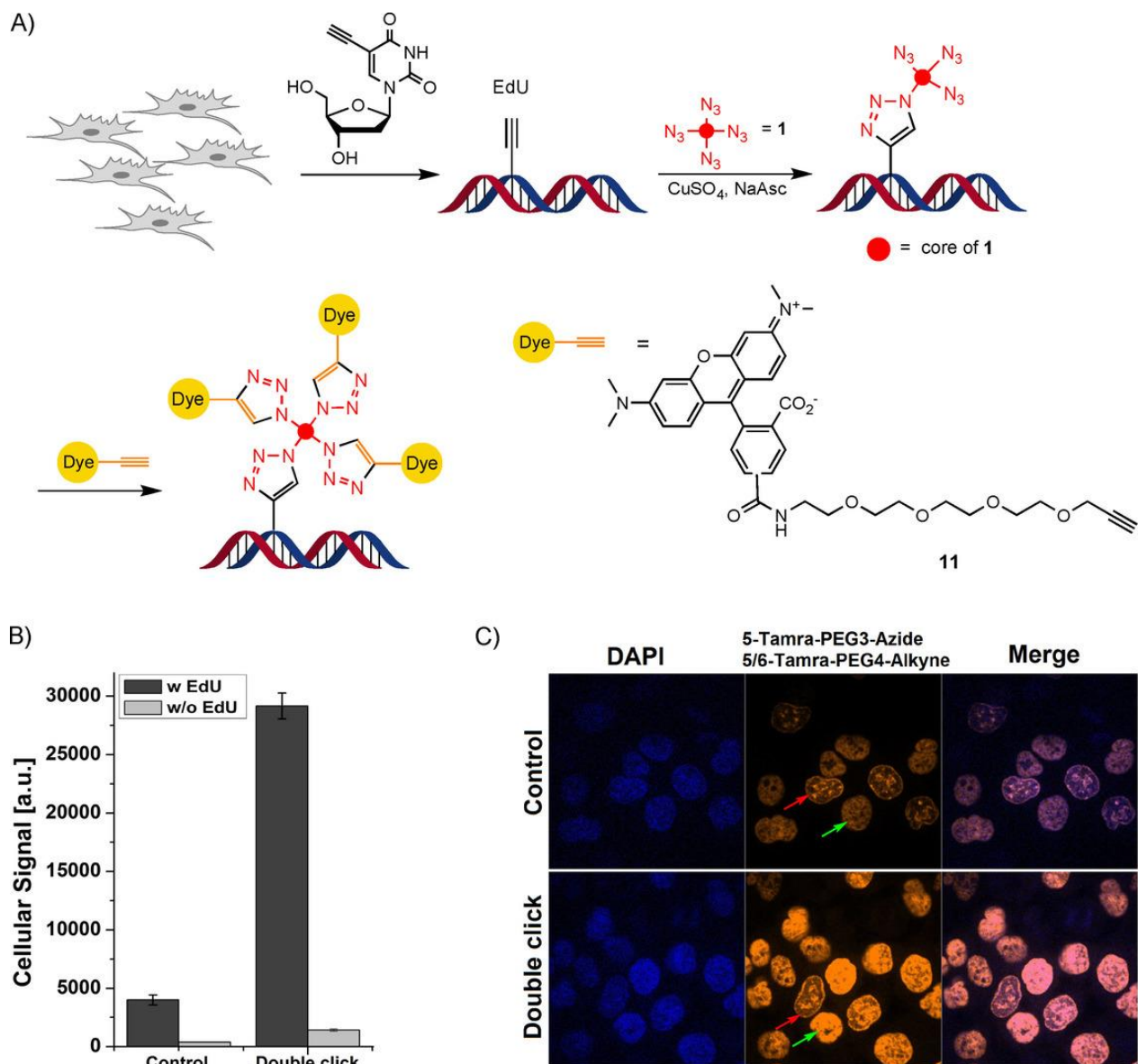


Figure 5.1: A) Depiction of the single dendrimer (double click) amplified cell-proliferation assay. Cells were grown in the presence of 5-ethynyl-dU. The cells were fixed, and the present alkynes were treated with tetraazide-dendrimer **1** in the presence of Cu^{I} (double click). The multiple-azide-containing DNA was then detected in situ with alkyne-modified dye **11** by again using the Cu^{I} -catalysed click reaction. B) The control experiment was performed by using the dendrimer-free standard proliferation assay with **10**. Double click shows data after dendrimer amplification. C) Fluorescence microscopy pictures of cells detected with the standard assay as control (top) and after dendrimer amplification (bottom). Red arrows show cells in the early S-phase with partial EdU incorporation. Green

arrows show cells in late S-phase, for which the DNA synthesis is almost finished and EdU is incorporated into the whole genome. Scale bars: 20 μm .

We noted that after extensive washing with guanidinium isocyanate, the background was reduced but was steadily higher than that in the non-dendrimer experiments. We speculated that this background problem may have been caused by dye-alkyne **11**, possibly because alkynes are known to react to some extent with nucleophiles. Thiol-containing nucleophiles are abundantly present in cells. Control experiments performed without the addition of tetraazide **1** confirmed this hypothesis and showed a still-high background signal even without the use of our dendrimers (figure S5.4). In order to solve the background problem and to increase the sensitivity (signal-to-noise ratio) of detection further, we next experimented with a double-dendrimer approach (figure 5.2), by which we first treated the fixed DNA with tetraazide **1**, and this was followed by an additional click reaction with tetraalkyne-dendrimer **2**. Then, we performed a final click reaction with TAMRA-azide **10** (figure S5.5). In this way, we planned to circumvent the use of the problematic dye-alkynes. For this experiment, we again cultured HeLa cells in μ -slides in the presence of 10 μm EdU for 2 h. The medium was removed, and 3.7% formaldehyde in 1 \times PBS-T was again added to fix the cells. We washed the cells two times with 1 \times PBS-T and permeabilised the cells with 0.5% Triton in 1 \times PBS-T for 20 min at RT. We then added the click cocktails successively: First, we added Cu^{I} and tetraazide **1**. We washed the cells twice with a 0.2 m acetate buffer pH 4.7, which was followed by two washing steps with 1 \times PBS-T, and we subsequently performed the second click reaction with tetraalkyne **2** and Cu^{I} for 1 h. The cells were again washed twice with 1 \times PBS-T. Finally, we added Cu^{I} and TAMRA-azide **10** to the cells and allowed the final click cocktail to penetrate the cells for 30 min. After the cells had again been washed twice with guanidinium isocyanate, we studied them by fluorescence microscopy. This time the experiment was a full success. We detected a strongly reduced background, not higher than that in the control experiment with just EdU (figure 5.2B, C). The obtained fluorescence signal was highly improved by a factor of 2.5. Most importantly, direct inspection of the cells by fluorescence microscopy showed a strongly improved signal-to-noise ratio (figures 5.2C and S5.5).

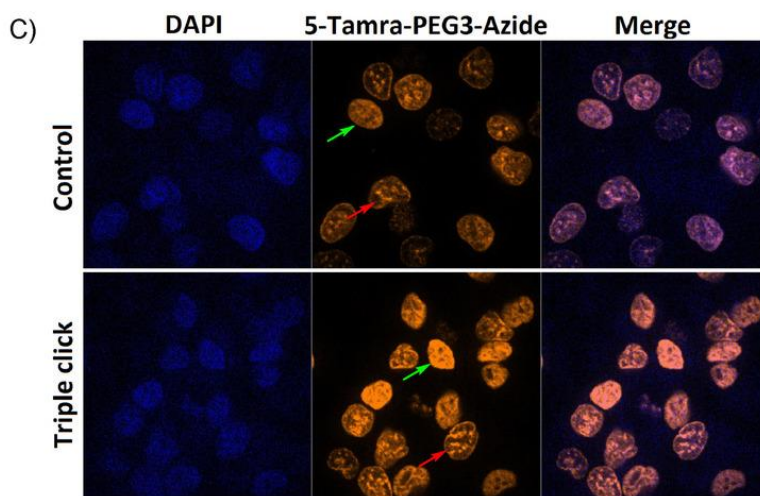
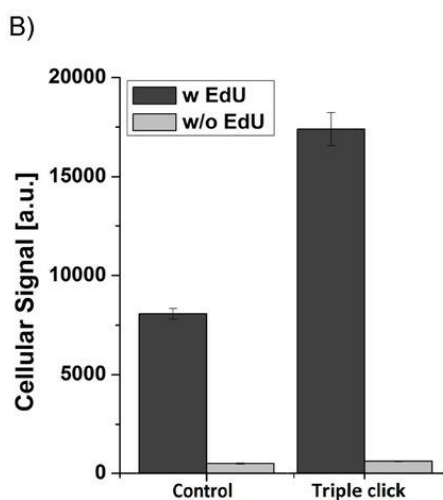
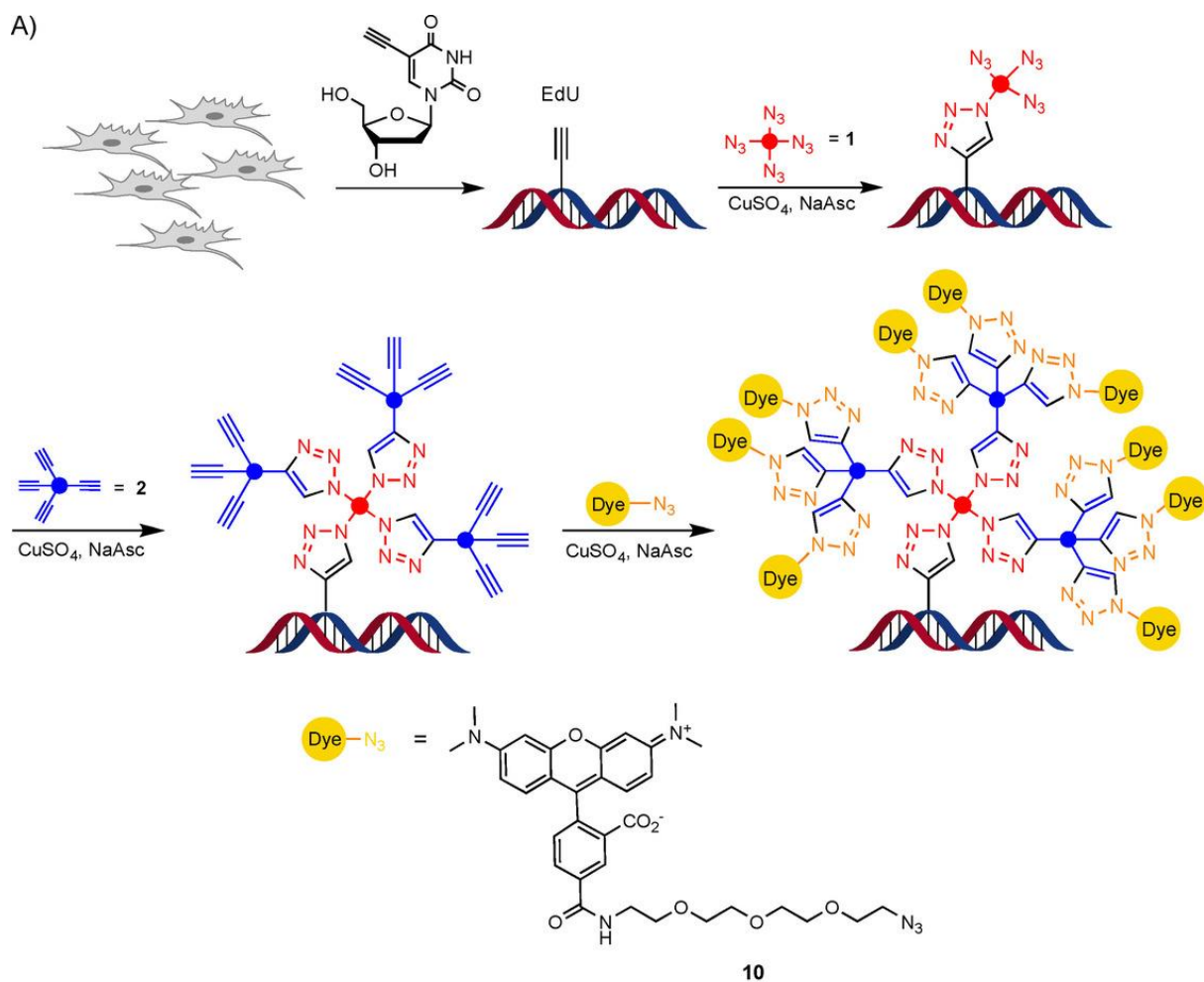


Figure 5.2: A) Depiction of the double dendrimer (triple click) amplified cell-proliferation assay. Cells were grown in the presence of 5-ethynyl-dU. After fixation and permeabilisation, the present alkynes are first treated with tetraazide-dendrimer **1** in the presence Cu^I . The

multiple-azide-containing DNA was then treated with tetraalkyne **2**. The so-double-modified DNA (triple click) was finally detected with azide-modified dye **10** again by using the Cu^I-catalysed click reaction. B) The control experiment was performed by using the dendrimer-free standard proliferation assay. Triple click shows data after double dendrimer amplification. C) Fluorescence microscopy pictures of cells detected with the standard EdU assay as control (top) and after double dendrimer amplification with triple click (bottom). Red arrows show cells in the early S-phase. Green arrows show cells in late S-phase. Scale bars: 20 μm .

Next, the new single- and double-dendrimer-based methods were applied for high-throughput screening (HTS). This method is the most widely used tool not only for the development of new pharmaceutical compounds but also for the measurement of the response of cells to different nutrients, mitogens, cytokines, growth factors and toxic agents [21]. With the signal amplification provided by our dendrimers, we were able to detect a strong, specific signal even if only a very small number of cells, such as just 100 cells, was present per well (figure 5.3). This is a significant improvement over contemporary methods that need 500 to 1000 cells per well, and thus, we can now reliably detect a small number of proliferating cells that would otherwise escape staining and detection. What we noted, however, was a reduction in the signal intensity in the double-dendrimer approach, which was likely due to self-quenching of the then densely packed fluorophores. To solve this, optimisation of the dendrimers is now required.

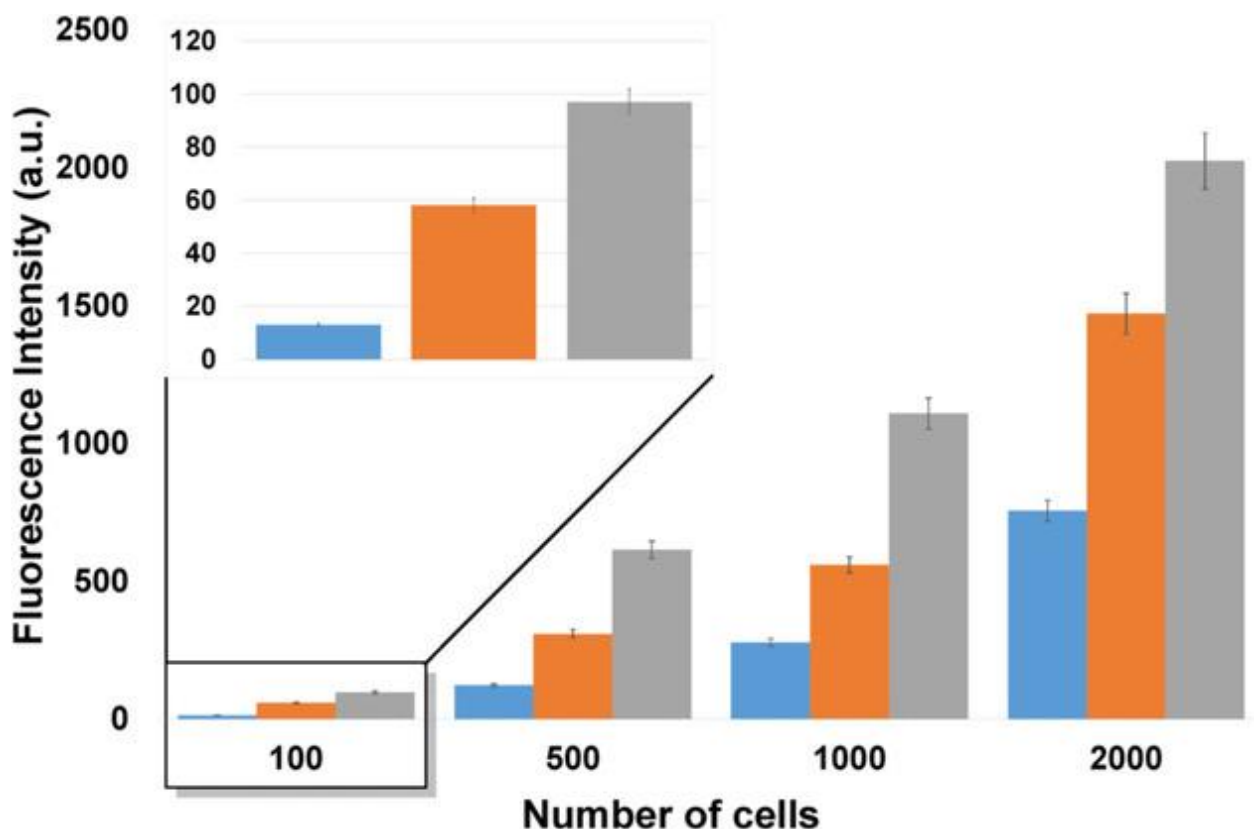


Figure 5.3: Application of the single and double dendrimer amplified assay in high-throughput screening. Cells were grown on a microplate with different densities (100, 500, 1000 and 2000 cells per well) and were incubated for 2 h with 5-ethynyl-dU at 37 °C. Negative control cells were grown without EdU labelling. The cells were fixed and permeabilised, and the present alkynes were treated with tetraazide dendrimer **1** and TAMRA-alkyne (double click, grey bars) or with tetraazide **1**, tetraalkyne **2** and TAMRA-azide (triple click, orange bars) in the presence of Cu^I in situ. Positive control cells were treated with TAMRA-azide in the presence of Cu^I (control, blue bars). The cellular signal of duplicate samples was measured with a Tecan microplate reader. After subtraction of the background fluorescence, it was possible to detect a stronger signal even with only 100 cells. Blue: standard click protocol; grey: single-dendrimer approach with dendrimer **1**; orange: double-dendrimer approach with dendrimers **1** and **2**.

In summary, click-based detection of cell proliferation is today state-of-art technology. We showed herein that by using a dendrimer-type tetraazide (i.e., compound **1**) and a dendrimer-type tetraalkyne (i.e., compound **2**), sandwich-type detection assays could be

established that yielded strongly improved signal intensities with low background and that gave higher signal-to-noise ratios for imaging and high-throughput-content assays. We expect that the so-improved cell-proliferation assay will be able to detect either slowly or even single proliferating cancer cells with unprecedented sensitivity.

5.3. References

1. Daidone MG, Silvestrini R. Prognostic and predictive role of proliferation indices in adjuvant therapy of breast cancer. *J Natl Cancer Inst Monogr.* 2001; (30):27-35.
2. Torp SH, Lindboe CF, Granli US, Moen TM, Nordtomme T. Comparative investigation of proliferation markers and their prognostic relevance in human meningiomas. *Clin Neuropathol.* 2001; 20(5):190-5.
3. Aleskandarany MA, Green AR, Benhasouna AA, Barros FF, Neal K, Reis-Filho JS, et al. Prognostic value of proliferation assay in the luminal, HER2-positive, and triple-negative biologic classes of breast cancer. *Breast Cancer Res.* 2012; 14(1):R3.
4. Wang M, Wu J, Guo Y, Chang X, Cheng T. The tripartite motif-containing protein 3 on the proliferation and cytokine secretion of rheumatoid arthritis fibroblast-like synoviocytes. *Mol Med Rep.* 2017; 15(4):1607-12.
5. Wieder T, Brenner E, Braumüller H, Bischof O, Röcken M. Cytokine-induced senescence for cancer surveillance. *Cancer and Metastasis Rev.* 2017; 36(2):357-65.
6. Thorat AS, Sonone NA, Choudhari VV, Devarumath RM, Babu KH. Plant regeneration from cell suspension culture in *Saccharum officinarum* L. and ascertaining of genetic fidelity through RAPD and ISSR markers. *3 Biotech.* 2017; 7(1):16.
7. Chen H, Gu X, Liu Y, Wang J, Wirt SE, Bottino R, et al. PDGF signalling controls age-dependent proliferation in pancreatic beta-cells. *Nature.* 2011; 478(7369):349-55.
8. Poss KD, Wilson LG, Keating MT. Heart regeneration in zebrafish. *Science.* 2002; 298(5601):2188-90.

9. Lu X, Horner JW, Paul E, Shang X, Troncoso P, Deng P, et al. Effective combinatorial immunotherapy for castration-resistant prostate cancer. *Nature*. 2017; 543(7647):728-32.
10. Jordan NV, Bardia A, Wittner BS, Benes C, Ligorio M, Zheng Y, et al. HER2 expression identifies dynamic functional states within circulating breast cancer cells. *Nature*. 2016; 537(7618):102-6.
11. Erb MA, Scott TG, Li BE, Xie H, Paulk J, Seo HS, et al. Transcription control by the ENL YEATS domain in acute leukaemia. *Nature*. 2017; 543(7644):270-4.
12. Evan GI, Vousden KH. Proliferation, cell cycle and apoptosis in cancer. *Nature*. 2001; 411(6835):342-8.
13. Evan G, Littlewood T. A matter of life and cell death. *Science*. 1998; 281(5381):1317-22.
14. Salic A, Mitchison TJ. A chemical method for fast and sensitive detection of DNA synthesis in vivo. *Proc Natl Acad Sci U S A*. 2008; 105(7):2415-20.
15. Ababou M, Dumaire V, Lecluse Y, Amor-Gueret M. Bloom's syndrome protein response to ultraviolet-C radiation and hydroxyurea-mediated DNA synthesis inhibition. *Oncogene*. 2002; 21(13):2079-88.
16. Cavanagh BL, Walker T, Norazit A, Meedeniya AC. Thymidine analogues for tracking DNA synthesis. *Molecules*. 2011; 16(9):7980-93.
17. Kolb HC, Finn MG, Sharpless KB. Click Chemistry: Diverse Chemical Function from a Few Good Reactions. *Angew Chem Int Ed Engl*. 2001; 40(11):2004-21.
18. Gramlich PM, Wirges CT, Manetto A, Carell T. Postsynthetic DNA modification through the copper-catalyzed azide-alkyne cycloaddition reaction. *Angew Chem Int Ed Engl*. 2008; 47(44):8350-8.
19. Gierlich J, Burley GA, Gramlich PM, Hammond DM, Carell T. Click chemistry as a reliable method for the high-density postsynthetic functionalization of alkyne-modified DNA. *Organic Letters*. 2006; 8(17):3639-42.

20. Nik-Zainal S, Van Loo P, Wedge DC, Alexandrov LB, Greenman CD, Lau KW, et al. The life history of 21 breast cancers. *Cell*. 2012; 149(5):994-1007.
21. Zanella F, Lorens JB, Link W. High content screening: seeing is believing. *Trends Biochem Sci*. 2010; 28(5):237-45.

5.4. Appendix

5.4.1. General Methods

Chemicals were purchased from Sigma-Aldrich, Alfa Aesar, TCI Chemicals or Acros Organics and used without further purification. Solutions were concentrated *in vacuo* on a Heidolph rotary evaporator. The solvents were of reagent grade and purified by distillation. Dry solvents were bought from Acros Organics or Sigma-Aldrich. Water was purified by a Milli-Q Plus system from Merck Millipore. Chromatographic purification of products was accomplished using flash column chromatography on Merck Geduran Si 60 (40-63 μM) silica gel (normal phase). Thin layer chromatography (TLC) was performed on Merck 60 (silica gel F254) plates. ^1H and ^{13}C -NMR spectra were recorded in deuterated solvents on a *Bruker ARX 400* spectrometer and calibrated to the residual solvent peak. Multiplicities are abbreviated as follows: s = singlet, d = doublet, t = triplet, q = quartet, m = multiplet, brs = broad signal. For assignment of the structures, additional 2D NMR spectra (COSY, HSQC, HMBC) were measured. High resolution electrospray ionization mass spectra (HRMS-ESI) were recorded on a *Thermo Finnigan LTQ-FT* (ESI-FTICR).

DNA Oligonucleotide synthesis was performed on an Applied Biosystems Incorporated 394 automated synthesizer. Phosphoramidites and solid supports columns were purchased from Glen Research, Link Technology or Baseclick.

Analytical RP-HPLC was performed using a *Macherey-Nagel Nucleodur 100-3 C18ec* column on *Waters Alliance 2996 Photodiode Array Detector, 2695 Separation Module* using a flow of 0.5 mL/min. Conditions: Buffer A = 0.1 M TEAA (triethylammonium acetate) in water; buffer B = 0.1 M TEAA in 80% acetonitrile. When needed, the product peaks were collected,

concentrated and characterized by Matrix Assisted Laser Desorption Ionization-Time of Flight (MALDI-TOF) on Bruker Daltonics Autoflex II.

5.4.2. Chemical Synthesis

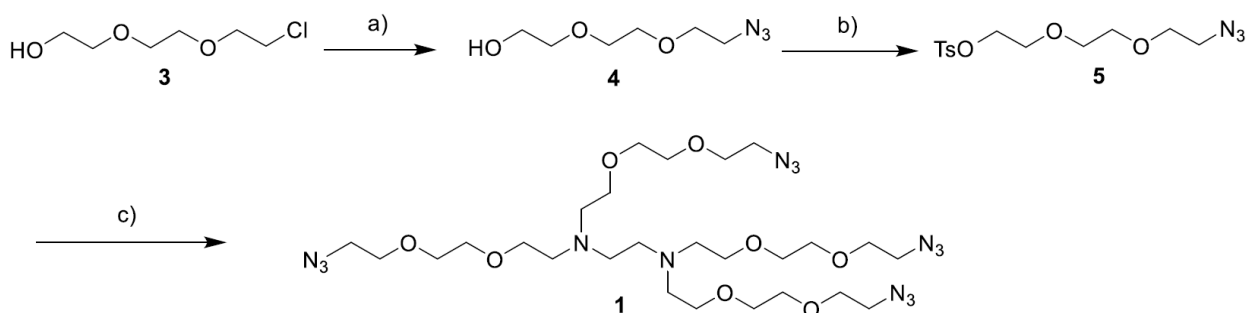


Figure S5.1: Synthesis of **1**. Reagents and conditions: a) NaN_3 , DMF, 90 °C o/n, 96%; b) TsCl, NEt_3 , CH_2Cl_2 , o/n, 90%; c) **5**, ethylenediamine, KOH, LiBr, DMF, 60 °C, o/n, 63%.

2-[2-(2-Azidoethoxy)ethoxy]ethanol (**4**)

2-[2-(2-Chloroethoxy)ethoxy]ethanol (**3**) (4.31 mL, 29.65 mmol) was dissolved in 200 mL of dry DMF under N_2 . NaN_3 (3.86 g, 59.3 mmol) was added, and the mixture was heated at 90 °C overnight. After 18 h, the solvent was removed under reduced pressure and the residue was partitioned between H_2O (50 mL) and EtOAc (150 mL). The aqueous phase was extracted again with 150 mL of EtOAc and the combined organic phases were combined, washed with brine, dried over Na_2SO_4 , filtered and evaporated. The crude product was purified by column chromatography (isohexane/EtOAc 1:4 \rightarrow 1:10) to afford **4** as a colorless oil (5.0 g, 96%).

$^1\text{H-NMR}$ (400 MHz, CDCl_3) δ = 3.77-3.71 (m, 2H), 3.68 (s, 6H), 3.62-3.58 (m, 2H), 3.43-3.37 (m, 2H) ppm.

$^{13}\text{C-NMR}$ (101 MHz, DMSO-d_6) δ = 72.4, 69.88, 69.82, 69.37, 60.31, 50.09 ppm.

2-(2-(2-Azidoethoxy)ethoxy)ethyl 4-methylbenzenesulfonate (**5**)

Compound **4** (5 g, 28.54 mmol) was dissolved in 100 mL of DCM at room temperature. The solution was then cooled to 0 °C and NEt₃ and TsCl were added. The mixture was then stirred overnight allowing to warm up to room temperature. After 18 hours, the reaction mixture was washed with 1 M HCl, H₂O, brine, dried over MgSO₄ and filtered. The solvent was removed under reduced pressure and the crude product was purified by column chromatography (isohexane/EtOAc 10:1) to yield **5** as a colorless oil (8.5 g, 90%).

¹H NMR (400 MHz, CDCl₃) δ = 7.77 (d, *J* = 8 Hz, 2H), 7.32 (d, *J* = 8 Hz, 2H), 4.13 (t, *J* = 6 Hz, 2H), 3.70-3.55 (m, 8H), 3.34 (t, *J* = 5 Hz, 2H), 2.42 (s, 3H) ppm.

**N1,N1,N2,N2-Tetrakis(2-(2-(2-azidoethoxy)ethoxy)ethyl)ethane-1,2-diamine
(tetraazide dendrimer 1)**

Ethylenediamine (150 mg, 167 μL, 1.66 mmol) was dissolved in 50 mL of dry DMF. KOH (613 mg, 10.8 mmol) and LiBr were added at RT. Compound **5** was then added dropwise as a solution in 20 mL of DMF, then the reaction was stirred for 2 hours at RT and heated at 60 °C overnight. After 20 hours, the solvent was removed under vacuum and the residue was retaken in EtOAc, washed with sat. NaHCO₃, brine, dried over Na₂SO₄ and filtered. Evaporation of the solvent afforded a yellowish oil that was purified by column chromatography (DCM/MeOH 30:1 → 10:1). 1.1 g of product was recovered (63%).

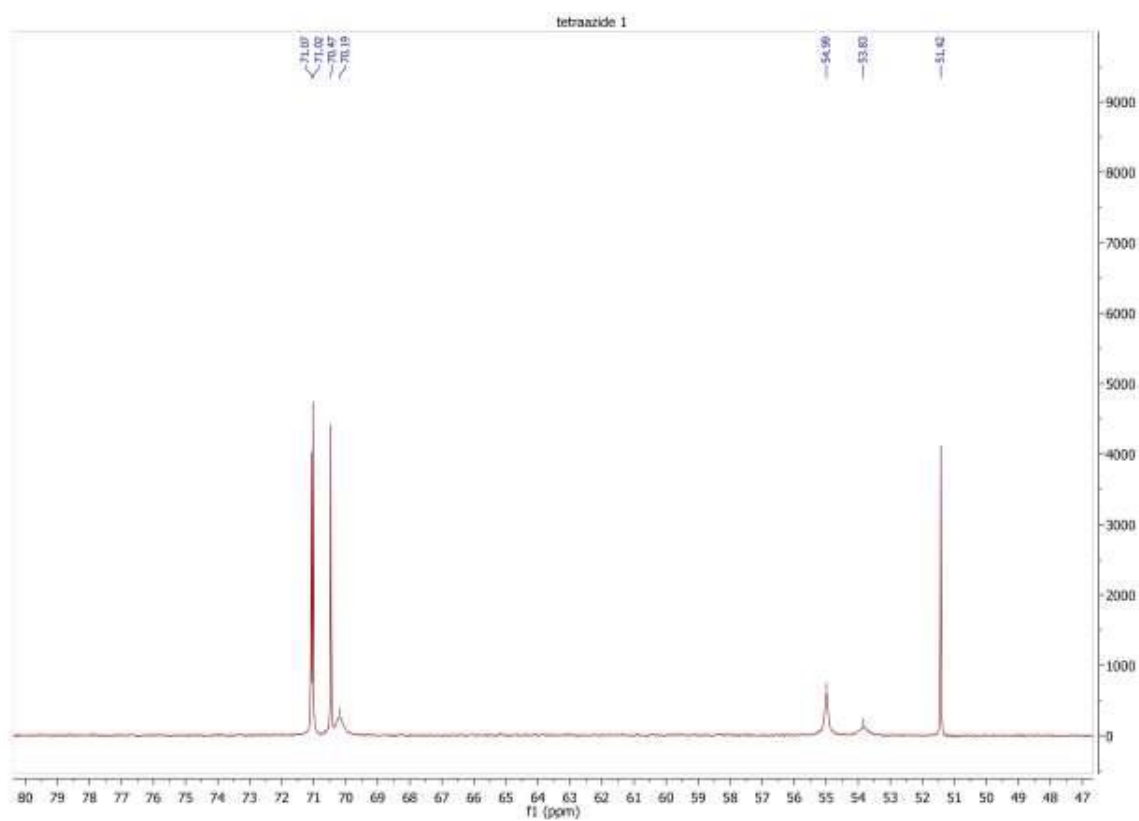
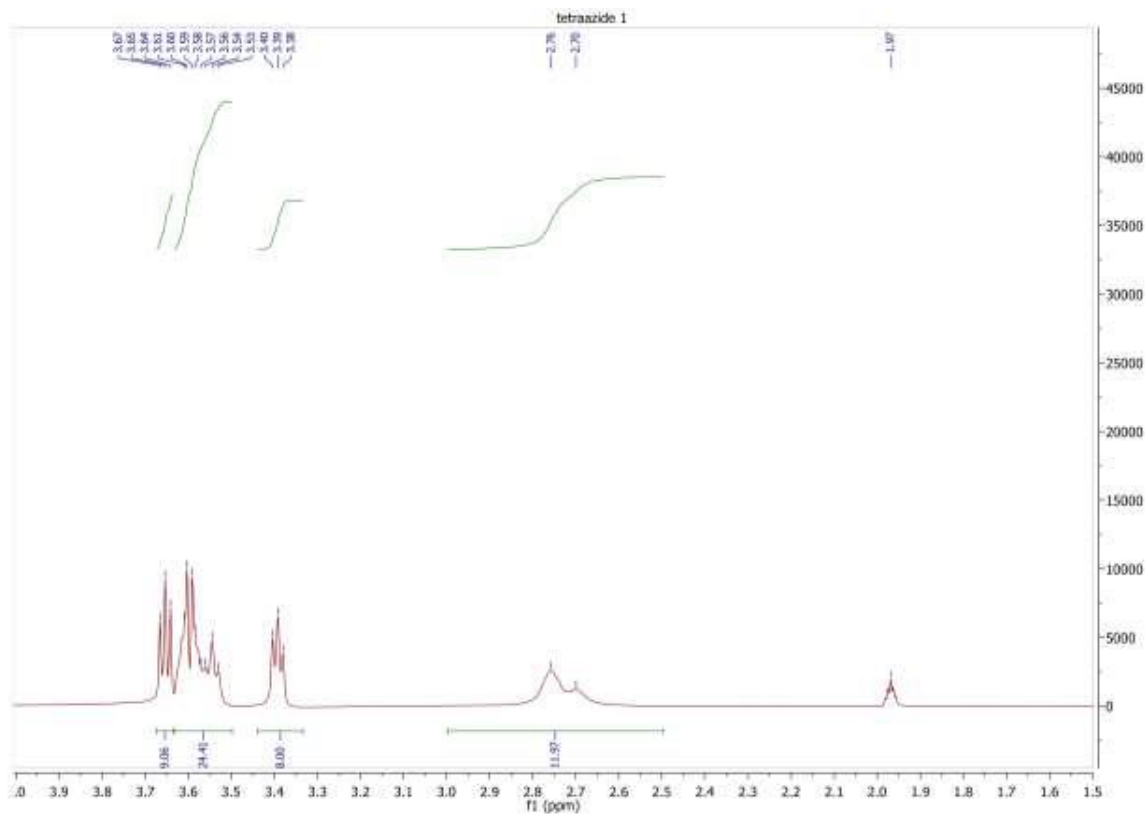
HR-MS (ESI+): calculated for C₂₆H₅₃N₁₄O₈⁺ 689.4165, found: 689.4159.

¹H-NMR (400 MHz, CD₃CN) δ = 3.58 (t, *J* = 6 Hz, 8H, 4 x N₃CH₂CH₂OR), 3.57-3.42 (m, 24H), 3.32 (t, *J* = 5 Hz, 8H, 4x N₃CH₂CH₂OR) 2.82-2.48 (brs, 12H, (RCH₂)₂ NCH₂CH₂N(CH₂)₂) ppm.

¹³C-NMR (101 MHz, CD₃CN) δ = 71.07, 71.02, 70.47, 70.19, 54.99, 53.83, 51.43

NMR spectra of **1**

5. Dendrimer-based signal amplification of click-labelled DNA in situ



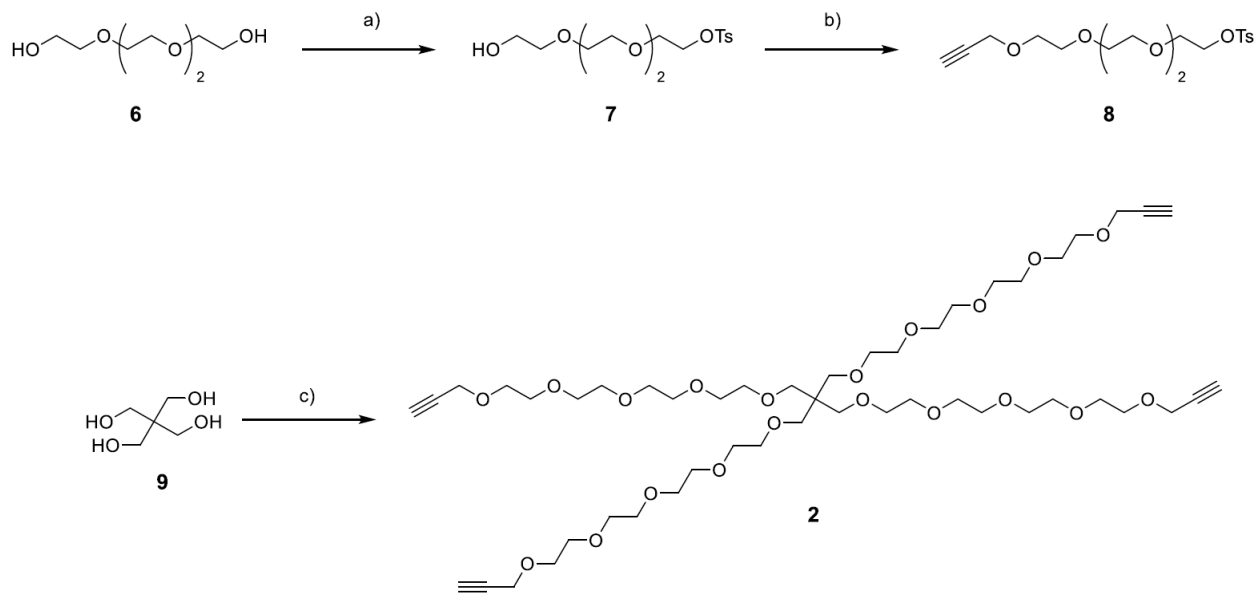


Figure S5.2: Synthesis of **2**. Reagents and conditions: a) TsCl, Et₃N, THF, RT, 48 h, 92 %; b) Propargyl bromide, NaH, THF, 0 °C to RT, 82%; c) **1**, K₂CO₃, acetone, 60 °C, 48 h, 30%.

2-(2-(2-(2-hydroxyethoxy)ethoxy)ethoxy)ethyl 4-methylbenzenesulfonate (**7**)

Tetraethylene glycol (29.25 g, 150.6 mmol) was dissolved in dry THF (100 mL) and triethylamine (122 g, 1.2 mol, 8.0 eq.) was added. The reaction was cooled down to 0 °C and a solution of tosyl chloride (28.71 g, 150.6 mmol, 1.0 eq.) in dry THF (50 mL) was added over a period of 1 h. After 48 h stirring at room temperature the solvent was removed *in vacuo*. The mixture was taken up in HCl (2 M, 150 mL) and extracted with DCM (4 × 150 mL). The combined organic layers were dried over MgSO₄ and filtered. After removal of the solvent *in vacuo* the crude product was purified by flash chromatography (Silica, DCM → DCM/MeOH (99:1 → 0:1)). The product was obtained as a colorless oil (48.27 g, 138.6 mmol, 92%).

¹H-NMR (400 MHz, CDCl₃): δ = 7.82-7.76 (m, 2H, CH_{arom.}), 7.37-7.30 (m, 2H, CH_{arom.}), 4.20-4.12 (m, 2H, CH₂), 3.73-3.52 (m, 14H, 7 × CH₂), 2.42 (s, 3H, CH₃), 2.38-2.31 (s, 1H, OH) ppm.

¹³C-NMR (100 MHz, CDCl₃): δ = 144.9 (C_{arom.}), 133.2 (C_{arom.}), 130.0 (2 × CH_{arom.}), 128.1 (2 × CH_{arom.}), 72.6 (CH₂), 70.9 (CH₂), 70.8 (CH₂), 70.6 (CH₂), 70.5 (CH₂), 69.4 (CH₂), 68.9 (CH₂), 61.9 (CH₂), 21.8 (CH₃) ppm.

HR-MS (ESI): $C_{15}H_{25}O_7S^+$ $[M+H]^+$, calc.: 349.1315, found: 349.1316

3,6,9,12-tetraoxapentadec-14-yn-1-yl 4-methylbenzenesulfonate (8)

2-(2-(2-(2-hydroxyethoxy)ethoxy)ethoxy)ethyl 4-methylbenzenesulfonate (10 g, 28.7 mmol) was dissolved in dry THF (50 mL) and added dropwise to a solution of NaH (60%, 1.38 g, 34.44 mmol, 1.2 eq.) in dry THF (50 mL) at 0 °C. Propargylbromide (80% in toluene, 31.85 mL, 287 mmol, 10 eq.) was subsequently added to the mixture and stirred for 2 h at RT. The reaction was carefully quenched by slow addition of MeOH and the solvents were removed *in vacuo*. H₂O was added and extracted with DCM (3 × 200 mL). The combined organic layers were dried over MgSO₄, the solvent removed *in vacuo* and the crude product was purified by column chromatography (Silica, DCM → DCM/MeOH (99:1 → 0:1)). X was obtained as a colorless oil (9.06 g, 23.4 mmol, 82%).

¹H-NMR (400 MHz, CDCl₃): δ = 7.81-7.78 (m, 2H, CH_{arom.}), 7.35-7.33 (m, 2H, CH_{arom.}), 4.21-4.18 (m, 2H, CH₂), 4.17-4.14 (m, 2H, CH₂), 3.70-3.56 (m, 14H, 7×CH₂), 2.44 (s, 3H, CH₃), 2.42 (m, 1H, CH) ppm.

¹³C-NMR (100 MHz, CDCl₃): δ = 145.0 (C_{arom.}), 133.1 (C_{arom.}), 130.0 (2 × CH_{arom.}), 128.1 (2 × CH_{arom.}), 78.8 (HC≡C), 75.2 (HC≡C), 70.8 (CH₂), 70.7 (CH₂), 69.4 (CH₂), 68.8 (CH₂), 67.7 (CH₂), 56.6 (CH₂), 55.9 (CH₂), 55.4 (CH₂), 21.8 (CH₃) ppm.

HR-MS (ESI): $C_{18}H_{30}O_7NS^+$ $[M+NH_4]^+$, calc.: 404.1737, found: 404.1739.

18,18-di(2,5,8,11,14-pentaoxaheptadec-16-yn-1-yl)-4,7,10,13,16,20,23,26,29,32-decaoxapentatriaconta-1,34-diyne (2)

Pentaerythritole (15 mg, 110.18 μmol) was dissolved in acetone (3 mL). 3,6,9,12-tetraoxapentadec-14-yn-1-yl 4-methylbenzenesulfonate (213 mg, 550.9 μmol, 5 eq.) and K₂CO₃ (76 mg, 550.9 μmol, 5 eq.) were added. After stirring at 60 °C for 48 h the solvent was removed *in vacuo*. H₂O was added and extracted with DCM (4 × 20 mL). The combined organic layers were dried over MgSO₄, the solvent removed *in vacuo* and the crude product

5.4. Appendix

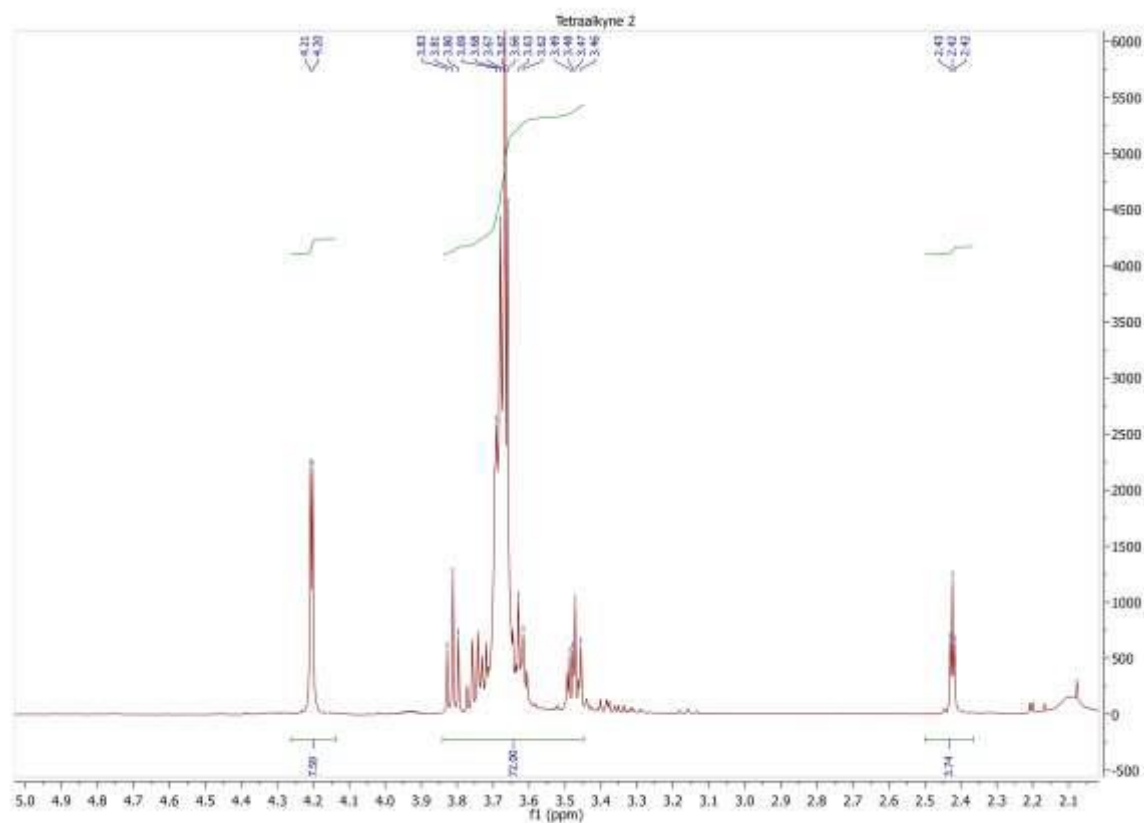
was purified by column chromatography ((Silica, DCM → DCM/MeOH (99:1 → 0:1)). The product was obtained as a colorless oil (33 mg, 33 μ mol, 30%).

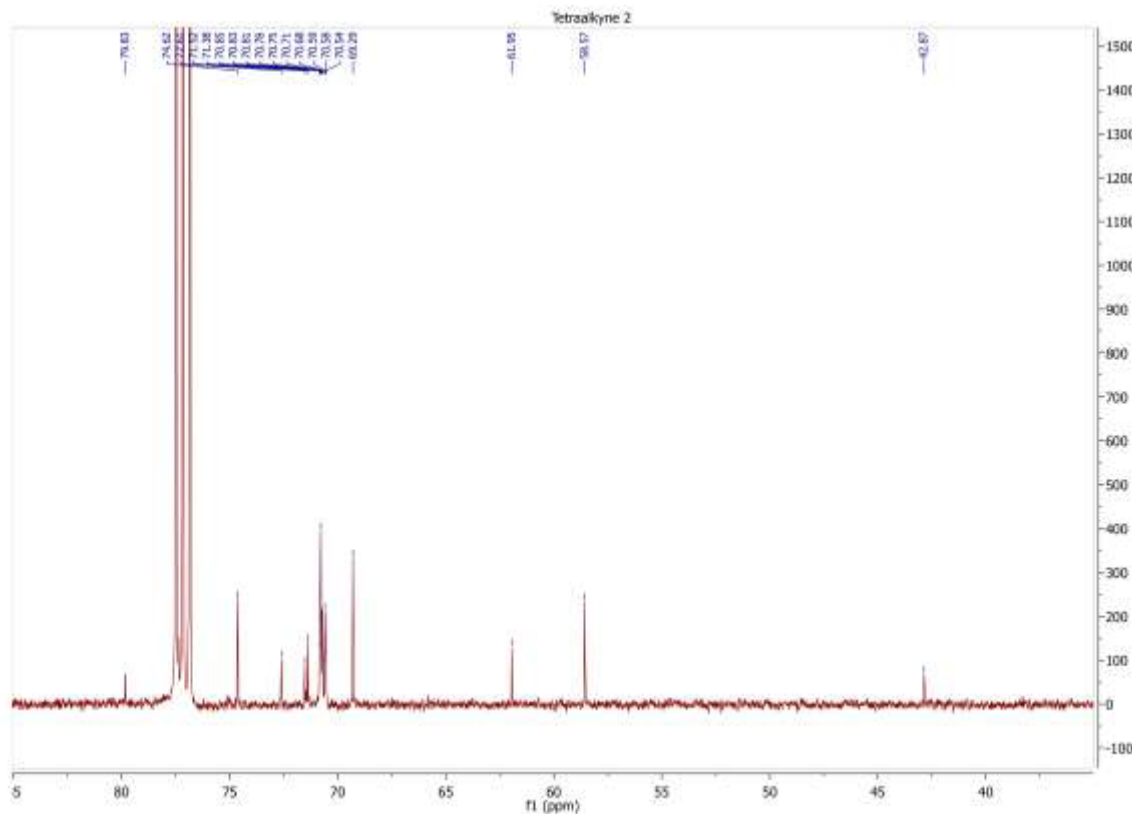
$^1\text{H-NMR}$ (599 MHz, CDCl_3): δ = 4.22-4.19 (d, ${}_3J$ = 2.4 Hz, 8H, CH_2), 3.85-3.40 (m, 72H, CH_2), 2.51-2.37 (t, ${}_4J$ = 2.4 Hz, 4H, CH_2) ppm.

$^{13}\text{C-NMR}$ (151 MHz, CDCl_3): δ = 79.83, 74.62, 72.61, 71.52, 71.48, 70.85, 70.83, 70.81, 70.78, 70.75, 70.71, 70.68, 70.59, 70.58, 70.54, 69.29, 61.95, 58.57, 42.87 ppm.

HR-MS (ESI): $\text{C}_{49}\text{H}_{85}\text{O}_{20}\text{Na}^{2+}$ $[\text{M}+\text{H}+\text{Na}]^{2+}$, calc.: 508.2760, found: 508.2755.

NMR spectra of **2**





5.4.3. Proof of principle of the click reactions on oligonucleotides

In order to prove that the strategy that we planned for the *in situ* detection of cell proliferation using click chemistry is applicable and yields predominantly the products shown in the main text, we performed experiments on synthetic oligonucleotides. We decided to perform the click reactions both in solution, purifying the main intermediates and products *via* HPLC and on solid phase, where we simply removed the excess of reagents with a few washing steps and then proceeded with the following click reaction. This second approach is more similar to the strategy that we ultimately applied for our cell studies and proved that it is possible to obtain the products that we wanted with good selectivity even without chromatographic purification of the intermediates. Both pathways were successful and yielded the desired products (oligonucleotide conjugated with multiple dyes) with good selectivity as a mixture of 5/6-TAMRA isomers. As expected, especially for the solid phase reactions, we observed a limited amount of cross-linked compound, where the

tetraazide binds two different oligonucleotides in the first step, and therefore can react with only two dyes in the second step (figure S5.3).

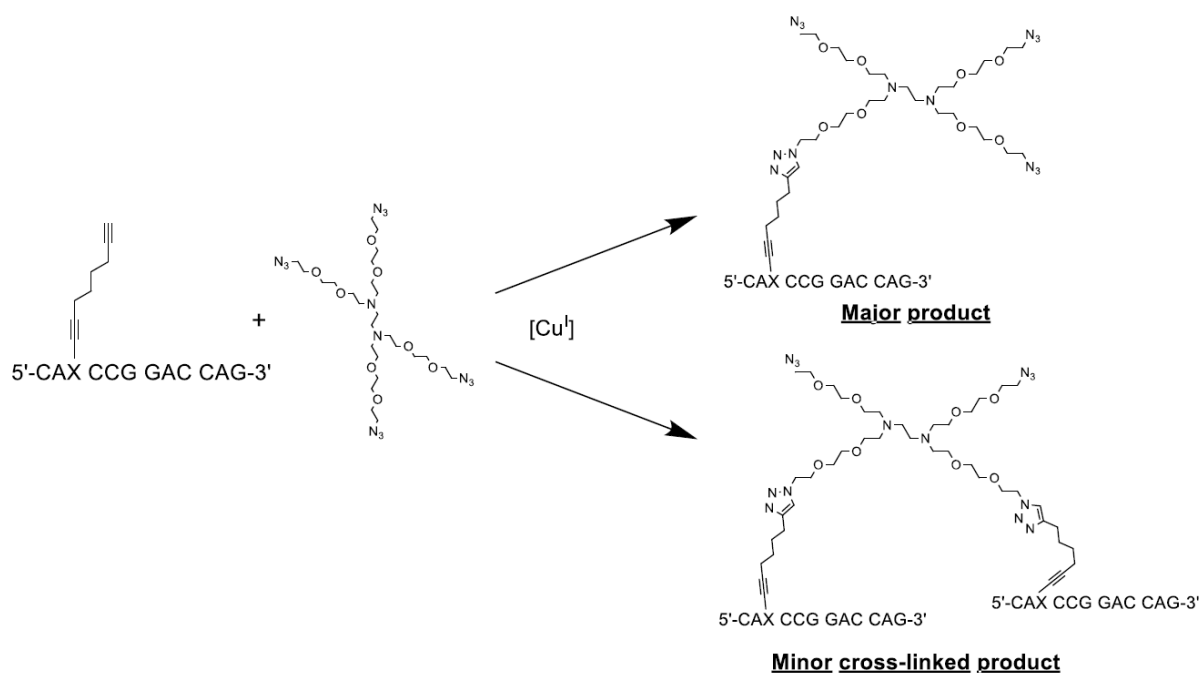


Figure S5.3: Reaction between oligonucleotides and the tetraazidedendrimer and possible products.

Sequence of the oligonucleotides used for the tests:

Oligonucleotide 1: 5'-CAX CCG GAC CAG-3' where X = C8-Alkynyl-dT; [M] = 3705.4

Oligonucleotide 2: 5'-TX TTT TTT T -3' where X = EdU; [M] = 2989.9

General procedure A (click in solution): The alkyne-modified oligonucleotide was dissolved in MQ water (concentration = 1 mM) and 3 μ L of this solution (3 nmol of oligonucleotide) were transferred in a vial for the click reaction. To this solution, H₂O (15 μ L), 1 M TEAA buffer (pH 7, 6 μ L), DMSO (27 μ L) and the azide or dye-alkyne solution (20 mM in DMSO, 3 μ L) were added. A CuSO₄/TBTA solution (1 mM in H₂O /DMSO 1:1, 3 μ L) was then added, followed by a freshly prepared solution of sodium ascorbate (2.5 mM, 3 μ L). The mixture was then shaken for 1 hour on a Thermomixer at 25 °C,

1200 rpm, and the solvent was then directly evaporated on a SpeedVac at 35 °C. All the products were analyzed and purified using RP-HPLC and identified using MALDI-TOF-MS.

Cyanoethyl deprotection: After solid phase oligonucleotide synthesis on a 200 nmol scale, part of the resin (approximately 50 nmol of oligonucleotide), was suspended in 500 µL of 10% DBU in dry acetonitrile to deprotect the cyanoethyl groups on the phosphates. The suspension was shaken on a Thermomixer at 30 °C for 1 h. After centrifugation, the DBU solution was decanted off and the resin was washed 5 times with 1 mL of dry acetonitrile.

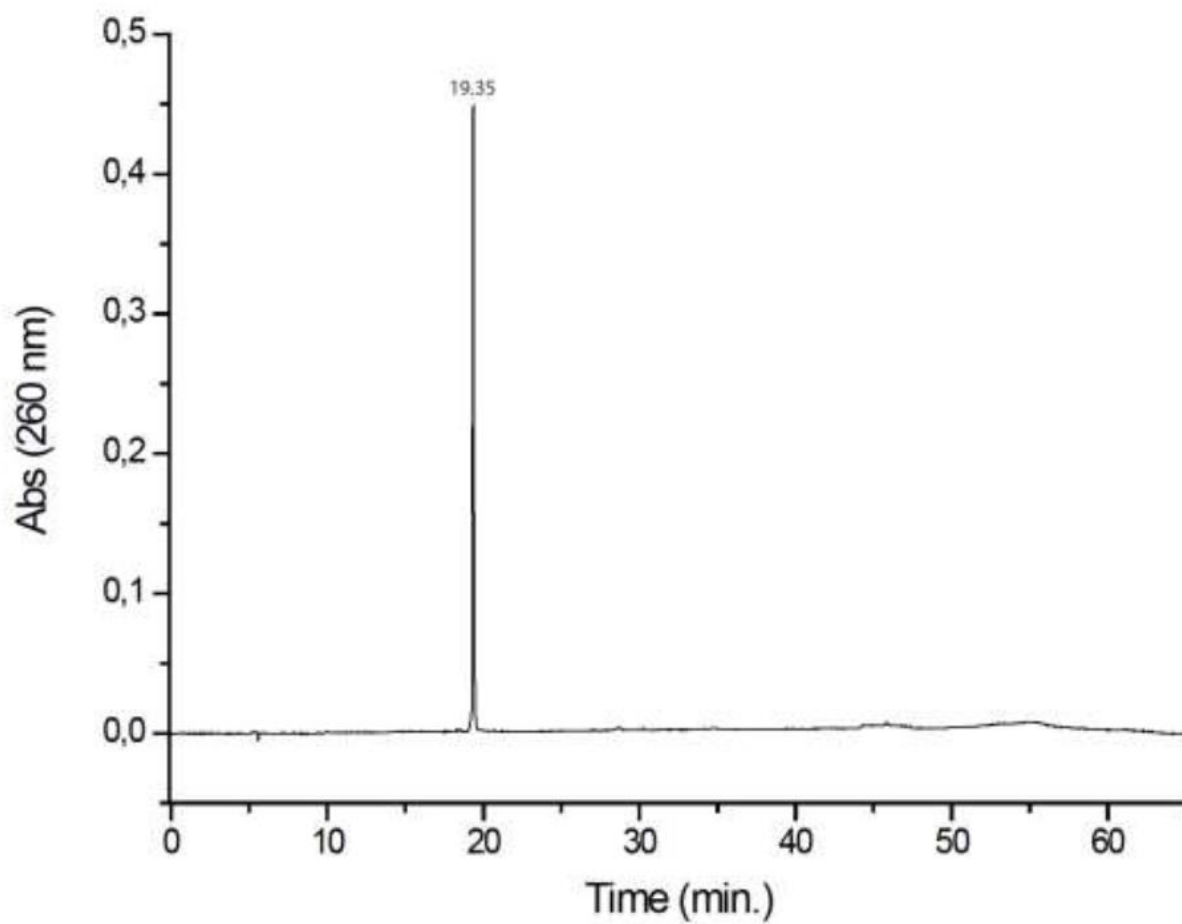
General procedure B (click on solid phase): The dried resin was suspended in 375 µL of H₂O/DMSO 1:2. To this, 1 M TEAA buffer (pH 7, 100 µL), the azide or dyealkyne solution (20 mM in DMSO, 50 µL) and the CuSO₄/TBTA solution (1 mM in H₂O /DMSO 1:1, 25 µL) were added, followed by a freshly prepared solution of sodium ascorbate (1 mM, 75 µL). After 1.5 h shaking on a Thermomixer at 25 °C, 1200 rpm, the mixture was centrifuged and the supernatant was discarded. The resin was then washed with H₂O (500 µL), MeCN (3 x 500 µL) and dried.

Standard cleavage procedure: The resin was suspended in 400 µL of 28-30% aqueous ammonium hydroxide and shaken at 30 °C for 1 h. After centrifugation, the supernatant was collected and the resin washed again with H₂O (2 x 200 µL). The solution was then evaporated on a SpeedVac at 35 °C to obtain the products that were analyzed by RP-HPLC and MALDI-TOF-MS and then purified.

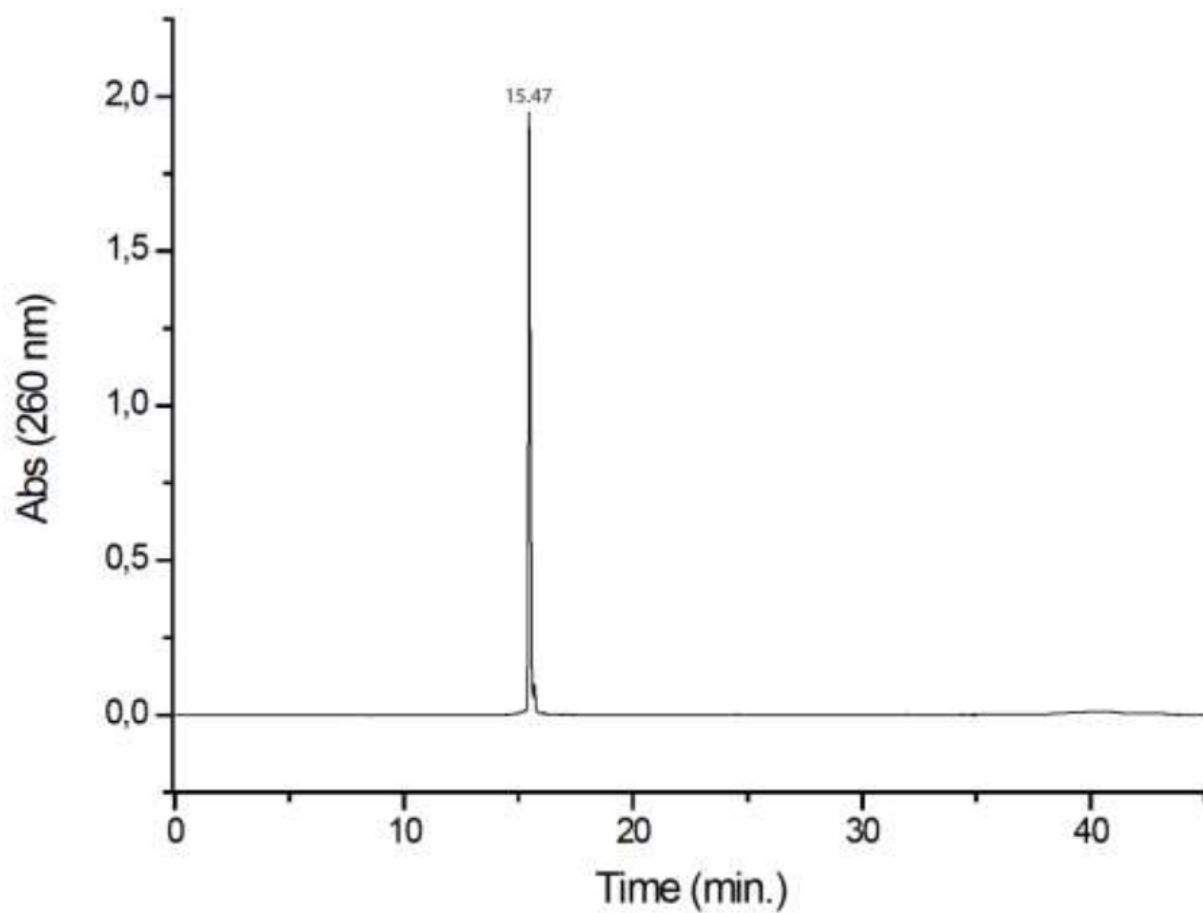
Cleavage procedure for TAMRA-containing oligonucleotides: The resin was suspended in 200 µL of a solution of tBuNH₂/MeOH/H₂O 1:1:3 solution and shaken at 40 °C for 1 hour. After centrifugation, the resin was washed twice with 200 µL of H₂O and the combined solutions were evaporated on a SpeedVac at 40 °C. The products were analyzed by RP-HPLC and MALDI-TOF-MS.

RP-HPLC chromatograms of the starting materials

Oligonucleotide 1 (0-70% B in 45 min)

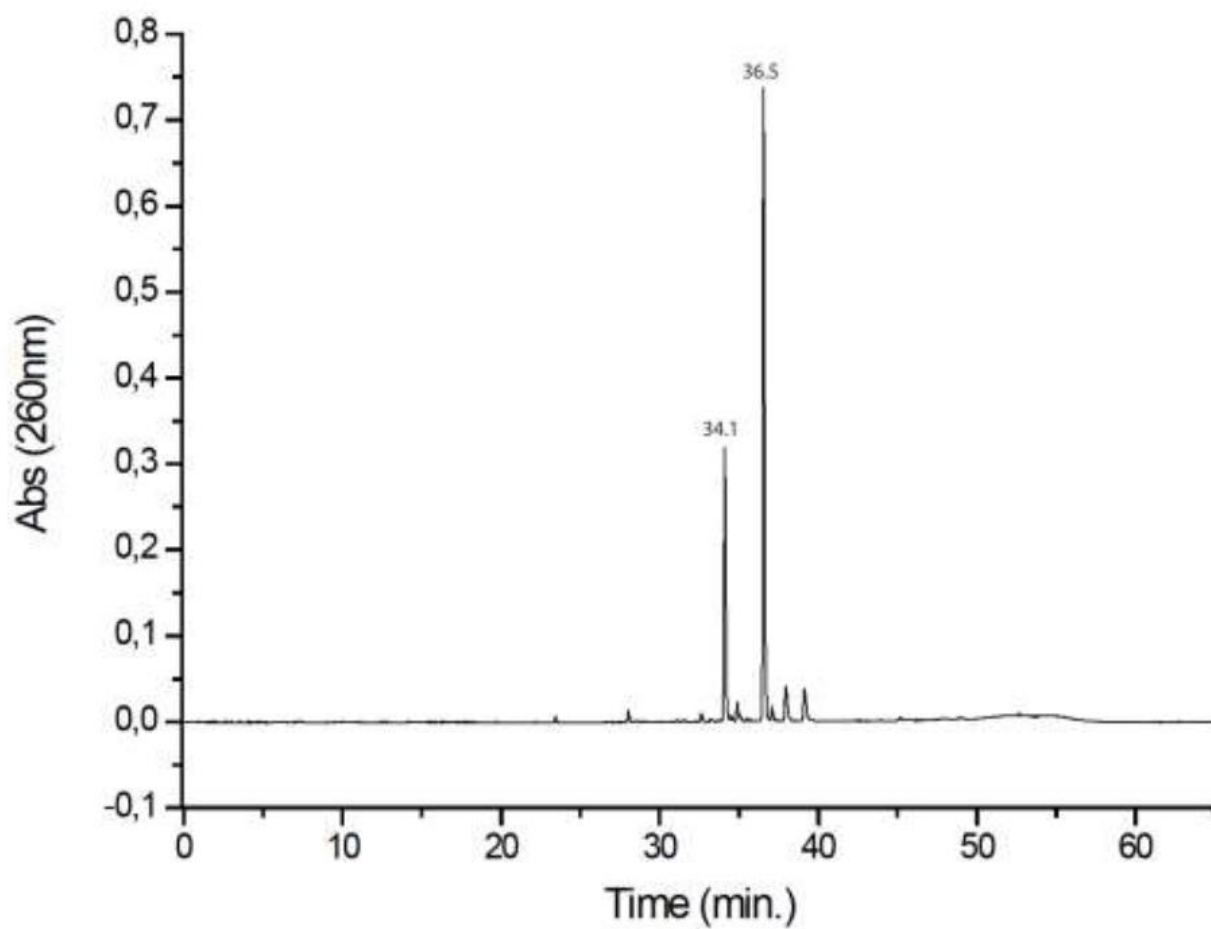


Oligonucleotide 2 (0-70% B in 33 min)

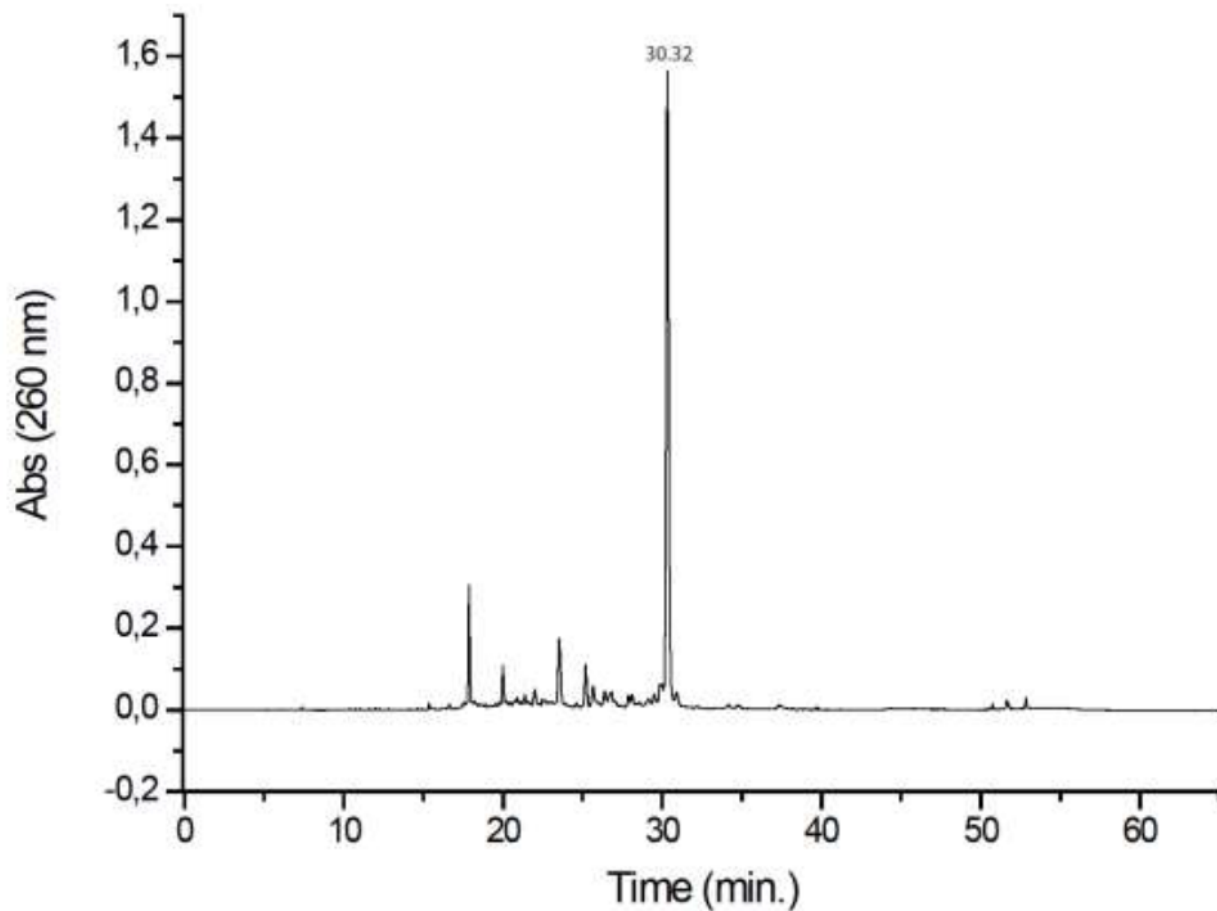


5/6-TAMRA-PEG4-alkyne

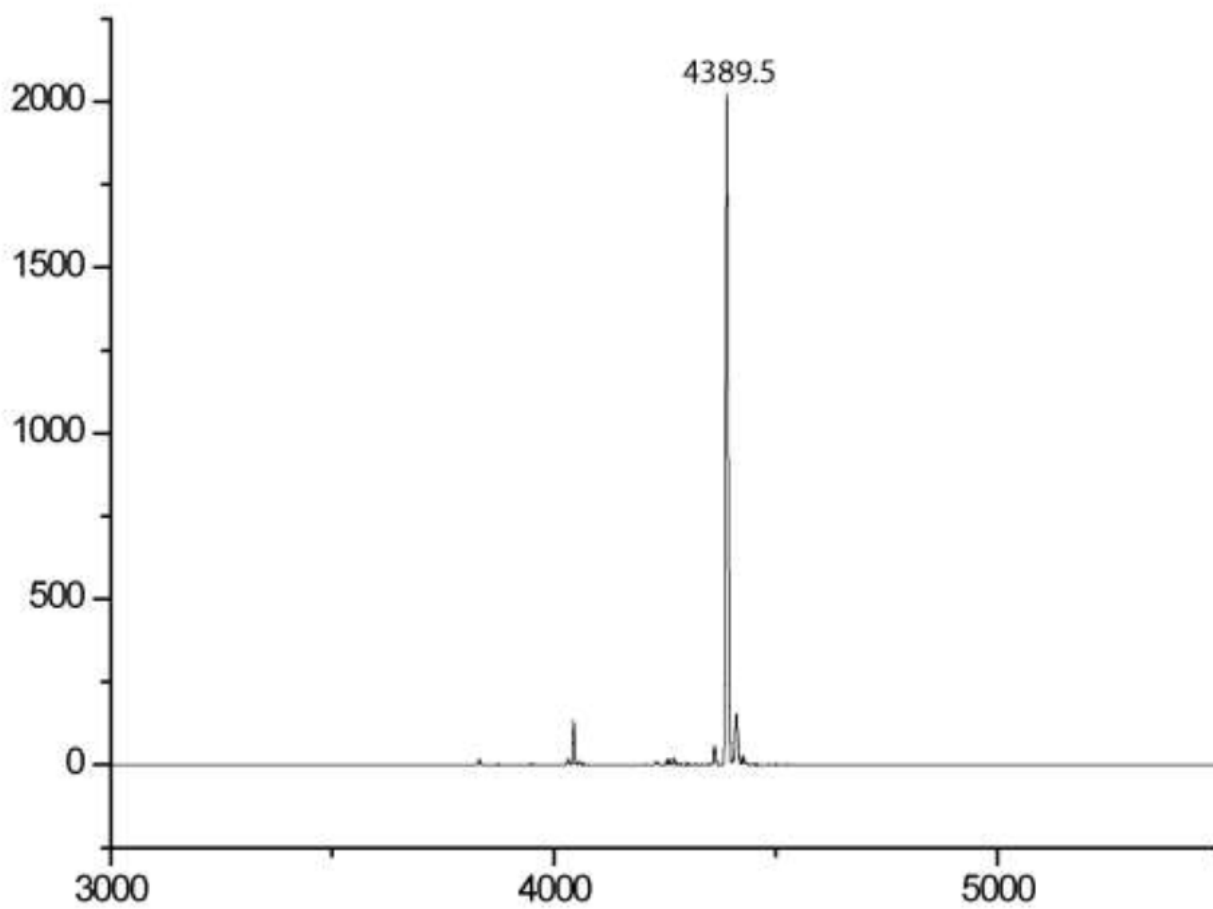
Method 0-70% B in 45 min (for click reactions in solution)

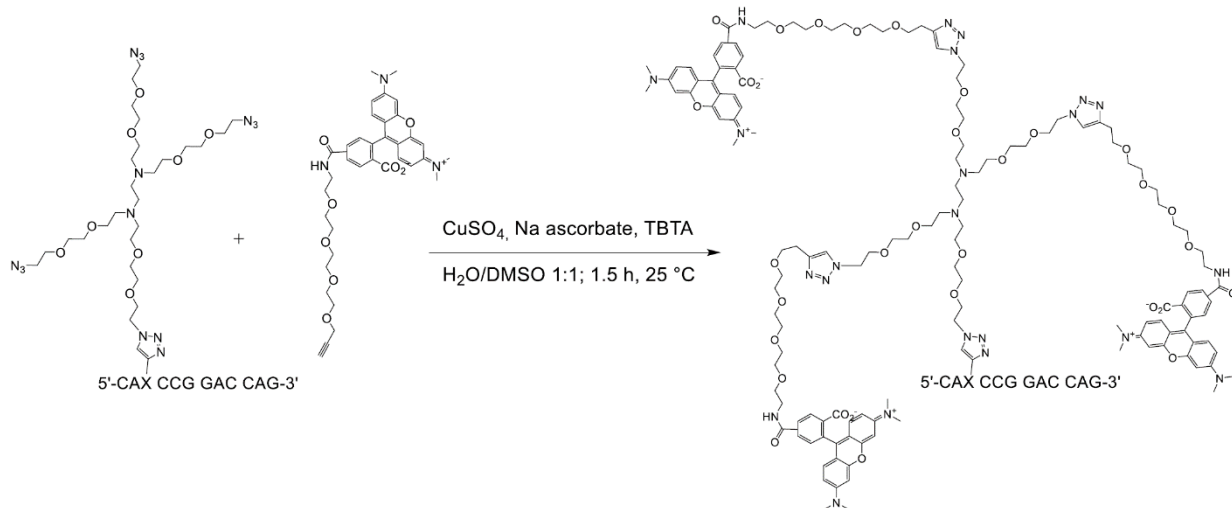


After the click reaction with the oligonucleotide **1** using the **general procedure A**, analysis via RP-HPLC showed a quantitative conversion of the starting material to the clicked products.

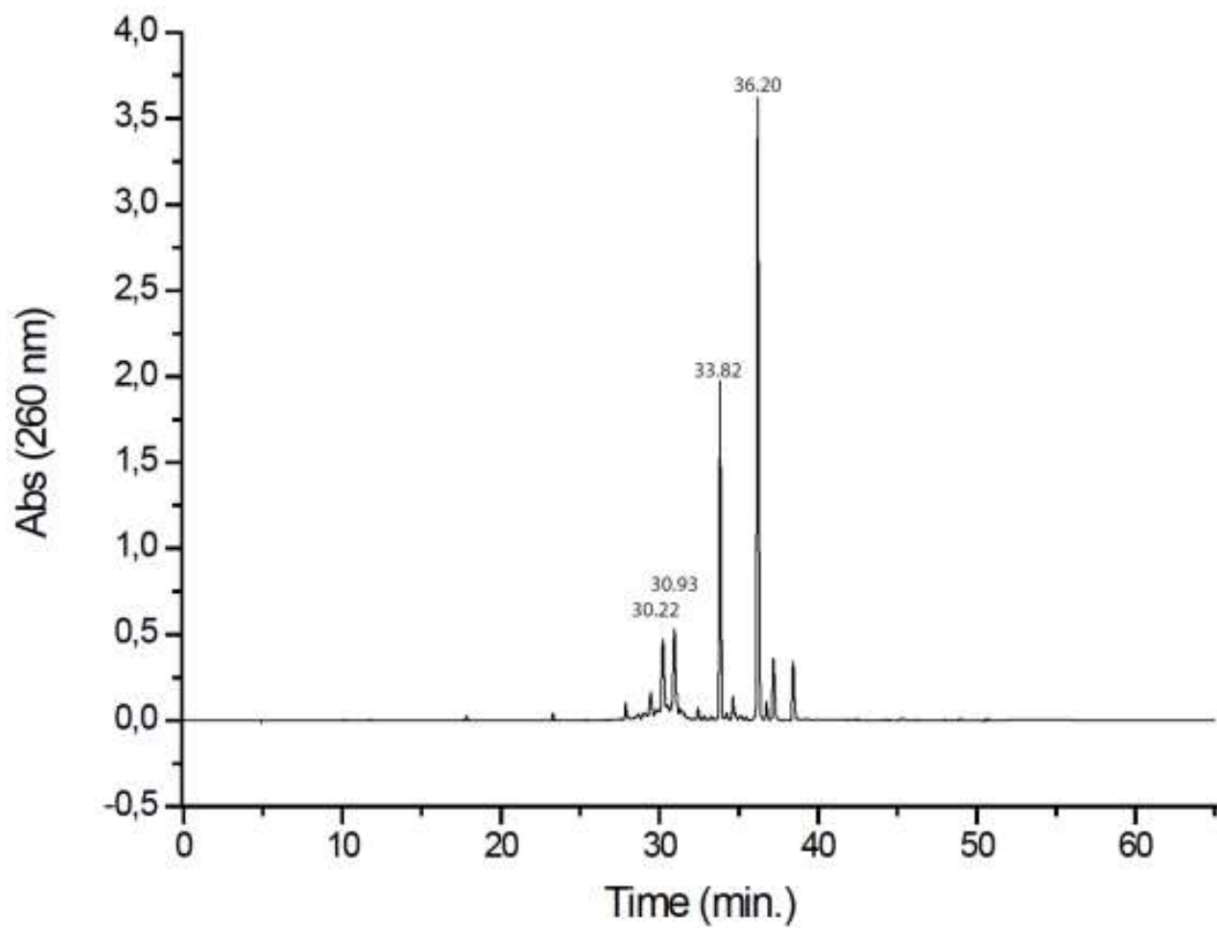


MALDI-TOF-MS: [M] calc. for oligonucleotide **1** + dendrimer = 4393.8 ; found = 4389.5.

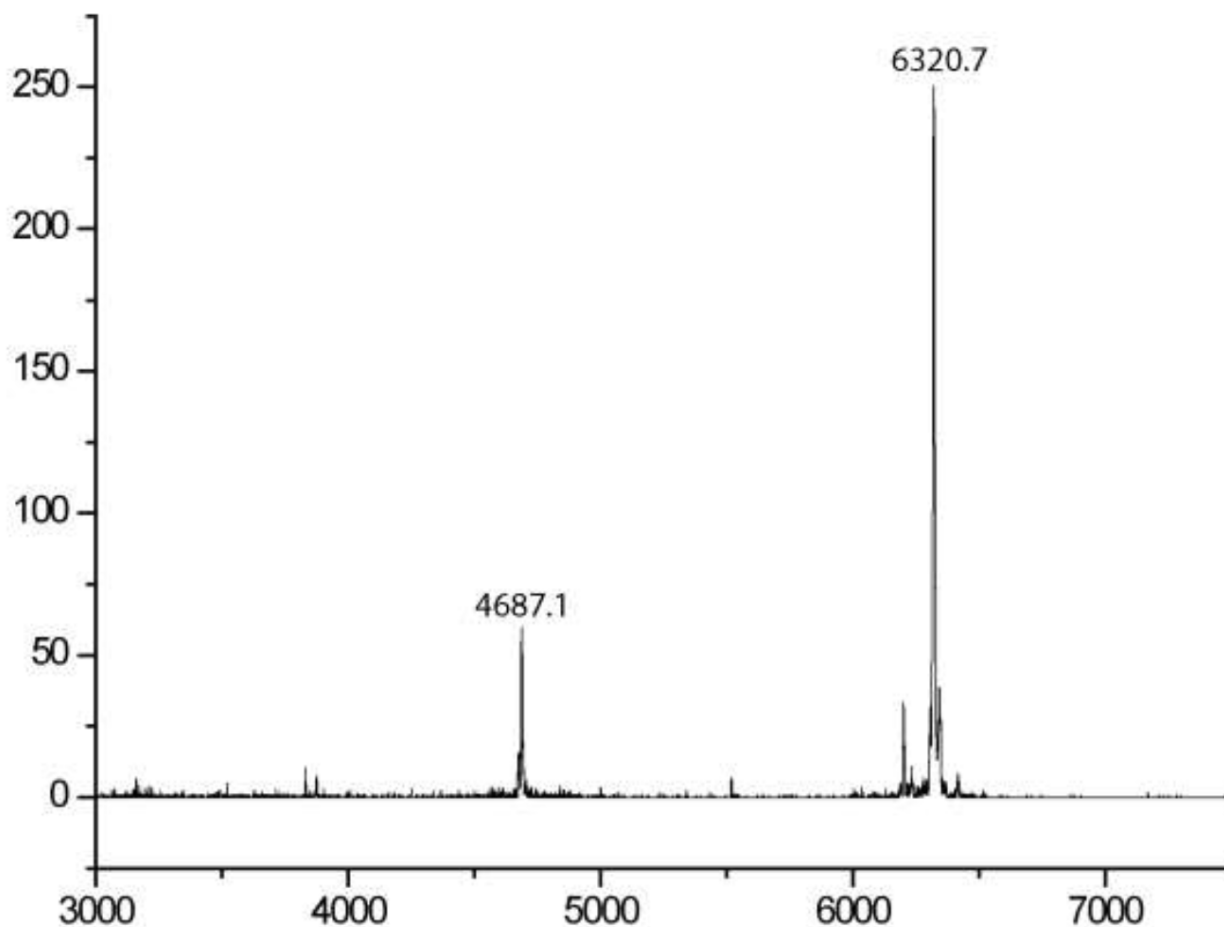


Click 2: Oligonucleotide from Click 1 + 5/6-TAMRA-PEG4-Alkyne

After the click reaction using the **general procedure A**, analysis via RP-HPLC and MALDI-TOF-MS showed a quantitative conversion of the starting material to the clicked products. For the HPLC analysis and purification, the TAMRA maximum absorption wavelength (546 nm) was also monitored to identify the clicked products. The two intense peaks at 33.8 and 36.2 min can be assigned to the unreacted dye, while the product peaks have t_R of 30.22 and 30.93 min (5/6-TAMRA isomers).



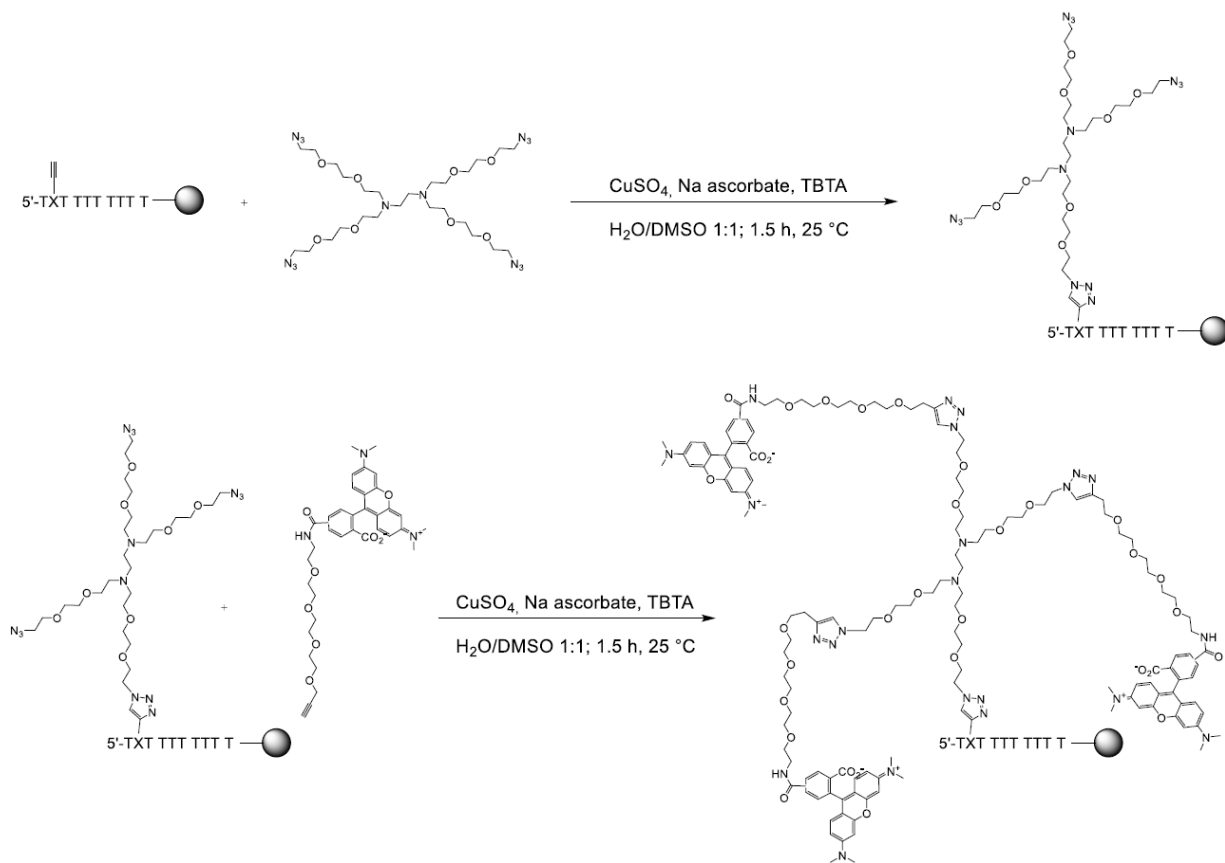
MALDI-TOF-MS: [M] calc. for oligonucleotide **1** + dendrimer + 3 dyes = 3705.4;
found = 6320.7, 4687.1 ([2 oligonucleotides **2** + dendrimer + 2 dyes]²⁻).

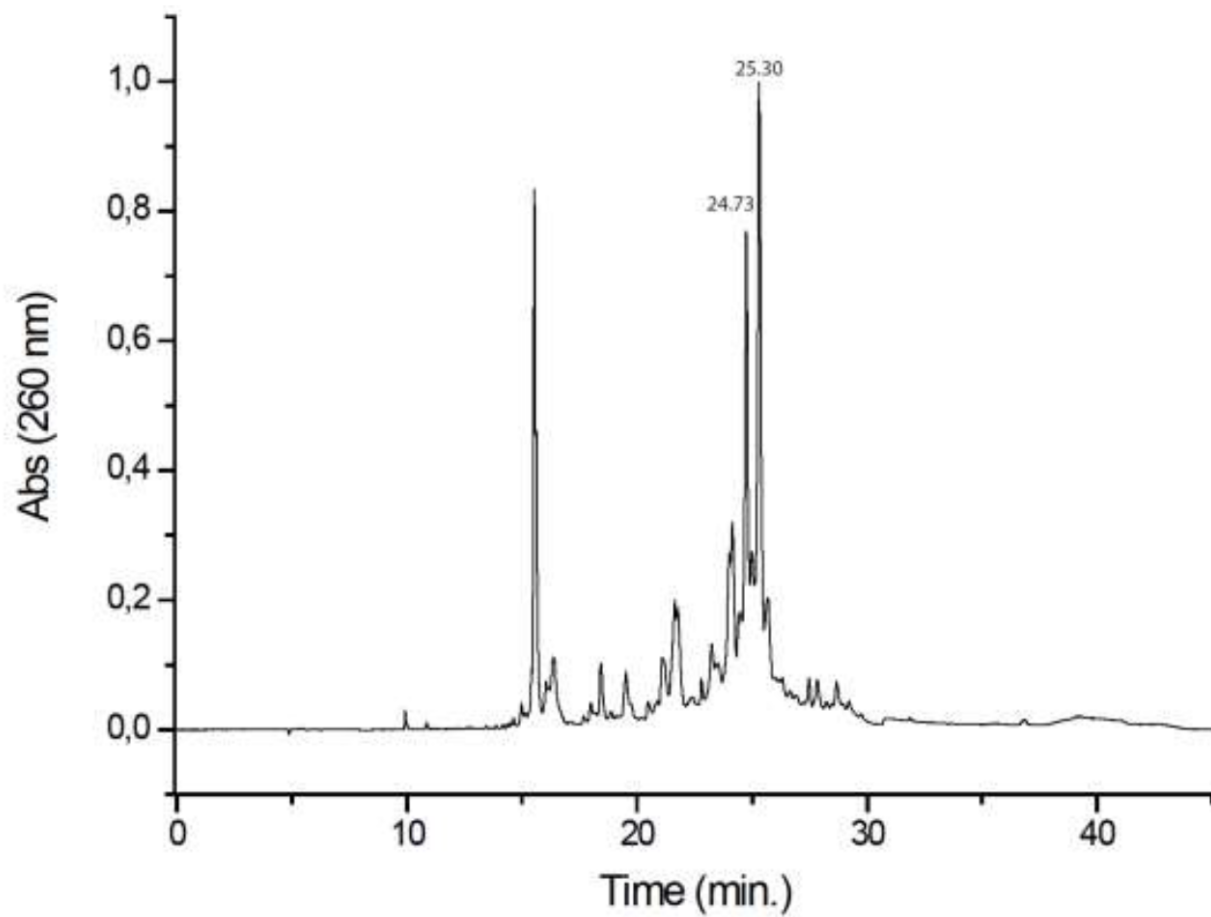


Click reactions on solid phase

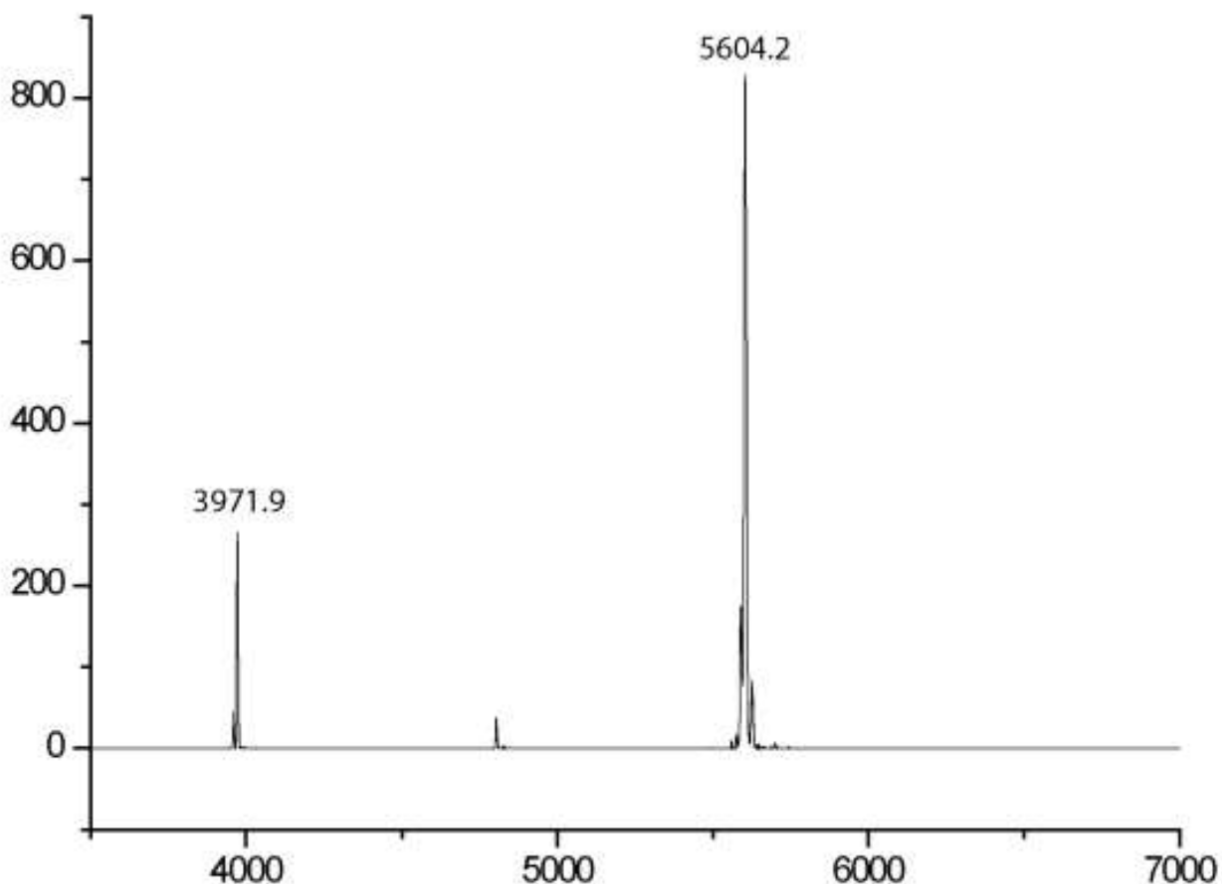
After solid phase synthesis of the **oligonucleotide 2** and DBU deprotection of the cyanoethyl groups of the phosphates, 2 click reactions were performed following the **procedure B** and the final product was analyzed by RP-HPLC and MALDI-TOF-MS.

5. Dendrimer-based signal amplification of click-labelled DNA in situ





MALDI-TOF-MS: [M] calc. for oligonucleotide **2** + dendrimer + 3 dyes = 5612.4; found = 5604.2, 3971.2 (2 oligonucleotides **2** + dendrimer + 2 dyes)²⁻).



Cell culture cell strains and EdU labelling *in vivo*

HeLa, HEK293T and HEK293-GFP (GFP-stable cell line from Amsbio Catalog No. SC001) cells were cultivated at 37 °C in water saturated, CO₂-enriched (5%) atmosphere. DMEM supplemented with 10% fetal bovine serum (FBS) (Invitrogen #10500-064), 1% penicillin and streptomycin (Sigma Aldrich # P0781), was used as growing medium. When reaching a confluence of 70% to 80%, the cells were passaged in a new culture flask. For staining experiments, 1.5 x 10⁴ cells were seeded in each well of a μ -Slide 8 Well from ibidi (ibiTreat, #1.5 polymer coverslip, catalog No. 80826) and cultured for two days or until a density of 80% is reached.

EdU dissolved in DMSO was added to the culture medium to a final concentration of 10 μM for 1 h (HEK-GFP) and 2 h (HEK and HeLa). The control cells without EdU feeding were exposed to the same volume of DMSO biological grade for the same period.

EdU staining *in situ* for the control experiments

All control experiments were accomplished using the EdU-Click kit from Baseclick GmbH containing the correspondent fluorescent dye and following the user manual.

EdU staining *in situ* with the double click approach

After EdU labelling, the cells were washed with phosphate buffered saline (137 mM NaCl, 10 mM Na_2HPO_4 , 1.8 mM KH_2PO_4 , 2.7 mM KCl), supplemented with 0.02% Tween (PBS-T) and fixed with 3.7% Formaldehyde in PBS for 15 minutes at RT. All following steps could be done outside the sterile bench. After two washing steps with PBS-T, the first click cocktail containing 20 μM tetraazide **1** was added to the cells. For this cocktail, the same buffers from the EdU-Click kit from Baseclick were used with the same final concentrations to prove, that any signal enhancement is caused by our dendrimer system. After 1 h incubation, the cells were washed twice with an acetic buffer pH 4.7 for 10 minutes each followed by two short washing steps with PBS-T.

The second click cocktail containing the dye-alkyne to a final concentration of 5 μM was then prepared and added to the cells and incubated for 30 minutes at RT. For the positive control, 20 μM of dye-azide were used. Light was avoided to prevent bleaching of the dyes. After staining, the cells were washed twice with a saturated solution of guanidinium isocyanate for 10 minutes respectively followed by two washing steps with PBS-T. When preparing the click cocktails, all buffers have to be fresh. If precipitation or changes of the colors happen, use another bench of the buffers or solutions. Cells were then stained with 200 ng/ μl DAPI for 10 minutes at RT and washed twice with PBS-T.

EdU staining *in situ* with the triple click approach

The same procedure, as described above, was used. After the first click reaction with 20 μM tetraazide **1** and the washing steps with acetic buffer and PBS-T, the second click cocktail containing 5 μM tetraalkyne **2** was added and incubated for 1 h at RT. After two washing steps with PBS-T, the click cocktail containing 20 μM dye-azide was then prepared and added to the cells and incubated for 30 minutes at RT. After staining, the cells were washed twice with a saturated solution of guanidinium isocyanate for each 10 minutes followed by two washing steps with PBS-T. Cells were then stained with 200 ng/ μl DAPI for 10 minutes at RT and washed twice with PBS-T.

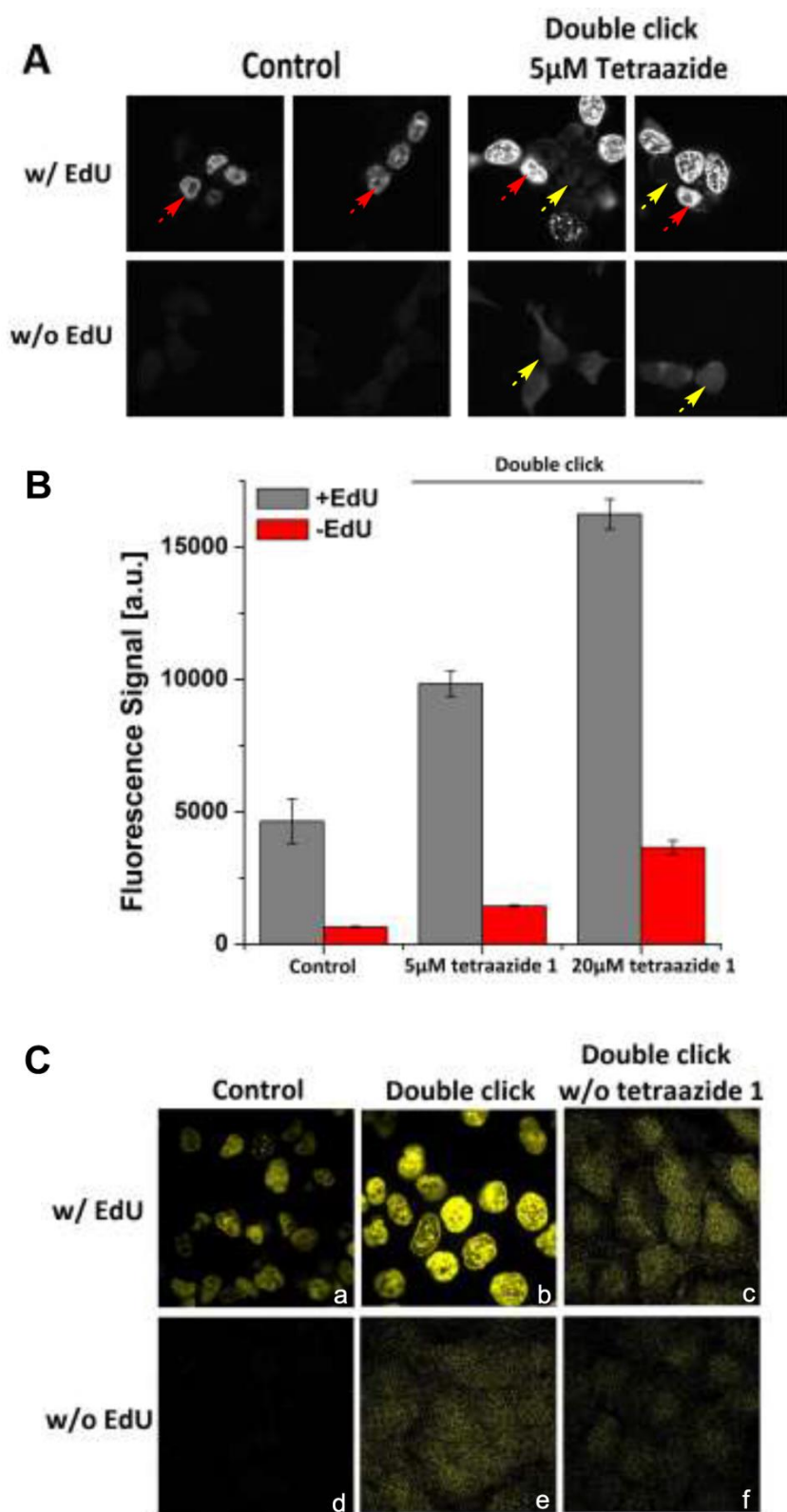


Figure S5.4: Development of the double click assay (simple dendrimer). A) A strong increase of the specific signal intensity (red arrows) was achieved with 5 μ M tetraazide 1

and 5 μM Cyanine 3-alkyne. This enhancement was coupled with an increase of background fluorescence (yellow arrows), which was not seen in the control cells stained using the standard *in situ* click assay with 5 μM dye azide. **B)** Using 20 μM tetraazide **1**, an enhancement of the signal intensity and the background were measured. **C)** To prove, that the signal intensity was generated by the combination of the tetraazide and the Cyanine 3-alkyne system, control experiments were done with EdU and Cyanine 3-alkyne (5 μM) (c), without EdU, with tetraazide and Cyanine 3-alkyne (5 μM) (e) and without EdU, without tetraazide and with Cyanine 3-alkyne (5 μM) (f). Positive control was performed with EdU, tetraazide and Cyanine 3-alkyne (5 μM). The negative controls c, e and f show only background fluorescence without any kind of specific signal. Controls a and d were stained with 20 μM Cyanine 3-azide.

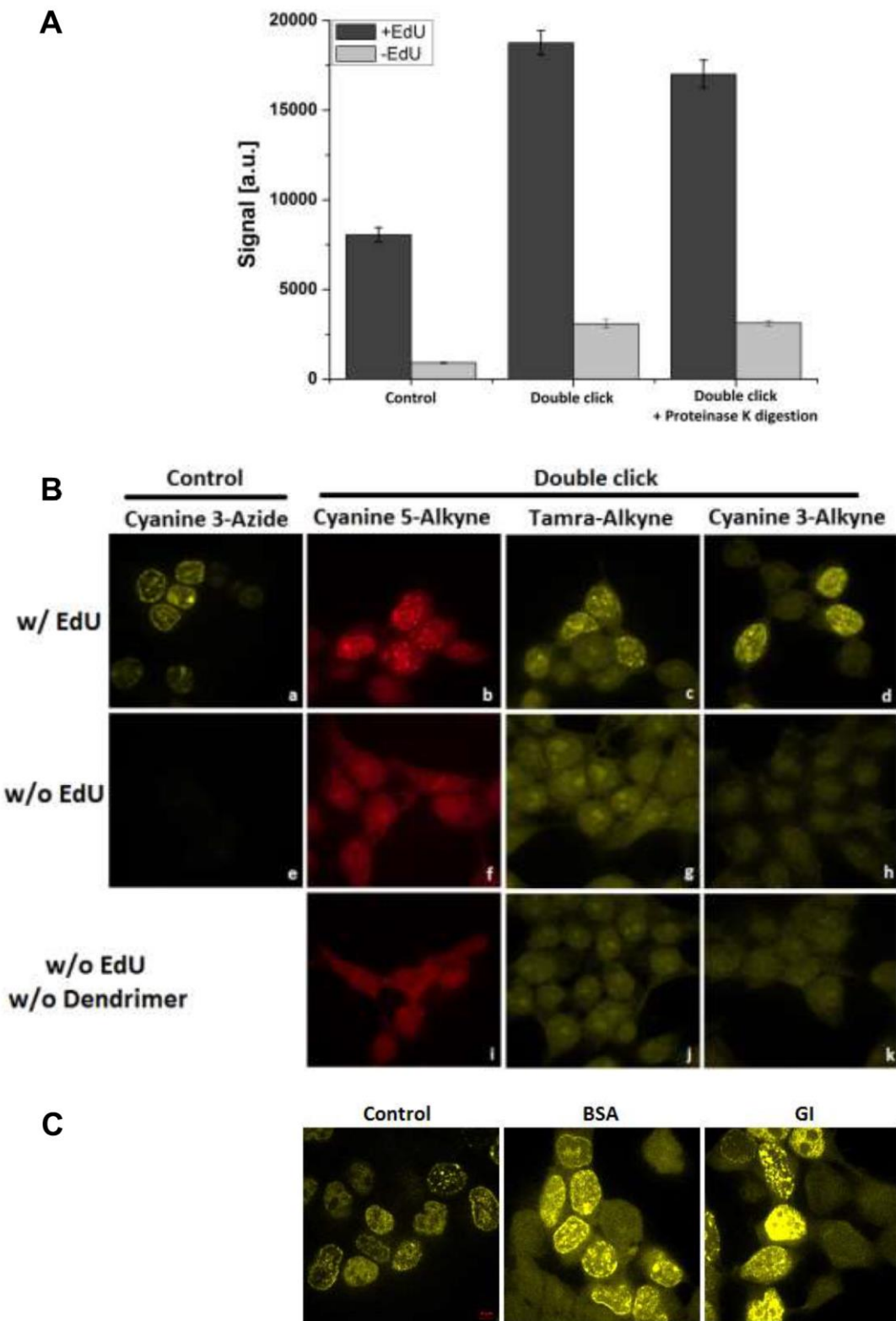
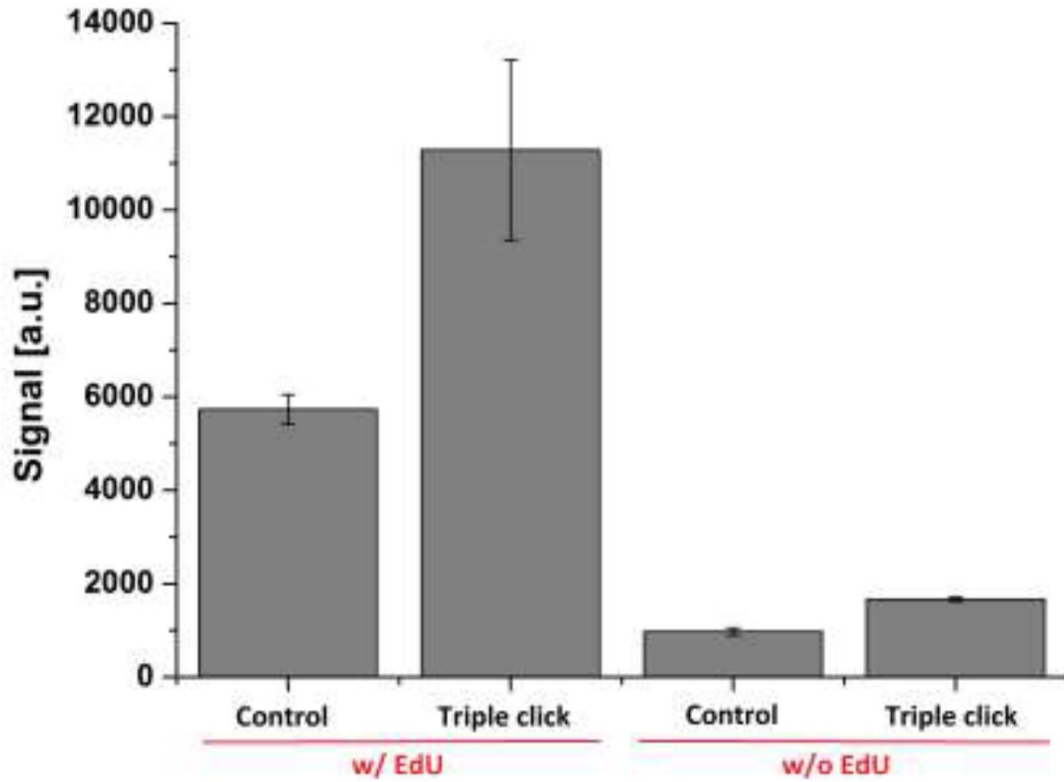


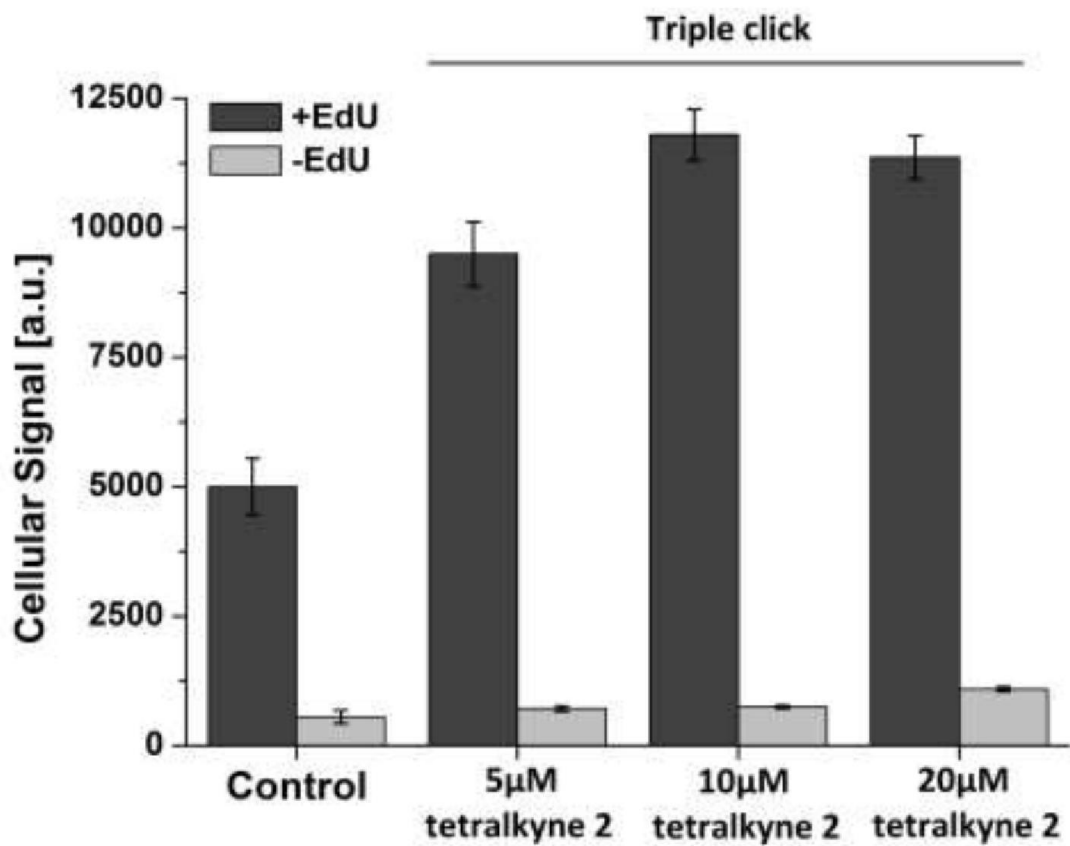
Figure S5.5: Improvement of the signal to background ratio of the double click assay.
A) Digestion of proteins in order to reduce cross linkers, which could be binding sides for

the alkyne-dye. Fixed and permeabilized cells were digested with 50 µg/ml Proteinase K at 37 °C for 1 h before performing double click assay with dendrimer **1** (20 µM) and Cyanine 3-alkyne (5 µM). Control cells were stained using the double click assay without Proteinase K digestion and with 20 µM Cyanine 3-azide. Positive control was the standard *in situ* click assay with cyanine 3-azide (20 µM). The specific signal intensity is after digestion slightly decreased. Negative controls without EdU labelling show no decrease in background signal intensity. **B)** Screening for dye alkyne. Positive control cells (a) labeled with EdU were stained with Cyanine 3-azide (20 µM). For the double click assay, cells were labeled with EdU and stained using dendrimer **1** (5 µM) followed by click reactions using either Cyanine 5-alkyne (b), Tamra-alkyne (c) or Cyanine 3-alkyne (d) (each 5 µM). The double click assay was successful using the different dye-alkynes. For the negative controls, cells were not labeled with EdU but either stained with the dendrimer **1** (20 µM) and the corresponding dye-alkyne (5 µM) (e-h) or only with the dye-alkyne (5 µM) (i-k). i-k were washed additionally over night with 3% BSA in PBS. They show how the dye-alkynes stuck strongly to the cells in an unspecific way. **C)** Screening for wash buffers. To decrease the unspecific bound dye-alkyne, a screening for organic (DMSO, DMF, Acetonitril, MeOH, EtOH) and inorganic washing solvents (H₂O, Urea, guanidinium isocyanate, BSA) was performed with different incubation times and temperatures (data not shown). The best washing buffer was guanidinium isocyanate (GI), which reduces the background signal of Tamra-alkyne by about 50% in comparison to 3% BSA in PBS, when used twice after the click reaction of the dye-alkyne and before DAPI staining for 10 minutes at RT.

A



B



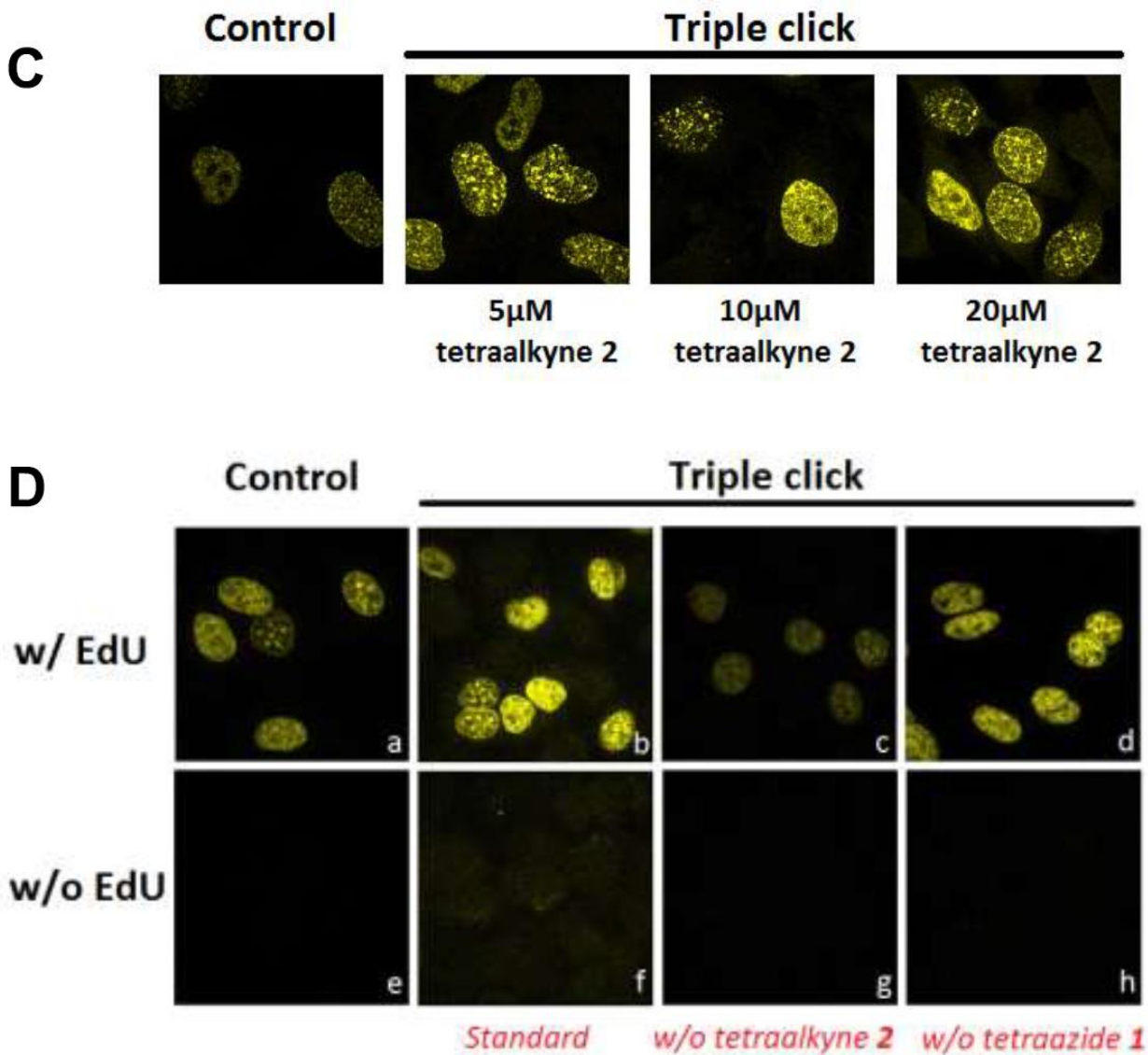


Figure S5.6: Development of the triple click assay (double dendrimer). **A)** An increase of the signal intensity and a reduced background signal were achieved using the double dendrimer approach. **B)** and **C)** Screening for the appropriate concentration of tetraalkyne 2. A titration for the concentration was done using 5, 10 and 20 μM of the tetraalkyne 2. The background intensity was dramatically reduced compared to the simple dendrimer assay. Furthermore, it was as low as the background in the control cells. The specific signal was doubled already with 5 μM tetraalkyne 2. **D)** In order to test, if the increase of the specific signal intensity is a result of the combination of 1, 2 and Tamra-azide, we performed control experiments either with 1 and without 2 (d, g) or with 2 and without 1 (d, h) respectively in presence or absence of EdU. Positive controls were the nondendrimer assay

with (a) and without (e) EdU. c) shows that after the first click reaction, most of the genomic alkynes reacted with tetraazide **1** resulting in a very weak specific signal. d) shows almost the same signal intensity as the positive control (a), because **1** cannot react with the genomic alkynes and is washed away before the click reaction with Tamra-azide.

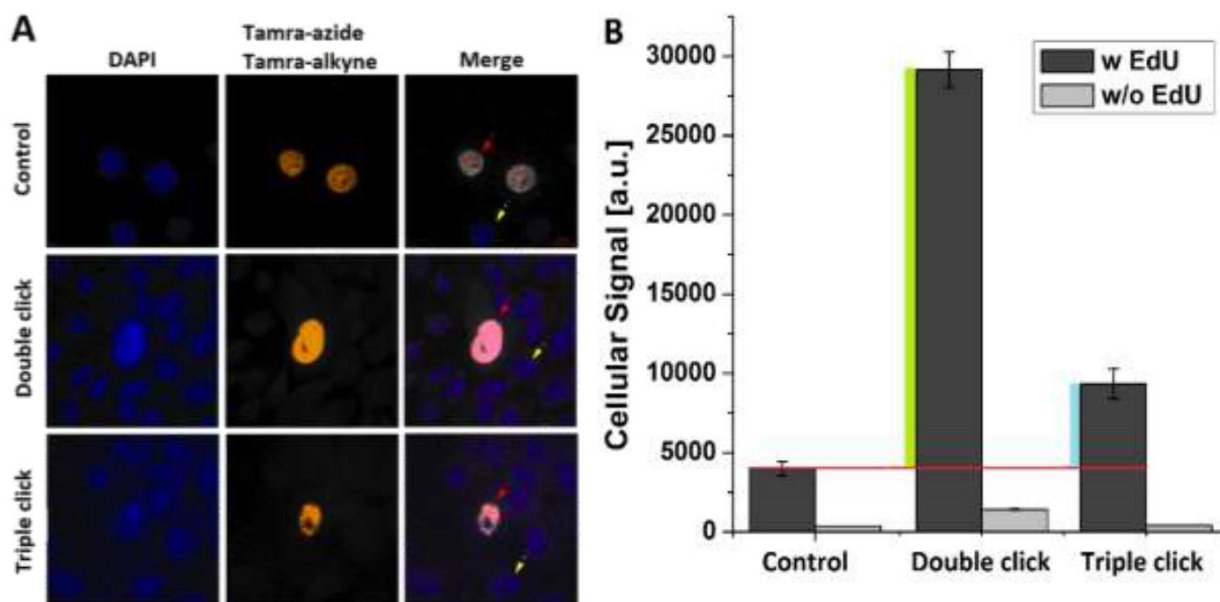


Figure S5.7: Direct comparison between the non-dendrimer, the double and triple click dendrimer approaches. A) Comparison of microscope images. The strongest signal of proliferating cells (red arrows) is achieved using the double click (20 μ M tetraazide **1** followed by 5 μ M Tamra-alkyne). The triple click (20 μ M tetraazide **1** followed by 5 μ M tetraalkyne **2** and 20 μ M Tamra-azide) showed a doubling of the specific signal intensity. Yellow arrows show non-proliferating cells **B)** Statistical quantifications. These quantifications approve the signal enhancement seen under the fluorescent microscope. The signal intensity is at least doubled using the triple click and four times higher than the control using the double click approach. All other results obtained so far were confirmed. Due to the binding of several fluorescent dyes at the dendrimer **2** using the triple click, the cellular signal intensity is reduced compared to double click approach using only dendrimer **1**. The reason for it could be the self-quenching of the fluorescent dyes.

5.4.4. High throughput screening

HeLa cells were seeded with different cell number (100, 500, 1000, 2000, 4000, 8000 cells) in a 96-well black microplate with a flat bottom (VWR) for 48 h. For each cell density, a duplicate was performed. Cells were fed with 10 μM EdU for 2 h. After fixation with 3.7% PFA in PBS at RT and permeabilization with 0.5% Triton in PBS-T for 15 min at RT, cells were incubated with 20 μM tetraazide **1** followed by incubation with 5 μM Tamra-alkyne for the double click assay. Cells were incubated with 20 μM tetraazide **1** followed by 5 μM tetraalkyne **2** than 20 μM Tamra-azide for the triple click assay. All incubations were done in presence of Cu(I). The control cells were reacted only with 20 μM Tamraazide in presence of Cu(I). Negative control cells without EdU labeling were reacted with the same corresponding reagents. The cellular intensities were measured with a microplate reader from Tecan for the positive and negative controls. Background intensity was measured and subtracted in order to calculate the specific signal intensity.

5.4.5. Microscopy and image analysis:

Confocal fluorescence images were acquired by the commercially available Zeiss Cell Observer SD equipped with a Yokogawa spinning disk unit. Single slices of multiple nuclei within one field of view were acquired. The laser power and exposure settings were equal for throughout the image acquisition. Using ImageJ, a rolling ball background subtraction was performed, followed by determination of the gray value of the brightest pixel (GVBP). Then, a threshold at 0.25 x GVBP was applied and the mean signal of the pixels above this threshold was measured. The mean of ten fields of view was taken and defined as signal for the respective condition.

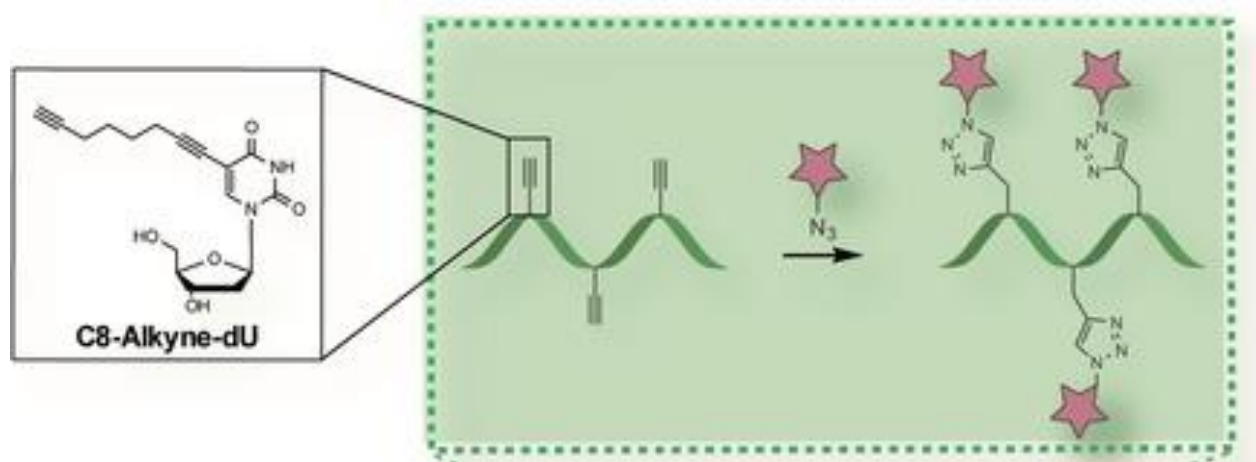
6. Supersensitive multifluorophore RNA-FISH for early virus detection and flow-FISH by using click chemistry

This chapter is based on the following publication:

Raddaoui N, Croce S, Geiger F, Borodavka A, Möckl L, Stazzoni S, Viverge B, Bräuchle C, Frischmuth T, Engelke H, Carell T. Supersensitive Multifluorophore RNA-FISH for Early Virus Detection and Flow-FISH by Using Click Chemistry. *Chembiochem*. 2020; 21:1–6.

Abstract

More is less! Increasing the number of fluorophores per oligonucleotide probe allows superb sensitivity, as the fewer the number of probes needed, the lower the background noise. With just a small number of triply labeled strands, RNA-FISH-based detection of RNA transcripts was possible in live cells, and a virus could be detected after only 4 hours.



The reliable detection of transcription events through the quantification of the corresponding mRNA is of paramount importance for the diagnostics of infections and diseases. The quantification and localization analysis of the transcripts of a particular gene allows disease states to be characterized more directly compared to an analysis on the transcriptome wide level. This is particularly needed for the early detection of virus infections as now required for emergent viral diseases, e. g. Covid-19. *In situ* mRNA analysis,

however, is a formidable challenge and currently performed with sets of single-fluorophore-containing oligonucleotide probes that hybridize to the mRNA in question. Often a large number of probe strands (>30) are required to get a reliable signal. The more oligonucleotide probes are used, however, the higher the potential off-target binding effects that create background noise. Here, we used click chemistry and alkyne-modified DNA oligonucleotides to prepare multiple-fluorophore-containing probes. We found that these multiple-dye probes allow reliable detection and direct visualization of mRNA with only a very small number (5–10) of probe strands. The new method enabled the *in situ* detection of viral transcripts as early as 4 hours after infection.

6.1. Introduction

Gene expression varies significantly between individual cells and it is strongly altered in disease states. Viral infections for example lead to early transcription of virus-specific genes that could be exploited for an early diagnosis and characterization of the infection. In general, basically all malfunctioning processes in cells induce transcriptional changes [1, 2]. These go in hand with altered levels of messenger RNAs (mRNAs). In extreme cases disease related mRNA may not be present at all in the normal state. In most cases however, the levels of specific mRNA will be changed, which requires reliable methods to quantify mRNA transcripts. Detection and quantification of a specific mRNA is thus highly desirable from a diagnostic point of view. Particularly informative are methods that allow the quantification of mRNA levels with spatial resolution. Currently, however, intracellular localization and quantification of mRNA faces a number of challenges that hinder routine use. The most common way to detect mRNA (or other RNAs) in cells is fluorescence *in situ* hybridization (RNA-FISH) [3]. The method reveals localization patterns of individual RNA transcripts in cells or tissues and as such, RNA-FISH is the method of choice for quantitative single-cell transcriptomic studies [4-8]. The currently available technology behind RNA-FISH technologies is based on multiple (up to 50) individual anti-sense single-stranded (ss) DNA probes, which are approximately 22 nucleotides long. Each probe oligonucleotide carries a single fluorophore, which is typically introduced as its activated NHS ester to an amino

group present at the 3'-end of the probe [4, 5]. The pooled fluorescent ssDNA probes are finally added to fixed and permeabilized cells for hybridization with the target RNA. The large number of probe strands in such experiments is needed to create a sufficiently strong fluorescence signal. However, generally the larger the number of probe oligonucleotides that are used, the larger is often also off-target staining, which obscures the signal-to-noise ratio. A solution to the problem is deconvolution software that is able to increase the specific signal [9]. From a chemical point of view reduction of the number of probe strands is desirable and this has led to efforts to modify the probe oligonucleotides with, for example, LNA to increase binding. Importantly, mRNA analysis based on flow-cytometry is so far very challenging with contemporary RNA-FISH.

Here we report a small FISH-probe set for mRNA, where every probe contains three fluorophores instead of just one. These multichromophore probes were conveniently prepared using the Cu^I-catalyzed azide-alkyne click reaction [10-19]. In order to avoid stacking of the fluorophores on top of each other, which might induce self-quenching, we chose a fluorophores with two additional sulfonate groups, which provide two negative charges per fluorophore. This is supposed to minimize the interaction with the fluorophores with each other and with the negatively charged DNA. Indeed, with this design a small number of probe strands (5–10) was found to be sufficient for the visualization of RNA transcripts. The new probes design allowed not only transcript quantification and localization by microscopy, but it also enabled transcript analysis using flow-cytometry.

6.2. Results and discussion

The new procedure based on click chemistry is illustrated in Figure 6.1. As a test-system for the mRNA-FISH we used a HEK293T cell line transfected with a plasmid containing the gene coding for the enhanced green fluorescent protein (eGFP). We synthesized ten DNA probe oligonucleotides targeting specific areas of the eGFP-mRNA transcript, with each one containing 22 nucleotides (Figure S6.1 in the Supporting Information). Into each of the ten DNA probe strands we inserted three C8-alkyne-dU building blocks at former dT positions (Figure 6.1 and Table S6.1) using phosphoramidites that we had developed previously [20].

6.2. Results and discussion

The ten triple-alkyne DNA probes were finally purified by HPLC and individually subjected to a click reaction with Eterneon-Red 645 azide (cyanine-5 analogue). The so obtained three Eterneon containing DNA probes (10×3) were finally purified by a simple ethanol precipitation. Due to the high efficiency of the click reaction, no further HPLC purification of the probes was required. For the probes prepared for the virus experiment (*vide infra*) we also confirmed the purity of the obtained probe strand by HPL chromatography (example shown in Figure S6.2). HPL chromatographic analysis of our 10×3 probe set proved good absorption and fluorescence properties (Figures S6.3 and S6.4).

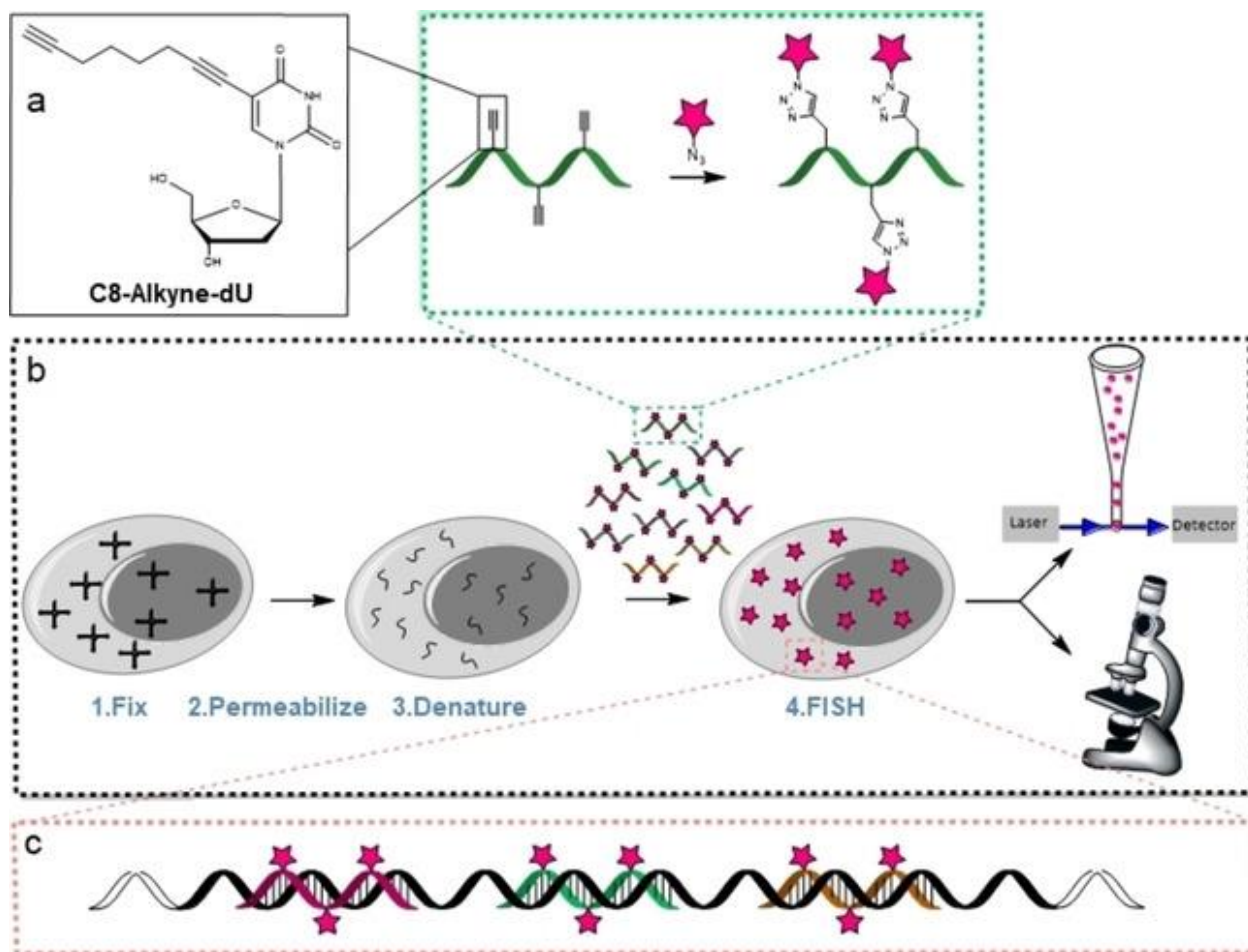


Figure 6.1: Depiction of RNA-FISH and schematic representation of the probe synthesis. a) Synthetic oligonucleotides with C8-alkyne-dU modifications in various positions were individually conjugated with a fluorescent dye azide. After reaction, the oligonucleotides were mixed to a probe set. b) The probe set was hybridized to the mRNA. After in situ

hybridization, the mRNA molecules can be detected by flow-cytometry and/or microscopy.
c) Depiction of the probes labeled with click chemistry hybridized to the target mRNA.

In order to compare the obtained data with the state-of-the-art we performed in parallel studies with a commercially available RNA-FISH probe set. The provider suggested for the requested detection a set of 30 probe oligonucleotides (Table S6.2) each one carrying one Quasar 670 fluorophore. The purchased oligonucleotide probes are shown in Figure S6.1.

In order to investigate the ability to detect RNA, we first performed *in vitro* experiments with isolated total-RNA obtained from wild-type HEK293T and HEK293T-eGFP, stably expressing the eGFP gene. The data are depicted in Figure S6.5, we obtained clearly visible spots with the (10×3) triple modified probes. Importantly, the 10×3 set provided bright spots even without the use of the special deconvolution software. In order to exclude that the high spot density obtained with the new probes is caused by unspecific binding, we performed a negative control with total RNA isolated from HEK293T cells not expressing the eGFP-protein (control probes). Here, as expected far fewer spots were obtained, which rules out this possibility.

After these *in vitro* experiments, we next investigated the properties of the 10×3 probe set in fixed cells (Figure 6.2). To this end, the HEK293T cells were grown on 8-well μ -Slide (ibidi) and transfected with a plasmid DNA containing a gene coding for eGFP. The cells were fixed and permeabilized using the standard protocols (see Materials in the Appendix). We next added the mixture containing our 10×3 probe set and as a positive control, we also performed an experiment with the 30×1 set. Both probe sets were incubated over night at 37 °C. After washing, we analyzed the cells by fluorescence microscopy. The result of the study is shown in Figure 6.2a. In order to quantify the background fluorescence signal, we calculated the signal intensity obtained after *in situ* hybridization of the probe sets lacking the eGFP-locus. This background signals for the 10×3 and 30×1 experiment were subtracted from 10×3 and 30×1 data sets obtained with the eGFP expressing cells (Figure 6.2b). As depicted in Figure 6.2a we saw for the 10×3 probe set diffraction-limited spots were detected showing clearly the presence of the complementary mRNAs (Figure 6.2a, red channel). The signal-to-noise ratio was strongly increased. A small caveat

is that we noted a slightly increased background signal with the 10×3 probe set (Figure 6.2b, dark gray bar) likely because the oligonucleotide containing three dyes are more hydrophobic, which may give slightly increased unspecific binding, which increases the background. This effect is obviously overcompensated by the strong increase of the fluorescence signal obtained from specific binding events.

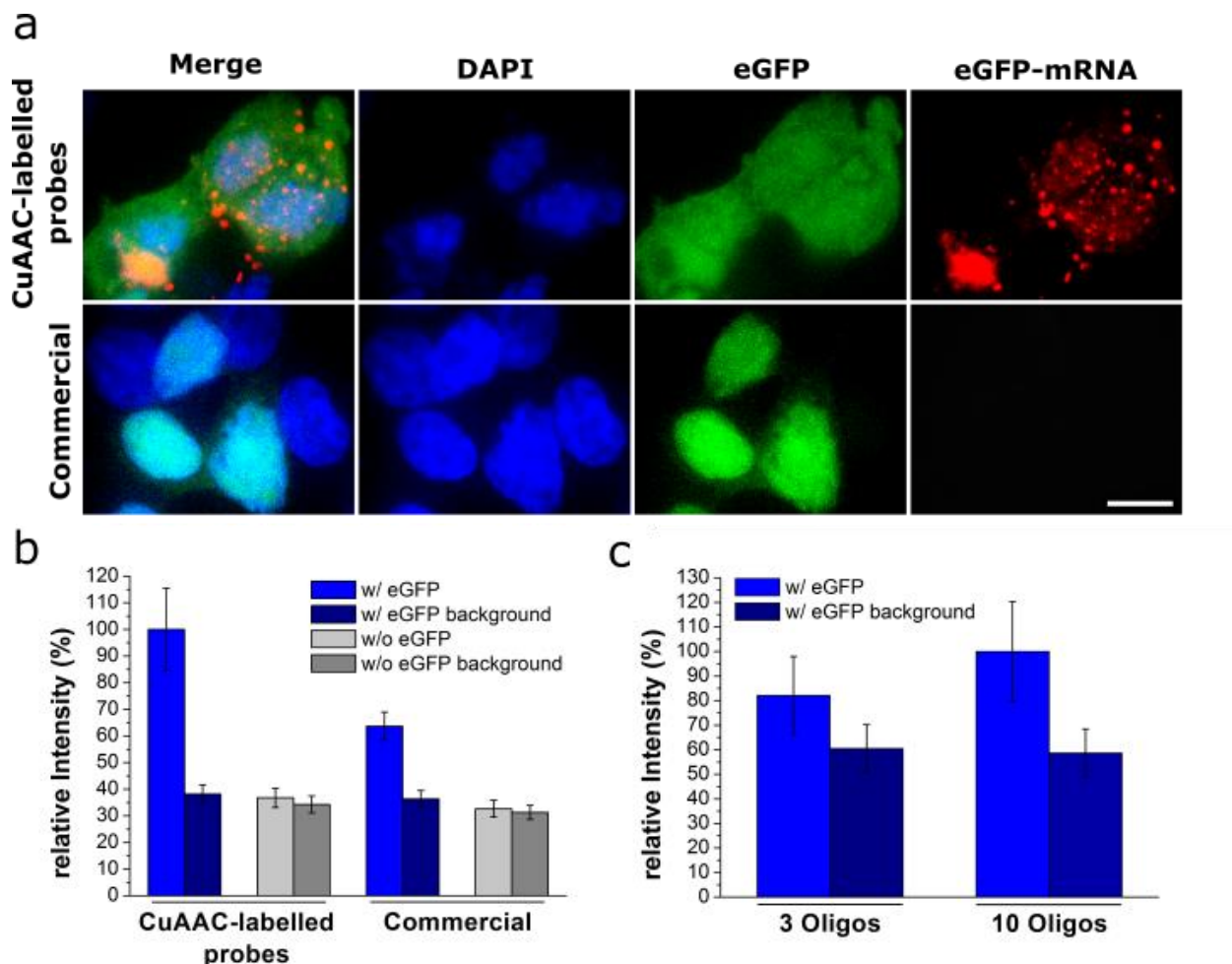


Figure 6.2: mRNA of eGFP-expressing HEK cells labeled with 10×3 and with 30×1 probe sets. a) FISH microscopy images of the 10×3 and 30×1 set of probes (scale bar: 10 μm) b) Comparison of the signal and background intensities. c) Signal and background obtained with CuAAC-labeled probes when using 3 and 10 oligos.

We next experimented with different number of probe strands and dye loading and found that the most reproducible data were indeed obtained with ten oligonucleotide probe

strands containing each three fluorophores. In our hands this probe design provided in all investigated cases the best signal-to-noise ratios (Figures 6.2c and S6.6).

We next investigated if we could further reduce the background signal when we performed the click reaction after *in situ* hybridization as shown in (Figure S6.7). For this study, we used a set of 10 probe strands with 3 alkyne units, hybridized them with the cellular mRNA and performed the CuAAC-reaction subsequently *in situ* with a TAMRA azide. While the signal-to-noise ratio indeed improved, we noted that we had to perform extensive washing in order to remove additional dye, which is typically used in large excess. This makes this procedure a little more accurate but cumbersome to perform.

We next investigated if the performance of the 10×3 probe design allows to detect mRNA even using flow-cytometry in a mixed cell population. For the experiment, we mixed HEK293T cells with and without eGFP-expression in a ratio 20:1 (95% HEK293T+5% HEK293T-eGFP). Then, flow-cytometric measurements of the mixed cell populations were performed at $\lambda_{\text{ex}}=488 \text{ nm}/\lambda_{\text{em}}=530 \text{ nm}$ for the detection of the eGFP protein. The correct ratio of the mixed cell population was nicely reproduced (Figure 6.3a). We then used the flow-FISH protocol described by Arrigucci et al. [17], which involves trypsinization and resuspension of cells. The cells in suspension were permeabilized, fixed and subsequently incubated with the probe sets. Again, we performed the study with the new 10×3 set in comparison to a classical 30×1 design. When we measured at $\lambda_{\text{ex}}=633 \text{ nm}/\lambda_{\text{em}}=660 \text{ nm}$, which is suitable for both the Eterneon-Red 645 azide and the Quasar 670 dye, in the absence of hybridized probes, a single population was observed (Figure S6.8i). The upper plot of Figure 6.3b shows the hybridization experiment using the classical probe set at 0.05 ng/ μL . Here, only a single population containing both GFP-positive and GFP-negative cells was detected at 660 nm. When the 10×3 probe set was used however at the same concentration (lower plot), the GFP-positive population nicely separated from the GFP-negative cells. When the separated population was gated (in blue), the exact proportion of cells expressing the eGFP was observed for the two different detection wavelengths. The same result with the classical 30×1 probe set was only obtained, when the concentration was increased fourfold to 0.2 ng DNA/ μL (Figure S6.8ii). These flow-FISH data show again that the 10×3 probe allows to perform flow-FISH.

6.2. Results and discussion

Although an exact comparison between the 10×3 and the 30×1 probe sets is not possible, because of the differences in the fluorophore, the connectivity of the fluorophore to the probe and the quality of the strands, we believe that the data support the idea that flow-FISH is possible with our new probe design that has a limited number of probe oligonucleotides each one carrying three fluorophores.

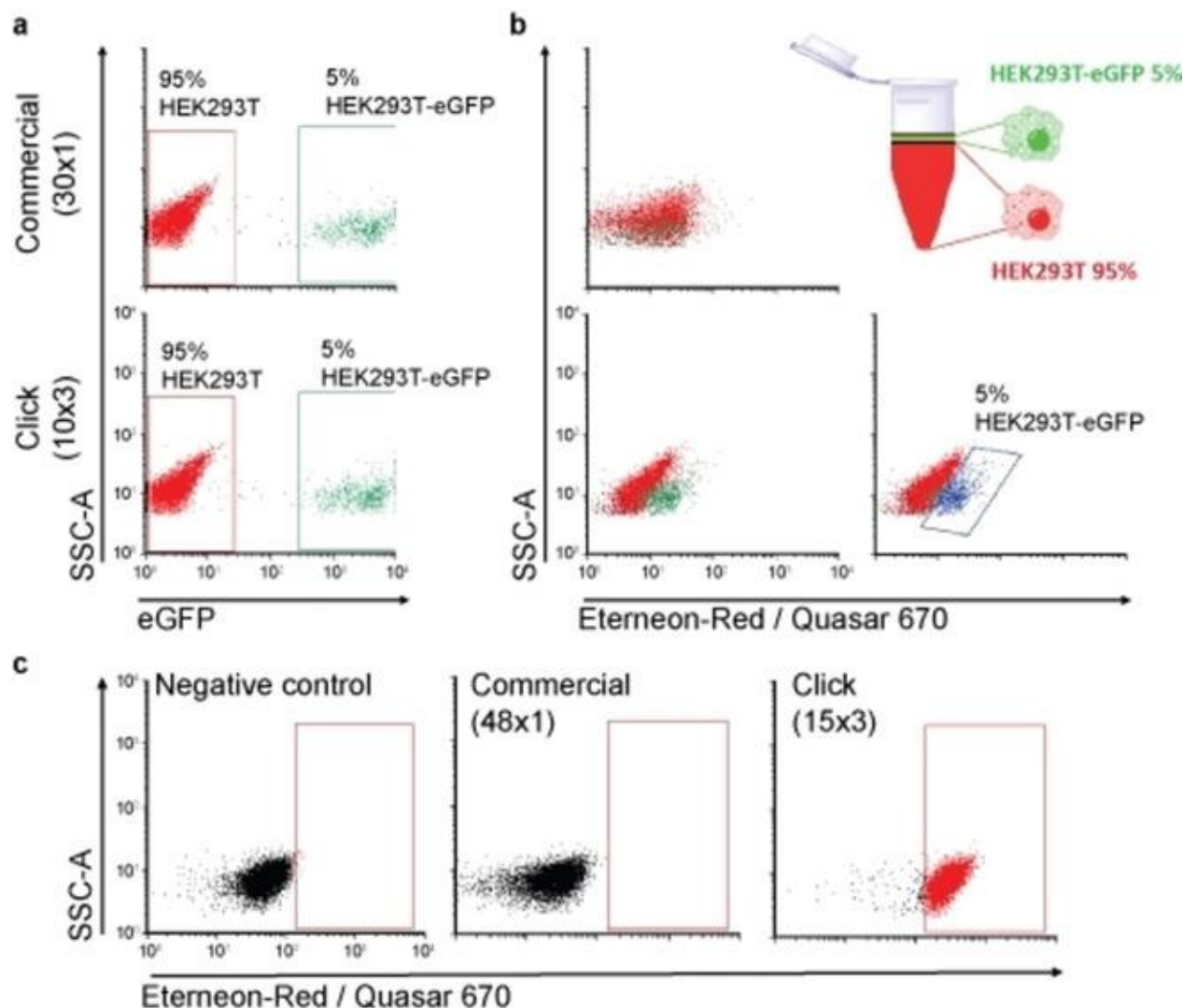


Figure 6.3: Flow cytometry analysis of mixed HEK293T and HEK293T expressing eGFP in a ratio 20:1. a) Mixing ratio determined on the basis of eGFP fluorescence. b) Mixing ratio determined by flow-FISH. At 0.05 ng/ μ L of probe, separation was only possible for the 10×3 set and establishes the same ratio when gated, in blue (5%). c) Flow-FISH for the detection of the endogenous ABL transcript.

In order to show that the new probe oligonucleotides are able to report transcription of a relevant endogenous gene by flow-cytometry, we next tested if the above method would be suitable for the detection of the ABL1-transcript. This time, we used a slightly larger 15×3 probe set. In order to again obtain comparative information we compared our design with a reported detection that used in this case 48 single labelled oligonucleotides (Semrau et al.) [5]. The results are depicted in Figure 6.3 c. While the 15×3 probe set with only 0.05 ng DNA/μL provides a clear shift in fluorescence compared to the negative control, the 48×1 probe set was under these conditions unable to provide a specific signal separation at this concentration.

We finally explored if the new (10×3) probe design enables imaging of RNA targets that are hard to image with conventional FISH probes. Such targets are characterized by extensive secondary structures that provides only few accessible sites for probe hybridization. We tested our probes by targeting a ~1 kb RNA viral transcript of the rotavirus A (RVA) gene segment-7. The idea was to test whether our set of probes detects these transcripts shortly after virus infection when the concentration of the transcript is expected to be very low. This specific target was chosen because of its extensive secondary structure that precludes hybridization of multiple probes, posing additional challenges for conventional FISH [21]. We fixed rotavirus-infected cells, 4 hours post infection and incubated them with the (10×3) DNA probe set targeting the RNA regions that were predicted to have less pronounced secondary structures [22]. To facilitate the detection of virus-infected cells, we took advantage of a stable cell line that expresses the rotavirus non-structural protein (NSP5) fused to eGFP (see Methods in the Appendix) [23].

After 4 hours post infection RVA, transcripts could be readily detected (Figure 6.4, top panel, red signal). No transcript specific signal was observed in mock-infected cells (Figure 6.4, bottom panel).

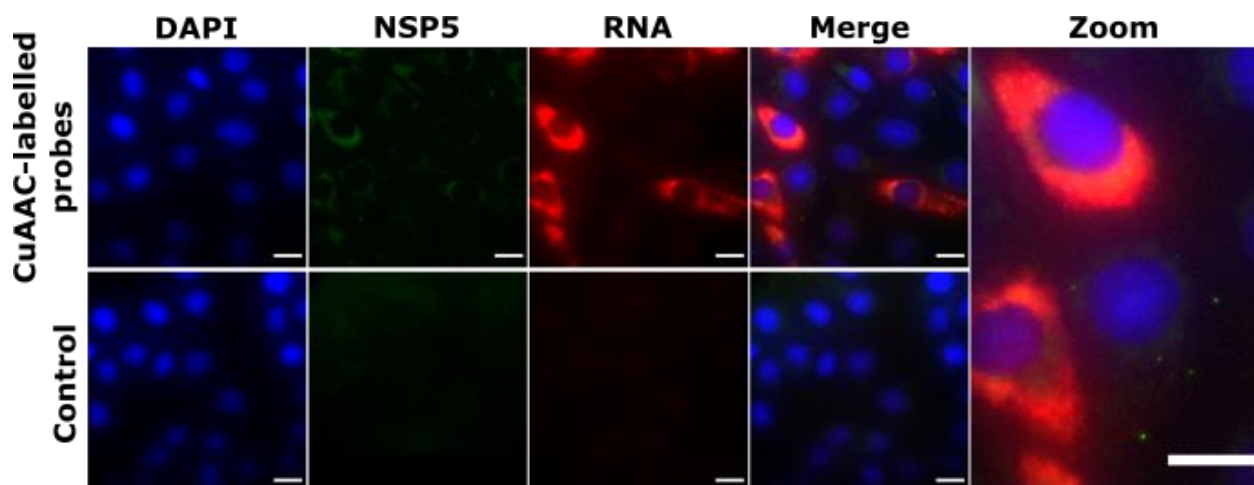


Figure 6.4: Rotavirus gene segment-7 RNA transcripts imaged with 10×3 probes. Upper panel: RNA transcripts (red) in virus-infected cells stably expressing rotavirus non-structural protein NSP5 fused to eGFP (green) detected 4 hours post infection. Lower panel: Mock-infected MA104 cells stably expressing NSP5-eGFP. Scale bars: 20 μ m.

In parallel, we also analyzed eGFP-NSP5-marked foci in RVA-infected cells to identify cells at a more advanced stage of infection (Figure 6.4, top panel, green signal). As expected, these cells showed higher levels of the RNA transcript fully consistent with an increase of the amount of viral RNA transcripts over the course of the viral infection.

Importantly, the increased sensitivity of the new 10×3 detection approach uncovered a number of interesting insights. First, the data show a large variation in the amount of transcripts in different cells at the onset of infection. These variations likely reflect differences in the transcriptional activities of different rotavirus particles [24, 25]. Furthermore, the transcripts do not seem to accumulate in a particular cellular compartment or in virus-induced organelles during early infection. These results thus show that the new 10×3 probe design is a significant step forward because it provides new biological insights.

6.3. Conclusions

We show here that by decreasing the number of probes and increasing the number of fluorophores on oligonucleotide probes using click chemistry provides fluorescent probe strands that allow efficient detection of RNA transcripts in live cells. The probes have a superb sensitivity and allow detection of transcripts that due to high secondary structure content provide only a limited number of binding sites. Self-quenching seems to play only a minor role, possibly because we used fluorophores that carry two negative charges each. The new probe design is so sensitive that it even allows flow RNA-FISH to be established for demanding flow cytometry applications. These results pave the way for the detection of small highly structure RNA transcripts and transcripts with low abundance. A potential application could be the monitoring of leukemia therapy by flow-FISH to prevent dangerous relapse cases or the very early detection of virus infections now needed for the detection of the Corona virus to reduce the diagnostic gap and prevent uncontrolled propagation of the disease.

6.4. References

1. Raj A, van Oudenaarden A. Nature, Nurture, or Chance: Stochastic Gene Expression and Its Consequences. *Cell*. 2008; 135(2):216–26.
2. Eldar A, Elowitz MB. Functional Roles for Noise in Genetic Circuits. *Nature*. 2010; 467(7312):167–73.
3. Itzkovitz S, van Oudenaarden A. Validating Transcripts with Probes and Imaging Technology. *Nat Methods*. 2011. 8(4 Suppl):S12–9.
4. Raj A, van den Bogaard P, Rifkin SA, van Oudenaarden A, Tyagi S. Imaging Individual mRNA Molecules Using Multiple Singly Labeled Probes. *Nat Methods*. 2008; 5(10):877–9.
5. Raj A, Tyagi S. Detection of individual endogenous RNA transcripts in situ using multiple singly labeled probes. In: *Single molecule Tools: Chapter 17, Fluorescence*

- based approaches, Part A; Walter, N G B T-M in E, Ed; Academic Press, 2010; 472:365–8.
- Semrau S, Crosetto N, Bienko M, Boni M, Bernasconi P, Chiarle R, et al. FuseFISH: Robust Detection of Transcribed Gene Fusions in Single Cells. *Cell Rep.* 2014, 6(1):18–23.
 - Muramoto T, Cannon D, Gierliński M, Corrigan A, Barton GJ, Chubb JR. Live Imaging of Nascent RNA Dynamics Reveals Distinct Types of Transcriptional Pulse Regulation. *Proc Natl Acad Sci U S A.* 2012; 109(19):7350–5.
 - Femino AM, Fay FS, Fogarty K, Singer RH. Visualization of Single RNA Transcripts in Situ. *Science* 1998; 280(5363):585–90.
 - Larsson C, Grundberg I, Söderberg O, Nilsson M. In Situ Detection and Genotyping of Individual mRNA Molecules. *Nat Methods.* 2010; 7(5):395–7.
 - Trcek T, Lionnet T, Shroff H, Lehmann R. mRNA Quantification Using Single-Molecule FISH in *Drosophila* Embryos. *Nat Protoc.* 2017; 12(7):1326–48.
 - Kolb HC, Finn MG, Sharpless KB.
Click Chemistry: Diverse Chemical Function From a Few Good Reactions. *Angew Chem Int Ed Engl.* 2001; 40(11):2004–21.
Click-Chemie: diverse chemische Funktionalität mit einer Handvoll guter Reaktionen. 2001; 113(11): 2056–75.
 - Gothelf KV, Jorgensen KA. Asymmetric 1,3-Dipolar Cycloaddition Reactions. *Chem Rev.* 1998; 98(2):863–910.
 - Bräse S, Gil C, Knepper K, Zimmermann V. Organic Azides: An Exploding Diversity of a Unique Class of Compounds. *Angew Chem Int Ed Engl.* 2005; 44(33):5188–240.
 - Tornøe CW, Christensen C, Meldal M. Peptidotriazoles on Solid Phase: [1,2,3]-triazoles by Regiospecific Copper(i)-Catalyzed 1,3-dipolar Cycloadditions of Terminal Alkynes to Azides. *J Org Chem.* 2002; 67(9):3057–64.

15. Rostovtsev VV, Green LG, Fokin VV, Sharpless KB. A Stepwise Huisgen Cycloaddition Process: copper(I)-catalyzed Regioselective "Ligation" of Azides and Terminal Alkynes. *Angew Chem Int Ed Engl.* 2002; 41(14):2596–9.
16. Gutmiedl K, Fazio D, Carell T. High-density DNA Functionalization by a Combination of Cu-catalyzed and Cu-Free Click Chemistry. *Chemistry.* 2010; 16(23):6877–83.
17. Gierlich J, Burley GA, Gramlich PME, Hammond DM, Carell T. Click Chemistry as a Reliable Method for the High-Density Postsynthetic Functionalization of Alkyne-Modified DNA. *Org Lett.* 2006; 8(17):3639–42.
18. Gramlich PME, Warncke S, Gierlich J, Carell T. Click-click-click: Single to Triple Modification of DNA. *Angew Chem Int Ed Engl.* 2008; 47(18): 3442–4.
19. Gramlich PME, Wirges CT, Manetto A, Carell T. Postsynthetic DNA Modification through the Copper-Catalyzed Azide–Alkyne Cycloaddition Reaction. *Angew Chem Int Ed Engl.* 2008; 47(44): 8350–8.
20. Hesse S, Manetto A, Cassinelli V, Fuchs J, Ma L, Raddaoui N, et al. Fluorescent Labelling of in Situ Hybridisation Probes Through the Copper-Catalysed Azide–Alkyne Cycloaddition Reaction. *Chromosome Res.* 2016; 24(3):299–307.
21. Arrigucci R, Bushkin Y, Radford F, Lakehal K, Vir P, Pine R, et al. FISH-Flow, a Protocol for the Concurrent Detection of mRNA and Protein in Single Cells Using Fluorescence in Situ Hybridization and Flow Cytometry. *Nat Protoc.* 2017; 12(6):1245–1260.
22. Borodavka A, Dykeman EC, Schrimpf W, Lamb DC. Protein-mediated RNA Folding Governs Sequence-Specific Interactions Between Rotavirus Genome Segments. *Elife.* 2017; 6:e27453.
23. Rodriguez F, Burrone OR, Eichwald C. Characterization of Rotavirus NSP2/NSP5 Interactions and the Dynamics of Viroplasm Formation. *J Gen Virol.* 2004; 85(Pt3):625–34.
24. Salgado EN, Upadhyayula S, Harrison SC. Single-Particle Detection of Transcription Following Rotavirus Entry. 2017; 91(18):e00651–17.

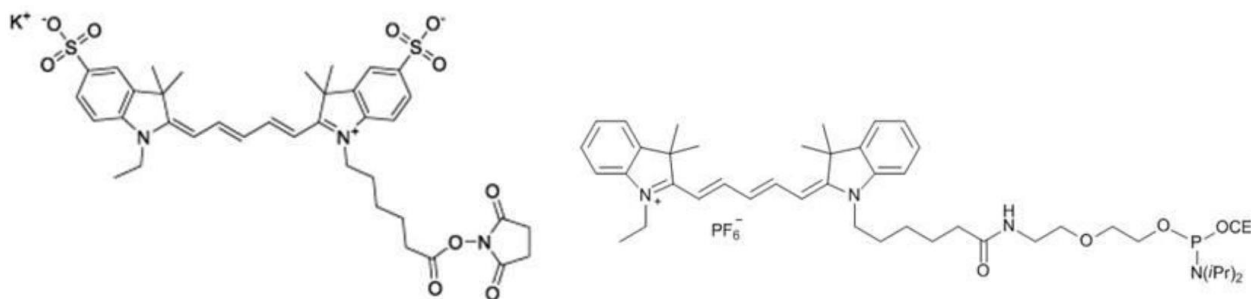
6.5. Appendix

25. Borodavka A, Desselberger U, Patton JT. Genome Packaging in Multi-Segmented dsRNA Viruses: Distinct Mechanisms With Similar Outcomes. *Curr Opin Virol.* 2018; 33:106–12.

6.5. Appendix

Eternion Red 645

Quasar 670



Probe design and sequences for eGFP mRNA

5'-ATGGTGAGCA AGGGCGAGGA GCTGTTCAAC GGGGTGGTGC CCATCTGGTTCGAGCTGGAC GGCGACGTAA ACGGCCACAA GTTCAGCGTG TCCGGCGAGG GCGAGGGCGA TGC
 3'-TACCACTCGT TCCCGCTCCT CGACAAGTGG CCCACCACG GGTAGGACCA GCTCGACTCG CCGCTGCATT TGCCGGTGT CAAGTCGCAC AGGCCGTCC CGCTCCCGCT ACG

1 TCGT TCCCGCTCCT CGACAAGT **2** CTG CCGCTGCATT TGCCGGTGT

CACCTAC GGCAAGTGA CCCTGAAGTT CATCTGCACC ACCGGCAAGC TGCCCGTGCC CTGGCCACC CTCGTGACCA CCCTGACCTA CGGCGTGAC TGCTTCAGCC GCTACCCC
 GTGGATGCCGTTCCGACT GGGACTTCAA GTAGACGTGG TGGCCGTTCC ACGGGCACGG GACCCGGTGG GAGCACTGGT GGGACTGGAT GCCGCACGTC ACGAAGTCGG CGATGGGG

3 TTCAA GTAGACGTGG TGGCCGT

GA CCACATGAAG CAGCACGACT TCTTCAAGTC CGCCATGCCC GAAGGCTACG TCCAGGAGCG CACCATCTTC TTCAAGGACG ACGGCAACTA CAAGACCCGC GCCGAGGTGA AGTT
 CT GGTGTACTTC GTCGTGCTGA AGAAGTTCAG GCGGTACGGG CTCCGATGC AGGTCTCTGC GTGGTAGAAG AAGTTCCTGC TGCCGTTGAT GTTCTGGGCG CGGCTCCACT TCAA

4 AGAAGTTCAG GCGGTACGGGCT **5** TTCTGC TGCCGTTGAT GTTCT **6** CTCCACT TCAA

CGAGGG CGACACCTG GTGAACCGCA TCGAGCTGAA GGGCATCGAC TTCAAGGAGG ACGGCAACAT CCTGGGGCAC AAGCTGGAGT ACAACTACAA CAGCCACAACGTATAT
 GCTCCC GCTGTGGGAC CACTTGGCGT AGCTCGACTT CCCGTAGCTG AAGTTCCTCC TGCCGTTGTA GGACCCCGTG TTCGACTCA TGTGTATGT GTCGGTGTG CAGATATA
 GCTCCC GCTGT **7** CTG AAGTTCCTCC TGCCGTTGT

CA TGGCCGACAA GCAGAAGAAC GGCATCAAGG TGAACCTCAA GATCCGCCAC AACATCGAGG ACGGCAGCGT GCAGCTCGCC GACCACTACC AGCAGAACAC CCCCATCGGC
 GT ACCGGCTGTT CGTCTTCTG CCGTAGITCC ACTTGAAGTT CTAGGCGGTG TTGTAGCTCC TGCCGTCGCA CGTCGAGCGG CTGGTGATGG TCGTCTTGTG GGGGTAGCCG

8 TGTAGCTCC TGCCGTCGCA CGT

GACGGCCCCG TGCTGTGCC CGACAACCAC TACCTGAGCA CCCAGTCCG CCTGAGC AAA GACCCCAACG AGAAGCGCGA TCACATGGTC CTGCTGGAGT TCGTGACCCG CGCC
 CTGCCGGGGC ACGACGACGG GCTGTTGGTG ATGGACTCGT GGGTCAGGGC GGACTC GTTT CTGGGGTTGC TCTTCGCGCT AGTGTACCAG GACGACCTCA AGCACTGGCG GCGG

9 GACGG GCTGTTGGTG ATGGACT

GGGATC ACTCTCGGCA TGGACGAGCTGTACAAGTAA-3'
 CCCTAG TGAGAGCCGT ACCTGCTCGA CATGTTCAAT-5'

10 GAGCCGT ACCTGCTCGA CATGT

Sense sequence of eGFP-mRNA Control anti-sense oligonucleotides CuAAA-labelled antti-sense oligonucleotides

Figure S6.1: Sequence of the eGFP transcript in grey, together with the sequence of the antisense 10x3 probes in red. The comparison 30x1 probes are shown in green/light green.

Oligonucleotide synthesis

Into each of the DNA strands, three C8-alkyne-dU building blocks were inserted at former dT positions using phosphoramidites developed before [1].

Table S6.1: Sequences of the 10 oligonucleotide RNA FISH probes and the positions of the C8-alkyne-dU building blocks. The Oligonucleotides listed below were generated for eGFP mRNA using the Stellaris RNA FISH probe designer (<https://www.biosearchtech.com/stellaris-designer>). The positions of the modifications are highlighted in blue.

Number	Sequence 5'-> 3'
1	TGA ACA G T CCT CGC C T TGC T
2	T G T GGC C G T TTA C G T CGC C G T C
3	TGC CGG TGG T G C AGA T G A ACT T
4	T C G GGC A T G GCG GAC T T G AAG A
5	T C T TGT AGT T G C CGT C G T CCT T
6	T G T CGC C T CGA ACT T C A CCT C
7	T G T TGC C G T CCT C T TGA AGT C
8	T G C ACG C T G CCG T C C TCG ATG T
9	T C A G G T AGT G G T TGT CGG GCA G
10	T G T ACA G T CGT CCA T G C CGA G

Click reaction

Each probe was prepared separately. The Cu(I)-catalyzed azide-alkyne cycloaddition (CuAAC) was performed combining 5 nmole of DNA oligo and 45 nmol dye azide: TAMRA-azide (baseclick GmbH) or Eterneon Red 647-azide (baseclick GmbH) in 20 μ L reaction volume in the presence of the catalyst CuBr 6.25 mM, tris(hydroxypropyl)triazolylmethylamine (THPTA) 12.5 mM, and 2.5% DMSO. The solution is then incubated for 1 h at 45 $^{\circ}$ C at 700 RPM protected from light and then cleaned by

standard EtOH precipitation before the application in FISH experiments. Further purification was not needed.

HPLC example

For RP-HPLC analysis of labelled probes, a Waters system (Waters e2695 Separation Modul and Waters 2998 PDA) equipped with the XBridge™ OST C18 column (2.5 µm, 4.6 mm x 50 mm) was used. Linear gradients of buffer A (0.1 M triethylammonium acetate, pH 7.5) to buffer B (0.1 M triethylammonium acetate in 80% acetonitrile, pH 7.5) were run at a flow rate of 1.5 mL/min at 40 °C column temperature. For detection of oligonucleotide mixtures 260 nm absorbance was chosen.

Method:

Buffer A: 100% to 70% in 8 min, 70% to 15% in 2 min, 15% to 0% in 1 min.

Buffer B: 0% to 30% in 8 min, 30% to 85% in 2 min, 85% to 100% in 1 min

HPL chromatogram example of the oligo before (i) and after click reaction (ii)

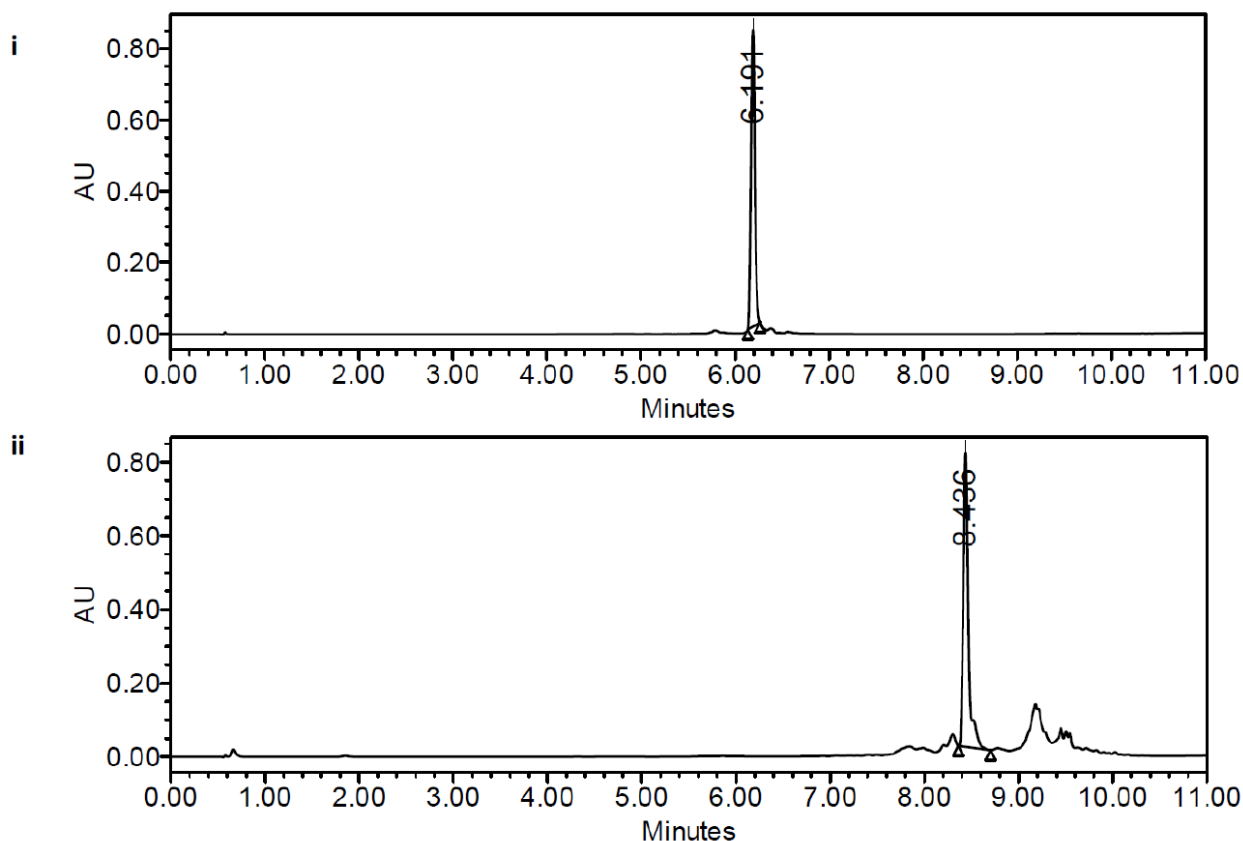


Figure S6.2: HPLC chromatogram of the probe before (i) and after the click reaction (ii).

Comparison of commercial set of probes and click probes

Analytical RP-HPLC was performed using a Macherey-Nagel Nucleodur 100-3 C18ec column on a Waters Alliance 2695 Separation Module coupled with a 2996 Photodiode Array Detector and a 2475 Multi wavelength Fluorescence Detector, using a flow of 0.5 mL/min. Linear gradients of buffer A (0.1 M triethylammonium acetate, pH 7.0) to buffer B (0.1 M triethylammonium acetate in 80% acetonitrile, pH 7.0) were run at a flow rate of 0.5 mL/min. For detection of oligonucleotide mixture 260 nm absorbance was chosen, while 647 nm absorbance was used to detect the fluorophore. Method: 0-60% B in 20 min, 60 to 100% B in 1 min, 100% B for 4 min.

Table S6.2: Sequence of the commercial FISH probes, consisting of 30 oligonucleotides with one dye each (30x1).

Number	Sequence 5'-> 3'
1	GCT CCT CGC CCT TGC TCA CCA T
2	ATG GGC ACC ACC CCG GTG AAC A
3	GTC GCC GTC CAG CTC GAC CAG G
4	CGC TGA ACT TGT GGC CGT TTA C
5	TCG CCC TCG CCC TCG CCG GAC A
6	GGT CAG CTT GCC GTA GGT GGC A
7	CGG TGG TGC AGA TGA ACT TCA G
8	GGC CAG GGC ACG GGC AGC TTG C
9	GGT CAG GGT GGT CAC GAG GGT G
10	GGC TGA AGC ACT GCA CGC CGT A
11	TGC TTC ATG TGG TCG GGG TAG C
12	GGC GGA CTT GAA GAA GTC GTG C
13	CCT GGA CGT AGC CTT CGG GCA T
14	TCC TTG AAG AAG ATG GTG CGC T
15	GCG GGT CTT GTA GTT GCC GTC G
16	TCG ATG CGG TTC ACC AGG GTG T
17	CCT TGA AGT CGA TGC CCT TCA G
18	TGC CCC AGG ATG TTG CCG TCC T
19	GTT GTA GTT GTA CTC CAG CTT G
20	GCC ATG ATA TAG ACG TTG TGG C
21	GAT GCC GTT CTT CTG CTT GTC G
22	GGC GGA TCT TGA AGT TCA CCT T
23	ACG CTG CCG TCC TCG ATG TTG T
24	GCT GGT AGT GGT CGG CGA GCT G
25	CCG TCG CCG ATG GGG GTG TTC T
26	GGT TGT CGG GCA GCA GCA CGG G
27	GCG GAC TGG GTG CTC AGG TAG T
28	CTC GTT GGG GTC TTT GCT CAG G
29	GCA GGA CCA TGT GAT CGC GCT T
30	GCT CGT CCA TGC CGA GAG TGA T

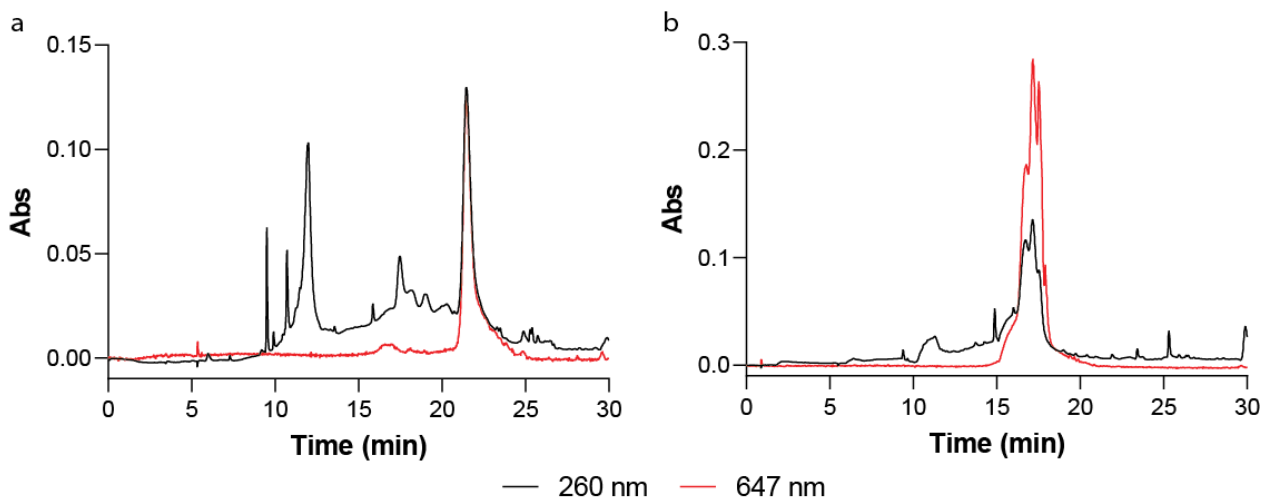


Figure S6.3: Comparison of (a) a commercial probe set (30x1 Quasar 670 dye) and (b) a clicked probe set (10x3 Eterneon-Red dye). Both sets were loaded in equal amounts, based on 260 nm absorbance. Both dyes are very similar cyanine-5 fluorophores.

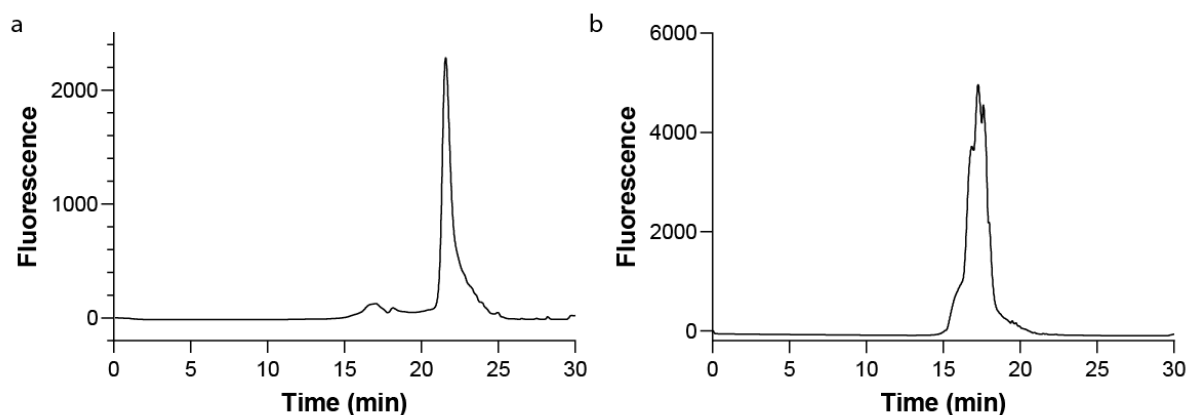


Figure S6.4: Fluorescence analysis: The fluorescence analysis of the two sets of probes confirm what described previously following the absorbance at 647 nm. Using the same amount of DNA, the commercial probes (a) show an overall lower fluorescence value than the click probes (b). Detection parameters: $\lambda_{\text{ex}}=647$ nm, $\lambda_{\text{em}}=665$ nm.

In-vitro-FISH with total RNA from eGFP-HEK293T cell line

Total RNA was extracted from eGFP-HEK293T cells using Total-RNA-kit, peqGOLD, catalogue number 732-2868 (VWR). FISH in total RNA was performed as reported in Semrau *et. al.* with minor changes. After DNase digestion, 0.5 μ l of total RNA was spotted in the center of an RNase-free cover slips, which was attached to a microscope slide. The total RNA spotted on cover slips were dried for 20 min at 80 °C. After fixation of the spots for 5 min at RT, a washing step with 2x saline sodium citrate (SSC) followed. Either the commercial (30x1, labelled with Quasar 670) or the CuAAC-labelled probes (10x3, Eterneon-Red 647 azide) were added to the spotted RNA in hybridization buffer (300 mM NaCl, 30 mM trisodium citrate, pH 7.0 in nuclease-free water, 10% (v/v) formamide) and incubated for 5 min at 80 °C. The hybridization buffer including the FISH probes was washed with washing buffer (300 mM NaCl, 30 mM trisodium citrate, pH 7.0, 10% (v/v) formamide in RNase-free water). The samples were imaged in presence of 2x SSC.

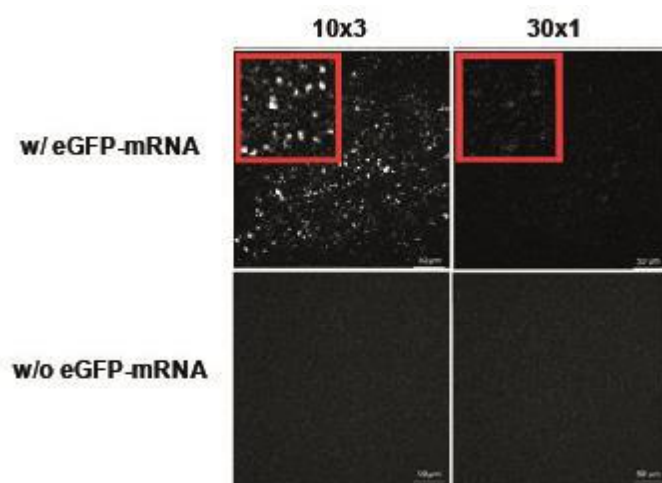


Figure S6.5: *In vitro* FISH experiment of total RNA extracted from eGFP-HEK293T cells. Total RNA from eGFPHEK293T cells hybridized with the CuAAC-labelled probes (10x3) showed a very high signal of diffraction limited spots. In the control experiment, total RNA from eGFP-HEK293T cells was hybridized with the commercial probe set (30x1). Only a very weak specific signal was detected. Scale bars: 50 μ m.

Titration for different numbers of triple labelled oligonucleotides

Since the oligonucleotides were labelled separately via click chemistry, a setting of different numbers of oligonucleotides to a probe set was possible. Four probe sets were prepared: 3x3, 5x3, 7x3 and 10x3 with 10 ng total amount of the oligonucleotides in each set. The sets were hybridized with fixed and permeabilized eGFPHEK293T and with HEK293T for the negative control without eGFP expression.

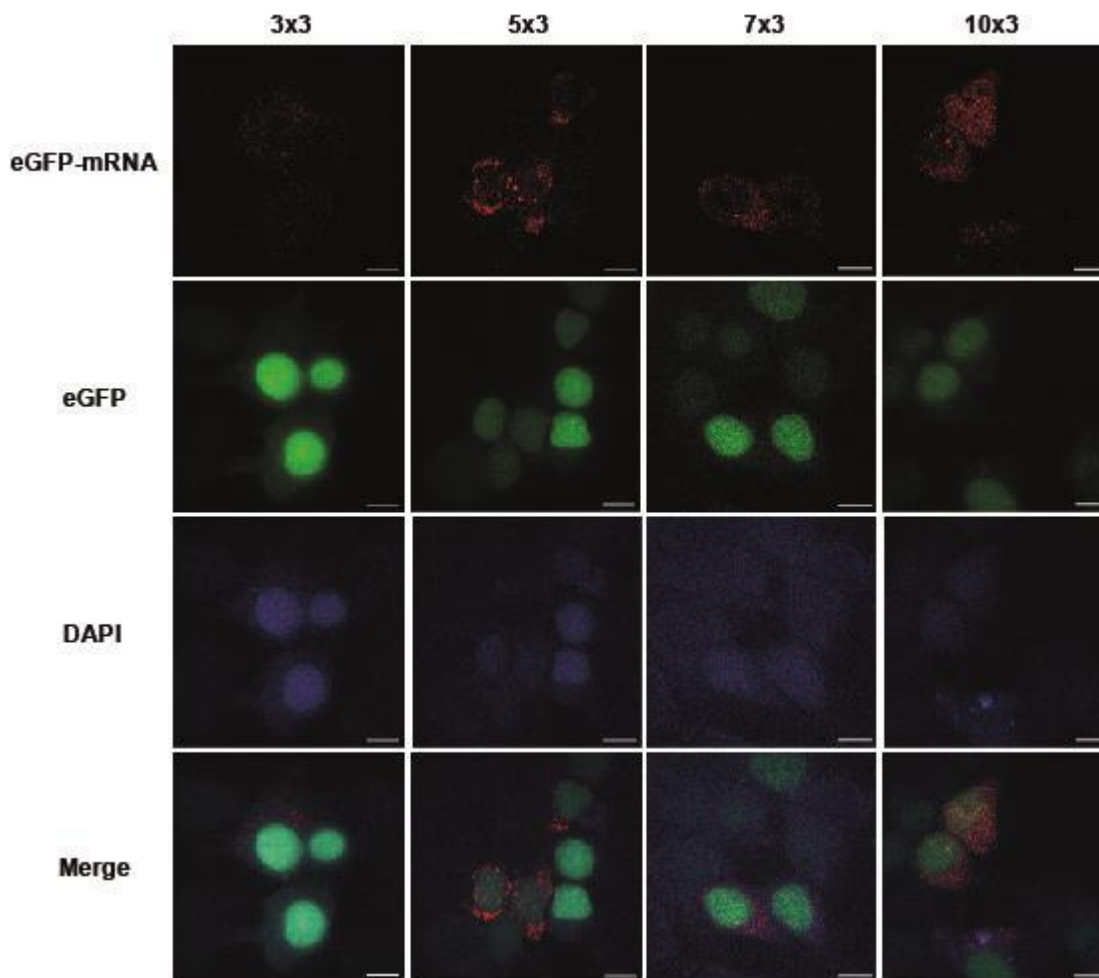


Figure S6.6: Differences in the signal intensities of eGFP-mRNA using different numbers of triple labelled probes (3x3, 5x3, 7x3 and 10x3) in eGFP-expressing HEK293T cells. Scale bar: 50 μm .

Click post hybridization

eGFP-HEK293T were grown in 8 chamber μ -slides cell culture plates (ibidi) until 80% cell density is reached. After removing the culture medium, cells were washed with 1x RNase-free phosphate saline buffer (PBS) and fixed 15 minutes at RT with the fixation buffer (4% paraformaldehyde (v/v) in nuclease-free PBS). Cells were then washed twice with 3% bovine serum albumin (BSA) in 1x PBS and permeabilized with 100% EtOH for at least 1 h at 4 °C. After permeabilization and removing of the EtOH, cells were washed twice with 3% BSA in 1x PBS. 5 pmol of each oligonucleotide in 150 μ L hybridization buffer (300 mM NaCl, 30 mM trisodium citrate, pH 7.0 in nuclease-free water, 10 % (v/v) formamide) was added to each chamber. The hybridization occurred for 3 h at 37 °C. The unbound oligonucleotides and the hybridization buffer were washed using 10 % washing buffer (300 mM NaCl, 30 mM trisodium citrate, pH 7.0, 10% (v/v) formamide in RNase-free water) followed by two washing steps with 3% BSA in 1x PBS. 250 μ L of click cocktail (CuSO₄ 50 μ M, THPTA 250 μ M, 7 equivalents 5-TAMRA-PEG3-azide to a final concentration of 25 μ M and NaAscorbate to final concentration of 2.5 mM) was added to the cells, which were then incubated 30 minutes at RT protected from light. After hybridization, cells were washed three times either with 3% BSA (w/v) or DMSO (5, 10, 20, 30, 40 and 50% in 1x PBS (v/v)). Afterwards, 2x SSC was added to the cells and analysis via microscopy was performed. The signal to noise ratio is reduced when the concentration of DMSO is increased. Scale bar: 50 μ m.

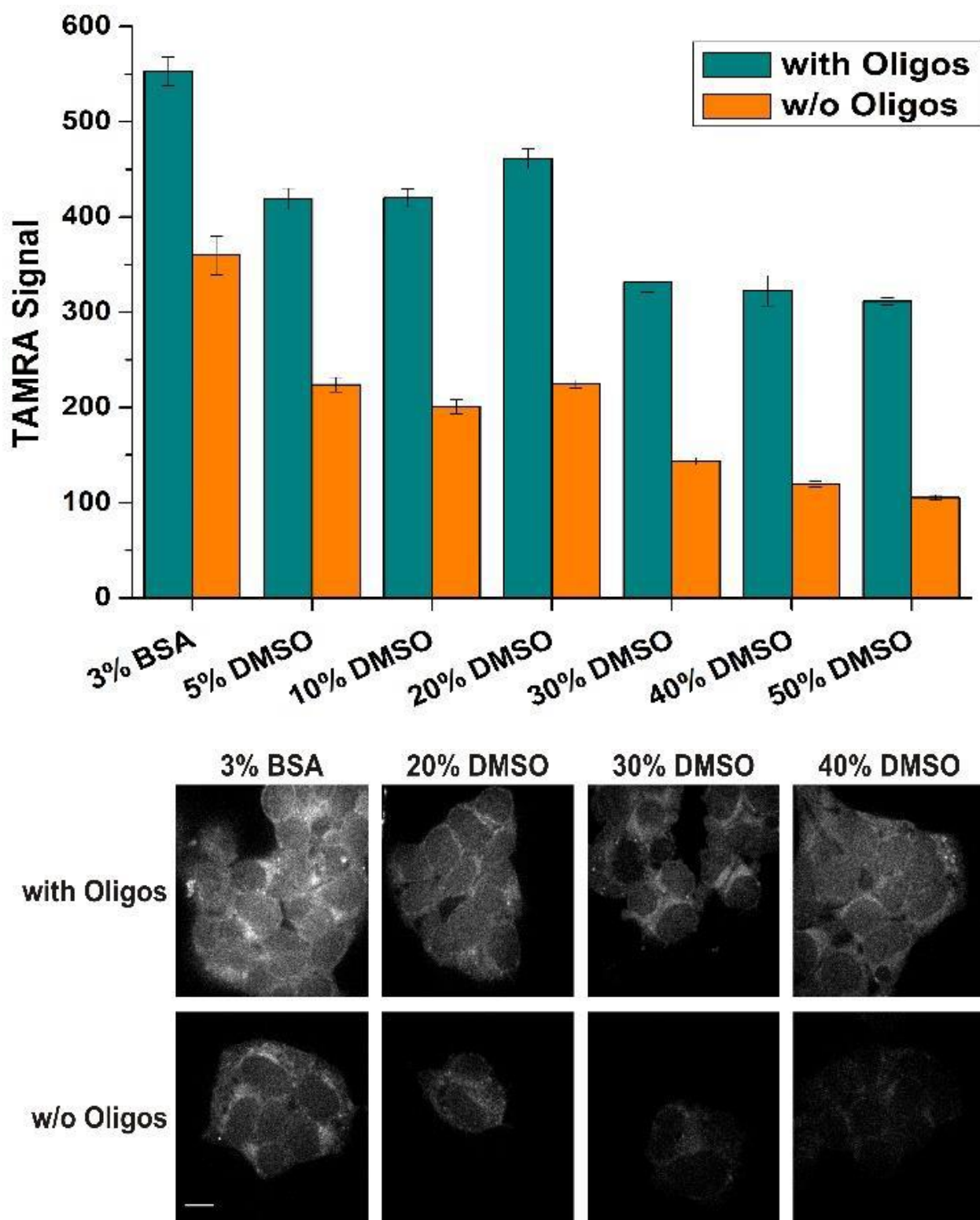


Figure S6.7: Click reaction of the FISH probes after hybridization.

Cell culture of human cell strains

HEK293T and HEK293T-eGFP cells were cultivated at 37 °C with CO₂-enriched (5%) atmosphere. Dulbecco's modified Eagle medium (DMEM) supplemented with 10% fetal bovine serum (FBS), 1% penicillin and streptomycin, was used as growing medium. When reaching a confluence of 70% to 80%, the cells were passaged in a new culture flask. For staining experiments, 1.5x10⁴ cells were seeded in each well of a μ -Slide 8 Well from ibidi (ibiTreat, #1.5 polymer coverslip, catalog No. 80826) and cultured for two days or until a density of 80% is reached.

FISH protocol for HEK293T cells

HEK293T cells were fixed with 4% (v/v) paraformaldehyde in nuclease-free phosphate saline buffer (PBS) for 10 min at room temperature. Samples were then washed twice with PBS, and the fixed cells were permeabilized with 70% (v/v) ethanol (200 proof) in RNase-free water and stored in ethanol at +4 °C for at least 12 hours prior to hybridization. Permeabilized cells were then re-hydrated for 5 min in a pre-hybridization buffer (300 mM NaCl, 30 mM trisodium citrate, pH 7.0 in nuclease-free water, 10% v/v formamide, supplemented with 2 mM vanadyl ribonucleoside complex). Re-hydrated samples were hybridized with an equimolar mixture of 10 RNA FISH DNA probes specific to bovine rotavirus strain RF gene segment 7 (62.5 nM final concentration, see Table S6.4) in a total volume of 200 μ l of the hybridization buffer (Stellaris RNA FISH hybridization buffer, SMF-HB1-10, Biosearch Technologies, supplemented with 10% v/v deionized formamide). After 4 hours of incubation at 37 °C in a humidified chamber, samples were briefly rinsed with the wash buffer (300 mM NaCl, 30 mM trisodium citrate, pH 7.0, 10% v/v formamide in nuclease-free water) after which a fresh aliquot of 300 μ l of the wash buffer was applied to each well and incubated twice at 37 °C for 30 min. After washes, nuclei were briefly stained with 300 nM 4',6-diamidino-2-phenylindole (DAPI) solution in 300 mM NaCl, 30 mM trisodium citrate, pH 7.0) and the samples were finally rinsed with and stored in the same buffer without DAPI prior to imaging.

Flow cytometry

FISH experiments for flow cytometry analysis were performed as described previously by Arrigucci et al [2].

Table 6.3: Sequences of the BCR and ABL FISH probes labelled with click chemistry. The sequences were generated using the Stellaris RNA FISH probe designer (<https://www.biosearchtech.com/stellaris-designer>). The positions of the C8-Alkyne-dU building blocks are highlighted with blue.

Number	Sequence 5'-> 3'
BCR#1	TAG CTC TTC TTT TCC TTG GC
BCR#2	A TC CGC TCG AAG TTG GAC CT
BCR#3	AAC TCG ACG TTC ACG TAG AA
BCR#4	TTT TTG CGC TCC ATC TGC AT
BCR#5	TTC AAC TCG GCG TCC TCG TA
BCR#6	A TG CTC TGG TAG GGC TGG TA
BCR#7	TCC GCA ATC CTC AAA ACT CC
BCR#8	TTC TCA TTG GAG CTG CAG TC
BCR#9	TTG TCC CGG AAC ATG CGG TA
BCR#10	A TC TGC GTC TCC ATG GAA GG
BCR#11	A CT CGC TNT AGT GGA CTC CA
BCR#12	A TC TGC TGA CTC GTC AGC AC
BCR#13	TTG TGG ATC TCG TAG AGC TC
BCR#14	TCA GGT TCT CGG AGA TTT CT
BCR#15	TGG CAT CTT TGT TGC TTC TG
ABL1#1	GCC ATT TTT GGT TTG GGC TT
ABL1#2	TTG ACT GGC GTG ATG TAG TT
ABL1#3	GTA ATG GTA CAC CCT CCC TT
ABL1#4	A TG ATG ATG AAC CAA CTC GG
ABL1#5	A TA ATG GAG CGT GGT GAT GA
ABL1#6	A TA GAC AGT GGG CTT GTT GC
ABL1#7	A TC TCC CAC TT GTCG TAG TT
ABL1#8	TTG TGC TTC ATG GTG ATG TC
ABL1#9	TCC TCC TTC AAG GTC TTC AC
ABL1#10	CTT TCA TGA CTG CAG CTT CT
ABL1#11	AGG TTC CCG TAG GTC ATG AA
ABL1#12	A TC TGA GTG GCC ATG TAC AG
ABL1#13	TAC CTT CAC CAA GTG GTT CT
ABL1#14	A TT TGA TGG GGA ACT TGG CT
ABL1#15	A TG GAG AAC TTG TTG TAG GC

Cells flow cytometer data were obtained using the BD FACS Canto II equipped with air cooled green (488 nm solid state; 20 mW laser output) and red (633 nm HeNe; 17 W output) lasers, and the data were analyzed with the FCS Express 6 (De Novo Software). The fluorescent detectors/filters relevant for this study were FITC (530 +/- 30 nm) and APC (660 +/- 30 nm), respectively. Acquisition was done with a flow rate of 10 μ L/min. FSC and SSC were used for detection of forward light scatter parameter and side light scatter parameter. The machine was cleaned before and after each measurement. The photomultiplier tube (PMT) voltage for each parameter was adjusted in order to have the cells displayed in the centre of the investigating plot.

After hybridization and wash, HEK293T or HEK293T-eGFP were immediately analysed by flow cytometer, the samples were maintained in buffer during acquisition.

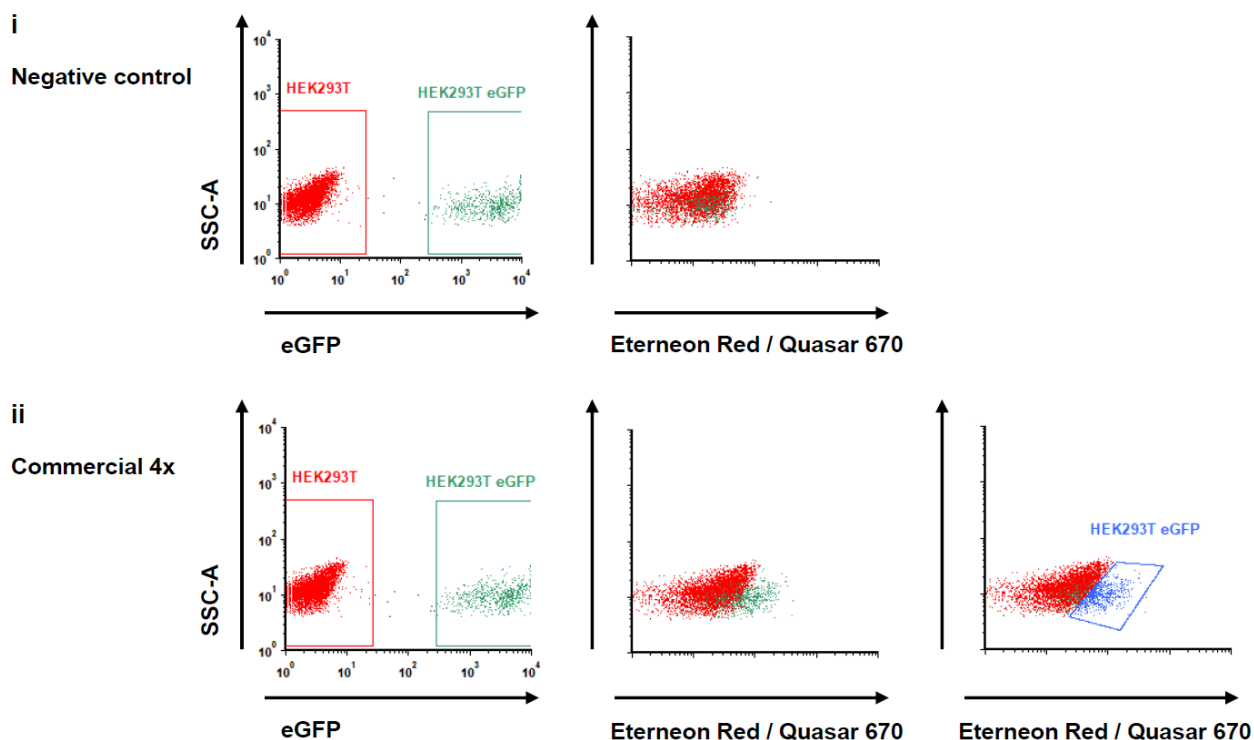


Figure S6.8: FACS Dot plot comparison of 30x1 and 10x3 probes. (i) The negative control of the experiment, where FISH was performed replacing the set of probes with the same volume of H₂O. A population of HEK293T and HEK293TeGFP was mixed in a ratio 20:1, and analyzed by FACS. The eGFP dot-plot reports the correct separation of the HEK293T and HEK293-eGFP. The Eterneon Red dot plot shows a mix of the two populations, as expected

(ii) Same result as the 10x3 probes was obtained with the 30x1 probes set by increasing the concentration four fold to 0.2 ng DNA/ μ l.

Cells and viruses

The rhesus monkey epithelial cell line MA104 stably expressing NSP5-EGFP [3] was cultured in DMEM (Dulbecco's modified Eagle medium, GlutaMax-I, 4.5 g/L glucose, ThermoFisher), supplemented with 10% fetal bovine serum (FBS), 1x MEM non-essential amino acids solution (Sigma), 1 mM sodium pyruvate (Sigma) and 500 μ g/ml G418 (Roche). Bovine rotavirus A strain RF (G6P6[1]) was a generous gift from Dr. Ulrich Desselberger (University of Cambridge, UK). It was grown in MA104 Clone 1 cell line (ATCC CRL-2378.1), as described previously [4]. For RNA imaging experiments, MA104 cells expressing NSP5-EGFP were seeded into Ibidi 8-well μ -slides and allowed to reach 90% confluency prior to the infection. Confluent MA104 cell monolayers were rinsed twice with DMEM medium without FBS for 10 minutes to remove any residual FBS, and were subsequently infected with trypsin-activated bovine rotavirus at multiplicity of infection, MOI = 20.

Rotavirus RNA imaging using RNA FISH

Rotavirus-infected and mock-infected MA104 controls were fixed with 4% (v/v) paraformaldehyde in nuclease-free phosphate saline buffer (PBS) for 10 min at room temperature. Samples were then washed twice with PBS, and the fixed cells were permeabilized with 70% (v/v) ethanol (200 proof) in RNase-free water and stored in ethanol at +4 °C for at least 12 hours prior to hybridization. Permeabilized cells were then re-hydrated for 5 min in a prehybridization buffer (300 mM NaCl, 30 mM trisodium citrate, pH 7.0 in nuclease-free water, 10% v/v formamide, supplemented with 2 mM vanadyl ribonucleoside complex). Re-hydrated samples were hybridized with an equimolar mixture of 10 RNA FISH DNA probes specific to bovine rotavirus strain RF gene segment 7 (62.5 nM final concentration, see Appendix Table 6.1) in a total volume of 200 μ l of the hybridization buffer (Stellaris RNA FISH hybridization buffer, SMF-HB1-10, Biosearch Technologies, supplemented with 10% v/v deionized formamide). After 4 hours of incubation at 37 °C in a

humidified chamber, samples were briefly rinsed with the wash buffer (300 mM NaCl, 30 mM trisodium citrate, pH 7.0, 10% v/v formamide in nuclease-free water, after which a fresh aliquot of 300 μ l of the wash buffer was applied to each well and incubated twice at 37 °C for 30 min. After washes, nuclei were briefly stained with 300 nM 4',6-diamidino-2-phenylindole (DAPI) solution in 300 mM NaCl, 30 mM trisodium citrate, pH 7.0) and the samples were finally rinsed with and stored in the same buffer without DAPI prior to imaging.

Fluorescent microscopy imaging

HEK cells were imaged on a Zeiss Cell Observer SD microscope equipped with a Yokogawa spinning disk unit CSU-X1 using a 1.40 NA 100x Plan-apochromat oil immersion objective (Zeiss). RNA FISH probes were imaged using 532/561 nm and a BP 690 filter, and eGFP signal was imaged with 488 nm laser excitation and a BP 525/50 filter, respectively. DAPI staining was visualized with 405 nm excitation using a BP 525/50 filter. Data analysis yielding the labeling efficiency was performed using ImageJ. Rotavirus RNA FISH probes imaging was carried out using a Nikon Ti-E widefield microscope equipped with a 100x 1.40 NA Plan Apochromat oil immersion objective, a CoolLED pE 4000 light source, a Zyla camera and a Quad DAPI/FITC/CY3/CY5 HC filter set. Z-series spanning the full cell volume with a step size of 0.5 μ m at 30% power with 55 ms exposure times at 385 nm for DAPI, 58% power with 500-ms exposure times at 470 nm for eGFP and at 35% power with 500 ms exposures at 550 nm for TAMRA were acquired and the final images represent maximum intensity projections calculated using ImageJ.

Table S6.4: Into each of the DNA strands designed, three C8-alkyne-dU building blocks were inserted at former dT positions using phosphoramidites developed before [1]. Sequences of the 10 oligonucleotide RNA FISH probes listed below were generated for the rotavirus A gene segment 7 (gene accession no. KF729693.1) using the Stellaris RNA FISH probe designer (<https://www.biosearchtech.com/stellaris-designer>). The position of the modifications is highlighted in blue.

Number	Sequence 5' -> 3'
1	A TT GTG GTA TAT TCA A TA CCA
2	AG T CCA TTA TTC TCG TTA TTG
3	G TT TTG CGC A TT TAT TAT T GGT
4	AAG G TA TCT TTC CAT TCA G TA
5	G TT CTT GTG TAG AGT CAT T ATT
6	A TA GCG TTA TGT CCA T TG GAT
7	ACC AAG TGT TTG TGT ATT TAA
8	TG T AAT CAC TAA CTT C TC CGT
9	CTG TAT GAC TGC TAC GTT C TC
10	G TG GTG TAG T TG TTG GAT T CAG

References

1. Gierlich J, Burley GA, Gramlich PME, Hammond DM, Carell T. Click Chemistry as a Reliable Method for the High-Density Postsynthetic Functionalization of Alkyne-Modified DNA. *Org Lett.* 2006; 8(17):3639–42.
2. Arrigucci R, Bushkin Y, Radford F, Lakehal K, Vir P, Pine R, et al. FISHFlow, a protocol for the concurrent detection of mRNA and protein in single cells using fluorescence in situ hybridization and flow cytometry. *Nat Protoc.* 2017; 12(6):1245–60.

3. Eichwald C, Rodriguez JF, Burrone OR. Characterization of rotavirus NSP2/NSP5 interactions and the dynamics of viroplasm formation. *J Gen Virol.* 2004; 85(Pt 3):625–34.
4. Cheung W, Gill M, Esposito A, Kaminski CF, Courousse N, Trugnan G, et al. Rotaviruses associate with cellular lipid droplet components to replicate in viroplasms, and compounds disrupting or blocking lipid droplets inhibit viroplasm formation and viral replication. *J Virol.* 2010; 84(13):6782–98.

7. Rotavirus Replication Factories Are Complex Ribonucleoprotein Condensates

This chapter is based on the following manuscript:

Geiger F, Papa G, Arter WE, Acker J, Saar KL, Erkamp N, Qi R, Bravo J, Strauss S, Krainer G, Burrone OR, Jungmann R, Knowles TPJ, Engelke H, Borodavka A. Rotavirus Replication Factories Are Complex Ribonucleoprotein Condensates. 2021; manuscript submitted.

Abstract

RNA viruses induce formation of subcellular organelles that provide microenvironments conducive to their replication. Here we show that replication factories of rotaviruses represent protein-RNA condensates that are formed via liquid-liquid phase separation. We demonstrate that rotavirus proteins NSP5 and NSP2 undergo phase separation *in vitro* and form RNA-rich condensates *in vivo* that can be reversibly dissolved by aliphatic diols. During infection, these RNA-protein condensates became less dynamic and impervious to aliphatic diols, indicating a transition from a liquid to solid state. Some aspects of assembly of rotavirus replication factories mirror the formation of cytoplasmic ribonucleoprotein granules, while the selective enrichment of viral transcripts appears to be a unique feature of these condensates. Such complex RNA-protein condensates that underlie replication of RNA viruses represent an attractive target for developing novel therapeutic approaches.

7.1. Introduction

To replicate successfully, RNA viruses compartmentalise their replicative enzymes within specialized organelles termed viral factories. These structures are viewed as virus assembly lines that support viral replication by sequestering and concentrating cognate nucleic acids and proteins. While most viral RNA replication requires membrane-enclosed replication compartments, experimental evidence from recent studies [1–4] suggests that liquid–liquid

phase separation (LLPS) may provide a simple solution to assembling RNA-rich replication factories via a process that is solely dependent upon physical forces [5–10].

Here we show that replication factories of rotaviruses (RVs), a large class of human and animal double-stranded RNA (dsRNA) viruses, are formed via phase separation of the viral non-structural proteins NSP5 and NSP2. Both proteins are indispensable for rotavirus replication, constituting the bulk of the replication factories, or viroplasm [11–16]. In RV-infected cells, large amounts of NSP5 and NSP2 rapidly accumulate in the cytoplasm, forming viroplasms as early as 2 hours post infection [12, 17, 18]. We demonstrate that upon mixing at low micromolar concentrations *in vitro*, or when co-expressed in cells, multivalent Ser/Glu-rich protein NSP5 and the viral RNA chaperone NSP2 spontaneously phase separate forming liquid condensates. Analysis of replication of the NSP5-deficient recombinant rotavirus in a cell line stably expressing NSP5 confirms that the condensate formation requires NSP5. Both rotavirus replication factories and NSP5/NSP2 condensates were rapidly and reversibly dissolved in the presence of small aliphatic alcohols, including 1,6-hexanediol, as well as lower molecular weight propylene diols, corroborating their liquid-like properties. We have validated our findings by employing a combinatorial droplet microfluidic platform, termed PhaseScan [19], to characterise the phase behaviour of the NSP5/NSP2 condensates and mapped out the phase boundary, at which they transition from a mixed one-phase, to a two-phase demixed state.

Finally, using single-molecule RNA fluorescence in situ hybridization (smFISH) and super-resolution DNA-PAINT imaging, we have shown that reversible dissolution of replication factory condensates releases rotavirus transcripts, followed by their reassociation upon removal of these compounds. At a later infection (>12 h) stage, the apparent shapes of rotavirus replication factories deviated from a perfect sphere, and did not dissolve in the presence of aliphatic diols. These observations were consistent with the decreased exchange of NSP5-EGFP between the cytoplasm and viroplasm during late infection, suggesting a liquid-to-solid transition that occurs during infection.

The emerging properties of these viral protein–RNA condensates in a large family of dsRNA viruses are remarkably similar to recent results emerging from studies of non-membrane-bound cytosolic ribonucleoprotein (RNP) organelles, including Processing (P) bodies and

stress granules. Their capacity to rapidly and reversibly respond to external stimuli amounts to a shift in our understanding of the replication of multi-segmented viral RNA genomes, providing the basis for viewing these RNA–protein condensates as an attractive target for developing novel antiviral therapeutics.

7.2. Results

Liquid-like Properties of Rotavirus Replication Factories

The dynamic nature of the RNA-rich viral cytoplasmic inclusions previously termed ‘viroplasms’, and their tendency to coalesce [17, 18] during rotavirus (RV) infection are reminiscent of other cytoplasmic liquid-like ribonucleoprotein cytosolic granules [20]. Such observations have prompted us to further investigate the liquid-like properties of viroplasms.

Previous reports demonstrated that the two viral proteins NSP5 and NSP2 constitute the bulk of viroplasms [13, 17, 21–23]. We used MA104 cell lines that fully support RV replication, whilst expressing low levels of the C-terminally EGFP- and mCherry-tagged NSP5 and NSP2, respectively [16, 17]. Upon RV infection, both cytosolic NSP2-mCherry [16] and NSP5-EGFP [18] relocalise into newly formed replication factories, thus making them suitable markers for live-cell imaging of these virus-induced organelles.

At 4 hours post infection (HPI), more than 90% of virus-infected NSP5-EGFP or NSP2-mCherry cell lines contained NSP5-EGFP or NSP2-mCherry-containing cytoplasmic granules, respectively. We were able to observe fusion events between these granules, irrespective of the fusion fluorescent reporter protein used (figure 7.1a), suggesting that these inclusions may have liquid-like properties.

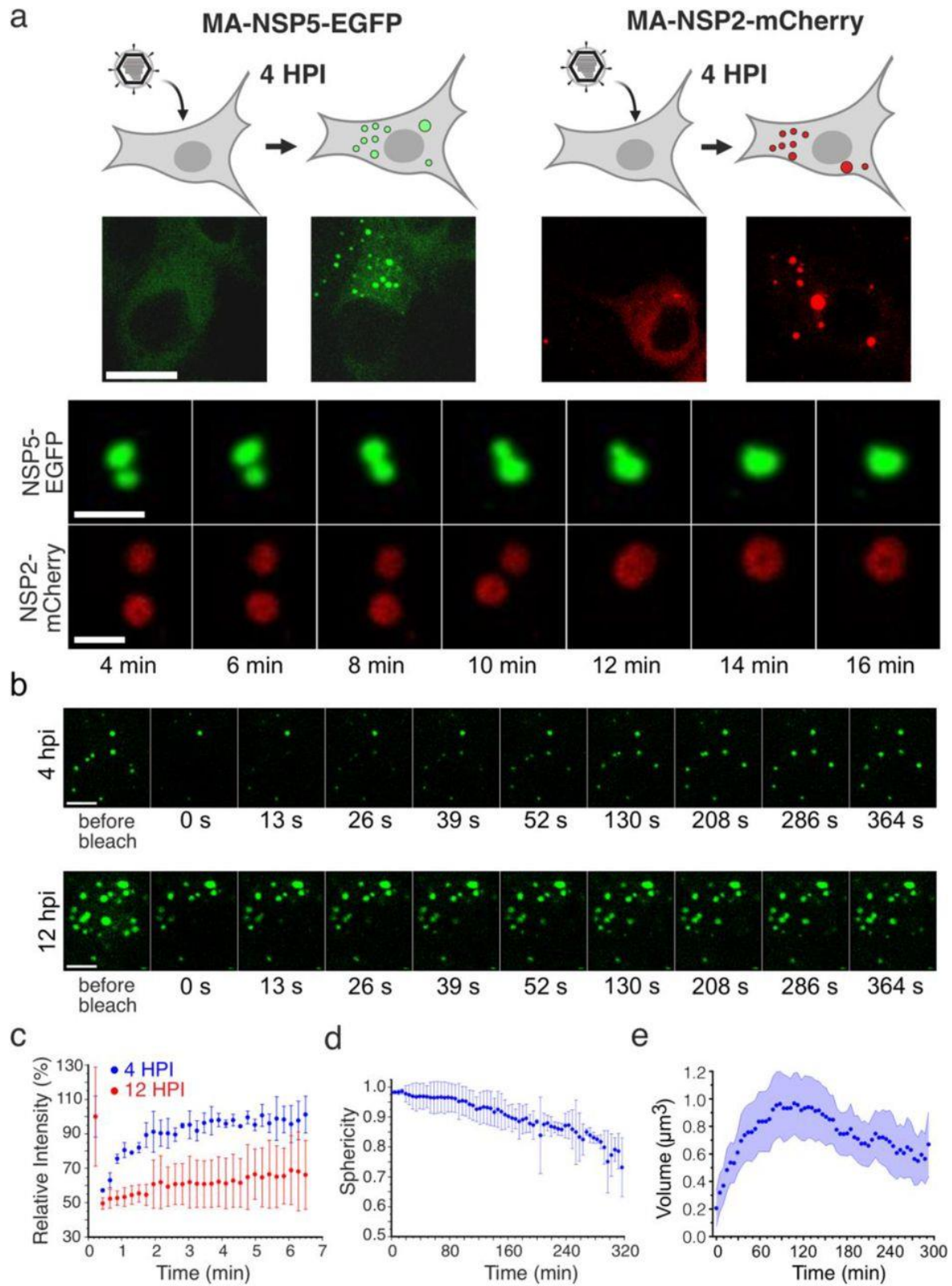


Figure 7.1: Liquid-like Properties of the Rotavirus Replication Factories. a) Dynamics of replication factories tagged with EGFP (NSP5-EGFP) and mCherry (NSP2-mCherry)

visualised in MA104-NSP5-EGFP and MA104-NSP2-mCherry rotavirus-infected cell lines. Live-cell confocal images (4-16 min) acquired after 4 hours post infection (HPI). Scale bars, 5 μm . b) Fluorescence recovery after photobleaching (FRAP) of EGFP-tagged replication factories after 4 HPI (early infection) and 12 HPI (late infection). c) Fluorescence Intensities after FRAP of EGFP-tagged replication factories after 4 HPI (blue) and 12 HPI (red) shown in b). Each data point represents mean \pm SD intensity values calculated for multiple NSP5-EGFP-tagged granules in 5 RV-infected cells. d) Sphericity of NSP5-EGFP-containing granules during RV infection. Each data point represents mean \pm SD sphericity values calculated for NSP5-EGFP-NSP5-tagged granules in cells detected in 15 frames. Data were recorded for 320 min immediately after 4 HPI when multiple NSP5-EGFP granules could be detected in RV-infected cells. e) Calculated volumes of NSP5-EGFP-tagged granules formed in RV-infected cells after 4 HPI as shown in d). The mean values decrease due to *de novo* formation of multiple smaller NSP5-EGFP granules that continuously assemble in cells between 4 HPI (t=0 min) and 9 HPI (t=300 min).

To assess the dynamics of NSP5-EGFP in these droplets, we photobleached viroplasms during 'early' (4 HPI) and 'late' (12 HPI) infection and measured fluorescence recovery over time (figure 7.1b). Fluorescence recovery after photobleaching (FRAP) studies of the 'early' viroplasms revealed a rapid (60–80 s) and complete (95–100%) fluorescence recovery. The kinetics and recovery percentage, however, decreased substantially for larger granules observed during late infection stages (figure 7.1c). The reduction in FRAP recovery suggests a change in the viscoelasticity of late viroplasms (i.e., they become more viscous or solid-like) during the course of infection.

As most typical properties of liquids are determined by their surface tension [24, 25], smaller liquid droplets coalesce and attain spherical shapes with the lowest volume-to-surface area ratios. To investigate the shape of viroplasms, we observed NSP5-EGFP-expressing RV-infected cells, and we found that at 4 hours post infection these structures are spherical (figure 1d and Materials and Methods). Time-resolved confocal microscopy of individual viroplasms (Materials and Methods) revealed that size of droplets increased over course of infection (figure 7.1a). In contrast, the calculated sphericities of these inclusions

decreased with time, suggesting loss of fluidity, consistent with the observed slower FRAP recovery rates during late infection (figure 7.1c).

We next examined the sensitivities of both early and late viroplasms towards the aliphatic alcohol 1,6-hexanediol (1,6-HD) which is commonly used as a chemical probe to differentiate between liquid-like and gel-like states of membrane-less organelles [26, 27]. We exposed cells infected with rotaviruses to 4% (*w/v*) 1,6-HD added to cell culture medium. Immediately after application of the compound (less than 30 s), early viroplasms were completely dissolved (figure 7.2a). When 1,6-HD was removed, NSP5-EGFP assemblies slowly reappeared, initially forming smaller assemblies that eventually coalesced into larger viroplasms (figure 7.2a). In contrast, when treated with 1,6-HD at 12 HPI, only a fraction of smaller viroplasms were dissolved, while larger viroplasms remained unaffected (figure 7.2a), suggesting that they have undergone a liquid-to-solid phase transition [28]. A brief (5 min) chemical crosslinking with 4% (*v/v*) paraformaldehyde prior to the application of the aliphatic alcohol also rendered the early infection (4 HPI) structures refractory to 1,6-HD treatment (figure S1a). Collectively, these results suggest that the assembly of viroplasms is driven by weak hydrophobic interactions that can be stabilised by chemical cross-linking. Additionally, we verified the 1,6-HD sensitivity of viroplasms assembled in the RV-infected cells producing NSP2-mCherry in lieu of NSP5-EGFP (figure S7.1b). Irrespective of the protein tagged (NSP5 or NSP2), or the fluorophore chosen, viroplasms responded similarly to the application of 1,6-HD.

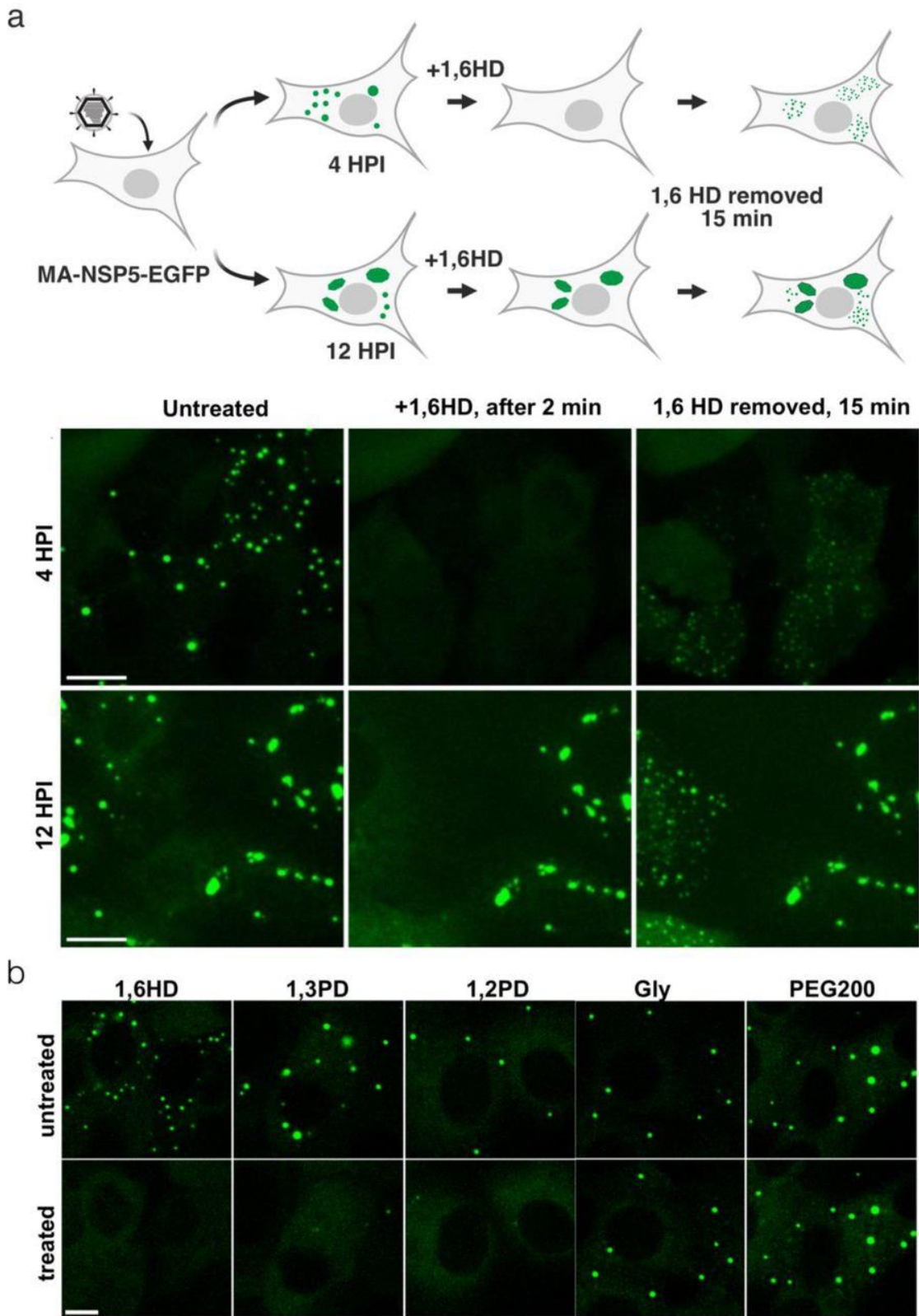


Figure 7.2: 1,6-hexanediol (1,6HD) differentiates early and late viral replication factories. a) Replication factories in MA104-NSP5-EGFP cells infected with RV at 4 HPI dissolve after

>30 s post application of 4% (w/v) 1,6HD added to the cell culture medium (middle panel). Removal of 1,6HD results reassembly of multiple EGFP-NSP5-containing droplets dispersed in the cytosol (right panel). Bottom, replication factories at 12 HPI: before application of 1,6HD (left), 2 min after application (middle), and 15 min after removal of 1,6HD from cell culture medium (left). Note larger viral factories that remain refractory to 1,6HD treatment. Scale bar, 50 μ m. b) Sensitivity of RV replication factories to aliphatic alcohols at 4 HPI. Left to right – 1,6-hexanediol (1,6HD); 1,3-propylene diol (1,3PD); 1,2-propylene diol (1,2PD, or propylene glycol); glycerol (Gly); polyethylene glycol 200 (PEG200). Top panels – before application and bottom panels – 1 min after application of these compounds (4% v/v). Scale bar, 30 μ m.

Rotavirus Replication Factories Are Dissolved by Small Aliphatic Diols

We posited that related aliphatic diols with similar physicochemical properties (e.g., hydrophobicity and molecular weight) to 1,6-HD, but less toxic for cells might exert similar effects on these condensates in cells. Remarkably, we identified two low molecular weight aliphatic diols (1,2- and 1,3-propane diols; denoted as 1,2-PD and 1,3-PD, respectively) that also dissolved viroplasms in RV-infected cells at 4 HPI (figure 7.2b).

Since both intracellular protein concentration and protein tagging may significantly affect the properties of the phase-separating system [10], we also carried out immunofluorescent staining of wild type MA104 cells infected with wild type RV before and after application of 1,6-HD and a non-toxic 1,2-PD (commonly known as propylene glycol, PG, figure S7.1c). Both alcohols completely dissolved viroplasms, further corroborating that the observed structures are formed via LLPS of NSP5 that accumulates during rotavirus infection.

As a final test, we used a recombinant NSP5-deficient (knock-out, KO) rotavirus [16] to infect three MA104 cell lines that stably produce NSP5, NSP5-EGFP and NSP2-mCherry. Viroplasms were only observed in the cells producing untagged NSP5 4-8 HPI (figure S7.1). In contrast, no viroplasms were detected in NSP2-mCherry and NSP5-EGFP cells, confirming that the untagged NSP5 is the key protein that drives LLPS. Together with our recent studies [16], these results also suggest that C-terminal tagging of NSP5 impairs its

function and RV replication, whilst not precluding NSP5-EGFP mixing with untagged NSP5/NSP2 condensates that are formed during RV infection. Viroplasms sensitive to 1,2-PD treatment were also formed in mouse embryonic fibroblasts several hours post RV infection (figure S7.2), suggesting that the observed NSP5-rich condensates are formed via LLPS in other cell types susceptible to RV infection.

Taken together, early infection stage viroplasms exhibit all the hallmarks of a liquid state: they are spherical and they coalesce; they exchange cytoplasmically dissolved proteins; they are reversibly dissolved by the aliphatic alcohols disrupting weak interactions that drive LLPS.

Rotavirus Viroplasm-forming Nonstructural Proteins Form Liquid Condensates

To move towards a better mechanistic understanding of liquid-liquid demixing of the two viroplasm-enriched proteins NSP5 and NSP2, we analysed their propensities to undergo LLPS. The high content of intrinsic disorder of NSP5, and its Gly/Ser and Asn/Glu-rich composition contribute to a number of several low complexity regions that typically favour weakly self-adhesive interactions required for phase separation. To this end, we first analysed the two proteins using our recently developed machine learning approach termed DeePhase [29] to identify LLPS-prone sequences. This hypothesis-free approach revealed several protein regions (LLPS score > 0.5) with high propensity for driving phase separation (figure 7.3a and b). Remarkably, sequences of NSP5, predicted to promote LLPS, were located within the two regions of the protein that had been previously demonstrated to be essential for viroplasm formation [17] (figure 7.3a, regions highlighted in green). One of these regions contained multiple negatively charged residues (figure 7.3a, C-terminal negatively charged residues shown in red), previously proposed to interact with the positively charged surfaces of NSP2 [30]. Similarly, DeePhase detected multiple NSP2 residues predicted to have high propensity to drive LLPS (figure 7.3b). Remarkably, structural analysis [31] of the octameric RNA chaperone NSP2 revealed that the majority of these residues presented multiple positively charged side chains (figure 7

.3c), including those previously demonstrated to bind NSP5 [30]. Given the highly charged natures of both proteins (NSP2, pI ~9 and NSP5, pI ~5.5), the observed phase separation is likely to be driven by both attractive electrostatic interactions (figure 7.3c), as well as hydrophobic interactions that are perturbed in the presence of the aliphatic alcohols, e.g., 1,6-HD and PG.

7. Rotavirus Replication Factories Are Complex Ribonucleoprotein Condensates

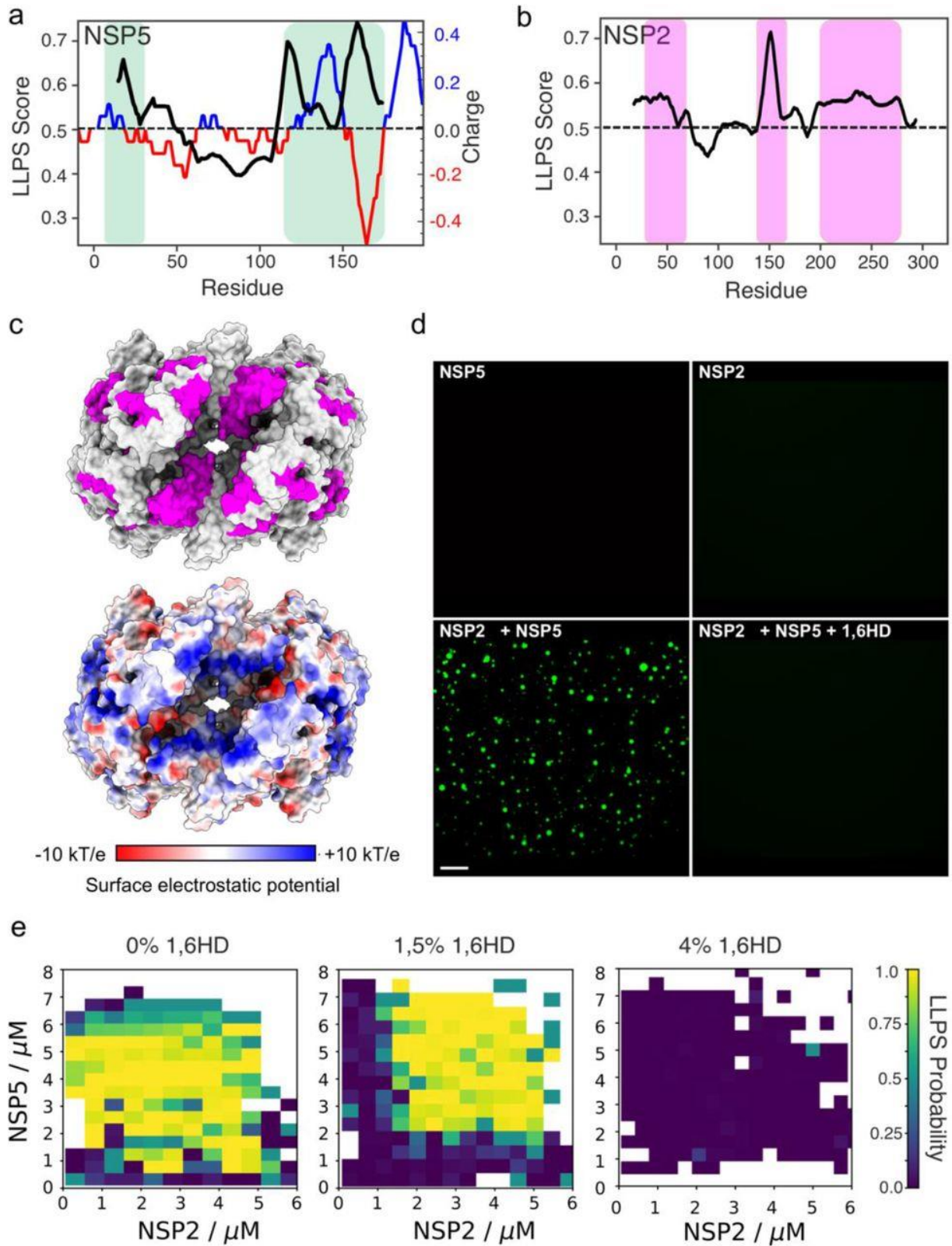


Figure 7.3: Rotavirus proteins NSP5 and NSP2 undergo liquid-liquid demixing. a) DeePhase prediction of the phase-separating properties of NSP5 (LLPS score of 0.6). Averaged score

with a 30-residue sliding window is shown as a black line. EMBOSS Protein charge plot shown as an alternating blue (positive charge) and red (negative charge) line. Green boxes denote protein residues of previously shown to be essential for viral factory formation in RVs. b) DeePhase prediction of the phase-separating properties of NSP2 (LLPS score of 0.3). Note residues with high propensity to undergo LLPS (highlighted). These NSP2 residues were mapped on the surface representation of the RNA chaperone NSP2 in magenta (c), *top*) and for comparison shown along with the surface electrostatic charge distribution of NSP2 (c), *bottom*). d) Atto488-labelled NSP5 (*top left*) and NSP2 (*top right*), 10 μ M each, and immediately after mixing (*bottom left*). NSP5/NSP2 droplets are dissolved in the presence of 5% 1,6HD (*bottom right*). Scale bar, 20 μ m. e) Phase diagrams generated through droplet microfluidics for the coacervation of NSP2 and NSP5, in the presence of 0% v/v (*left*), 1.5% v/v (*middle*), and 4% v/v (*right*) 1,6-hexanediol. Phase diagrams were generated from N = 2206, 2035 and 1470 data points for each 1,6-hexanediol concentrations, respectively, and the data were used to construct the LLPS probability plots.

To confirm these results from our *in-silico* predictions, we next examined the behavior of the recombinant untagged NSP5 and the C-terminally His-tagged NSP2. In solution, each protein was monodisperse (Materials and Methods). Circular dichroism analysis of NSP5 suggested that regions of protein disorder contributed to almost 40% of the spectrum (figure S7.3). Such low-complexity intrinsically disordered regions commonly underpin LLPS of proteins [9, 24, 32, 33], in agreement with *in silico* predictions.

In isolation, NSP5 and NSP2 samples did not form any microscopically detectable condensates in the micromolar concentration regime (figure 7.3d, upper panel). Immediately upon mixing, 5–10 μ M of each protein, multiple micron-sized droplets were formed (figure 7.3e). These droplets were dissolved by 1,6-HD (figure 7.3e), confirming that the observed droplets represented NSP5/NSP2 condensates, consistent with the effects of the aliphatic alcohol *in vivo*.

To further characterise the phase behavior of NSP5/NSP2 condensates, we generated phase diagrams for these protein mixtures alone and in the presence of 1,6-HD. Using high-throughput droplet microfluidics (figure S7.4), we obtained phase diagrams for a range of

NSP5 and NSP2 concentrations (figure 7.3e and figure S7.5), revealing coacervation of the proteins occurred in the low micromolar regime. NSP5/NSP2 protein mixtures remained homogenous in the presence of 4% (w/v) 1,6-HD, with a detectable change in the phase-separation behavior observed even at lower 1,5% (w/v) 1,6-HD concentration. Given the potential electrostatic contribution of negatively and positively charged residues of NSP5 and NSP2, we also examined the salt-dependence of the NSP5/NSP2 condensate formation *in vitro*. Above 0.5 M NaCl concentration, NSP5/NSP2 coacervation was severely inhibited (figure S7.5), supporting the idea that NSP5/NSP2 coacervation is driven by both hydrophobic and electrostatic interactions between the two multivalent proteins.

Viroplasms Are Complex Ribonucleoprotein Condensates That Accumulate RV RNAs

Given that viroplasms are viewed as sites of viral RNA replication [13, 34], and NSP2 is a multivalent RNA chaperone [35–37], we then examined RNA composition and the effects of aliphatic alcohols on RNA distribution in viroplasms. smFISH analysis of the RV genomic segment 3 (Seg3) and segment 4 (Seg4) transcript distribution in MA104-NSP5-EGFP cells revealed that NSP5-EGFP marked viroplasms contained both types of transcripts at 4 HPI (figure 7.4a, *left*). Treatment of RV-infected cells with an aliphatic diol PG resulted in rapid disassembly of these ribonucleoprotein granules and re-localisation of the RV transcripts into the cytoplasm (figure 7.4a, *middle*). Removal of these compounds from the cell culture medium for 15 min prior to cell fixation and imaging permitted reformation of smaller NSP5-EGFP granules containing both Seg3 and Seg4 transcripts. Confocal microscopy of the RNA signals suggests that Seg3 and Seg4 RNA transcripts remained intact upon viroplasm dissociation, consistent with rapid (~15 min) reformation of multiple RNA-rich granules upon removal of PG.

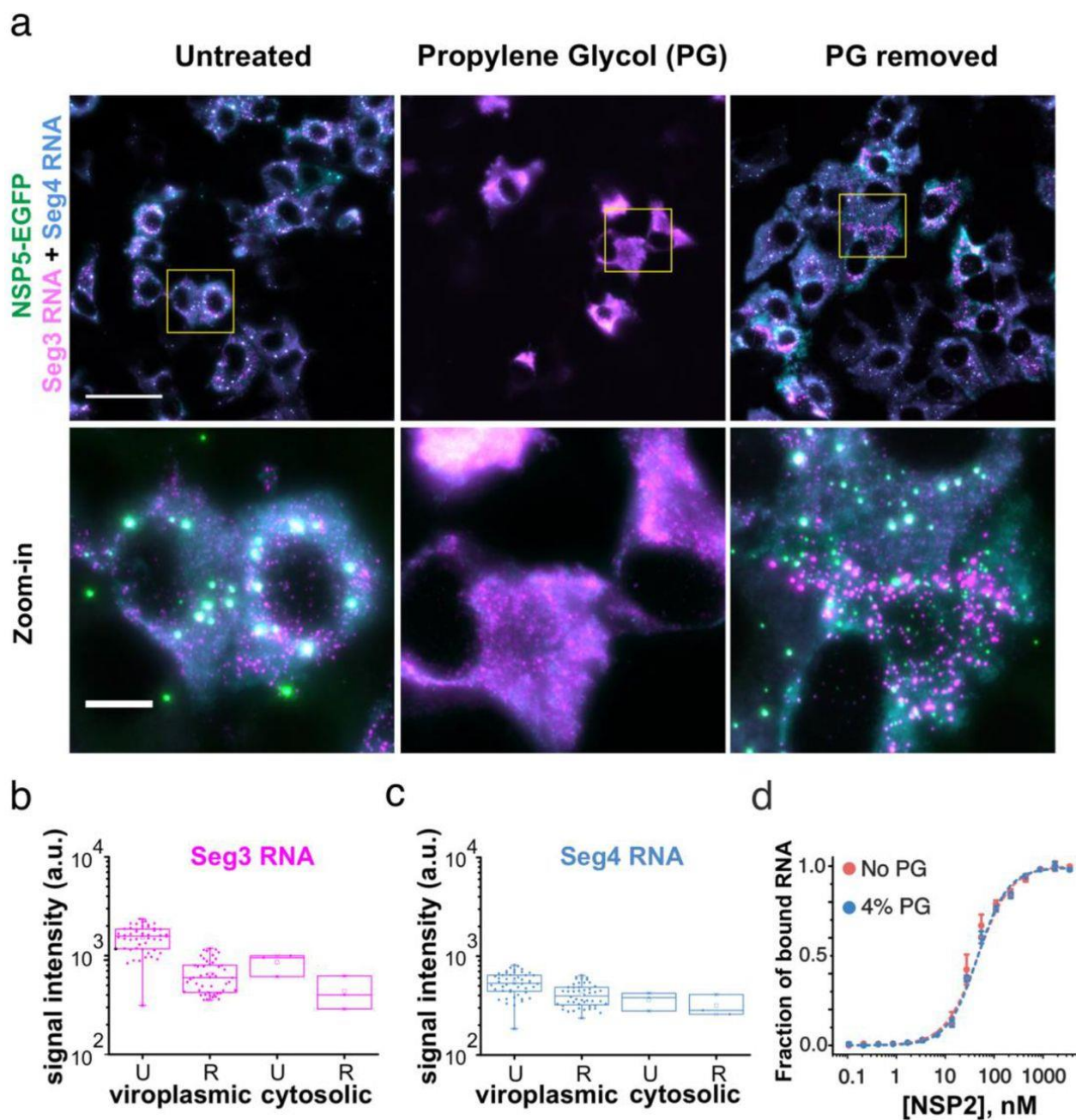


Figure 7.4: Rotavirus replication factories are RNA-protein condensates sensitive to propylene glycol. a) RV-infected MA-NSP5-EGFP cells at 6 HPI. NSP5-EGFP-tagged viral factories (green) are rapidly dissolved in the presence of 4% (v/v) propylene glycol (PG, *middle*). Viral RNA-protein condensates rapidly reform (<10 min) after removal of propylene glycol (PG) from the cell culture medium (*right*). Rotavirus transcripts Seg3 RNA (magenta) and Seg4 RNA (cyan), with with colocalising Seg3 and Seg4 RNA signals (white) were detected by smFISH. Scale bars: 50 μm , zoomed-in regions: 10 μm . b)-c) Changes in

the localisation of Seg3 and Seg4 RNAs and their relative distribution between the viroplasm and the cytosol before (Untreated, U), and 15 min after PG treatment (Recovery, R). Median and quartile values of integrated signal intensities (normalised by area) for each channel for viroplasms ('viroplasmic'), and individual cells (N=9, 'cytosolic') are shown. d) Binding of NSP2 to a fluorescently labelled 20-mer ssRNA in the presence of 4% propylene glycol (PG), measured by fluorescence anisotropy.

A fraction of RV transcripts formed multiple RNA clusters outside NSP5-EGFP granules (figure 7.4a), suggesting that the viral transcripts aggregate independently of the ability of NSP5 and NSP2 to form liquid condensates. Analysis of the integrated RNA signal intensities before and after PG treatment revealed that the amount of transcripts did not dramatically change during these treatments (figure 7.4b and c), confirming their reversible redistribution in the cytoplasm of infected cells. Interestingly, after recovery not all NSP5/NSP2 condensates were equally enriched in viral RNAs, further corroborating viral RNA re-distribution and exchange between these granules. Our recent studies indicate that rotavirus RNA oligomerisation is dependent on NSP2 [35–38].

The apparent affinity of NSP2 for RNA was identical in the presence of 4% (v/v) PG (figure 7.4d), suggesting that despite the observed perturbation of the NSP5/NSP2 condensates with aliphatic diols, NSP2–RNA complexes did not dissociate under those conditions.

This aspect of viroplasm formation remarkably resembles the formation of other complex ribonucleoprotein condensates, e.g., paraspeckles, in which RNA foci did not dissociate in the presence of aliphatic diols, despite the apparent dissolution of paraspeckles [39]. We therefore characterised the RNA foci formed in RV-infected cells during early infection using super-resolution DNA-PAINT approach [40] combined with smFISH. This super-resolution technique exploits transient binding of fluorescent DNA probes ('imagers') to complementary, RNA-bound 'docking' DNA strands (figure 7.5a and b). At 4 HPI, Seg3 transcripts could be detected as submicron-sized RNA clusters (figure 7.5d), similar to those seen in diffraction-limited images (figure 7.4a). 3D DNA-PAINT imaging of NSP2 condensates in RV-infected cells confirmed that early infection condensates contain only few viral transcripts, suggesting that NSP5/NSP2 coacervation spontaneously occurs during

early RV infection, and it is not nucleated by the transcribing viral particles present in cells. Furthermore, 3D DNA-PAINT imaging of Seg3 RNA foci revealed that they became less isotropic (i.e., loss of sphericity) by 6 HPI (figure S7.6), mirroring the overall decrease in sphericity of viroplasms during late infection. Given the resistance of RNA foci to aliphatic diols, and rapid (10–15 min) reformation of smaller condensates upon removal of these compounds, it is possible that such viral RNA aggregates could seed the nucleation of new NSP2/NSP5 condensates in cells [41]. Taken together, these results confirm that early infection viroplasms should be regarded as liquid RNP granules [42–45].

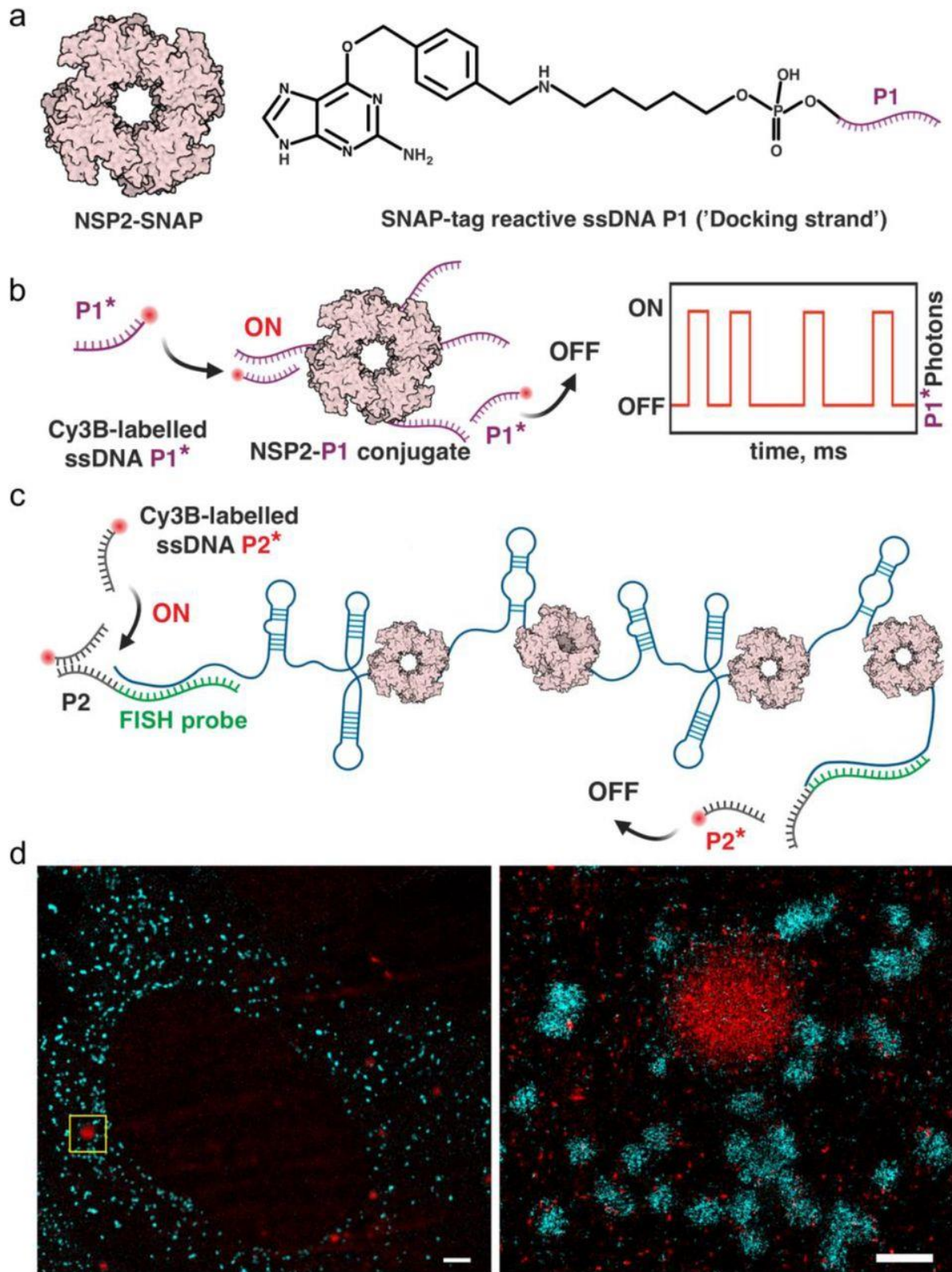


Figure 7.5: Super-resolution DNA-PAINT analysis of RV replication factories. a) DNA-labelling scheme of NSP2 for DNA-PAINT imaging. Low levels of SNAP-tagged NSP2 (a

doughnut-shaped NSP2 octamer) are produced in a stable MA104 cell line. A SNAP-tag reactive benzylguanine (BG) DNA derivative (P1 ssDNA docking strand) can form a stable thioether bond with NSP2-SNAP. b) Detection of NSP2-rich condensates formed in RV-infected cells using DNA-PAINT approach. Transient binding and dissociation of a Cy3B-dye labelled ssDNA probe P1* (complementary to ssDNA P1) generates blinking at the target sites (ON/OFF) used for stochastic super-resolution imaging. c) Similarly, smFISH of Seg3 transcripts is combined with DNA-PAINT approach by installing orthogonal P2 ssDNA docking sites into the Seg3-specific FISH probes d) A combined super-resolved image of NSP2-rich condensates (NSP2-SNAP in red) and Seg3 transcripts (cyan) in RV-infected cells 4 HPI. Scale bars = 2 μm (*left*), 500 nm (*right*).

7.3. Discussion

Previous studies uncovered protein composition of viroplasms, suggesting that these cytoplasmic inclusions are formed when NSP5 is co-expressed with NSP2 and/or the viral capsid protein VP2 [14, 15, 17, 23, 46], even in the absence of RV infection. Here, from multiple lines of evidence, we revealed that rotavirus viroplasms represent ribonucleoprotein condensates that are formed via phase separation of NSP5 and NSP2: First, cytosolic inclusions formed by NSP5/NSP2 are initially spherical; second, two or more NSP5-rich droplets can fuse and relax into a sphere; third, infection with the NSP5-deficient rotavirus mutant does not yield these droplets, unless NSP5 is produced *in trans*; fourth, these droplets are formed upon NSP5 and NSP2 mixing *in vitro*, and when these proteins are co-expressed *in vivo*; finally, NSP2/NSP5 droplets can be instantly dissolved when treated with aliphatic alcohols known to disrupt multivalent interactions driving liquid-liquid phase separation. Our findings that distinct compounds other than 1,6-hexanediol but with similar physicochemical properties can reversibly dissolve viroplasms in RV-infected cells reinforces the idea that these inclusions represent liquid condensates. Furthermore, these compounds did not dissolve viroplasmic condensates after chemical cross-linking. Importantly, the observed condensates are formed exclusively when the untagged version of NSP5 is co-expressed in cells along with either NSP2, or VP2 [17, 46], as

well as during RV infection. Thus, the formation of the observed condensates reflects the unique physicochemical properties of NSP5/NSP2, and is not artifactual due to over-expression or fluorescent tagging [47, 48].

NSP5 and NSP2 have been long established to be major binding partners and the key protein residents of RV replication factories [12, 14, 16, 17]. Given the multivalent RNA and NSP5-binding nature of NSP2, the observed phase-separation of these proteins at low micromolar concentration is consistent with the reports of their aggregation-prone behaviour upon mixing at higher micromolar concentrations [30, 35]. By exploring the phase boundary using the PhaseScan, we have shown that the degree of NSP5/NSP2 coacervation is determined by the concentrations of both interacting partners. Thus, our model predicts that the kinetics of NSP5/NSP2 condensate formation depends on the intracellular concentration of both NSP5 and NSP2, the production of which would be expected to directly correlate with the number of infectious particles per cell. Indeed, previous observations [49] suggesting that the kinetics of viroplasm formation increase in direct correlation with the multiplicity of infection fully support our model.

Current views of replication factory formation in RVs are dominated by the idea of multiple viral proteins being recruited into viroplasms in a specific order [15, 17, 23, 46, 50] resulting in their particular organization [51]. Here, we propose a unifying model for viroplasm assembly (figure 7.6) that takes into account extensive existing data on their structural organisation accrued over several decades, and amounts to a step change in our understanding of these replication factories in these viruses. We propose that RV viroplasms represent condensates formed by NSP5/NSP2 coacervation. Initially, these condensates behave as dynamic fluids, and change in their viscoelastic properties (e.g., fluidity) during infection, concomitant with changes in viral protein phosphorylation [15, 16, 23, 52–55] and the ratio of RNA:protein in these inclusions. Other cellular biomolecular condensates have been shown to contain hundreds of distinct molecular species [56], acting as membraneless protein-rich liquid condensates that selectively partition biomolecules and can promote specific nucleic-acid remodeling events [6]. Despite their complex and dynamic composition, typically, only a few protein residents are required to form these condensates [9, 10, 56, 57]. Given its high propensity to undergo LLPS, and multiple lines of

evidence demonstrating its indispensable role in the formation of viroplasms [12, 16, 17, 52, 53], we propose that the rotavirus NSP5 acts as the primary scaffold required to form these condensates. Knocking out NSP5 abolishes formation of these structures even when other viral proteins are present during infection [16] (figure S7.1), while NSP5 co-expression with RV multivalent RNA-binding proteins, e.g., NSP2, [17, 21] results in formation of such condensates. Our *in vitro* results fully corroborate the model for NSP5/NSP2 condensate formation, further suggesting that the observed condensation does not require phosphorylation of proteins *in vitro*, despite multiple phosphorylated forms of NSP5 detected in rotavirus-infected cells [16, 52, 54]. This result suggests the phosphorylation of NSP5 is not a prerequisite for coacervation, but it is likely to play important roles in regulation of the molecular selectivity and specificity of these condensates, thus allowing their protein and RNA composition change during infection. Similarly, phosphoregulation of protein condensates has been demonstrated for a number of membraneless organelles *in cellulo* and *in vitro* [58, 59]. Other condensate residents are concentrated within these coacervates, often by direct interactions with scaffolds, but are not required for condensate formation and referred as clients [56].

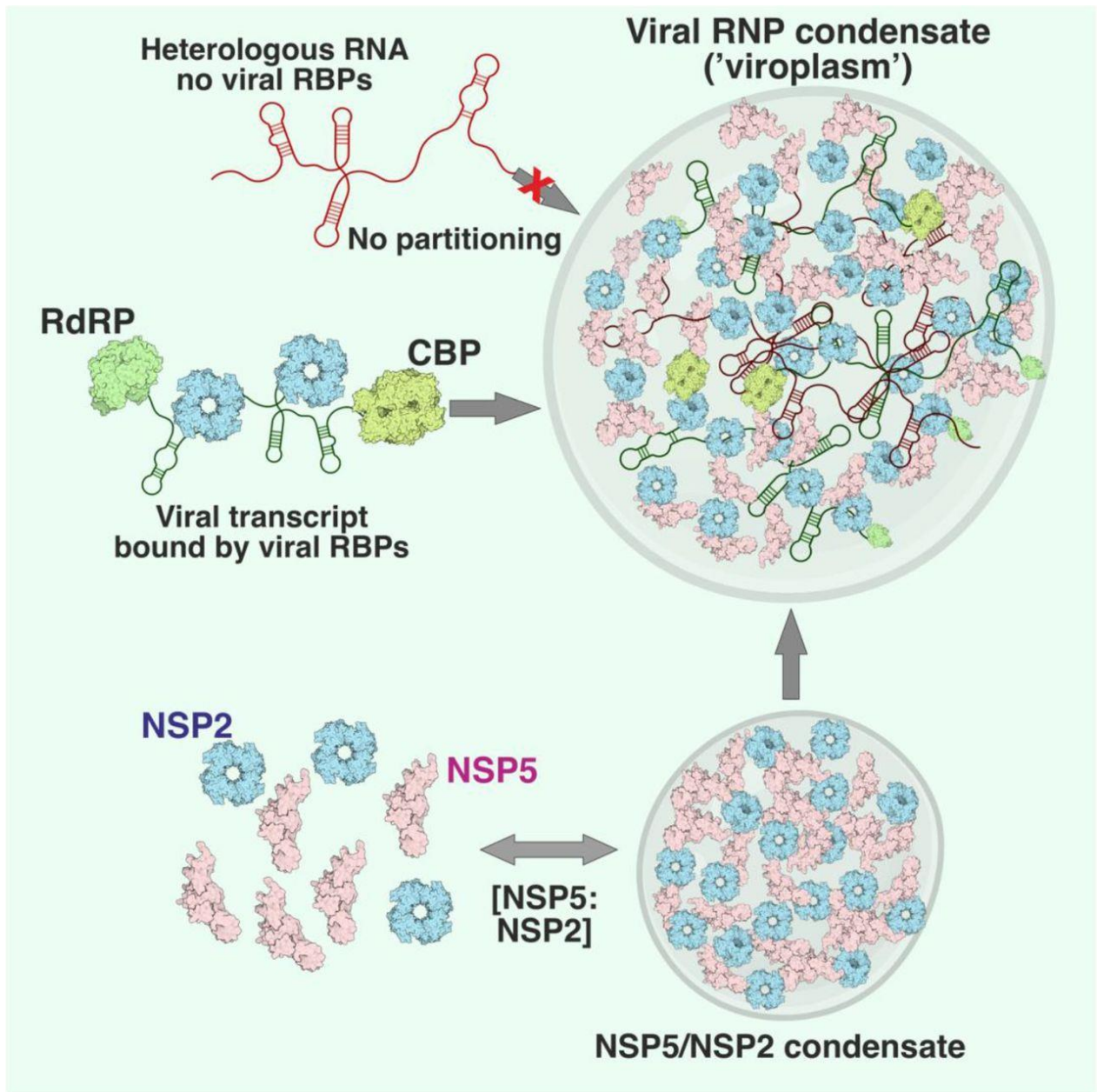


Figure 7.6: Proposed model of LLPS-driven formation of viral replication factories in rotaviruses. Multivalent Asp/Glu- and Ser-rich protein NSP5 (pink) acts as a scaffold that binds multivalent RNA chaperone NSP2 (cyan doughnut-shaped octamers), and potentially other RNA-binding clients. NSP5 and NSP2 readily undergo coacervation at low micromolar concentrations, also forming condensates in cells previously described as ‘viroplasm-like structures’. Cognate viral transcripts undergo enrichment in these condensates via a mechanism distinct from other known RNP granules. Mechanistically, this could be achieved by specific protein-RNA recognition, e.g., the viral RNA-dependent RNA

Polymerase (RdRP) that recognises conserved sequences of all eleven distinct RV transcripts, and undergoes partitioning into NSP5/NSP2 condensates due to its high nM affinity for both proteins [1, 2]. Other similarly sized RNAs (red) lacking the viral proteins with high affinity for NSP5/NSP2 proteins are excluded from these condensates. Other multivalent RNA-binding proteins (RBPs), i.e., the viral cap-binding protein (CBP), and multiple copies of NSP2 can form the RNP complexes that can be absorbed into the NSP2/NSP5 condensates, and released from them by dissolving the condensates. Such RNP condensates are known to promote RNA-RNA interactions in cells, while simultaneously acting as ‘molecular filters’ for concentrating viral transcripts, both mechanisms being conducive to a multi-RNA genome assembly in rotaviruses.

Viral RNA-binding proteins (e.g., viral RNA-dependent RNA polymerase, RdRP, and a cap-binding protein, figure 7.6) concentrate in these structures, and have been demonstrated to strongly bind NSP5 [50, 60], but not being sufficient to form viroplasm-like structures on their own, thus fulfilling the criteria of client proteins that partition into NSP5/NSP2 condensates. Lipid bilayers [61], microtubules [62] and tubulin [63] can promote nucleation of biomolecular condensates and spatially regulate the kinetics of their formation in cells. Association of lipid droplets [64, 65] and tubulin [15, 49] with viroplasms is thus entirely consistent with our model of formation of viral replicative factories in RV-infected cells. Similarly to the early and late infection stage viroplasms, changes in the viscoelastic properties of liquid condensates that decrease fluidity over time are common for many other systems that undergo LLPS [28, 66, 67]. Recent super-resolution imaging studies of these organelles in RV-infected cells proposed that distinct viral proteins are organized into multiple concentric layers [51]. The proposed model explains the relevance of these findings, as even very simple condensates show characteristics of multilayered behavior [33]. Distinct layers are likely to form via different molecular interaction networks that lead to different viscoelastic properties, such as those observed in nucleoli [68], P-granules [32] and nuclear speckles [69].

Implications for selective RNA recruitment and RNA-RNA interactions required for segmented genome assembly

Coacervation of the viral RNA chaperone NSP2 [35, 38, 70] associated with multiple viral transcripts would accelerate formation of inter-molecular RNA–RNA interactions between them. Several processes may contribute to stabilisation of sequence-specific inter-molecular RNA-RNA contacts [44, 71], while promoting intra-molecular duplex melting via interactions with multiple arginine side chains of NSP2 [72] concentrated in the viroplasmic liquid phase [6]. Recent evidence argues that intermolecular RNA-RNA interactions play a role in forming and determining the composition of distinct cytoplasmic, RNA-rich ribonucleoprotein granules [42–44, 73, 74]. Coalescence of multiple RNA-binding proteins and non-translating mRNAs lacking fixed stoichiometry can occur during cellular stress, giving rise to stress granules [73]. Similarly, viroplasms accumulate non-polyadenylated, untranslated viral transcripts and viral RNA-binding proteins. While stress granules are highly enriched in poly(A)-binding proteins associated with mRNAs, non-polyadenylated viral transcripts are likely to be bound by the viral RNA-dependent RNA polymerase (RdRP), previously reported to have nM affinity for both NSP2 and NSP5 (figure 7.6). We propose that RV replication factories represent a unique case of specialized RNP granules that promote accumulation of viral transcripts to minimise spurious promiscuous RNA–RNA interactions with non-cognate host cell RNAs [44]. Our findings have several important ramifications for future studies of rotavirus replication mechanisms, posing many outstanding questions that arise from recognition of the LLPS-driven assembly of viroplasms, and potentially of other viral replication factories in segmented dsRNA viruses that exhibit similar liquid-like behavior in cells [75, 76]. The proposed LLPS-driven mechanism of viroplasm formation offers a unified model that explains multiple results from previous efforts to explain their assembly, and establishes LLPS as an attractive target for antiviral intervention [77].

7.4. Materials and Methods

Cells and Viruses

Rotavirus A strains (Bovine rotavirus strain RF and simian rotavirus SA11) were propagated as previously described [78, 79]. MA104 (ATCC CRL-2378.1) and its derivatives MA-NSP2-mCherry and MA-NSP5-EGFP stable cell lines were generated and maintained as described in [16, 17]. Lentiviral vector pAIP-NSP2-SNAP was generated using a synthetic SNAP tag-coding DNA (GenPart, Genscript) inserted into a double digested with *MluI/EcoRI* pAIP-NSP2-mCherry vector [16]. MA104-NSP2-SNAP cell line was then generated as previously described [16]. Briefly, 7×10^6 HEK293T cells were seeded in 10-cm² tissue culture dishes 24 h before transfection. For each well, 2.4 µg of pMD2-VSV-G, 4 µg of pMDLg pRRE, 1.8 µg of pRSV-Rev, and 1.5 µg of pAIP-NSP2-SNAP DNA constructs were co-transfected using Lipofectamine 3000 (Sigma-Aldrich) following the manufacturer's instructions. After 48 h, the virus was harvested, filtered through a 0.45 µm polyvinylidene fluoride filter, and immediately stored at -80°C. For lentiviral transduction, MA104 cells were transduced in six-well plates with 1.2 ml of the lentivirus-containing supernatant for 2 days. Cells were then selected by growing cells in DMEM supplemented with 10% FBS and puromycin (5 µg/mL) for 4 days. NSP5 immunostaining was carried out as previously described [16].

Image data acquisition

Confocal imaging was conducted on a Zeiss Cell Observer SD inverted confocal microscope with a Yokogawa CSU-X1 spinning disk unit from Zeiss (Jena, Germany). The microscope was equipped with a 1.40 NA 63x Plan apochromat oil immersion objective from Zeiss. Measurements were performed at room temperature. Photo bleaching for FRAP experiments was done with a 488 nm laser at 100% intensity and 3000 ms exposure time, then the recovery was observed for 60 frames every 30 seconds. EGFP was imaged using a 488 nm laser at 20% intensity and 200 ms exposure time and mCherry was imaged with a 561 nm laser at 20% intensity and 200 ms exposure time. Images recorded as z-stacks

consisted of either 10 or 50 frames, with a 0.5 μm distance between them, depending on the sample. In the excitation path a quad-edge dichroic beamsplitter (FF410/504/582/669-Di01-25 \times 36, Semrock) was used. For two color detection of EGFP and mCherry a dichroic mirror (660 nm, Semrock) and band-pass filters 525/50 and 690/60 (both Semrock) were used in the detection path. Separate images for each fluorescence channel were acquired using two separate electron multiplier charge coupled devices (EMCCD) cameras (Photometrics Evolve™). Image acquisition was controlled using the Zeiss Zen (blue edition) 2011 Software (Zeiss). Widefield imaging was conducted with the Eclipse Ti-E inverted microscope from Nikon (Tokyo, Japan). The images were acquired with a 0.7 NA 60x S Plan Fluor ELWD oil immersion objective from Nikon. Measurements were performed at room temperature. A pE-4000 illumination system (CoolLED) was used as light source. DAPI was imaged using a 385 nm LED at 33% intensity and 55 ms exposure time. EGFP and ATTO 488 were imaged using a 470 nm LED at 41% intensity with 300 ms exposure time and 7% intensity with 55 ms exposure time respectively. mCherry was imaged with a 550 nm LED at 36% intensity and 300 ms exposure time. The light path was regulated with a Dapi/FITC/Cy3/Cy5 Quad HC Filter Set (Semrock). The images were acquired using a scientific complementary metal-oxide-semiconductor (sCMOS) camera (Andor Technology). Image acquisition was controlled using the NIS-Elements AR V.4.50 Software (Nikon).

Image Data Processing

The recorded pictures were processed with ImageJ (v.1.52p) [80]. Data of the FRAP experiments was also analysed with ImageJ. Distinct visible granules were selected manually as ROIs before bleaching. The recovery curve over a time span of 13 minutes (corresponding to 60 frames) was calculated for each ROI. The displayed values are median intensities of five ROIs. Other parameters, including fusion events, velocity or sphericity, were analysed with Imaris (v 8.2.0, Bitplane, AG Zurich, Switzerland). The viral granules were marked as ROIs based on their size and high fluorescence intensity. Then the centre of image mass R of the detected fluorescence volume in each ROI is calculated with the voxel (camera pixel) intensity m_i , the center of a voxel r_i and the sum of voxel intensities M .

$$R = \frac{1}{M} \sum_{i \in IsoSurface} m_i r_i$$

The coordinates of the centre of image mass of the ROIs was tracked for the duration of the experiment. From the resulting values the velocity was calculated as the change of the centre of image mass coordinates between two frames divided by the frame time (4.9 min). 65 ROIs were observed over a time span of 5.2 hours.

Sphericity Ψ was calculated as the ratio of the surface area of a sphere with the same volume as the given particle V_p to the surface area of the particle A_p .

$$\Psi = \frac{\pi^{\frac{1}{3}}(6V_p)^{\frac{2}{3}}}{A_p}$$

Mean sphericity values were calculated for 65 ROIs monitored for EGFP-marked granules observed for over 6 h. Fusion events were counted when two separate ROIs overlap and their volumes were treated as a single volume. 1037 ROIs were observed over 8 hours. If not stated otherwise, data points in the figures represent mean values averaged over all measured ROIs. Measurements were all performed in biological triplicates. The data presentation was done with OriginPro (Version 8.0891, OriginLab Corporation, Northampton, MA, USA). Where appropriate, schematics of figures were prepared using **BioRender.com**

NSP5 and NSP2 expression and purification

Recombinant NSP2 (strains SA11 and RF) were expressed and purified, as previously described [35]. NTA-affinity purified NSP2 fractions were further purified over a HiTrap SP cation-exchange column. The concentrated peak fractions were resolved on a Superdex 200 10×300 GL column and pre-equilibrated with RNase-free SEC buffer (25 mM HEPES-Na, pH 7.5, 150 mM NaCl) to ensure high purity and homogeneity of the preparation. While a functional form of the RNA chaperone NSP2 can be produced and purified under native conditions [31, 35], and its C-terminally His-tagged version supports viral replication [37], previous attempts to natively purify a full-length untagged NSP5 were not successful [30,

81]. We therefore expressed and purified NSP5 under denaturing conditions, followed by its refolding. Full-length recombinant NSP5 (strain RF) was expressed and isolated from bacterial pellets as inclusion bodies as previously described [35]. Washed inclusion bodies were solubilized in 6 M guanidinium hydrochloride and the protein-containing fraction was then subjected to a refolding protocol following step-wise dialysis [81]. After refolding, NSP5-containing fractions were further purified over an ImpRes Q column (GE). The concentrated peak fractions were further resolved on a Superdex 200 10×300 column pre-equilibrated with SEC buffer (25 mM HEPES-Na, pH 7.5, 150 mM NaCl) to ensure homogeneity of the preparation. Quasi-elastic scattering analysis of a monodisperse NSP5 sample revealed a hydrodynamic radius ~ 6.8 nm, consistent with the previously proposed decameric organization [81].

DeePhase predictions

The propensity of the protein sequences to form condensates was estimated using the DeePhase model. Briefly, individual predictions relied on featuring the protein sequences by estimating a number of explicit sequence-specific parameters (sequence length, hydrophobicity, Shannon entropy, the fraction of polar, aromatic and positively charged residues and the fraction of sequence estimated to be part of the low complexity region and intrinsically disordered region) as well as implicit word2vec algorithm-based embeddings. The used model had been trained on previously constructed datasets including sequences with varying propensity to undergo LLPS as has been described in [29]. In order to evaluate how the LLPS-propensity of each protein sequence varied along its length, the full sequences were divided into 20 amino acid long fragments and the propensity of each fragment to undergo LLPS was evaluated. For the final result, individual predictions from 10 consecutive fragments were averaged.

Circular Dichroism Spectroscopy and Dynamic Light Scattering

Samples were prepared by dialyzing NSP5 against 10 mM phosphate buffer pH 7.4, 50 mM sodium fluoride. Spectra were acquired in a 1 mm path length quartz cuvette (Hellma) using a Chirascan plus spectrometer (Applied Photophysics) with a 1 nm bandwidth and a step size of 1 nm. An average of 3 scans (190-280 nm) were used for the final spectra, measured at 20°C and 90°C. Data were fitted to determine the secondary structure content using BeStSel [82].

NSP5 samples (1 mg ml⁻¹) were injected on a TSKgel G6000PWxl SEC column (Tosoh) pre-equilibrated with the SEC buffer (see above) at 21°C and a flow-rate set to 0.4 ml min⁻¹. Dynamic (Quasi-Elastic) light scattering (QELS) measurements were carried out using an AKTA pure system (GE Healthcare) connected to a DAWN HELEOS and Optilab TrEX for QELS (Wyatt). On-line QELS was carried out using WyattQELS DLS Module to measure the translational diffusion and corresponding hydrodynamic radius of the eluting fraction. Autocorrelation functions (ACFs) were fitted to a single exponential to determine diffusion coefficients and corresponding hydrodynamic radii (Rh) of the oligomeric NSP5 species using ASTRA software (Wyatt).

PhaseScan

Device fabrication

Polydimethylsiloxane (PDMS, Corning) devices for droplet generation and multilayer well-devices for droplet collection and imaging were produced on SU-8 (Microchem) moulds fabricated via photolithographic processes as described previously [83–85].

Phase diagram generation

Phase diagrams were produced using droplet microfluidics in a similar manner to that described previously [19]. Syringe pumps (neMESYS modules, Cetoni) were used to control flows of protein solutions, consisting of 22 µM NSP5 supplemented with 6.4 µM Alexa647 dye (carboxylic acid, ThermoFisher) or 8 µM His-tagged NSP2 labelled with 8 µM Atto488-nitrilotriacetic acid (NTA, Sigma), and buffer (0.5 × phosphate saline buffer, PBS, pH 7.4).

Appropriate quantities of 1,6-hexanediol were pre-mixed into all solutions before droplet generation. The aqueous flow rates were configured to vary automatically according to pre-set gradients, with constant total flow rate of 60 $\mu\text{L}/\text{h}$, to scan phase space between nominal concentrations of 0.9–7.3 μM and 0.30–6.5 μM for NSP5 and NSP2, respectively FC-40 oil (containing 1.5% (v/v) fluorosurfactant, RAN biotechnologies) was introduced to the device at a constant flow rate of 50 $\mu\text{L}/\text{h}$ for microdroplet generation. For further details see Supporting Information.

Imaging

Directly after generation, microdroplets were transferred into a droplet-trapping device [86] to ensure droplets were maintained in a well-spaced, stationary configuration for imaging. Microscopy data was acquired with an AxioObserver D1 microscope (Zeiss) equipped with a 5x air objective and a high-sensitivity camera (Evolve 512, Photometrics). Appropriate filter sets were used for EFGP (49002, Chroma Technology) and AlexaFluor 647 detection (49009, Chroma Technology). Representative data are presented in figure S7.5.

Droplet detection and data analysis

Acquired images were analysed using a custom-written Python script. Droplets were fitted as circles in the images. Non-circular droplets or erroneous detections were filtered and removed. From the fitted circular areas, the total intensity was calculated and normalised to obtain the intensity per unit volume (calculated using the fitted diameter), and converted to concentrations by comparison to calibration images acquired with known concentrations of NSP2/Atto488 and NSP5/Alexa647 mixtures. Droplets were classified as phase-separated or homogeneous according to the presence or absence of at least two connected pixels >5 standard deviations from the mean pixel intensity. Representative classification output is presented figure S7.5. Droplet classification, NSP2 and NSP5 concentration were then combined on a per-droplet basis to produce phase diagrams. Two-dimensional probability maps were constructed by division of the phase space (NSP2 vs. NSP5 concentration) into regular squares. The proportion of homogeneous or phase-separated droplets present in each region of phase space was calculated, before being passed through the error function

(erf) to classify the phase-separation propensity of each region as represented by the colourmap.

Affinity measurements by fluorescence anisotropy

Fluorescence anisotropy measurements with AlexaFluor488 dye-labelled 20-mer RNA, as described previously [70], were performed at 25°C using a POLARstar Omega plate reader (BMG Labtech) in Greiner 384 well black polypropylene plates. Serial 2-fold dilutions of NSP2 and σ NS were titrated into 5 nM RNA in 50 mM Tris-HCl pH 7.5, 50 mM NaCl, 1 mM EDTA, 0.05% Tween-20 in a total volume of 50 μ l and equilibrated at room temperature for 15 minutes prior to measurements were taken. Where required, buffers were supplemented with 4% v/v 1,2-propanediol. Raw Anisotropy (r) values were calculated as follows:

$$r = \frac{(I_{\parallel} - I_{\perp})}{(I_{\parallel} + 2I_{\perp})}$$

Where I_{\parallel} and I_{\perp} are the parallel and perpendicular emission signals, respectively. Normalized anisotropy values were plotted as a function of protein concentration and fitted to a Hill equation using OriginPro 9.0.

Single-molecule Fluorescence in situ Hybridisation (smFISH) and TagPAINT

Rotavirus-infected and mock-infected MA104 cell controls, where appropriate, were fixed with 4% (v/v) methanol-free paraformaldehyde in nuclease-free phosphate saline buffer (PBS, Sigma) for 10 min at room temperature. Samples were then washed twice with PBS, and fixed cells were permeabilised with 70% (v/v) ethanol (200 proof) in RNase-free water, and stored in ethanol at +4°C for at least 12 hours prior to hybridization, and no longer than 24 h. Permeabilized cells were then re-hydrated for 5 min in a pre-hybridization buffer (300 mM NaCl, 30 mM trisodium citrate, pH 7.0 in nuclease-free water, 10 % v/v Hi-Di formamide (Thermo Scientific), supplemented with 2 mM vanadyl ribonucleoside complex). Re-hydrated samples were hybridized with an equimolar mixture

of DNA probes specific to the RNA targets (RVA strain SA11 and EGFP sequences), 62.5 nM final concentration, see SI Table 1, in a total volume of 200 μ l of the hybridization buffer (Stellaris RNA FISH hybridization buffer, Biosearch Technologies, supplemented with 10% v/v Hi-Di formamide). After 4 hours of incubation at 37°C in a humidified chamber, samples were briefly rinsed with the wash buffer (300 mM NaCl, 30 mM trisodium citrate, pH 7.0, 10 % v/v formamide in nuclease-free water, after which a fresh aliquot of 0,3 ml of the wash buffer was applied to each well and incubated twice at 37°C for 30 min. After washes, nuclei were briefly stained with 300 nM 4',6-diamidino-2-phenylindole (DAPI) solution in 300 mM NaCl, 30 mM trisodium citrate, pH 7.0) and the samples were finally rinsed with and stored in the same buffer without DAPI prior to the addition of the photostabilising imaging buffer (PBS containing an oxygen scavenging system of 2.5 mM protocatechuic acid, 10 nM protocatechuate-3,4-dioxygenase supplemented with 1 mM (\pm)-6-hydroxy-2,5,7,8-tetramethylchromane-2-carboxylic acid (Trolox) [87].

TagPAINT imaging [88] was carried out for SNAP-tagged NSP2-expressing cells infected with RVs. After fixation, cells were permeabilized with PBS supplemented with 0.2% Triton-X100 for 3 min, and then subsequently incubated with 50 mg ml⁻¹ BSA in PBS for 10 min. 5 μ M benzylguanine (BG)-conjugated DNA (Biomers.com) dissolved in PBS supplemented with 0.2% Tween-20 (PBST) was incubated with fixed cell samples for 15 min. The samples were then washed with 0.4 ml of PBST several times, to remove any non-specifically adsorbed ligand. Finally, the samples were incubated with gold nanoparticles in PBST for 10 min before mounting for DNA-PAINT imaging.

DNA-PAINT Imaging

Microscope configuration

DNA-PAINT imaging was carried out on an inverted Nikon Eclipse Ti microscope (Nikon Instruments) equipped with the Perfect Focus System using objective-type total internal reflection fluorescence (TIRF) configuration (oil-immersion Apo SR TIRF, NA 1.49 100x objective). A 200 mW 561 nm laser beam (Coherent Sapphire) was passed through a clean-up filter (ZET561/10, Chroma Technology) and coupled into the microscope objective using

a beam splitter (ZT561rdc, Chroma Technology). Fluorescence light was spectrally filtered with an emission filter (ET575lp, Chroma Technology) and imaged with a sCMOS camera (Andor Zyla 4.2) without further magnification, resulting in an effective pixel size of 130 nm after 2×2 binning. Images were acquired using a region of interest of 512×512 pixels. The camera read-out rate was set to 540 MHz, and images were acquired with an integration time of 200 ms.

Sample preparation, imaging and data analysis

5'-ATACATTGA-Cy3B-3' (Metabion) was used as ssDNA 'imager' for visualising Seg 3 RNA target. 20,000 frames were acquired for each target. These were generated using the Stellaris RNA FISH probe designer (<https://www.biosearchtech.com/stellaris-designer>), using each gene-specific ORF sequence as inputs and level 2 masking. The resulting pools of probes were then further filtered to remove the sequences targeting the RNA transcripts sequences with higher propensity to form stable intra-molecular base-pairing. 5'-TAATGAAGA-Cy3B-3' (Metabion) was used as ssDNA 'imager' for a complementary benzylguanine (BG)-conjugated oligonucleotide DNA (Biomers.com) for reacting with the SNAP-tagged NSP2. Imager strands were diluted to 100 pM (Seg3 RNA), and 300 pM (SNAP-tagged NSP2), respectively. Drift correction was performed with a redundant cross-correlation and gold particles used as fiducial markers. Fluorescence data were subjected to super-resolution reconstruction using Picasso software package [89, 90].

7.5. References

1. Nikolic J, Le Bars R, Lama Z, Scrima N, Lagaudrière-Gesbert C, Gaudin Y, et al. Negri bodies are viral factories with properties of liquid organelles. *Nat Commun.* 2017; 8(1):58.
2. Heinrich BS, Maliga Z, Stein DA, Hyman AA, Whelan SPJ. Phase transitions drive the formation of vesicular stomatitis virus replication compartments. *MBio.* 2018; 9(5):1-10.

3. Alenquer M, Vale-Costa S, Etibor TA, Ferreira F, Sousa AL, Amorim MJ. Influenza A virus ribonucleoproteins form liquid organelles at endoplasmic reticulum exit sites. *Nat Commun.* 2019; 10(1):1–19.
4. Guseva S, Milles S, Jensen MR, Salvi N, Kleman JP, Maurin D, et al. Measles virus nucleo- and phosphoproteins form liquid-like phase-separated compartments that promote nucleocapsid assembly. *Sci Adv.* 2020; 6(14):eaaz7095.
5. Brangwynne CP, Tompa P, Pappu RV. Polymer physics of intracellular phase transitions. *Nat Phys.* 2015; 11:899–904.
6. Nott TJ, Craggs TD, Baldwin AJ. Membraneless organelles can melt nucleic acid duplexes and act as biomolecular filters. *Nat Chem.* 2016; 8(6):569–75.
7. Bergeron-Sandoval LP, Safaee N, Michnick SW. Mechanisms and Consequences of Macromolecular Phase Separation. *Cell.* 2016; 165(5):1067–79.
8. Alberti S. Phase separation in biology. *Curr Biol.* 2017; 27(20):R1097–R1102.
9. Wang J, Choi JM, Holehouse AS, Lee HO, Zhang X, Jahnel M, et al. A molecular grammar governing the driving forces for phase separation of prion-like RNA binding proteins. *Cell.* 2018; 174(3):688–699.e16.
10. Alberti S, Gladfelter A, Mittag T. Considerations and Challenges in Studying Liquid-Liquid Phase Separation and Biomolecular Condensates. *Cell.* 2019; 176(3):419–434.
11. Aponte C, Poncet D, Cohen J. Recovery and characterization of a replicase complex in rotavirus-infected cells by using a monoclonal antibody against NSP2. *J Virol.* 1996; 70(2):985–91.
12. Fabbretti E, Afrikanova I, Vascotto F, Burrone OR. Two non-structural rotavirus proteins, NSP2 and NSP5, form viroplasm-like structures in vivo. *J Gen Virol.* 1999; 80(Pt 2):333–39.
13. Silvestri LS, Taraporewala ZF, Patton JT. Rotavirus replication: Plus-sense templates for double-stranded RNA synthesis are made in viroplasms. *J Virol.* 2004; 78(14):7763–74.

7.5. References

14. Contin R, Arnoldi F, Campagna M, Burrone OR. Rotavirus NSP5 orchestrates recruitment of viroplasmic proteins. *J Gen Virol.* 2010; 91(Pt 7):1782–93.
15. Criglar JM, Hu L, Crawford SE, Hyser JM, Broughman JR, Venkataram BV, et al. A novel form of rotavirus NSP2 and phosphorylation-dependent NSP2-NSP5 interactions are associated with viroplasm assembly. *J Virol.* 2014; 88(2):786–98.
16. Papa G, Venditti L, Arnoldi F, Schraner EM, Potgieter C, Borodavka A, et al. Recombinant Rotaviruses Rescued by Reverse Genetics Reveal the Role of NSP5 Hyperphosphorylation in the Assembly of Viral Factories. *J Virol.* 2019; 94(1):e011110-19.
17. Eichwald C, Rodriguez JF, Burrone OR. Characterization of rotavirus NSP2/NSP5 interactions and the dynamics of viroplasm formation. *J Gen Virol.* 2004; 85(Pt 3):625–634.
18. Eichwald C, Arnoldi F, Laimbacher AS, Schraner EM, Fraefel C, Wild P, et al. Rotavirus viroplasm fusion and perinuclear localization are dynamic processes requiring stabilized microtubules. *PLoS One.* 2012; 7(10):e47947.
19. Arter WE, Qi R, Krainer G, Welsh TJ, Xu Y. Rapid Generation of Protein Condensate Phase Diagrams Using Combinatorial Droplet Microfluidics. *bioRxiv.* 2020; 2020.06.04.132308.
20. Shin Y, Brangwynne CP. Liquid phase condensation in cell physiology and disease. *Science.* 2017; 357(6357):eaaf4382.
21. Berois M, Sapin C, Erk I, Poncet D, Cohen J. Rotavirus nonstructural protein NSP5 interacts with major core protein VP2. *J Virol.* 2003; 77(3):1757–63.
22. Taraporewala ZF, Jiang X, Vasquez-Del Carpio R, Jayaram H, Prasad BVV, Patton JT. Structure-function analysis of rotavirus NSP2 octamer by using a novel complementation system. *J Virol.* 2006; 80(16):7984–94.
23. Criglar JM, Anish R, Hu L, Crawford SE, Sankaran B, Prasad BVV, et al. Phosphorylation cascade regulates the formation and maturation of rotaviral replication factories. *Proc Natl Acad Sci U S A.* 2018; 115(51):E12015–E12023.

24. Brangwynne CP. Soft active aggregates: Mechanics, dynamics and self-assembly of liquid-like intracellular protein bodies. *Soft Matter*. 2011; 7:3052–3059.
25. Bergeron-Sandoval LP, Michnick SW. Mechanics, Structure and Function of Biopolymer Condensates. *J Mol Biol*. 2018; 430(23):4754–4761.
26. Lin Y, Mori E, Kato M, Xiang S, Wu L, Kwon I, et al. Toxic PR poly-dipeptides encoded by the C9orf72 repeat expansion target LC domain polymers. *Cell*. 2016; 167(3):789–802.e12.
27. Kroschwald S, Maharana S, Simon A. Hexanediol: a chemical probe to investigate the material properties of membrane-less compartments. *Matters*, 2017; 3:e201702000010.
28. Patel A, Lee HO, Jawerth L, Maharana S, Jahnel M, Hein MY, et al. A Liquid-to-Solid Phase Transition of the ALS Protein FUS Accelerated by Disease Mutation Article A Liquid-to-Solid Phase Transition of the ALS Protein FUS Accelerated by Disease Mutation. *Cell*. 2015; 162(5):1066–77.
29. Saar KL, Morgunov AS, Qi R, Arter WE, Krainer G, Lee AA, et al. Machine learning models for predicting protein condensate formation from sequence determinants and embeddings. *bioRxiv*. 2020; 2020.10.26.354753 (2020).
30. Jiang X, Jayaram H, Kumar M, Ludtke S, Estes MK, Prasad BVV. Cryoelectron microscopy structures of rotavirus NSP2-NSP5 and NSP2-RNA complexes: implications for genome replication. *J Virol*. 2006; 80(21):10829–35.
31. Jayaram H, Taraporewala Z, Patton JT, Prasad BVV. Rotavirus protein involved in genome replication and packaging exhibits a HIT-like fold. *Nature*. 2002; 417(6886):311–5.
32. Wei MT, Elbaum-Garfinkle S, Holehouse AS, Chen CCH, Feric M, Arnold CB, et al. Phase behaviour of disordered proteins underlying low density and high permeability of liquid organelles. *Nat Chem*. 2017; 9(11):1118–1125.
33. Choi JM, Holehouse AS., Pappu RV. Physical Principles Underlying the Complex Biology of Intracellular Phase Transitions. *Annu Rev Biophys*. 2020; 49:107–133.

7.5. References

34. Patton JT, Silvestri LS, Tortorici MA, Vasquez-Del Carpio R, Taraporewala ZF. Rotavirus genome replication and morphogenesis: role of the viroplasm. *Reoviruses: Entry, Assembly and Morphogenesis* (ed. Roy P) 169–187 (Springer Berlin Heidelberg, 2006).
35. Borodavka A, Dykeman EC, Schrimpf W, Lamb DC. Protein-mediated RNA folding governs sequence-specific interactions between rotavirus genome segments. *Elife*. 2017; 6:e27453.
36. Bravo JPK, Borodavka A, Barth A, Calabrese AN, Mojzes P, Cockburn JJB, et al. Stability of local secondary structure determines selectivity of viral RNA chaperones. *Nucleic Acids Res*. 2018; 46(15):7924–7937.
37. Bravo JPK, Kira B, Venditti L, Gail EH, Davidovich C, Lamb DC, et al. Structural basis of rotavirus RNA chaperone displacement and RNA annealing. *bioRxiv*. 2020; 2020.10.26.354233.
38. Borodavka A, Desselberger U, Patton JT. Genome packaging in multi-segmented dsRNA viruses: distinct mechanisms with similar outcomes. *Curr Opin Virol*. 2018; 33:106–12.
39. Yamazaki T, Souquere S, Chujo T, Kobelke S, Chong YS, Fox AH, et al. Functional Domains of NEAT1 Architectural lncRNA Induce Paraspeckle Assembly through Phase Separation. *Mol Cell*. 2018; 70(6):1038–1053.e7.
40. Dai M, Jungmann R, Yin P. Optical imaging of individual biomolecules in densely packed clusters. *Nat Nanotechnol*. 2016; 11(9):798–807.
41. Garcia-Jove Navarro M, Kashida S, Chouaib R, Souquere S, Pierron G, Weil D, et al. RNA is a critical element for the sizing and the composition of phase-separated RNA–protein condensates. *Nat Commun*. 2019; 10(1):3230.
42. Lin Y, Protter DSW, Rosen MK, Parker R. Formation and maturation of phase-separated liquid droplets by RNA-binding proteins. *Mol Cell*. 2015; 60(2):208–19.

43. Khong A, Matheny T, Jain S, Mitchell SF, Wheeler JR, Parker R. The Stress Granule Transcriptome Reveals Principles of mRNA Accumulation in Stress Granules. *Mol Cell*. 2017; 68(4):808–820.e5.
44. Van Treeck B, Parker R. Emerging Roles for Intermolecular RNA-RNA Interactions in RNP Assemblies. *Cell*. 2018; 174(4):791–802.
45. Rhine K, Vidaurre V, Myong S. RNA Droplets. *Annu Rev Biophys*. 2020; 49:247–65.
46. Buttafuoco A, Michaelsen K, Tobler K. Conserved Rotavirus NSP5 and VP2 Domains Interact and Affect Viroplasm. *J Virol*. 2020; 94(7):e01965-19.
47. Alberti S, Saha S, Woodruff JB, Franzmann TM, Wang J, Hyman AA. A User’s Guide for Phase Separation Assays with Purified Proteins. *J Mol Biol*. 2018; 430(23):4806–4820.
48. Mitrea DM, Chandra B, Ferrolino MC, Gibbs EB, Tolbert M, White MR, et al. Methods for Physical Characterization of Phase-Separated Bodies and Membrane-less Organelles. *J Mol Biol*. 2018;430(23):4773–4805.
49. Carrão-Torres JJ, Gutiérrez M, Arias CF, López S, Isa P. Characterization of viroplasm formation during the early stages of rotavirus infection. *Virol J*. 2010; 7:350.
50. Arnoldi F, Campagna M, Eichwald C, Desselberger U, Burrone OR. Interaction of Rotavirus Polymerase VP1 with Nonstructural Protein NSP5 Is Stronger than That with NSP2. *J Virol*. 2007; 81(5):2128–37.
51. Garcés Suárez Y, Martínez JL, Hernández DT, Hernández HO, Pérez-Delgado A, Méndez M, et al. Nanoscale organization of rotavirus replication machineries. *Elife*. 2019; 8:e42906.
52. Poncet D, Lindenbaum P, L’Haridon R, Cohen J. In vivo and in vitro phosphorylation of rotavirus NSP5 correlates with its localization in viroplasms. *J Virol*. 1997; 71(1):34–41.
53. Mohan KVK, Muller J, Som I, Atreya CD. The N- and C-terminal regions of rotavirus NSP5 are the critical determinants for the formation of viroplasm-like structures independent of NSP2. *J Virol*. 2003; 77(22):12184–92.

7.5. References

54. Sen A, Agresti D, Mackow ER. Hyperphosphorylation of the rotavirus NSP5 protein is independent of serine 67 or NSP2 and the intrinsic insolubility of NSP5 is regulated by cellular phosphatases. *J Virol.* 2006; 80(4):1807–16.
55. Sotelo PH, Schümann M, Krause E, Chnaiderman J. Analysis of rotavirus non-structural protein NSP5 by mass spectrometry reveals a complex phosphorylation pattern. *Virus Res.* 2010; 149(1):104–8.
56. Ditlev JA, Case LB, Rosen MK. Who ' s In and Who ' s Out — Compositional Control of Biomolecular Condensates. *J Mol Biol.* 2018; 430(23):4666–4684.
57. Langdon EM, Gladfelter ASA. New Lens for RNA Localization: Liquid-Liquid Phase Separation. *Annu Rev Microbiol.* 2018; 72:255–271.
58. Bah A, Vernon RM, Siddiqui Z, Krzeminski M, Muhandiram R, Zhao C, et al. Folding of an intrinsically disordered protein by phosphorylation as a regulatory switch. *Nature.* 2015; 519(7541):106–9.
59. Aumiller WM, Keating CD. Phosphorylation-mediated RNA/peptide complex coacervation as a model for intracellular liquid organelles. *Nat Chem.* 2016; 8(2):129–37.
60. Viskovska M, Anish R, Hu L, Chow D, Hurwitz AM, Brown NG, et al. Probing the sites of interactions of rotaviral proteins involved in replication. *J Virol.* 2014; 88(21):12866–81.
61. Feng Z, Chen X, Wu X, Zhang M. Formation of biological condensates via phase separation: Characteristics, analytical methods, and physiological implications. *J Biol Chem.* 2019; 294(40):14823–14835.
62. Maucuer A, Desforges B, Joshi V, Boca M, Kretov DA, Hamon L, et al. Microtubules as platforms for probing liquid–liquid phase separation in cells – application to RNA-binding proteins. *J Cell Sci.* 2018; 131(11):jcs214692.
63. King MR, Petry S. Phase separation of TPX2 enhances and spatially coordinates microtubule nucleation. *Nat Commun.* 2020; 11(1):270.

64. Cheung W, Gill M, Esposito A, Kaminski CF, Courousse N, Chwetzoff S, et al. Rotaviruses associate with cellular lipid droplet components to replicate in viroplasms, and compounds disrupting or blocking lipid droplets inhibit viroplasm formation and viral replication. *J Virol*. 2010; 84(13):6782–98.
65. Crawford SE, Desselberger U. Lipid droplets form complexes with viroplasms and are crucial for rotavirus replication. *Curr Opin Virol*. 2016; 19:11–5.
66. Conicella AE, Dignon GL, Zerze GH, Broder H, Ordine AMD. TDP-43 α -helical structure tunes liquid – liquid phase separation and function. *Proc Natl Acad Sci U S A*. 2020; 117(11):5883–94.
67. Ray S, Singh N, Kumar R, Patel K, Pandey S, Datta D, et al. α -Synuclein aggregation nucleates through liquid – liquid phase separation. *Nat Chem*. 2020; 12(8):705–16.
68. Feric M, Vaidya N, Harmon TS, Mitrea DM, Zhu L, Richardson TM, et al. Coexisting Liquid Phases Underlie Nucleolar Subcompartments. *Cell*. 2016; 165(7):1686–97.
69. Fei J, Jadalaha M, Harmon TS, Li ITS, Hua B, Hao Q, et al. Quantitative analysis of multilayer organization of proteins and RNA in nuclear speckles at super resolution. *J Cell Sci*. 2017; 130(24):4180–92.
70. Bravo JPK, Borodavka A, Barth A, Calabrese AN, Mojzes P, Cockburn JJB, et al. Stability of local secondary structure determines selectivity of viral RNA chaperones. *Nucleic Acids Res*. 2018; 46(15):7924–37.
71. Marenduzzo D, Finan K, Cook PR. The depletion attraction: An underappreciated force driving cellular organization. *J Cell Biol*. 2006; 175(5):681–6.
72. Hu L, Chow D, Patton JT, Palzkill T, Estes MK, Prasad BVV. Crystallographic analysis of rotavirus NSP2-RNA complex reveals specific recognition of 5' GG sequence for RTPase activity. *J Virol*. 2012; 86(19):10547–57.
73. Wheeler JR, Matheny T, Jain S, Abrisch R, Parker R. Distinct stages in stress granule assembly and disassembly. *Elife*. 2016; 5:e18413.
74. Tauber D, Tauber G, Khong A, Van Treeck B, Pelletier J, Parker R. Modulation of RNA Condensation by the DEAD-Box Protein eIF4A. *Cell*. 2020; 180(3):411–426.e16.

7.5. References

75. Desmet EA, Anguish LJ, Parker JSL. Virus-mediated compartmentalization of the host translational machinery. *mBio*. 2014; 5(5):e01463-14.
76. Campbell EA, Reddy VRAP, Gray AG, Wells J, Simpson J, Skinner MA, et al. Discrete Virus Factories Form in the Cytoplasm of Cells Coinfected with Two Replication-Competent Tagged Reporter Birnaviruses That Subsequently Coalesce over Time. *J Virol*. 2020; 94(13):e02107-19.
77. Wheeler RJ, Lee HO, Poser I, Pal A, Doleman T, Kishigami S, et al. Small molecules for modulating protein driven liquid-liquid phase separation in treating neurodegenerative disease. *bioRxiv*. 2019; 721001.
78. Desselberger U, Richards J, Tchertanov L, Lepault J, Lever A, Burrone O, et al. Further characterisation of rotavirus cores: Ss(+)RNAs can be packaged in vitro but packaging lacks sequence specificity. *Virus Res*. 2013; 178(2):252–63.
79. Arnold M, Patton JT, McDonald SM. Culturing, Storage, and Quantification of Rotaviruses. *Curr Protoc Microbiol*. 2009; Chapter 15:Unit 15C.3.
80. Schindelin J, Arganda-Carreras I, Frise E, Kaynig V, Longair M, Pietzsch T, et al. Fiji: An open-source platform for biological-image analysis. *Nat Methods*. 2012; 9(7):676–82.
81. Martin D, Ouldali M, Ménétrey J, Poncet D. Structural organisation of the rotavirus nonstructural protein NSP5. *J Mol Biol*. 2011; 413(1):209–21.
82. Micsonai A, Wien F, Bulyáki E, Kun J, Moussong E, Lee Y, et al. BeStSel: A web server for accurate protein secondary structure prediction and fold recognition from the circular dichroism spectra. *Nucleic Acids Res*. 2018; 46(W1):W315–W322.
83. McDonald JC, Duffy DC, Anderson JR, Chiu DT, Wu H, Schueller OJ, et al. Fabrication of Microfluidic Systems in Poly(dimethylsiloxane). *Electrophoresis*. 2000; 21(1):27–40.
84. Arter WE, Yusim Y, Peter Q, Taylor CG, Klenerman D, Keyser UF, et al. Digital Sensing and Molecular Computation by an Enzyme-Free DNA Circuit. *ACS Nano*. 2020; 14(5):5763–71.

85. Mazutis L, Gilbert J, Ung WL, Weitz DA, Griffiths AD, Heyman JA. Single-Cell Analysis and Sorting Using Droplet-Based Microfluidics. *Nat Protoc.* 2013; 8(5):870–91.
86. Labanieh L, Nguyen TN, Zhao W, Kang DK. Floating droplet array: An ultrahigh-throughput device for droplet trapping, real-time analysis and recovery. *Micromachines (Basel).* 2015; 6(10):1469–82.
87. Aitken CE, Marshall RA, Puglisi JD. An oxygen scavenging system for improvement of dye stability in single-molecule fluorescence experiments. *Biophys J.* 2008; 94(5):1826–35.
88. Nieves DJ, Hilzenrat G, Tran J, Yang Z, MacRae HH, Baker MAB, et al. TagPAINT: covalent labelling of genetically encoded protein tags for DNA-PAINT imaging. *R Soc Open Sci.* 2019; 6(12):191268.
89. Jungmann R, Avendaño MS, Woehrstein JB, Dai M, Shih WM, Yin P. Multiplexed 3D cellular super-resolution imaging with DNA-PAINT and Exchange-PAINT. *Nat Methods.* 2014; 11(3):313–8.
90. Schnitzbauer J, Strauss MT, Schlichthaerle T, Schueder F, Jungmann R. Super-resolution microscopy with DNA-PAINT. *Nat Protoc.* 2017; 12(6):1198–228.

7.6. Appendix

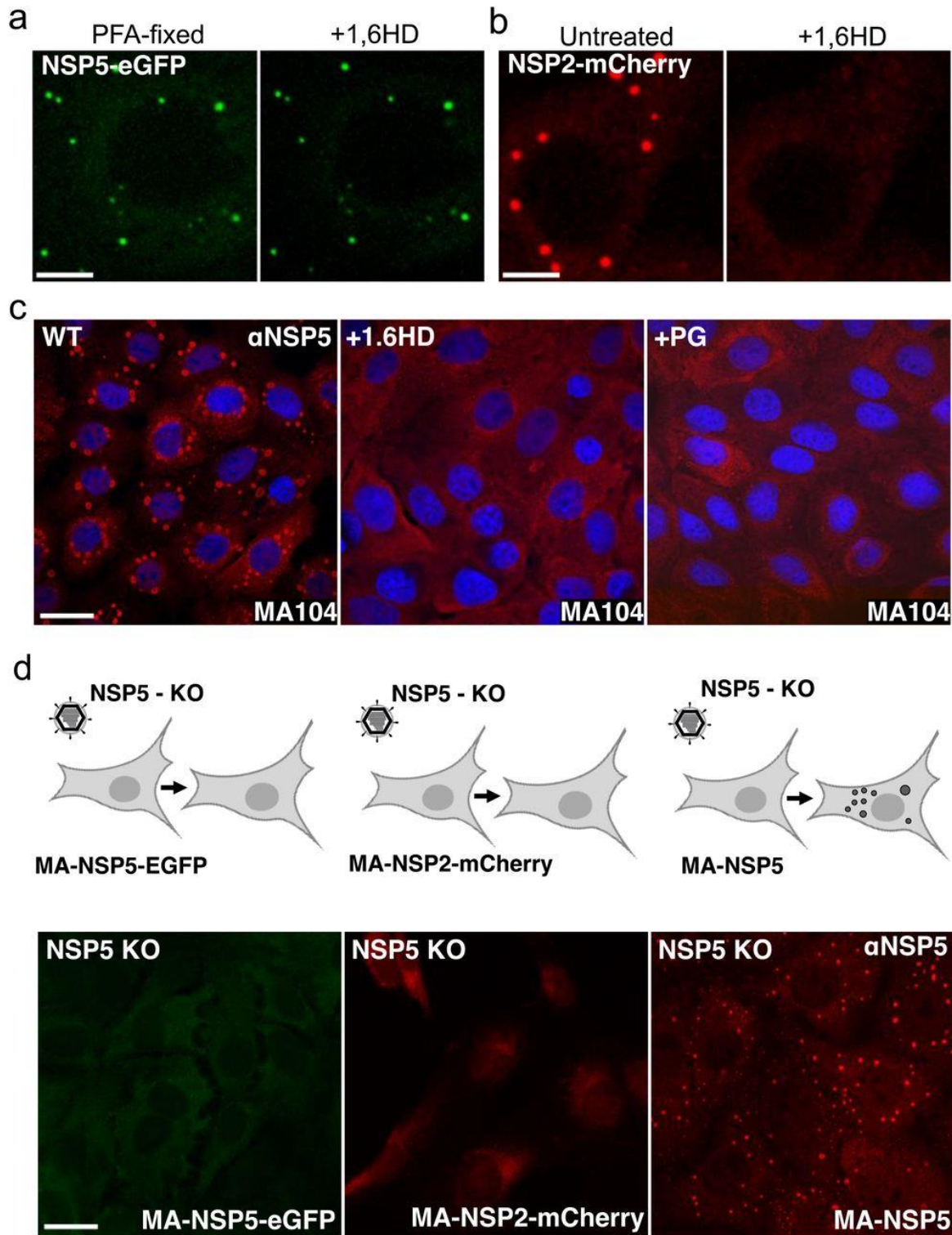


Figure S7.1: a) RV-infected MA104-NSP5-EGFP cells (4 HPI) fixed with 4% (v/v) paraformaldehyde for 5 min (PFA-fixed, left panel). Application of 1,6HD (5%) does not

dissolve NSP5-EGFP granules after chemical cross-linking with PFA (right). b) Live-cell images of RV-infected MA104-NSP2-mCherry cells, shown in Fig.1, at 4 HPI. NSP2-mCherry-tagged replication factories dissolve upon application of 4% (v/v) 1,6HD (SI Movie). Scale bars, 10 μ m. c) Immunofluorescent (IF) staining of viral replication factories in RV-infected MA104 cells 6 HPI, before (left), and after a brief (5 min) application of 4% 1,6HD or propylene glycol (PG), respectively, prior to PFA fixation and IF detection of NSP5 (red). Nuclei are stained with DAPI (blue). d) Recombinant rotavirus NSP5 KO (NSP5 knockout) infection of MA104-derived stable cell lines producing NSP5-EGFP (*left, diffuse EGFP signal*), NSP2-mCherry (*middle, diffuse mCherry signal*), and the wild type NSP5 (*right, NSP5-rich condensates, IF staining*). All cells were fixed and imaged 8 h after infection with NSP5-KO RV. Scale bar, 10 μ m.

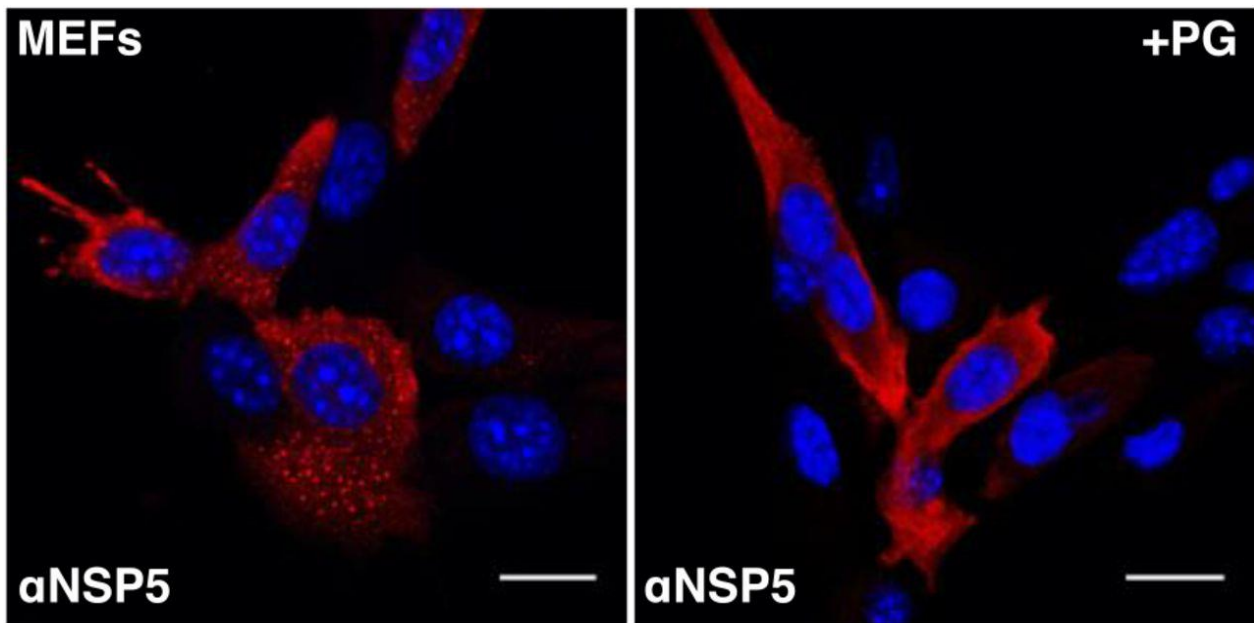


Figure S7.2: IF staining of NSP5-rich condensates (replication factories) in RV-infected Murine Embryo Fibroblasts (MEFs), 6 HPI. Left – untreated RV-infected MEFs; right – RV-infected MEFs 5 min after treatment with 4% (v/v) propylene glycol (PG). Nuclei – DAPI staining (blue), NSP5 – red. Scale bar 15 μ m.

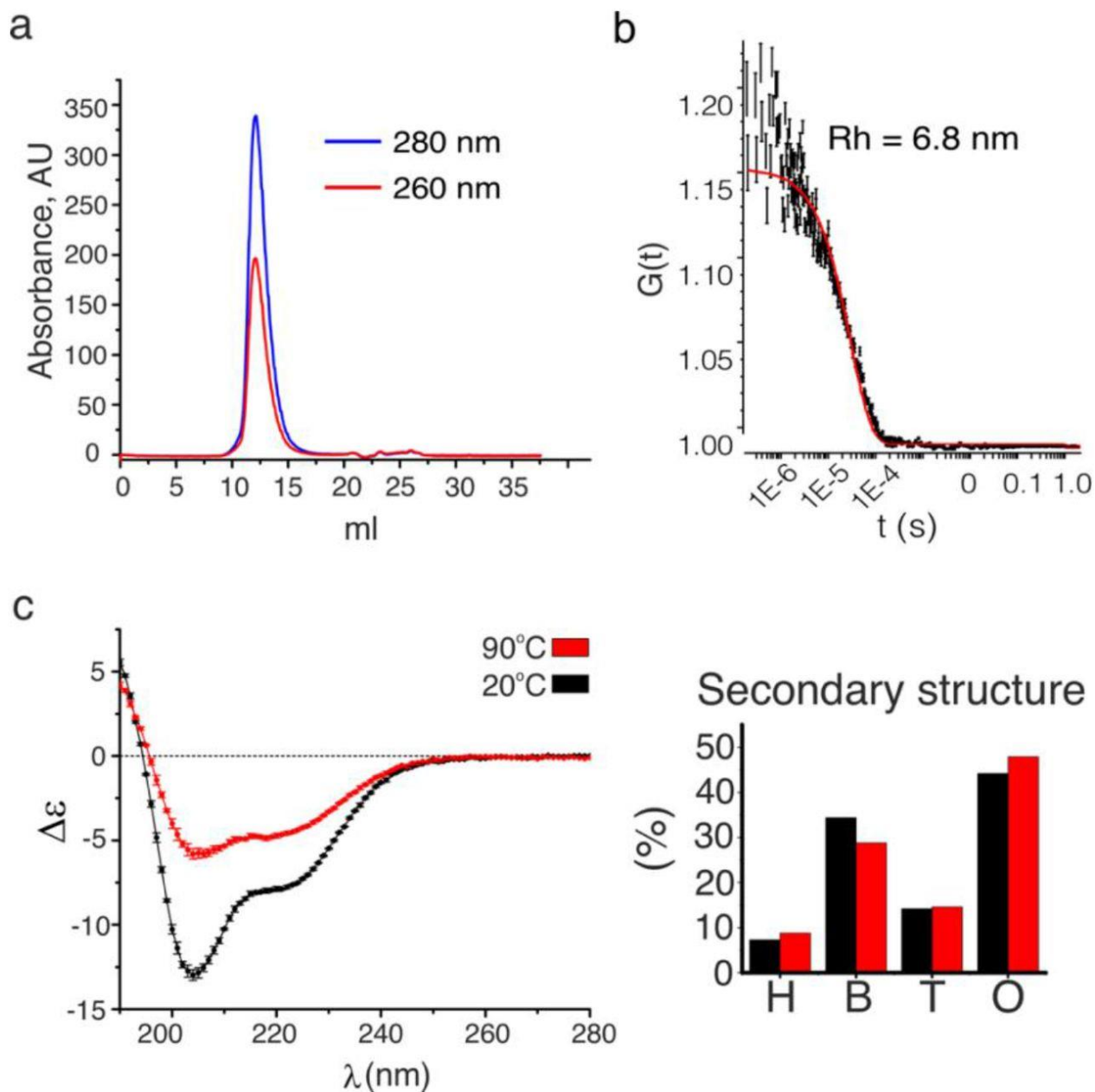


Figure S7.3: a) Size-exclusion (SEC) analysis (Superdex 200 Increase 10/300 GL) of the purified recombinant protein NSP5. After purification and refolding, the protein was monodisperse and free of nucleic acids, as judged by the A_{260}/A_{280} ratio. b) Quasi-elastic scattering analysis of the SEC peak fraction shown in a), with the calculated hydrodynamic radius, $R_h \sim 6,8$ nm. c) Circular dichroism (CD) spectra of NSP5 acquired at 25°C (black) and after thermal denaturation at 90°C (red). Secondary structure analysis of NSP5 determined by spectral deconvolution of the CD spectra recorded at 25°C (black) and after the thermal denaturation (red). H – helices, B – β -sheets, T – turns, O – disordered.

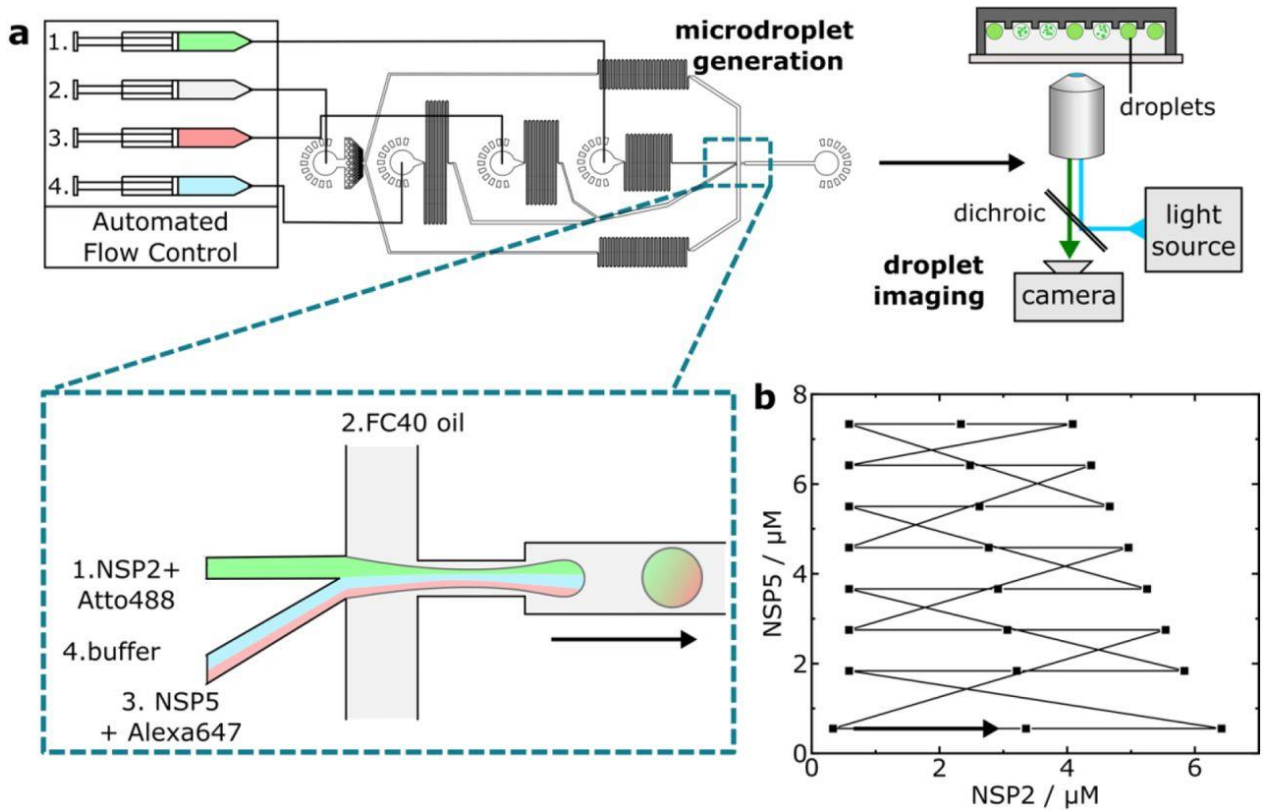


Figure S7.4: a) Droplets were generated using a microfluidic device controlled by automated syringe pumps. Combination of aqueous droplet components prior to the droplet-generating junction (inset) enables variation in droplet solution composition. Droplets are collected (6 min collection time) off-chip, before undergoing analysis by epifluorescence microscopy. b) Flow profile for NSP2 and NSP5 concentrations as produced by automated flow control in droplet generation. Flow set points (black squares) are maintained for 7 s, with the overall flow programme lasting 168 s. The arrow indicates the beginning of the continuous flow programme loop.

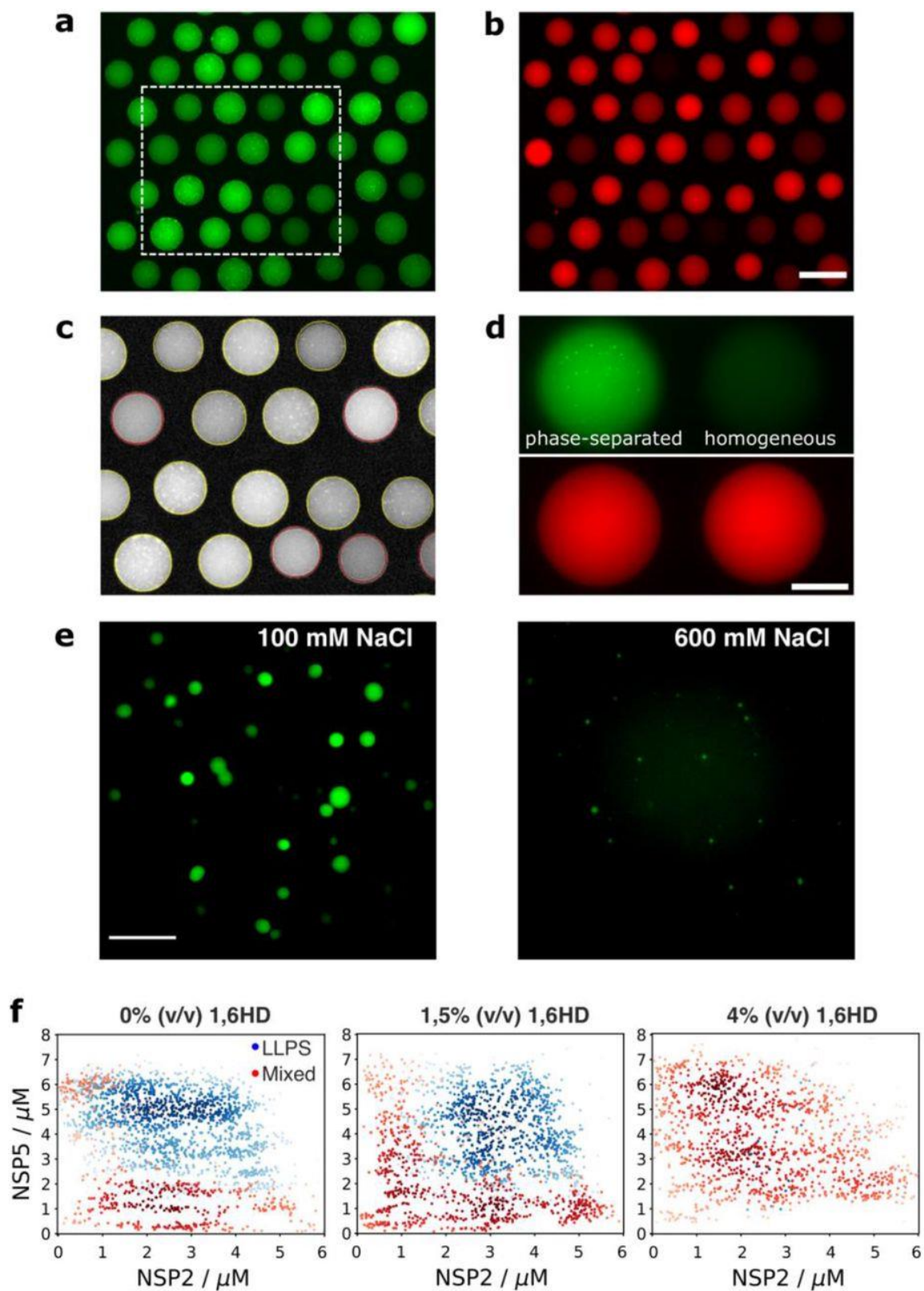


Figure S7.5: a)-d) Representative epifluorescence data for 0% v/v 1,6-hexanediol phase diagram of trapped microdroplets and barcode fluorescence imaged in a) 488 and b) 647

channels. Scale bar = 200 μm . c) Fit of droplet outlines and phase-separation classification output for region enclosed by dashed box in (a), red and yellow outlines denote droplet classification as homogeneous and phase-separated, respectively. d) Representative images of microdroplets and barcode fluorescence classified as phase-separated (left) and homogenous (right) imaged in 488 (upper) and 647 (lower) channels. Scale bar = 100 μm . e) Epifluorescence data for NSP5/NSP2 condensates (5 μM each) formed in the presence of 100 mM and 600 mM NaCl, 488 nm excitation. Scale bar = 10 μm . f) Phase diagrams generated through droplet microfluidics for the coacervation of NSP2 and NSP5, in the presence of 0% v/v (*left*) 1.5% v/v (*middle*) and 4% v/v (*right*) 1,6-hexanediol. Each point corresponds to one droplet microenvironment, with the presence or absence of phase separation denoted by red and blue colouring, respectively. The opacity of each point corresponds to the local density of data for each phase separation classification. Phase diagrams were generated from $N = 2206$, 2035 and 1470 data points for each 1,6-hexanediol concentrations, respectively.

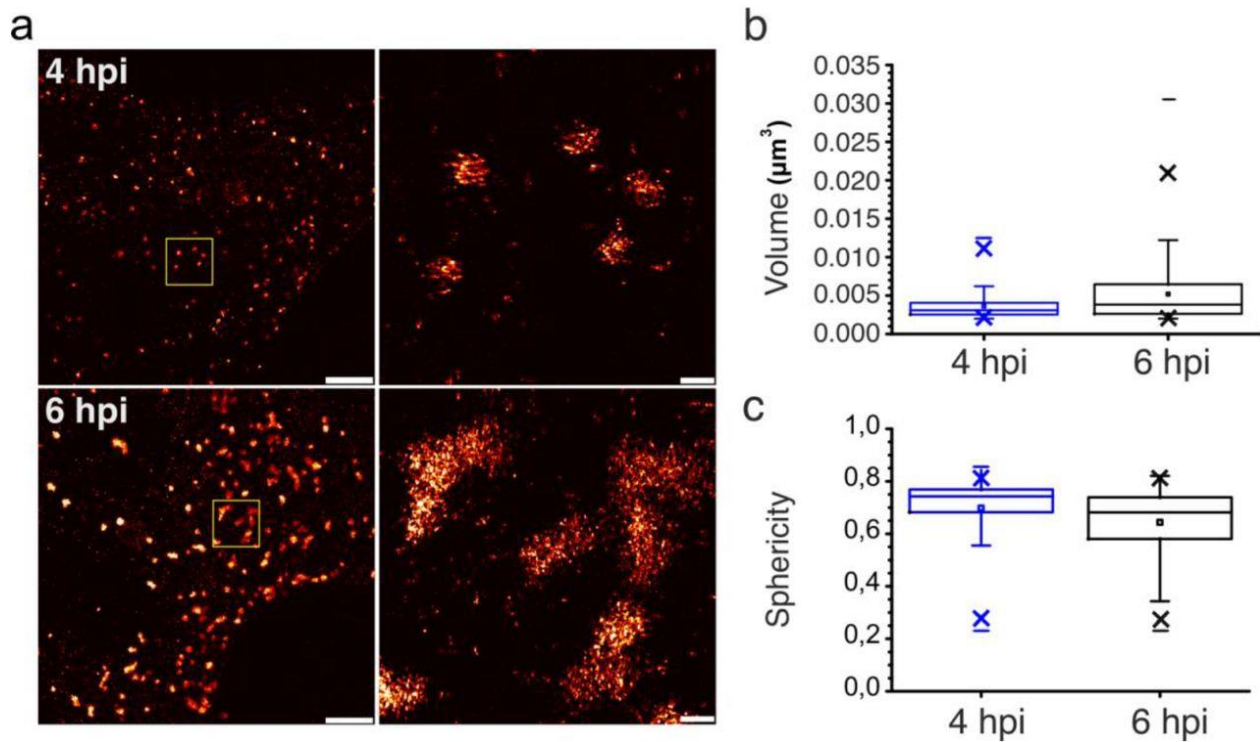


Figure S7.6: Seg3 RNA foci in RV-infected cells at 4 and 6 HPI imaged through 3D DNA-PAINT. Scale bars, 2 μm (left) and 200 nm (zoomed-in, right). b)-c) Distribution of calculated volumes and sphericities of the Seg3 RNA-containing granules in RV-infected cells at 4 HPI (N=704) and 6 hpi (N=698), shown in b). At the 0,001 level, the two distributions are significantly different between 4 and 6 hpi, assessed by the two-sample Kolmogorov-Smirnov test.

8. Conclusion and Outlook

Mechanical properties of porous hydrogels have a great impact on cancer cell migration. Their migratory phenotype is strongly influenced by fiber stiffness, confinement and their adhesion behavior. While some effects in three dimensional hydrogels resemble those on surfaces, there were also strong differences.

To investigate the influence of different hydrogel structures on single cell migration, two differently structured collagen gels were developed. High temperature (HT) gels with thin fibers and small pore sizes were polymerized at 37° C and low temperature (LT) gels with thicker fibers and larger pore sizes were handled on ice during gelation. LT gels are made of clearly visible, stiff fibers, in contrast to the thin fibers in HT gels, which are about ten times softer. The pores in both gel types are comparable to the size of cells and contain the same amount of adhesion sites, however the local amount of adhesion sites on collagen fibers is higher on the thicker fibers of the LT gels.

MDA-MB-231 cancer cells embedded in HT gels showed a slow, subdiffusive behavior with mostly round phenotypes, due to the absence of compliance. In LT gels, cells explored a larger space over time, yet the observed speed and track displacement was also small and confined. Most cells in LT gels developed pseudopods. In both gels cells showed a tendency toward backtracking. These rather slow, adhesive phenotypes were reduced by adding TGF- β to LT gels, which induced more amoeboid cells with superdiffusive behavior. The amoeboid phenotype occurs due to the decreased adhesion, induced by TGF- β and has fairly straight invasion trajectories in LT gels with a high migration speed.

Highest speeds and longest track displacements are achieved at pores that are no larger than a cell. Hence, low adhesion, pores, which are no larger than cell size, and comparably high fiber stiffness offers best conditions for migration. Here, the fiber stiffness allows for good force transmission and low adhesion prevents confinement due to long lasting focal adhesions. Accordingly, amoeboid migration is mainly observed between two parallel fibers at a distance of about cell size and slightly smaller. This allows for fairly straight movement along the parallel fibers and for easy movement without barriers for the nucleus to pass. The pseudopodial state is the state, in which cells reside most often in LT gels and from

which they switch to other phenotypes. This might be due to the inhomogeneous meshwork, within which cells have to probe the different directions with pseudopods before transitioning into the most favored phenotype. The low fiber stiffness observed in HT gels blocks force transmission along the fibers, independent of the cell behavior or phenotype, resulting in inhibited migration. Hence, sufficient fiber stiffness is a prerequisite of migration and reducing it is a save measure to inhibit migration independent of cell type. This encourages therapeutic efforts that target the extracellular matrix stiffness, which increases with age and cancer progression. A low fiber stiffness, e.g. attained by therapeutic, does not only impair movement itself, but also prevents establishment of motile amoeboid phenotypes.

To study cancer cell aggregates in highly oriented hydrogel networks, a microfluidic channel setup was introduced. The resulting collagen network preserves the flow field such that the fiber orientation mirrors the streamlines of the flow. The area around the upstream facing side of spheroids embedded in the collagen gel is an exception, due to the combination of the rod-shaped geometry of the fibers and the altered flow direction around the spheroid. This created a tangential and radial fiber orientation, at the upstream and downstream side respectively, in reference to the spheroid surface.

Invasion processes from cell aggregates involve a transition from densely packed, jammed state to an unjammed state with loose cell-cell interactions, followed by isolation of single invading cells. The influence of this specific fiber orientation leads to a biased invasion along fibers oriented radially with respect to the spheroid. This behavior was described by a model assuming Brownian diffusion with much larger step size along fibers compared to that perpendicular to them. This confirms that the bias towards faster invasion along radially oriented fibers is caused by the much larger step size, or cell speed, along fiber orientation. With further refinement of the model in the future, the influence of jamming, slippage, proliferation and other effects may be incorporated. This may provide more insight into the influence of fiber orientation on invasion and could for example decipher whether the effect of fiber orientation is mainly due to contact guidance or influenced by collective effects. In summary, the microfluidic platform presented here offers a well-defined system for studying directional bias of invasion in oriented hydrogels and its

origins. Furthermore, this system can be useful in cancer research, tissue engineering or wound healing.

Another useful technique in cancer research are cell-proliferation assays. Their sensitivity and effectivity were improved herein with a sandwich-type approach. For this purpose cells were grown in the presence of 5-ethynyl-dU (EdU) and fixed. Then, the EdU was functionalized with a dendrimer-type tetraazide via Cu^I-catalysed alkyne-azide click reactions. By adding an alkyne-modified dye via another click reaction, three dye molecules could be attached to each azide group in the DNA, instead of one. This number could be further increased by using a dendrimer-type tetraalkyne, instead of an alkyne-modified dye, in combination with an azide-modified dye. This way, nine dye molecules were attached to each azide group in the DNA. These assays yielded enhanced signal intensities, with better signal-to-noise ratios, compared to comparable commercial products. The improved signal intensities make the sandwich-type approach more suitable for imaging and high-throughput-content assays. The best results yielded the assay with three dye molecules per azide group, presumably because more dye molecules too close together resulted in quenching effects. In the future, these improved cell-proliferation assays may help detecting slowly proliferating cancer cells with high sensitivity.

This higher concentration of dyes on detection molecules was also used to improve detection of viral gene expression. The number of fluorophores on oligonucleotide probes, used in the RNA-FISH detection method, was increased via click chemistry. This allowed the use of less probe strands with more or less constant intensity at the sites of interest at the same time. Quenching effects were countered by the introduction of fluorophores that carry two negative charges each. Due to the lower number of probes necessary the off-target binding decreased and the detection of transcripts with high secondary structure content and thus limited number of binding sites became possible. This design allows a sensitive and efficient visualization, quantification and localization of RNA transcripts in live cells and enables transcript analysis using flow-cytometry. This improved FISH method could be used in early detection of virus infections to reduce the diagnostic gap and prevent uncontrolled propagation of the disease. NSP5 and NSP2 play an essential role in the

8. Conclusion

rotavirus viral genome replication and can be detected via the mRNA encoding these proteins.

Rotavirus viroplasms are ribonucleoprotein condensates that are formed from spherical inclusions of NSP5 and NSP2, via phase separation. NSP5 and the NSP2 protein form liquid condensates when mixed at low micromolar concentrations *in vitro*, or when NSP2 and the untagged version of NSP5 are co-expressed in cells. The resulting droplets were instantly dissolved when treated with aliphatic alcohols, because they disrupted multivalent interactions driving liquid–liquid phase separation (LLPS). The kinetics of NSP5/NSP2 condensate formation depends on the intracellular concentration of both NSP5 and NSP2 and only a few protein residents are required to form these condensates, with NSP5 acting as the primary scaffold. The condensates behave as dynamic fluids and change their fluidity during infection, accompanied by a changed RNA composition, ratio of RNA to protein and chemical cross-linking. These alterations make the droplets more resistant to dissolution by aliphatic alcohols. The proteins did not require phosphorylation to form condensates *in vitro*, but it plays an important role in regulating molecular selectivity and specificity of these condensates. The rotavirus replication factories also represent a unique case of specialized RNP granules that promote accumulation of viral transcripts to minimise spurious promiscuous RNA–RNA interactions with non-cognate host cell RNAs. The proposed LLPS-driven mechanism of viroplasm formation offers a unified model that explains their assembly, and suggests the RNA-protein condensates as an attractive target for antiviral intervention, due to their rapid and reversible response to external stimuli.